The Chemo-Chronodynamical Structure of the Inner Milky Way

Shola Maria Linz-Wylie

München 2022

The Chemo-Chronodynamical Structure of the Inner Milky Way

Shola Maria Linz-Wylie

Dissertation
an der Fakultät für Physik
der Ludwig–Maximilians–Universität
München

vorgelegt von
Shola Maria Linz-Wylie
aus Boston, United States of America

München, den 1 Juni 2022

Erstgutachter: Ortwin Gerhard
Zweitgutachter: Rolf-Peter Kudritzki
Tag der mündlichen Prüfung: 4. Juli 2022

"There is a theory which states that if ever anyone discovers exactly what the Universe is for and why it is here, it will instantly disappear and be replaced by something even more bizarre and inexplicable. There is another theory which states that this has already happened."
—Douglas Adams, 'The Restaurant At The End Of The Universe.'

Contents

List of Figures

Zusammenfassung

Die Milchstraße ist einzigartig unter allen Galaxien im Universum, denn wir befinden uns innerhalb der Milchstraße, was uns erlaubt diese detailliert zu untersuchen, indem wir Sterne individuell auflösen können und zu unterschiedlichen evolutionären Phasen beobachten können. Die galaktische Archäologie nutzt diesen einzigartigen Vorteil, indem die Milchstraße als Benchmark für die Überprüfung von Theorien der Formation von Scheibengalaxien und deren Entwicklung im kosmologischen Kontext dient. Während unsere Position uns diesen Vorteil liefert, ist die Sicht innerhalb der Milchstraße durch Extinktion und Überlagerung von Sternenpopulationen erschwert. Trotzdem ist es in den letzten Jahren gelungen große Vermessungen mit sehr präzisen Informationen zu der Position, Kinematik und chemischen Zusammensetzung sowie einer respektablen Altersschätzung von Millionen von Sternen innerhalb der Galaxie zusammenzustellen. In dieser Arbeit werden die hochpräzisen Beobachtungen mit den modernsten Modellen kombiniert, um die aktuelle chemisch-dynamische Struktur der inneren Milchstraße mit Fokus auf den Bulge, den Balken und deren Umgebung offenzulegen. Diese Region ist von besonderem Interesse, da Rückschlüsse auf die Entstehungsgesichte der gesamten Galaxie vom Status der inneren Galaxie geschlossen werden können.

In dieser Arbeit nutzen wir die zwei spektroskopischen Vermessungen ARGOS und APOGEE, welche den Bulge und den Balken abdecken. Die beiden Vermessungen sind komplementär zu einander, da APOGEE im Gegensatz zu ARGOS viele Sterne in niedrigen galaktischen Breitengraden beobachtet, während hingegen ARGOS eine höhere Abdeckung in den hohen galaktischen Breitengraden hat. Allerdings wurden beide Vermessungen mit unterschiedlicher Auflösung sowie in unterschiedlicher Wellenlänge beobachten und verschiedene Verarbeitungstechniken führen zu unterschiedlichen Skalierungen zwischen ARGOS und APOGEE. Im ersten Kapitel dieser Arbeit (Chapter 2) werden diese Unterschiede korrigiert, indem die datenbasierende Methode „The Cannon“ benutzt wird, um den ARGOS Katalog auf APOGEE zu rekalibrieren. Der rekalibrierte Katalog, genannt A2A Katalog, wird mit dem APOGEE Katalog kombiniert und wird für die Untersuchung der chemisch-dynamischen Struktur der inneren Milchstraße benutzt (Chapter 2). Wir untersuchen die Verteilung von Eisen und Magnesium sowie deren Elementhäufigkeitsgradienten. Darüberhinaus betrachten wir die Varianz der Metallizität und der Eisen-Magnesium Verteilung in Bezug auf die Position und Kinematik der Sterne. Die Ergebnisse lassen auf einen galaktischen Bulge und Balken mit einer komplexen und einzigartigen Struktur schließen: Ein Balken mit positiven horizontalen Metallizitätsgradienten, einem Bulge mit negativen vertikalen Metallizitätsgradienten, welcher im Zentrum abflacht, ein X-geformter Bulge, welcher ausgeprägter in Metallizität und Magnesium als in stellarer Dichte ist, und eine kinematische Abhängigkeit zwischen den Sternen des Bulges und des Balkens in Abhängigkeit der Metallizität, ausgenommen Sterne mit hoher Metallizität. Der Vergleich mit N-Body Modellen für die Struktur von Bulge und Balken befürwortet, dass die innere Milchstraße ursprünglich aus mehreren Scheiben bestand.

Während die Distanzen zu den Sternen es uns erlaubt die Elementhäufigkeitsstrukturen der inneren Milchstraße zu kartieren, habe wir keine Informationen über Bereiche, die nicht von den Vermessungen beobachtet wurden, beispielsweise zwischen den Sichtlinien der beiden Vermessungen. Allerdings liefert die revolutionäre astrometrische Vermessung Gaia kinematische 3D Informationen für die Sterne der APOGEE Vermessung in unserer Auswahl. Der zweite Teil dieser Arbeit (Chapter 3) nutzt diese Information, um die Sterne in dem aktuellsten Potential der inneren Milchstraße zu integrieren und somit die Umlaufbahnen der Sterne zu bestimmen. Die Umlaufbahnen haben den Vorteil gegenüber Beobachtungen von einzelnen Sternen, dass sie das ganze Volumen abdecken und somit es ermöglichen räumliche Lücken zu füllen. Des Weiteren setzen sich verschiedene galaktischen Komponenten durch unterschiedliche Verteilungen von Umlaufbahnen zusammen, sodass diese dadurch leichter separiert werden können. Verteilungen von Metallizität, Alter und Dichte der Umlaufbahnen werden durch die Überlagerung von den APOGEE Umlaufbahnen erstellt (Chapter 3). Diese Verteilungen zeigen eine neue Struktur, welche sich um den Balken der Milchstraße befindet: Der innere Ring. Dieser innere Ring ist elliptisch, mit starker radialer und geringer vertikaler Ausprägung bestehend aus Sternen mittleren Alters und in etwa einer Durchschnittsmetallizität der Metallizität der Sonne entsprechend. Durch den Vergleich der Altersverteilung des inneren Rings und dem flachen Balken, ergibt sich für das Alter des Balkens ein unteres Limit von 7 Gyr. Im dritten Teil dieser Arbeit (Chapter 4) werden durch Selektionsfunktionen die Umlaufbahnen der Sterne von APOGEE und A2A korrigiert, um Strukturen der inneren Milchstraße mit hohen und niedrigen Magnesiumanteil zu untersuchen. Der Ursprung von Sternen mit hohem Magnesiumanteil ist immer noch umstritten. Die Ergebnisse dieser Arbeit zeigen, dass ein Teil der Sterne mit hohem Magnesiumanteil Teil des in-situ Halo sind, eine Komponente welche durch Gaia in der lokalen Nachbarschaft beobachtet wurde, aber auf Grund der Überlagerung von verschiedenen Sternpopulationen schwer im Inneren der Milchstraße identifiziert werden kann. Viele der Sterne mit hohem Magnesiumanteil sind Teil der inneren dicken Scheibe, somit reduziert die Identifizierung von Sternen mit hohem Magnesiumanteil im inneren in-situ Halo das mögliche Phasenraumvolumen für einen klassischen Bulge.

Nimmt man die Ergebnisse zusammen, ergibt ich eine detaillierte und konsistente Sicht auf die Struktur der innere Milchstraße. Diese Sicht bietet nicht nur eine neue detaillierte Sicht auf die Sternenpopulationen im Inneren der Milchstraße, sondern liefert auch neue Erkenntnisse für die Entstehungsgesichte der Galaxie.

Abstract

The Milky Way is unique among all the galaxies in the Universe in that we reside within it allowing us to study it in great detail using individually resolved stars at different evolutionary stages. The field of Galactic archaeology exploits this unique advantage, treating the Milky Way as a benchmark to test theories of disk galaxy formation and evolution in a cosmological context. However, while our position gives us this advantage, it also comes with the cost that much of our field of view is obstructed by extinction and crowding. Despite this, in the recent years a number of large surveys have provided high precision stellar positions, kinematics, and chemistries as well as decent age estimates of millions of stars across the Galaxy. In this work, high precision observational data is combined with state-of-the-art models to reveal the current chemodynamical structure of the inner Milky Way, specifically the bulge, bar, and surrounding region. This region is of particular interest as the formation history of the entire Galaxy can be inferred from the inner Galaxy's current state.

In this work, we use two spectroscopic surveys that cover the bulge and bar, the ARGOS and APOGEE surveys. These surveys are complementary in that APOGEE observes many stars at low Galactic latitudes missed in ARGOS, while ARGOS observes many stars at high latitudes sparsely covered by APOGEE. However, the different resolutions, observed wavelengths, and data processing techniques cause scale differences between ARGOS and APOGEE. The first part of this work (Chapter 2) rectifies this using the data driven method, The Cannon, to re-calibrate the ARGOS catalog to the APOGEE scale. The re-calibrated catalog, the A2A catalog, is then combined with the APOGEE catalog and used to investigate the inner Milky Way's chemodynamical structure (Chapter 2). Detailed iron and magnesium maps are built and the abundance gradients and variance of the metallicity and iron-magnesium distributions with position and kinematics are studied. The picture that emerges from our results of a bulge and bar with a complex and unique structure: a bar with a positive horizontal metallicity gradient, a bulge with a negative vertical metallicity gradient that flattens in the central kpc, an X-shaped bulge that is stronger in metallicity and magnesium than in density, and a kinematic dependence of the bulge and bar stars on metallicity that is absent for the stars with the highest metallicities. From comparing with recent N-body bulge and bar models, these results support a multi-disc origin for the inner Milky Way.

While stellar distances allow us to map out the abundance structure of the inner Milky Way, we are still limited by not having information where the surveys choose not to observe such as in between the sight lines. However, the revolutionary Gaia astrometric survey provides 3D kinematic information for the APOGEE stars in our sample. The second part of this work (Chapter

3) uses this information, integrating the stars within a state-of-the-art bar bulge potential of the inner Milky Way to obtain their orbits. Orbits have the advantage that unlike a single star with a single position, they cover a 3D space allowing them to fill in spatial gaps not covered by the survey. Furthermore, different Galactic components are populated by different distributions of orbits making separating them easier. Metallicity, age, and orbital density maps are built through superimposing the APOGEE orbits (Chapter 3). These maps reveal a new structure encircling the Milky Way's bar: the inner ring. This inner ring is elliptical, radially thick, vertically thin, middle aged, and roughly solar in mean metallicity. Through comparing its age distribution with that of the planner bar, a lower limit for the bar's formation time is estimated to be 7 Gyr. The third part of this work (Chapter 4) uses the selection function corrected orbits of APOGEE and A2A stars to investigate the orbital structure of the high and low magnesium abundance inner Milky Way. The origin of the high magnesium stars is still debated and the results of this thesis show that a fraction of the high magnesium stars are part of the in-situ halo, a component that was previously detected with Gaia in the solar neighborhood but difficult to identify in the inner Milky Way due to the overlap of multiple populations. Many of the high magnesium stars are part of the inner thick disk, thus the detection of the inner in-situ halo further reduces the plausible phase space volume for a classical bulge.

Together the results of this thesis provide a detailed and consistent view of the inner Milky Way. This new look at the inner Milky Way not only provides a new detailed look at the stellar populations of the inner Milky Way but also gives new insights on the Galaxy's formation history.

Chapter 1

Introduction

1.1 A brief history of astronomy research

In some ways astronomy can be thought of as humanity's first science as it is one of the first instances of people recording their observations. There was good reason to do so; apart from pure curiosity, charting the positions of celestial objects allowed ancient people to keep track of time. Thus, astronomy was important for religious, agricultural, and navigational reasons.

The first recorded astronomical observations that we know of were made by the Babylonians around 1600 B.C. in which they documented the positions of planets and times of eclipses. It was only later around 500 B.C. during the Greek empire, that astronomical data was used to build cosmological frameworks based in mathematics. The philosopher, Plato, first suggested a geocentric solar system model, later developed by Heraclides, where the Moon, Sun and planets orbited the Earth on perfect circles (Editors 2021). A few decades later, the philosopher, Aristarchus, suggested an alternate model, the heliocentric model, where the moon still orbited the Earth but the Sun was at the centre with the Earth and other planets orbiting it on perfect circles (Evans 2020). For many reasons the heliocentric solar system model was largely dismissed at the time and for many centuries following it. For example, before Newton's laws of motion it was thought that if the Earth was orbiting another body then one would feel its movement which, of course, we do not. Furthermore, no parallaxes were visible in the stars which was thought should be the case if the Earth were moving along a circular orbit. Later, the astronomer and mathematician, Ptolemy, applied a mathematical framework to the geocentric model, compiled in a thirteen book series (Jones 2020, 2021). In this book he logically outlines evidence for the geocentric model such as if all objects fall towards the Universe's centre (as was believed) then the Earth must be at the centre otherwise objects, when dropped, would not fall towards the Earth's centre. Also in this work, he expands the simple geocentric solar system model of Heraclides, adding epicycles to the orbits of the planets to explain their retrograde motion. Amazingly, although we now know it is incorrect, his model could accurately predict the motions of many celestial objects.

After the fall of the Roman empire, the Roman Catholic Church adopted the Ptolemy geocentric model as doctrine and for the following centuries it was widely accepted as fact. However, with time observations became more accurate and it became increasingly difficult to predict the

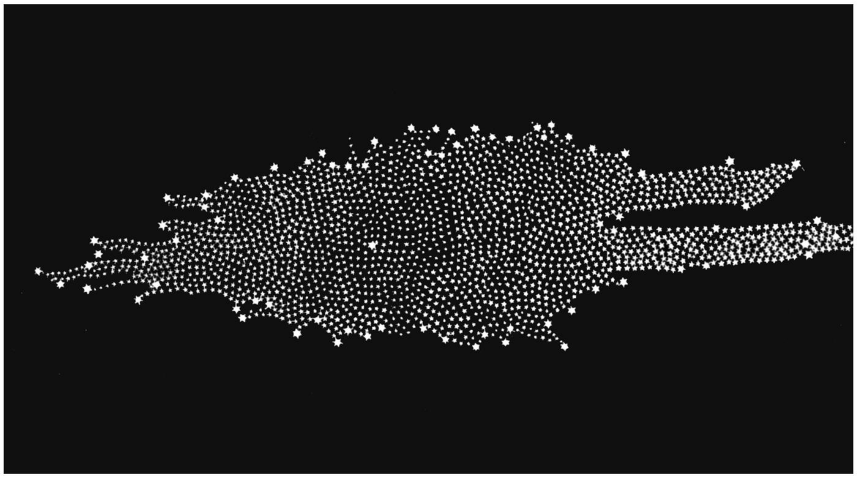

Figure 1.1: Fig. 4 from Herschel (1785) showing a stellar map of the Milky Way. The big star at the center is the Sun.

movement of celestial objects using the Ptolemy model. Furthermore, problems arose with the Ptolemy model that sewed doubt in many astronomers. For example, to predict the movement of some of the celestial objects, Ptolemy placed Earth slightly off centre invalidating the argument that Earth must be at the centre to explain why objects fall towards it. In 1500 A.D., Nicolaus Copernicus revolutionized astronomy by publishing a heliocentric model of the solar system (Westman 2022). While not simpler than the Ptolemy geocentric model, this model could also predict the positions of many celestial objects. To explain the lack of stellar parallaxes, he argued that the stars were much farther away than originally thought, thus expanding the size of the Universe in peoples' beliefs. The heliocentric model of Copernicus was very complicated partially due to him also assuming that the planets followed perfect circles. Johannes Kepler, using the meticulous data complied by the astronomer Tycho Brahe, discovered that the orbit of Mars could be easily fit by an ellipse with the Sun at one focus (Westman 2021). The motion of planets on ellipses erased the need to epicycles in the geocentric model. The final nails in the coffin for the geocentric solar system model were discovered by the astronomer, Galileo Galilei (Van Helden 2022). Using a three inch refracting telescope, he observed that the size of the planets change with their phase, something that would be impossible in the geocentric model as the planets would always remain the same distance from the Earth. He also observed moons orbiting around Jupiter; clear evidence of celestial objects not orbiting Earth. He also discovered imperfections in the Universe which destroyed the view that the solar system must be perfect. These imperfections included spots on the Sun and creators on the Moon. Lastly, Galileo observed that the Milky Way was composed of many stars, disproving the previously held belief that it was intersection between the terrestrial and celestial spheres.

Galileo's observation not only proved that our solar system was heliocentric but also that the Milky Way consists of many stars and nebulaes. In 1750, the astronomer Thomas Wright published his theory that the Milky Way was a flat sea of stars containing our solar system. In the same text he also suggests that the observed faint nebulaes could be outside of our Milky Way,

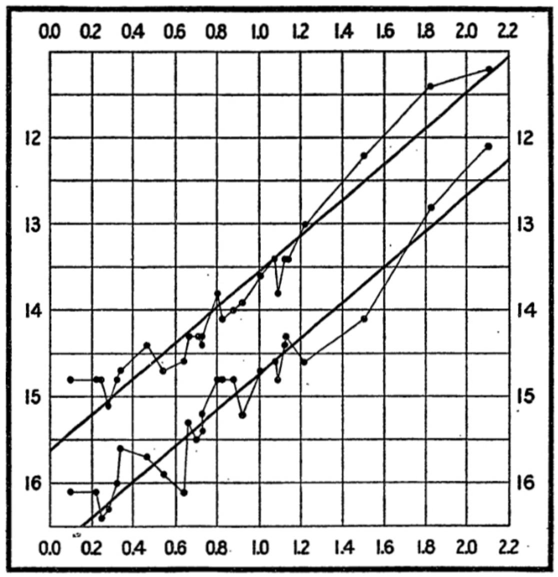

FIG. 2.

Figure 1.2: A plot from Leavitt & Pickering (1912) showing the relation between the logarithm of the period of a Cepheid star (x-axis) and its minimum and maximum magnitude (y-axis).

expanding the known Universe. In 1774, the astronomer William Herschel built the world's first large telescope and used it compile extensive stellar catalogs. He found that on one side of the sky, the density of stars was increased (Herschel 1785). Though he did not know it at the time, he was observing the dense centre of the Galaxy. He was also the first to propose a Milky Way model that was disk shaped. His model is shown in Fig. 1.1. However, he wrongly assumed that the Sun was at the centre of the Galaxy. Importantly, he also discovered that nebulae in the Messier catalogue were in fact groups of stars. Henrietta Leavitt was astronomer who worked as a computer at the Harvard College Observatory at the turn of the 19th century. Her job as a computer was to measure and catalog the brightness of stars from photographic plates. Henrietta Leavitt made the revolutionary discovery that the luminosity of a type of star called a Cepheid variable is related to its period. The plot from their paper Leavitt & Pickering (1912) showing this relation is given in Fig. 1.2. This discovery gave astronomers the first "standard candle" and a way to measure the distances to stars within 20 million light years. Previous to this discovery astronomers could only measure distance up to 100s of light years using parallax and triangulation methods. Years later the astronomer Edwin Hubble, using Cepheid variables and the relation discovered by Leavitt calculated that the Andromeda galaxy was roughly a million light-years away (we now know it is roughly 2.5 million light-years away) confirming that it is an external Galaxy. Thus the size of the known Universe was again expanded.

1.2 The Milky Way

1.2.1 How galaxies form and evolve: the ΛCDM model

The standard model of cosmological structure formation is known as ΛCDM which stands for Λ-cold dark matter. The two main principles of this model are given in its name: the cosmological constant Λ and coldness of the dark matter.

The first principle, Λ, is a term in Einstein's field equations of general relativity that represents the energy of the vacuum also known as dark energy. It is the component which exerts a negative pressure on the Universe, causing it to expand at an accelerated rate. According to the latest measurements by Planck (Planck Collaboration et al. 2020), dark energy dominates the mass-energy budget of the Universe, comprising nearly 70% of it ($\Omega_\Lambda = 0.6847 \pm 0.0073$). The rest of the budget is taken by matter with a negligible fraction from radiation. Normal matter (baryons) makes up roughly 5% of the mass-energy budget ($\Omega_b = 0.0493 \pm 0.0022$) while dark matter makes up roughly 26% ($\Omega_c = 0.2645 \pm 0.0033$). Together, these three components nearly add to one as the Universe is extremely close to being flat, though not exactly ($\Omega_k = 0.0007 \pm 0.0019$). This flatness is the result of an brief period of exponential expansion (expansion factor $\sim e^{60}$) that was triggered by an early phase transition in the Universe where vacuum energy was converted into matter and radiation. This event, known as inflation (Guth 1981), blew up initially tiny quantum fluctuations to cosmic scales, creating small density fluctuations on an otherwise homogeneous distribution.

The second principle, the coldness of the dark matter, refers to the non-relativistic velocities of its particles. This characteristic allowed cold dark matter to efficiently clump in the early Universe. The density fluctuations created during inflation quickly became amplified by gravity with small dark matter clumps merging to form larger dark matter clumps - a process called hierarchical aggregation. About 380,000 years after the big bang, the Universe had cooled enough such that baryons could decouple from radiation and begin to clump in the gravity wells already created by the dark matter. Galaxies, including our home galaxy, form in the cores of these halos as cold gas accreates and hot gas cools, condenses, and fragments there forming stars. As larger and larger dark matter halos continue to merge, groups of galaxies form creating galaxy clusters and, at larger scales, the cosmic web.

The ΛCDM model has successfully explained a large number of cosmological observations such as the Universe's accelerating expansion (Riess et al. 1998; Perlmutter et al. 1999), the statistics of cosmic microwave background (CMB) and large scale structure (Page et al. 2003), and the observed light element abundances (hydrogen, deuterium, helium, and lithium) (Steigman 2007; Iocco et al. 2009; Cyburt et al. 2016). However, there are still many issues/inconsistencies with the ΛCDM model. For example, Big Bang nucleosynthesis predicts that 5 times more lithium should be present in old, metal-poor Milky Way halo stars than what is observed (Fields 2011). This is called the Lithium Problem. However, a number of solutions have been proposed such as by varying Nature's fundamental constants, specifically the fine-structure constant, at the primordial nucleosynthesis epoch the amount of present day lithium can be increased (Clara & Martins 2020). A list of observations that are at tension with the ΛCDM model is given in Perivolaropoulos & Skara (2021).

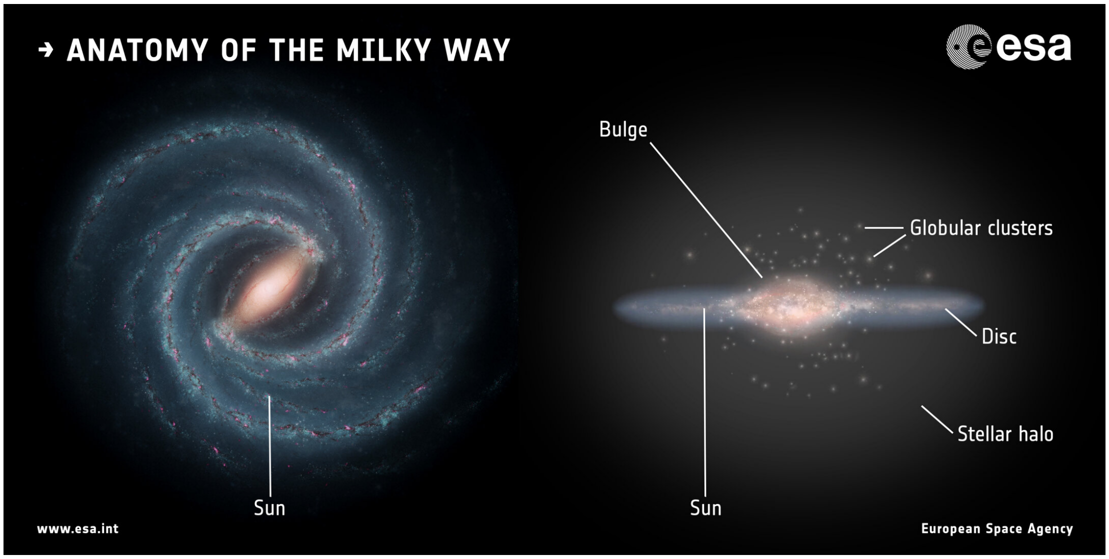

Figure 1.3: Artist's illustration of the Milky Way (left, credit: NASA/JPL-Caltech) and a schematic showing the Milky Way's main structures (right, credit: ESA).

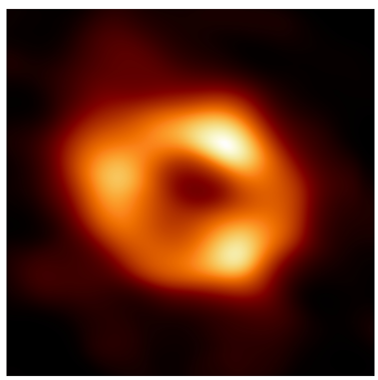

Figure 1.4: Event Horizon Telescope image of Sgr A*. Image taken from Castelvecchi (2022).

1.2.2 The Milky Way's current structure

The Milky Way is a barred spiral disk galaxy (Hubble type: SBbc, see Figure 1.3 showing an artist's impression of the Milky Way). It can be divided into four main components: the nuclear stellar bulge, the bar/bulge, the disk (thin and thick), and the halo. The inner Milky Way, the focus of this thesis, is contributed to by each of these components by varying degrees. A schematic is shown in Figure 1.3 depicting the different components. In this section we explain their basics characteristics.

The nuclear stellar bulge

In the early 1950s, radio astronomers discovered a peculiar bright radio source located within the Galaxy's central regions (Piddington & Minnett 1951). This radio source, known as Sgr A, was later officially recognized as the centre of the Galaxy by the International Astronomical Union after Oort & Rougoor (1960) showed that its location coincided with the dynamical centre of the rapidly rotating inner H1 disk. Thus, Sgr A's location marks zero longitude and latitude in the Galactic coordinate system. A few years later, it was discovered that Sgr A was actually composed of overlapping discrete components of which one was Sgr A*, a bright and compact source at $(l, b) = (-0.056°, -0.046°)$, now known to be the Galaxy's super massive black hole (SMBH) and the main emission source of Sgr A (Balick & Brown 1974; Reid & Brunthaler 2004). Since Sgr A's discovery, many authors have attempted to measure its distance (R_0) using various different methods such as direct distance measurements of H2O masers and stars near Sgr A* (Reid et al. 2009; Eisenhauer et al. 2003; Ghez et al. 2008; Gillessen et al. 2009a) and secondary estimates which determine R_0 from identifying the centroids of various populations with good distance estimates (Groenewegen et al. 2008; Majaess 2010; Griv et al. 2020, 2021). In all, Bland-Hawthorn & Gerhard (2016) finds from combining the R_0 estimates and corresponding uncertainties from many authors that the best estimate for the Galactic centre's distance is: $R_0 = 8.2 \pm 0.1$ kpc. More recently, Gravity Collaboration et al. (2019) using a star orbiting Sgr A*, S2, find a similar geometric distance to the Galactic centre of $R_0 = 8.178 \pm 0.013_{|\mathrm{stat}} \pm 0.022_{|\mathrm{sys}}$ kpc.

Confirmation that Sgr A* is a SMBH comes from measurements of its enormous mass, which is lead to it being far too dense to be explained by any other known astrophysical mechanism. The precise mass measurements were determined by Gillessen et al. (2009b) who used adaptive optics to trace the stellar orbits of roughly 30 stars within the central arcsec over 16 years. They found that all orbits, including the complete orbit of S2, are consistent with a common enclosed mass of $M_\bullet = 4.31 \pm 0.06_{|stat} \pm 0.36_{|R0} \times 10^6 M_\odot$. More recently, Gravity Collaboration et al. (2019) found a similar mass estimate of $M_\bullet = 4.154 \pm 0.014 \times 10^6 M_\odot$ from analysing the orbit of S2. The fact that our Galaxy hosts a SMBH at its centre is not surprising as central SMBHs are common in external galaxies (Kormendy & Richstone 1995; Gebhardt et al. 2003). In fact, this year (2022) the first pictures of a Sgr A*, shown in Fig. 1.4, was taken by Castelvecchi (2022) using the Event Horizon Telescope.

Surrounding Sgr A* is the densest known stellar cluster in the Galaxy, the nuclear star cluster (NSC), shown in the right plot of Fig. 1.5. NSCs are common in external galaxies and generally have radii of a few parsec, luminosities of order $10^5 - 10^8 L_\odot$, and masses of order $10^6 - 10^8 M_\odot$ which scale with host galaxy mass (Ferrarese et al. 2006; Schödel et al. 2014). The Milky Way's NSC was found by Schödel et al. (2014) though fitting a Sersic profile to SPITZER/IRAC 4.5μm data to have a total luminosity of $L_{4.5,\mathrm{NSC}} = (4.1 \pm 0.4) \times 10^7 L_\odot$ and a half-light radius of $r_{h,\mathrm{NSC}} = (4.2 \pm 0.4)$ pc. Through analysing star count and kinematic data, Chatzopoulos et al. (2015) found that the dynamical mass contained within 4 kpc is $(8.9 \pm 1) \times 10^6 M_\odot$ which assuming a Sersic model leads to a total mass for the NSC of $M_{\mathrm{NSC}} = (1.8 \pm 0.3) \times 10^7 M_\odot$. The stars composing the Galaxy's NSC are mostly old giant stars (Schödel et al. 2020), however a number of massive early-type stars have also been seen especially in the sub-parsec disk close to Sgr A* (Paumard et al. 2006; Bartko et al. 2009).

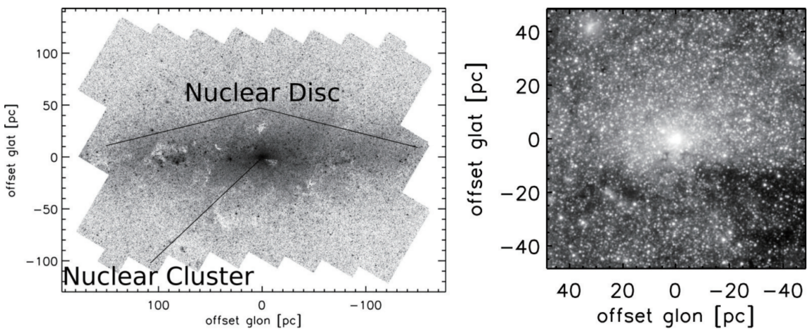

Figure 1.5: Spitzer IRAC 4.5 μm images of the nuclear disk and star cluster. Left: Extinction/dust-corrected median smoothed image of the nuclear disk and cluster. Right: Image of the nuclear star cluster. Sgr A* is at the very center of the image. Figure taken from Schödel (2021).

The NSC is itself embedded in an inner disk called the nuclear stellar disk (NSD). The NSD dominates the 3D mass distribution from $\sim$ 30 pc to $\sim$ 300 pc. By fitting axisymmetric self-consistent equilibrium dynamical models to line-of-sight velocities from the KMOS spectroscopic survey (Fritz et al. 2021) and proper motions from VIRAC, (Sormani et al. 2022) found that the NSD is very thin, with an exponential scale height and radius of $28.4^{+5.5}_{-5.5}$ pc and $88.6^{+9.2}_{-6.9}$ pc respectively, and has an estimated total stellar mass of $M_{NSD} = 10.5^{+1.1}_{-1} \times 10^8 M_\odot$ ($\sim$ 10% of the Galactic bulge's mass).Various tracers, such as OH/IR stars, SiO masers, and APOGEE stars, have been used to obtain the rotational velocity of the NSD, finding a rotational velocity of 120kms^{-1} at a radius of $\sim$ 100 pc (Lindqvist et al. 1992; Habing et al. 2006; Schönrich et al. 2015). Together, the Srg A*, the NSC, and the NSD compose the structure known as the nuclear stellar bulge (NSB), shown in the left plot of Fig. 1.5.

The bulge and bar

Bulges are dense vertically extended structures that inhabit the central kpc of disk galaxies. While they can exhibit much variety, bulges are generally classified into two main types: i) classical bulges and ii) pseudo bulges. Classical bulges form early in violent mergers that induce intense but quick bursts of star formation. They are spheroidal, featureless, and dispersion supported. Pseudo bulges form secularly through disk instabilities which redistribute a galaxy's angular momentum, driving gas and stars towards its central kpc. They are rotationally supported and undergo slow but steady star formation (Kormendy & Kennicutt 2004).

While visible with the naked eye in the southern hemisphere, the Milky Way's bulge is challenging to study due to its high extinction and crowding. However, it is now well established, and can be seen in the mid infrared unWise images in Fig 1.6, that the Galactic bulge is X-shaped (Ness & Lang 2016). This is further supported by the detection of the split red clump: two equally spaced over-densities in the red clump distribution on the near and far side of the bulge (see end of Section 1.3.1 for a discussion on red clump stars; McWilliam & Zoccali 2010; Nataf

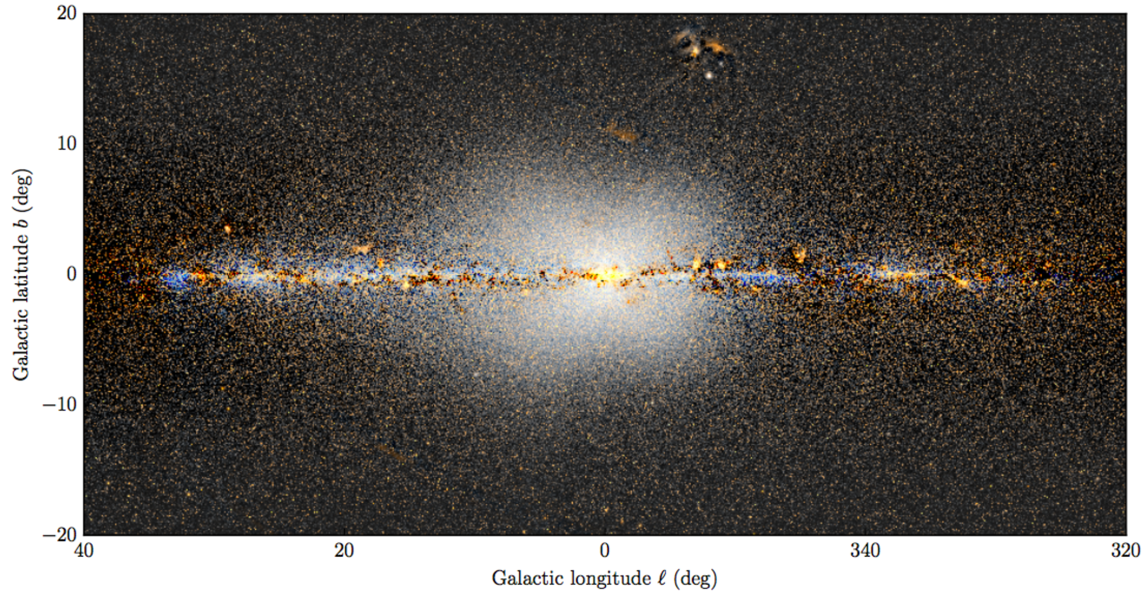

Figure 1.6: A contrast inhanced unWISE image of the Galactic bulge in the 3.4 μm and 4.6 μm bands. The bulge's X-shape is clearly visible. Figure taken from Ness & Lang (2016).

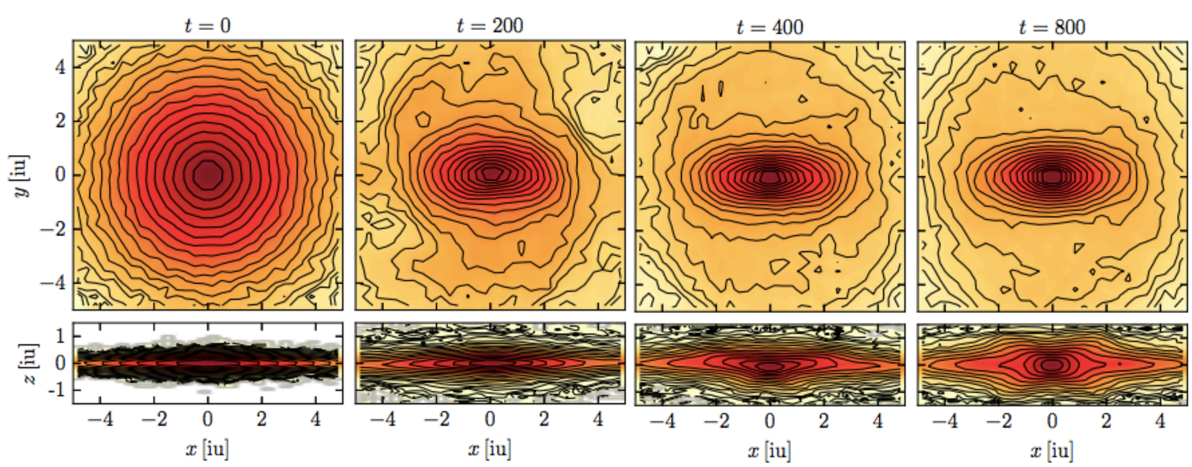

Figure 1.7: An N-body simulation of a disk forming a bar and subsequently a b/p bulge. Figure created by Matthieu Portail.

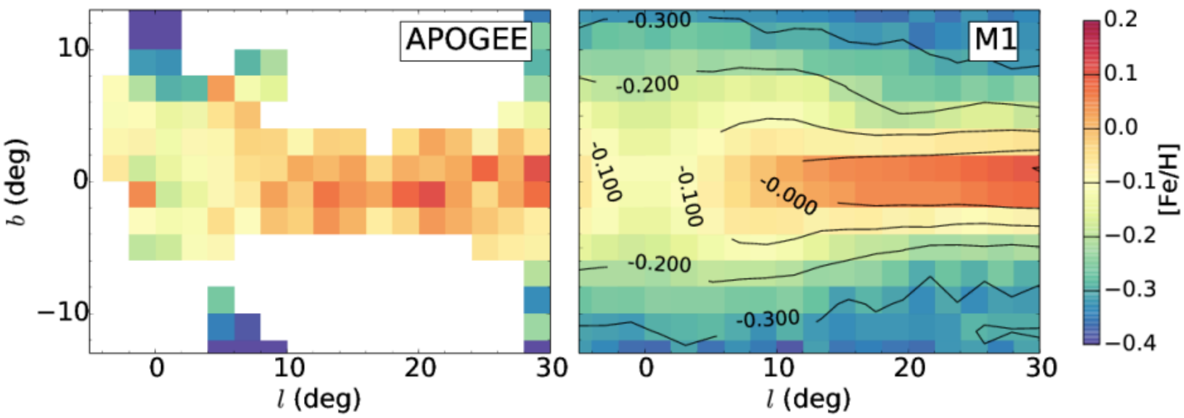

Figure 1.8: The metallicity distribution in the bulge and bar in Galactic longitude and latitude coordinates as seen by APOGEE DR13 data (left) and as predicted by the Fragkoudi et al. (2017) multi-disk model (right). Figure adapted from Fragkoudi et al. (2017).

et al. 2010). This X-shaped morphology is characteristic of a type of pseudo bulge called a boxy-peanut (b/p) bulge. A b/p bulge forms when a bar in a galaxy becomes vertically unstable and undergoes the buckling instability, causing it to 'puff-up' into a vertically extended peanut-like structure (Combes et al. 1990; Raha et al. 1991; Debattista & Sellwood 2000; Martinez-Valpuesta & Shlosman 2004). Snapshots from an N-body model that starts of as a disk and subsequently forms a bar and b/p bulge are shown in Fig. 1.7 (Courtesy of Matthieu Portail). A b/p bulge is this 3D inner region of a bar. They are common in external galaxies with Kruk et al. (2019) estimating that up to roughly 70% of disk galaxies host b/p bulges when projection effects are accounted for.

The Galactic bulge has a negative vertical metallicity gradient such that the stars that are closer to the plane are more metal rich than the stars at larger heights (Zoccali et al. 2008; Johnson et al. 2011; Gonzalez et al. 2013), see left plot of Fig. 1.8. Initially, this was taken as proof that Milky Way's bulge was a classical bulge as it was thought that violent relaxation during the bar and buckling instabilities would erase any preexisting metallicity gradients present in the initial disks (Pipino et al. 2008). However, Martinez-Valpuesta & Gerhard (2013) showed that this was not true as violent relaxation is too inefficient to do so. We now know that the gradient is the result of the fractional contributions of the different stellar populations present in the bulge changing with height i.e. the fraction of metal-rich stars decreases with increasing height, while the fraction of metal-poor stars increases (Ness et al. 2013a). Martinez-Valpuesta & Gerhard (2013) showed that an N-body disk with an initially steep radial metallicity gradient can produce a b/p bulge with a vertical metallicity gradient as stars with larger initial radii are mapped by the bar to larger heights. This model could also reproduce the cylindrical rotation, a characteristic of b/p bulges, observed in the Galactic bulge. However, Di Matteo et al. (2015) showed that such a model cannot reproduce the kinematics of the individual stellar populations when separated by metallicity. Fragkoudi et al. (2017) created an N-body b/p bulge model from three initially co-spatial disks with differing scale heights, lengths, and abundance distributions.

This b/p bulge model was not only able to reproduce the vertical metallicity gradient observed by APOGEE but also the positive horizontal metallicity gradient along the bar. The metallicity distribution in the bulge and bar predicted by this model is shown in the right plot of Fig. 1.8 while the metallicity distribution as seen by APOGEE DR13 data is shown in the left plot. While it is clear that the Milky Way hosts a b/p bulge, a small classical bulge may still be present. However, using a N-body model that well reproduces the BRAVA bulge data, Shen et al. (2010) found that a classical bulge, if present, could not have a mass greater than 8% of the Galaxy's disk mass and that a classical bulge is not needed to reproduce the observed kinematics of the Milky Way's bulge.

b/p bulges in external galaxies are observed to be embedded in planar bars that extend outside of their 3D bulge regions (Bureau et al. 2006). This is corroborated by N-body simulations which find that the buckling instability only thickens in inner regions of a bar, leaving the outer bar flat. This outer bar region is referred to as the long bar or the flat bar. The Milky Way also has a long bar extending outside of its b/p bulge. The Galactic long bar was first observed by Hammersley et al. (2000) as a stellar over density extending from the bulge region to $l \sim 28^\circ$ and later confirmed using NIR and MIR star count data from the UKIDSS and SPITZER GLIMPSE surveys (Cabrera-Lavers et al. 2007, 2008). Later, Wegg et al. (2015) used red clump stars from the combined 2MASS, UKIDSS, VVV, and GLIMPSE surveys and found that the Galactic long bar has an angle of $28^\circ - 33^\circ$ with respective to the line of sight and a half length of $R_{lb} = 5 \pm 0.2$ kpc. Additionally, Wegg et al. (2015) found evidence of two components with different scale heights in the long bar region: the thin bar component with a scale height of 180 pc who's density decreases exponentially with distance from the b/p bulge and a super thin component with a scale height of 45 pc who's density increases with distance from the b/p bulge such that it dominates at the bar end.

Together the b/p bulge and the long bar undergo solid body rotation about the Galactic centre. Their rotational frequency, called the pattern speed (Ω_b), is an essential parameter as it controls the length of the bar by setting the corotation radius (R_c), a radius beyond which x1-orbits, considered the backbone of the bar, cannot extend (Contopoulos 1980). At R_c the angular speed of disk stars on circular orbits equals the pattern speed such that in the bars reference frame, the disk stars at R_c would be stationary. Bars can slow down by transferring angular momentum to the dark halo causing the corotation radius to move outward and them to grow. Portail et al. (2017a) fit a set of N-body bulge models to multiple Milky Way bulge data sets and found that the model with a pattern speed of $39.0 \pm 3.5 \mathrm{kms^{-1}kpc^{-1}}$ provided the best fit to the data. Sanders et al. (2019) found a pattern speed of $41.0 \pm 3.0 \mathrm{kms^{-1}kpc^{-1}}$ through applying the continuity equation to Gaia and VVV proper motion data (their measurement decreases to $31.0 \pm 1.0 \mathrm{kms^{-1}kpc^{-1}}$ when including data on the far side of the bulge). More recently, Clarke & Gerhard (2022) compared a set of N-body models fit to multiple Milky Way bulge data sets using the made-to-measure (M2M) method to VIRAC proper motion data in the bulge and bar and found the model with a pattern speed of $35.4 \pm 0.9 \mathrm{kms^{-1}kpc^{-1}}$ best reproduces the data. While these measurements vary all agree that the Milky Way's bar is a long-slow bar.

As stated earlier the bulge has a clear vertically metallicity gradient. Rojas-Arriagada et al. (2020) found that the bulge's vertically gradient is -0.09 dex/kpc within 0.7 kpc from the Galactic plane and -0.44 dex/kpc between 0.7 kpc and 1.2 kpc from the plane. Outside of 1.2 kpc, they find that the gradient again flattens. Using a sample of 938 red clump stars, Wegg et al. (2019b) finds a much steeper vertical gradient in the bar region of -1.1 ± 0.2 dex/kpc. While most agree that the bulge and bar have vertical metallicity gradients, the metallicity of the bar as compared to the surrounding disk is still debated. Wegg et al. (2019b) finds that Galactic bar stars are on average more metal rich, $\langle[\mathrm{Fe/H}]\rangle = 0.3$ dex, than inner disk stars, $\langle[\mathrm{Fe/H}]\rangle = 0.03$ dex. On the other hand, using APOGEE and Gaia data, Bovy et al. (2019) finds that the bar is more metal poor than the inner disk around the bar. Hasselquist et al. (2020), in agreement with Bovy et al. (2019), using APOGEE stars finds that the end of the bar is more metal rich than the surrounding disk. Bovy et al. (2019) and Hasselquist et al. (2020) also examine the age distribution of stars in the bar and bulge. Bovy et al. (2019) finds that the bulge and bar are old and that the stars become younger towards the surrounding disk. Hasselquist et al. (2020) also finds that close to the plane the stars in the bulge are predominantly old and that their age decreases outward towards the disk. They also find a non-negligible fraction of in-plane stars with ages between 2 and 5 Gyr, metallicities between 0.2 and 0.4 dex, and distances from the centre between 2 and 3.5 kpc. The presence of young stars is in agreement with Bensby et al. (2018) who found from studying the ages of microlensed dwarf and sub-giant stars that 35% of stars with $[\mathrm{Fe/H}] > 0$ dex have ages younger than 8 Gyrs. This is at tension with CMD derived ages that consistently find that the bulge is old (Ortolani et al. 1995; Kuijken & Rich 2002; Clarkson et al. 2008; Gennaro et al. 2015). Despite the model of Fragkoudi et al. (2017) (see Fig. 1.8) reproducing the vertical and horizontal gradients of the bulge seen in the APOGEE data, it remains unclear how how the metallicity structure is connected to the dynamical structure and history of the bar.

The Galactic disk(s)

Outside the central 5 kpc, the Galactic disk, the Galaxy's most massive stellar component, dominates. The Galactic disk is rotationally supported with most stars following circular orbits about the Galactic centre. The Sun is located in the disk between two primary spiral arms at a height of 20.8 ± 0.3 pcs above the plane (Bennett & Bovy 2019). This vantage point gives us a clear view of the stellar halo and outer bulge, while complicating analyses of the large scale non-axisymmetries of the Galaxy. Furthermore, source confusion and dust make projecting the extended disk difficult. Thus, important disk parameters such as scale heights and lengths remain uncertain.

In the early 1980s, Gilmore & Reid (1983) found from analysing the stellar luminosity function of 12,500 stars towards the southern Galactic pole that the Galactic disk's vertical structure was well fit by a double exponential profile indicating the presence of two components: the thin and thick disks. This dual-disk system for the MW is not unique as observations have shown that they are common in the local universe (Yoachim & Dalcanton 2006; Comerón et al. 2011; Pinna et al. 2019). Since this discovery, much effort has been made to characterise these disks and quantify the differences between them. The most reliable measurements of the thin and thick disks' density structures come from Jurić et al. (2008) who calculated the photometric distances of $\sim 48 \times 10^6$ SDSS stars across 6500 deg^2 of the sky and out to distances of 20 kpc from the Sun allowing them to map the 3D density distribution of the nearby disk and halo. They found that the scale heights are 300 pc for the thin disk and 900 pc the thick disk. There is much more extinction in the plane of the Galactic disk than towards the poles making determination of the disk

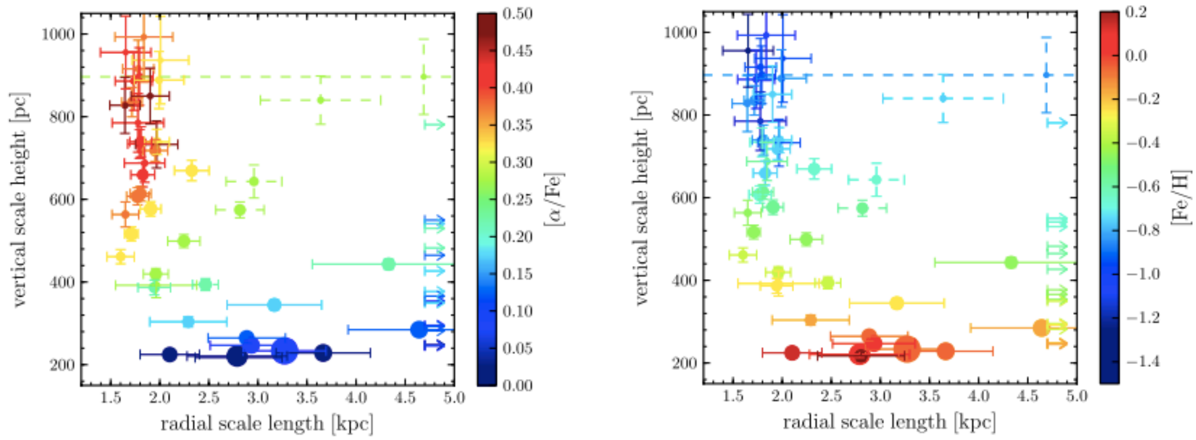

Figure 1.9: The dependence of scale length on scale height of the different sub-populations separated using [Fe/H] and [α/Fe]. Left: Scale length vs scale height colored by the [α/Fe] of the populations. Right: Scale length vs scale height colored by the [Fe/H] of the populations. The larger the markers are, the larger the total surface-mass density of the [Fe/H]-[α/Fe] distribution used to select the population is. Figure adapted from Bovy et al. (2012)

scale length(s) very difficult. Jurić et al. (2008) using M dwarfs estimated that the scale length of the thin disk is 2.6±0.52 kpc. However, Bovy et al. (2012) found that by dividing stars in the disk into small bins of [Fe/H] and [α/Fe], that each sub-population's density distribution could be fit by a single-exponential profile in both the radial and vertical directions. Furthermore, the older the population the larger scale height and the smaller scale length it had ranging from 200 pc to 1 kpc and 3 to 2 kpc and respectively, see Fig. 1.9. However, the disk is dominated by old stars. Another important parameter is the thick disk's normalisation i.e. the density of the thick disk to the thin disk: $f_\rho = \rho^T/\rho^t$. However there are large discrepancies between the values measured by different studies due to degeneracies between the normalisation and the scale lengths of the two disks. Bland-Hawthorn & Gerhard (2016) analysed the results from 25 different photometric surveys and found that $f_\rho = 4\% \pm 2\%$.

The thin and thick disks have different chemical and age distributions indicating separate formation histories. Specifically, the metallicity distributions (MDF) of the thin and thick disks have been found to peak around 0 dex and -0.5 dex respectively (Bensby et al. 2014). Furthermore, for a given metallicity the thick disk has been found to be more alpha enhanced than the thin disk (Bensby et al. 2014; Recio-Blanco et al. 2014; Fuhrmann et al. 2017). Thick disk stars are also generally older than those of the thin disk with thick disk stars having ages greater than 8 Gyr (Bensby et al. 2014). These differences indicate that the thick disk formed earlier on and under went faster chemical enrichment than the thin disk (See Sec. 1.3.2 for a discussion on alpha enrichment as a chemical clock). Lastly, due to the age velocity dispersion relation, the older stars in the disk, and thus the thick disk stars, have a higher velocity dispersion relation (Strömberg 1925; Wielen 1977). This is a result of diffusion in phase space due to gravity fluctuations.

When examining the [α/Fe] -[Fe/H] distribution in the disk, two strong over-densities appear,

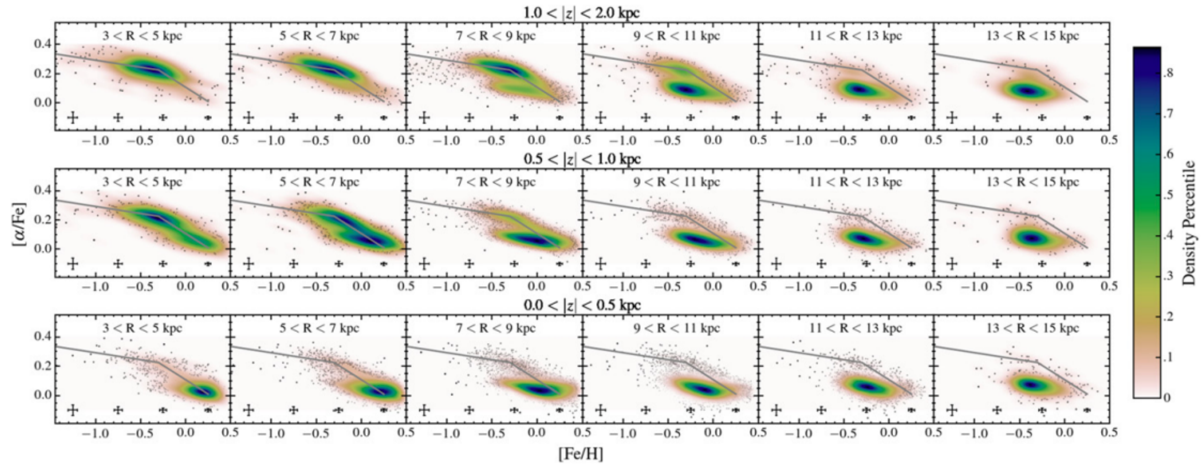

Figure 1.10: The [α/Fe] -[Fe/H] distribution of APOGEE stars as a function of radius, R, and absolute height from the plane, |Z|. Figure taken from Hayden et al. (2015).

one at low [Fe/H]-high [Mg/Fe] and one at high [Fe/H]-low [Mg/Fe] shown in Fig. 1.10. To investigate how this dichotomy arises, Grand et al. (2018) analysed a suite of high resolution cosmological zoom-in Auriga simulations of Milky Way like halos. They find that there are two main avenues to achieve this dichotomy: i) an early centralised starburst process in the inner disc; and ii) a shrinking disk process in the outer disc. In the early centralised starburst process an early and intense [α/Fe]-rich star formation period triggered by gas-rich mergers is followed by a slow little-activity period of [α/Fe]-poor star formation. In the shrinking disk process a period of [α/Fe]-rich star formation in the outer disk forms the [α/Fe]-rich sequence and is followed by a decrease in gas accretion causing the gas disk to decrease in size triggering the a drop in the star formation rate. During this period the gas becomes [α/Fe]-poor and further low metallicity gas accretion causes the [α/Fe]-poor sequence to grow. In APOGEE data in the inner disc, the α-poor sequence is at higher [Fe/H] than the α-rich sequence while in the outer disk the two sequences overlap in [Fe/H], see Fig. 1.10. This indicates that both avenues found by Grand et al. (2018) occurred in the Milky Way. Additionally, Lian et al. (2020a) presents a chemical evolution model that can reproduce the [α/Fe]-[Fe/H] distribution of the inner disk where an initial early star burst is quickly quenched and followed by period of low-level star formation and eventually a second star burst triggered by the infall of pristine gas.

The halo

The final major Galactic component is the halo which can be subdivided into three parts: the stellar halo, the gaseous halo, and the dark halo.

The classical view of the stellar halo is that of a smooth encircling stellar distribution built when the Galaxy first collapsed and further contributed to by in-falling structures such as dwarf galaxies (Eggen et al. 1962; Searle & Zinn 1978). Its stars are generally old, metal poor, α-rich and show little to no rotation. In the recent years this picture of the halo has evolved, we now

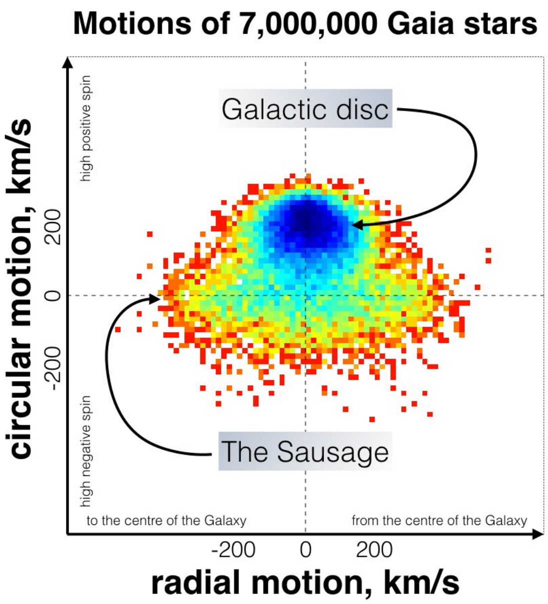

Figure 1.11: The velocity distribution of $\sim$ 7 million Gaia stars. The peaked distribution around 200 km/s in circular velocity is built from disk stars while the distribution that is extended in radial velocity and shows little rotation is built from Gaia sausage stars (notice how the distribution looks like a sausage). Credit: V. Belokurov (Cambridge, UK) and Gaia/ESA

know that the halo isn't smooth but instead shows significant substructure (Schlaufman et al. 2009; Carlin et al. 2016; Shank et al. 2022). This substructure is the remnant of accreted satellite galaxies which have yet to relax due to the halo's long dynamical timescales. Cosmological simulations predict that the Galaxy likely accreted $\sim$ 100 satellites over its lifetime of which one to two early very massive ones contributed the majority of the halos stellar mass. In fact, Belokurov et al. (2018) recently found evidence that the local stellar halo (< 30 kpc) is dominated by the debris left over from a major merger between the Milky Way and a dwarf Galaxy, dubbed the "Gaia Sausage", approximately 8-10 Gyr ago (Sahlholdt et al. 2019; Bonaca et al. 2020). Using a sample of Main Sequence stars from the Gaia DR2 and SDSS catalogs they found a huge number of stars of extremely radial orbits with little rotation, see Fig. 1.11. This velocity distribution is inconsistent with the prolonged accretion of multiple satellites but can instead by explained by a single large merger. In the solar neighborhood Haywood et al. (2018b) found that when plotting the CMD of kinematically selected halo stars, a red and blue main sequence appear. They attribute the blue sequence to the Gaia Sausage merger and suggest that the red sequence is the in-situ halo or proto disk whose orbits were heated by the merger. Belokurov et al. (2020) analysed the chemistry, ages, and kinematics of near-by bright stars and found evidence of the in-situ halo which smoothly transitions from the thick disk. Simulations show that this in-situ halo should have its highest densities in the bulge (Grand et al. 2020); see chapter 4 for further investigation.

The density distribution of the stellar halo has been studied using a variety of tracers with good distances (e.g. RR Lyrae, blue horizontal branch stars, red giants, near-main sequence turnoff stars) and has been generally fit by a spherical/axisymmetric density model with a single/double power law or a Sersic radial profile and with inner and outer flattening parameters (Deason et al. 2011; Xue et al. 2015; Pila-Díez et al. 2015; Hernitschek et al. 2018; Sesar et al. 2013). Bland-Hawthorn & Gerhard (2016) found from analysing the density profiles obtained with the different tracers that they generally agreed on an inner halo flattening and inner power-law slope of 0.65 ± 0.05 and -2.5 ± 0.3 respectively but disagreed on the outer halo flattening with RR Lyrae and blue horizontal branch studies finding no gradient in the outer flattening and red giants and near-main sequence turnoff studies finding an outer flattening of 0.8 (Xue et al. 2015; Pila-Díez et al. 2015). For the models with a double power law, the break radius has been found to be around 25 ± 10 kpc with an inner density slope of around -2.5 ± 0.3 and a steeper outer density slope ranging between -3.7 and -5.0 depending on the tracer used. Determination of the mass of the halo is tricky as it requires an estimate of total mass to tracer used as well as extrapolation to regions beyond that covered by a survey. Bell et al. (2008) estimated from fitting models with double power law density distributions to the distribution of 4 million near-main sequence turnoff SDSS stars that the mass of the stellar halo within 40 kpc was approximately $(3.7 \pm 1.2) \times 10^8 M_\odot$. Bland-Hawthorn & Gerhard (2016) added this to 50% of the mass $(2-3 \times 10^8 M_\odot)$ estimated for the four biggest sub-structures within 40 kpc, the Sagittarius Stream, the Galactic Anti-Center Stellar Structure, the Virgo Over-density, and the Hercules-Aquila Cloud estimating a total stellar mass for the halo of $4-7 \times 10^8 M_\odot$. From analyzing a 18.8 million main-sequence halo stars within 20 kpc Bond et al. (2010) found a mean rotation of 40 km/s and halo velocity dispersions of $(\sigma_r^s, \sigma_\theta^s, \sigma_\phi^s) = (141, 75, 85) \pm 5$ km/s. The dispersion in radius has been found to decrease significantly with increasing radius reaching 100 km/s at 20 kpc and 35 km/s at 150 kpc.

Diffuse hot plasmas have been observed to surround the disks of massive nearby disk galaxies (Anderson & Bregman 2011; Hodges-Kluck et al. 2018; Das et al. 2020). It is therefore not much of a stretch to assume that our Galaxy's disk is surrounded by diffuse hot plasma, i.e. a hot halo, as well. Its existence would explain the depletion of H1 gas in all dwarfs within 270 kpc (Grcevich & Putman 2009) as early heating of the gas via vigorous early star formation in the dwarfs and subsequent ram pressure stripping by a hot halo would remove it (Iorio & Belokurov 2019). Further evidence comes from the detection of gas at zero red-shift in the spectra of far away sources like AGNs (Yao et al. 2012; Gupta et al. 2012; Fang et al. 2015). These observations imply gas densities of $10^{-5} - 10^{-3} \mathrm{cm}^{-3}$ and temperatures around 10^6K for the hot halo (Stanimirović et al. 2002; Sembach et al. 2003; Henley et al. 2010; Gatto et al. 2013). Martynenko (2022) built a model assuming a power-law for the electron density radial profile and a spherical profile for the metallicity distribution which they then fit to 431 sight lines for O-VII emission and 7 electron density constraints obtained from studies of ram-pressure stripping. They derive a mass of $5.5^{+3.2}_{-3.1} \times 10^{10} M_\odot$ which is consistent with results found by other authors (Anderson & Bregman 2010; Nuza et al. 2014; Kaaret et al. 2020).

The final and most massive component of the halo is its virialized dark matter component, the dark halo. An important parameter, the viral radius (r_{vir}), is the radius within which the average density (ρ_{vir}) is equal to the critical density of the Universe times an over density constant: $\rho(< r_{vir}) = \rho_{crit}(z)\Delta_c$. The dark halo's mass is often defined as the viral mass (M_{vir}) which is the mass contained within the viral radius. Often $\Delta_c = 200$, giving another mass estimator and radius, M_{200} and r_{200} respectively. One method to obtain the viral mass is the timing mass argument (Kahn & Woltjer 1959). In this argument, the mass of the Milky Way and M31 must be large enough to explain their movement towards each other and eventual collision/merger (gravitational attraction) over coming the expansion of the Universe. Assuming that M31 is of similar mass to the Milky Way, this method provides an upper limit of $M_{vir} \lessapprox 1.6 \times 10^{12} M_\odot$ for the Milky Way (van der Marel et al. 2012; Bland-Hawthorn & Gerhard 2016). Other methods to determine the viral mass are the kinematic analysis of tracers such as halo stars, globular clusters, hypervelocity stars, streams, and satallite galaxies and analysis of the Milky Way's local escape velocity. These methods give a range of mass estimates for M_{200} of $0.46 - 2.62 \times 10^{12} M_\odot$ with the analysis of halo stars producing the lowest estimates (Dehnen et al. 2006; Xue et al. 2008; Watkins et al. 2010; Kafle et al. 2012; Gibbons et al. 2014; Necib & Lin 2022; Wang et al. 2022; Slizewski et al. 2022). Bland-Hawthorn & Gerhard (2016) compute an average mass of the Galaxy obtained from halo stellar kinematic studies of $M_{200} = 1.1 \pm .3 \times 10^{12} M_\odot$ and $M_{vir} = 1.3 \pm .3 \times 10^{12} M_\odot$. The shape of the dark halo is another important parameter. While spherically symmetric Navarro–Frenk–White (NFW) profile:

$$\rho_{\mathrm{NFW}}(r) = \frac{\rho_0}{\frac{r}{r_s}\left(1 + \frac{r}{r_s}\right)^2} \tag{1.1}$$

can to the first order approximate the density profile of dark halos, dark matter only N-body simulations have found their shapes to be triaxial/prolate. However, these simulations are missing a crucial component - baryons. When baryons are included processes such as radiative cooling, star formation, and AGN and super novae feed back produce non-linear effects causing the redistribution of angular momentum and changes to the dark matter distribution. In simulations including baryons, the final dark matter halo shapes tend to be more spherical and oblate, especially near their centres. Measurements of the Milky Way's dark halo shape have been attempted using various tracers such as halo stars (Smith et al. 2009; Loebman et al. 2014; Wegg et al. 2019a), solar neighborhood disk stars (Olling & Merrifield 2000), tidal streams (Helmi 2004; Küpper et al. 2015; Bovy et al. 2016a), globular clusters (Posti & Helmi 2019), and HI distribution flaring (Olling & Merrifield 2000; Banerjee & Jog 2011). The different tracers used result in the findings of each study applying to different spatial scales. However, when this is accounted for, the studies still show inconsistencies. Law et al. (2009) found that the inconsistencies can be partially alleviated by assuming a triaxial dark halo which results in a non-axisymmetric Galactic potential.

1.3 Galactic Archaeology

Galactic archaeology is a field of astronomy that analyses the chemistry, age, and dynamics of stars to shed light on the history of the Milky Way. Thus, precise stellar distances, chemistry, and ages are required.

1.3.1 Stellar distances

In this subsection we discuss the different methods used to obtain the distances of stars both near-by and far. As star's brightness is intrinsically linked to how we determine its distance, we therefore also discuss how the brightness of a star is measured.

The magnitude scale

The Greek astronomer Hipparchus invented a brightness scale for stars where a value of one was assigned to the brightest stars while a value of 6 was assigned to the dimmest. This assigned brightness value was called a star's apparent magnitude (m). Since the time of Hipparchus, astronomers have expanded and revised this to be a logarithmic scale such that a one apparent magnitude decrease indicates that the brightness has increased by 2.512, a two apparent magnitude decrease indicates that the brightness has increased by 2.512^2, a three apparent magnitude decrease indicates that the brightness has increased by 2.512^3, and so on. On this scale, the Sun has an apparent magnitude of $m\odot = -26.83$ mag.

What astronomers actually measure is the radiant flux F which is the number of watts of a star's light received by one square meter of detector. This value depends on both the energy emitted by the star per second, also called the star's intrinsic luminosity (L), and the distance of the star from Earth:

$$F = \frac{\mathrm{L}}{4\pi \mathrm{r}^2}. \tag{1.2}$$

The ratio of the radiant fluxes of two stars with a five magnitude difference in apparent magnitude is:

$$\frac{F_2}{F_1} = 100^{(\mathrm{m}_1 - \mathrm{m}_2)/5}. \tag{1.3}$$

A star's absolute magnitude (M) is defined as the apparent magnitude it would have if it were at a distance of 10 pc from the Sun. The difference between a star's apparent magnitude and its absolute magnitude is an important quantity called the star's distance modulus and is related to the stars distance away from Earth:

$$\mathrm{m} - \mathrm{M} = 5\log_{10}(d) - 5, \tag{1.4}$$

where d is in parsecs (see next subsection). A star's absolute magnitude can be written in terms of its intrinsic luminosity using the equation:

$$\mathrm{M} = \mathrm{M}_{\odot} - 2.5\log_{10}\left(\frac{\mathrm{L}}{\mathrm{L}_{\odot}}\right) \tag{1.5}$$

where $\mathrm{M}_{\odot} = +4.74$, the Sun's absolute magnitude (not its mass).

Distance techniques

On Earth, simple trigonometry allows the distance of a faraway mountain to be measured by calculating its difference in angular position when observed from two points separated by a known distance. This method, called trigonometric parallax, can also be applied to obtain the distances of planets in our solar system and nearby stars. However, the diameter of the Earth is too small to detect any shift in angular position of the nearby stars. Instead one must use the diameter of the Earth's orbit around the Sun, measuring the position of the stars from two points separated by 6 months in time. When the positions are measured in this manner, the stars appear to exhibit an annual back-and-forth motion with respect to the much farther away stars that remain stationary. A star's actual motion through space, its proper motion, can also sometimes be observed however this is easily separable from its apparent motion due to Earth's orbit as it is not periodic. Using trigonometry, the distance (d) can be related to the parallax angle (p) by:

$$\mathrm{d} = \frac{1\mathrm{AU}}{\tan p} \approx \frac{1}{p}\mathrm{AU}, \tag{1.6}$$

where $\tan p \approx p$ for small angles and AU is a measure of distance between the Earth and the Sun. Through converting radians to arcseconds (1 radian = 206264.806") and defining a new distance unit, parsecs (pc), as 1pc = 206264.806 AU, Equ. 1.6 can be rewritten as:

$$\mathrm{d} = \frac{1\mathrm{pc}}{p''}. \tag{1.7}$$

Thus a star 1pc away from the Sun would have a parallax of 1". Earth's nearest neighbor, Proxima Centauri, has a parallax of 0.77". For reference, if Earth's orbit were the size of a dime, then Proxima Centauri would be at a distance of 2.4 km from us. Thus, the measuring the parallaxes of stars is incredibly difficult and it is no wonder that ancient astronomers could not detect the parallaxes of visible stars and concluded that our solar system/Universe was geocentric (see Section 1.1). The first to measured the parallax of a star was Friedrich Wilhelm Bessel in 1838 who over the course of four years measured a parallax angle of 0.316" for the star 61 Cygni (distance of 3.48 pc). Nearly 200 years later, the instruments used to measure parallaxes have significantly improved. In the 1990s the European Space Agency's Hipparchus Space Astrometry Mission (Perryman et al. 1997) was able to measure the parallaxs of over 118,000 stars to accuracies of 0.001"(distances of 1000 pc). More recently, the Gaia mission, launched in 2013, determined the parallax and proper motion of over a 1 billion stars with $\sim$ 20 microarcseconds and $\sim$ 200 microarcseconds accuracy at 15 mag and 20 mag respectively. In the next data release expected in the summer of 2022, Gaia will provide the full astrometric solution (sky positions, parallaxes, and proper motions) of 1.46 billion sources (Gaia Collaboration et al. 2021).

For large distances where parallax measurements fail, astronomers can use astronomical light sources with known intrinsic luminosities called "standard candles" to determine distances. Essentially, the farther away a source is, the dimmer it will appear to an observer as the light must spread over a larger area. If the true intrinsic luminosity of a star is known, then using equations 1.5 and 1.4, the distance of the star can be determined. There are many types of standard candles with varying degrees of accuracy. For example, the periods of some pulsating stars are correlated to their intrinsic luminosity. Thus, if a star can be identified as belonging to one of these types of pulsating stars, then its intrinsic luminosity and therefore distance can be estimated from its period. Variable stars with known luminosity-period relations include Cepherid variables, RR

Lyrae variables, and Mira variables (Leavitt & Pickering 1912; Minniti et al. 2010; Luck & Lambert 2011; Genovali et al. 2014; Soszyński et al. 2014; Iwanek et al. 2021; Nikzat et al. 2022). Another standard candle is the the tip of the red giant branch (Anderson 2022; Oakes et al. 2022). After core hydrogen burning, a low mass star will begin to burn hydrogen in a shell around the core, causing helium ash to accumulate in the core. The star will then begin to decrease in temperature and increase significantly in luminosity on the H-R diagram. When the core reaches a temperature of $\sim 10^8$ K, helium burning in the core turns on and the luminosity of the star sharply decreases and the star becomes bluer (see Sec. 1.3.2 for a more through discussion). This creates a sharp discontinuity in the H-R diagram that is observable in the infared and optical. The luminosity of a star at the tip of the red giant branch is predictable as it depends on the electron-degenerate core's temperature. Thus, if a star can be identified as being at the tip of the red giant branch, then its luminosity and therefore distance can be determined. Another type of standard candle, and one that is used often in this thesis, are red clump stars (Wegg et al. 2015; Bovy et al. 2016b). Red clump stars are core helium burning stars that were once similar to the Sun. Red clump stars tend to have a luminosity independent of their rough age or composition as their cores must be roughly the same mass to have undergone the helium flash at the tip of the red giant branch. Red clump stars are common in the Galaxy and have absolute magnitudes around $M_{rc} = -1.61 \pm 0.22$ mag (Alves 2000).

Another distance determination method is isochrone fitting. In this method, the photometric magnitude and a set of spectroscopically measured parameters like effective temperature, surface gravity, and metallicity (and sometimes parallax) are used to find the closest evolutionary model track to the data. The point on the evolutionary model track that is closest to the data gives the estimated absolute magnitude of the star which using equation 1.4 can give the distance to the star. Queiroz et al. (2020) uses Bayesian isochrone-fitting to obtain the distances of 388,815 APOGEE stars including both giant and dwarf stars.

Lastly, a relatively new way to obtain the distances of stars involves machine learning in which a set of stars with known distances is used to train a model that can predict the distances of a set of stars without known distances. Leung & Bovy (2019a) uses this method to obtain the distances of 150,000 APOGEE giant stars with less than 10% uncertainty. Specifically, they create a deep neural network trained on stars common to both APOGEE and Gaia that exploits the relationship between spectra and luminosity to obtain spectro-photometric distances of giant stars. This method works for giant stars as the carbon and nitrogen abundances of red giants, information available in their spectra, is dependant upon stellar mass.

1.3.2 Stellar abundances

With the exception of the lightest elements (hydrogen, helium, and a tiny amount of Lithium), the chemical history of the Milk Way is dominated by the nuclear processes occurring within the cores of stars over many generations. Other factors such as the influence of environment type on the kinds of stars born or how the gas from stellar evolution is recycled are also important to the Galaxy's nucleogenesis. However, the best way to probe the chemical history of the Milk Way is to examine its stars.

Chemical tagging is a process where the chemical abundances in a star's photosphere, its

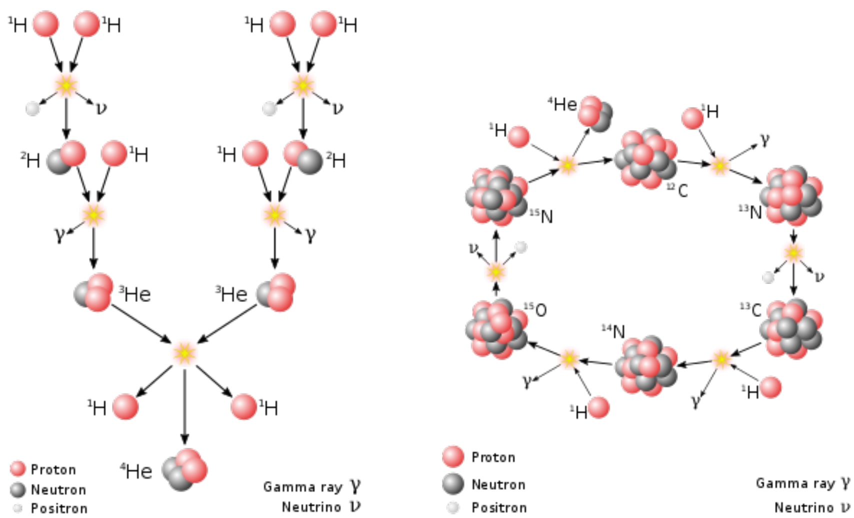

Figure 1.12: Schematic showing the pp chain (left) and the CNO cycle (right). Figure adapted from Wikipedia.

outer shell, are measured. Over most of their lifetimes, the envelopes of stars remain relatively unpolluted by nucleosynthesis, preserving the initial chemical composition of the gas (interstellar medium, IMF) they were born from. Low mass stars have lifetimes close to that of the Galaxy making them particularly useful Galactic evolution fossils. In this section we explain where heavier elements in the Galaxy come from and how they can be used to peer into the the Galaxy's past. Additionally, we explain how chemical abundance measurements are obtained as well as the relevant nomenclature.

Nucleosynthesis

A star is born when the internal pressure within a giant molecular cloud becomes insufficient to balance the cloud's self gravity triggering gravitational collapse. This imbalance occurs either because of cooling or because of external pressures which upset the cloud's delicate equilibrium. The mass at which this occurs when the role of external pressure is excluded is the Jeans mass:

$$\mathrm{M_J} \simeq \left(\frac{5k\mathrm{T}}{G\mu \mathrm{m_H}}\right)^{3/2} \left(\frac{3}{4\pi\rho_0}\right)^{1/2} \tag{1.8}$$

A single giant molecular cloud can produce 100s of stars at various masses during one episode of star formation. These stars will have roughly the same ages and chemical composition and often form gravitationally bound groups known as a star clusters (see Chapter 2 of Carroll & Ostlie (2006) for an introduction on star formation).

After star formation is finished, if the star is massive enough, it will begin core hydrogen fusion, settling it into a state of equilibrium. The rate at which this fusion occurs depends on electromagnetic forces, the gas's thermal state, and quantum tunneling probability meaning the rate is highly dependant on the gas's density, composition, and temperature. Depending on the

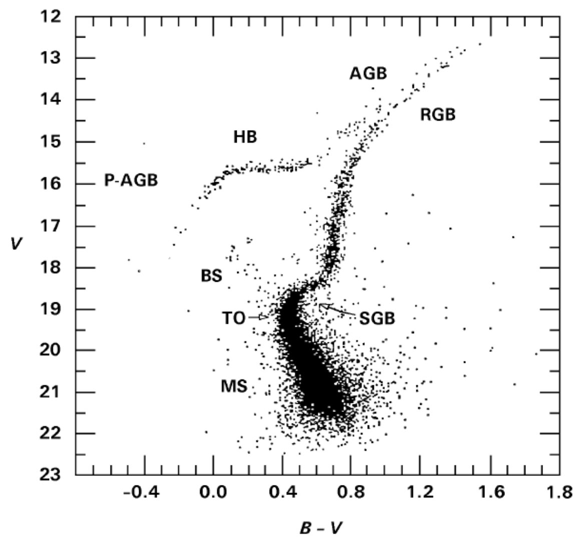

Figure 1.13: Color-magnitude diagram of the globular cluster M3. The x-axis gives the color of the stars and the y-axis gives the magnitudes of the stars in the visual band. The different evolutionary phases are labeled: main sequence (MS), sub giant branch (SGB), red giant branch (RGB), horizontal branch (HB), a asymptotic giant branch (AGB), and post-asymptotic giant branch (P-AGB). The main sequence turn-off (TO) and the blue stragglers (BS) are also labeled. Figure taken from Raffelt (2008).

mass of the star, hydrogen fusion takes place via two main channels: the pp chain and the CNO cycle. Both channels are depicted in Fig. 1.12. The pp chain starts with two protons fusing to produce a deuterium atom (^{2}H), a positron, and a neutrino. The deuterium atom then fuses with a third proton producing a ^{3}He nucleus and a gamma ray. The ^{3}He nucleus then fuses with another ^{3}He nucleus producing a stable ^{4}He and two protons. In total, the pp chain takes four protons and makes one stable ^{4}He, photons, and neutrinos. The pp chain is only an efficient fusion method for stars with masses less than 1.3 $M_{\odot}$. For higher mass stars, fusion occurs via the CNO cycle. The CNO cycle also takes four protons and creates one stable ^{4}He however unlike the pp chain it uses carbon, nitrogen, and oxygen atoms as catalysts. The phase of core hydrogen burning is called the **main sequence phase** and is the longest phase of a star's life.

When the hydrogen in the core runs out, the fusion via the pp chain or CNO cycle halts and the core begins to contract. However, the temperature of the core is so great that a shell around the core begins to fuse hydrogen to helium. The temperature of the core is so high in fact that the shell produces more energy than during core hydrogen burning causing the stars to increase in luminosity, expand its envelope and a decrease in effective temperature. The core increases in mass and becomes almost isothermal. At some point the core's mass reaches the Schönberg-Chandrasekhar limit and begins to rapidly contract which in turn causes the star to expand, cool, and become redder. This phase of the stars life is called the **sub giant branch**. Fig. 1.13 shows a color magnitude diagram for the old globular cluster, M3 (Raffelt 2008). Notice how the stars become redder on the sub giant branch as compared to the main sequence.

The expansion and cooling cause the opacity of the envelope to increase which in turn causes a convection zone to develop near the stellar surface. The depth of the convection zone increases with time and an almost adiabatic temperature gradient appears over most of the stellar interior. The convection causes the efficiency of the energy transportation to rise and the star begins to quickly travel up the **red giant branch**, the next phase of the stars life. The significant increase in luminosity along the red giant branch can be seen in Fig. 1.13 for M3. At some point the convection is so deep that material which was altered via the fusion process is brought to the surface. This is called the first dredge up. For stars with masses less than 1.8 $M_\odot$ the core contracts until it becomes strongly election degenerate. Furthermore, an inverted temperature gradient develops do to cooling from neutrino losses. At some point the temperature and density are so high that the triple α process begins (helium burning) where three helium nuclei are converted to a ^{12}C nucleus. This reaction is explosive and the generated luminosity reaches 10^{11} $L_\odot$. However, most of this energy does not reach the stellar surface instead being absorbed by the envelope. This explosion happens at the tip of the red giant branch and is called the core helium flash as it only occurs for a few seconds. Stars with masses greater than 1.8 $M_\odot$ burn helium within their cores without becoming degenerate and therefore do not undergo the helium flash. In addition to the triple α process, interactions between carbon and helium atoms slowly turns some of the carbon into oxygen.

A shell of hydrogen still burns and dominates the star's luminosity. However, the helium burning core expands, pushing the shell to larger radii, which in turn cools it causing the stars luminosity to decreases rapidly. The stellar envelope subsequently begins to contract, squeezing the hydrogen burning shell, increasing the star's energy output. The temperature rises, and both the core and envelope become convective. This causes the star to move horizontally in the color magnitude diagram (see Fig. 1.13) and this phase of its evolution is accordingly called the **horizontal branch**. At some point the mean molecular weight of the core increases so much that the core begins to contract and the envelope expands and cools. Very soon after this, helium becomes depleted in the core replaced by an inert carbon and oxygen core. A helium burning shell of develops, pushing the envelope outwards.

The next phase of evolution is the **asymptotic giant branch** where the star increases significantly in luminosity and decreases in temperature (see Fig. 1.13). During this phase two shells are burning, an outer hydrogen shell and a dominant inner helium shell. Convection again deepens with the decreasing temperature of the envelope and brings helium to the surface of the star. This is called the second dredge-up. Later along the asymptotic giant branch the two shells compete in dominance causing pulsations in the star's luminosity. The period of the pulsations is dependent upon the star's mass making pulsating stars great standard candles. Stars on the asymptotic giant branch suffer significant mass loss. The next steps of the stars evolution are highly dependant upon its initial mass. The cores of stars with initial masses less than 4 $M_\odot$ will never get hot enough to ignite further fusion. The cores of stars with initial masses between 4 $M_\odot$ and 8 $M_\odot$ undergo some further nucleosynthesis producing oxygen, neon, and magnesium.

Late in the asymptotic giant branch phase, stars loose a significant amount of mass creating thick dust clouds around the remaining star. The cloud keeps expanding and becomes optionally thin. Stars with masses between 1 $M_\odot$ and 5 $M_\odot$ then enter the **post-asymptotic giant branch** phase and become progressively bluer moving horizontally across the color magnitude diagram.

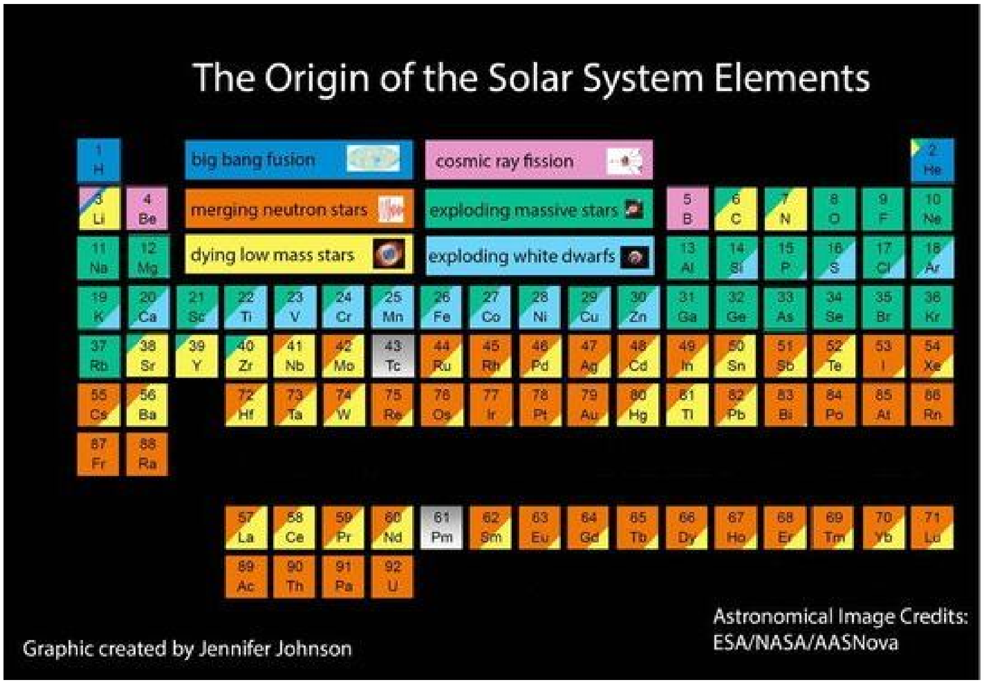

Figure 1.14: Schematic showing cosmic origin of the different elements in the periodic table. Credit: Jennifer Johnson

During this phase the star undergoes even more mass loss and looses its entire envelope revealing the hot core which will become a white dwarf. Finally, the white dwarf surrounded with expanding gas is called a planetary nebula. See chapter 13 of Carroll & Ostlie (2006) for a more in depth description of these processes.

For stars more massive than 8 $M_{\odot}$, their cores are hot enough to burn carbon, then neon, then oxygen, and eventually silicon. The end result is a iron core which cannot be burned as fuel as the fusion of iron consumes energy rather than producing it. Each burning phase is faster than the previous phase. For example, a stars with a mass of 10 $M_{\odot}$ will take 2 million years to burn helium but 1 day to burn silicon. The iron core cannot support itself against gravity and collapse triggering a supernovae (see next section). The end result is either a black hole or a neutron star.

Types of supernovae

There are a wide variety of supernovae (SN). However, following the scheme described by Filippenko (1997), they can divided into two main types: at maximum brightness Type II SN have hydrogen lines in their spectra and Type I SN do not. Type I SN can be further divided into Type Ia SN which show silicon lines, Type Ib SN which show no silicon lines but do show helium lines, and Type Ic SN which do not show silicon or helium lines at maximum brightness. There are further ways to subdivide and classify SN, however for this thesis only Type II SN and Type Ia SN are important.

Type II SN are a type of SN called core-collapse SN which occur when the cores of massive evolved stars collapse. Specifically, at the end of a massive stars life it will have an iron ash core which cannot generate further energy for the star as the reactions that generate nuclei with higher masses than iron are endothermic meaning that they require energy as opposed to producing it. At some point the contracting iron core becomes so hot that the photons can break apart heavy nuclei, a processes called photodisintegration. This process is very endothermic causing the thermal energy which supported the core to be removed. Furthermore, heavy nuclei and protons from photodisintegration capture free elections which previously contributed in supporting the star via electron degeneracy pressure. This results in a huge amount of energy escaping as neutrinos. The core then begins to rapidly collapse. Shocks generated by the collapse of the core expel the envelope and remaining nuclear-processed material. When the expelled material becomes optically thin, approximately 10^{42} J of energy are released as photons. The luminosity of this event is on the scale of the brightness of an entire galaxy. If the initial mass of the star was less than 25 $M_{\odot}$ then the core will become a neutron stars supported by neutron degeneracy. If the mass of the initial star is even greater it will become a black hole. Core-collapse supernovae produce a huge amount of α-elements and some iron-peak elements (see green elements in Fig. 1.14). See section 3 of chapter 15 of Carroll & Ostlie (2006) for a more in depth explanation.

In Type Ia SN, the lack of hydrogen spectral lines indicates that the star had its hydrogen envelope stripped prior to the SN. Type Ia SN differ from Type II SN in that they are the product of a binary stellar system. Initially, two main sequence stars orbit each other with one star being more massive and therefore evolving faster. At some point, the more massive star becomes a red giant or super giant and overflows its Roche lobe and begins to transfer mass to the less massive star. Eventually, the mass transfer rate is so high that the stars become a contact binary meaning the degerate core of the initially more massive star shares its envelope with the main sequence initially less massive star. The stars spiral inward and the envelope is ejected. What remains is a binary system with a cooling white dwarf and a main sequence star. At some point the main sequence star, the initially less massive of the two, evolves, becomes a red giant, and transfers mass to the white dwarf. Again the two stars share a common envelop which is also ejected. The second star also becomes a white dwarf and the system is two white dwarfs tightly orbiting each other. The less massive white dwarf dissolves into a disk which the other white dwarf accretes. The mass of accreting white dwarf becomes greater than the Chandrasekhar limit, the point at which electron degeneracy pressure cannot withstand self gravity, causing it to explodes as a Type Ia SN. This event produces a huge amount of iron-peak elements and is the main iron source in the Universe (see light blue elements in Fig. 1.14). See section 3 of chapter 18 of Carroll & Ostlie (2006) for a more in depth explanation.

The [α/Fe] chemical clocks

Abundance ratios can be good probes of the IMF, star formation rate (SFR), and timescales of chemical evolution. In particular, following the time-delay model of Matteucci & Greggio (1986), the ratio of α-elements (Carbon, Oxygen, Neon, Magnesium, Silicon, Sulfur, Argon, Calcium) abundance to iron abundance provides a useful chemical clock as Type II SN produce α-elements and iron and Type I SN produce no α-elements and a comparable amount of [Fe/H] as Type II SN (Maoz & Graur 2017). The reason that [α/Fe] makes a good chemical clock is

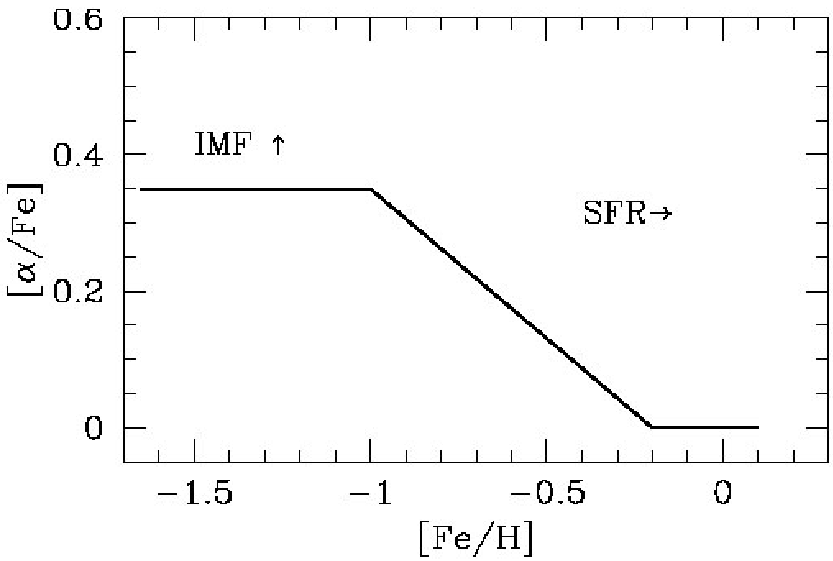

Figure 1.15: Schematic showing the evolution of [α/Fe] with [Fe/H] and how it changes with IMF and SFR. The "knee" occurs when Type Ia SN turn on. Figure taken from McWilliam (1997).

due to the timescales of SN Types I and II. Type II SN occur when a massive star runs out of fuel and its core collapses. Because massive stars burn their fuel quickly, they have short lives meaning that the production of α-elements is quick, on the scale of 40-250 Myr (De Donder & Vanbeveren 2003). On the other hand, Type Ia SN occur when a white dwarf's mass is pushed past the Chandrasekhar limit by accretion (see previous section for more details). White dwarfs are the end stage of low to intermediate mass stars and as such require much longer timescales to occur than Type II SN, on the scale of 4-5 Gyrs for the disk of a spiral galaxies (Matteucci & Recchi 2001).

Fig. 1.15 shows a schematic of the predicted chemical evolution of [α/Fe] as a function of [Fe/H]. If the SFR is high, the gas will become more enriched in [Fe/H] before the first Type Ia SN as there will be more Type II SN. Once the Type Ia SN turn on, a huge amount of [Fe/H] is produced and [α/Fe] decreases significantly. Thus the position in the schematic in Fig. 1.15 where [α/Fe] begins to decrease, known as the "knee", will be at higher [Fe/H] for higher SFRs. Furthermore, the IMF (Kroupa et al. 1993; Salpeter 1955) of a population can be predicted from [α/Fe]. Specifically, if the IMF has more massive stars there will be more Type II SN. Thus, the [α/Fe] of the plateau before the knee will be at larger [α/Fe] due to the increase in α-elements produced. Lastly, the formation timescale of a population can be approximated by the fraction of stars below the knee as the knee marks the time that the Type Ia SN turn on.

As discussed in Section 1.2.2 the disk's [α/Fe]-[Fe/H] distribution shows a clear dichotomy with the high and low [α/Fe] stars taken as the chemical thick and thin disks respectively. The [α/Fe]-[Fe/H] distribution of the disk and bulge have been used to infer their formation histories. For example, the position and strength of the two over-densities in the [α/Fe]-[Fe/H] plane vary

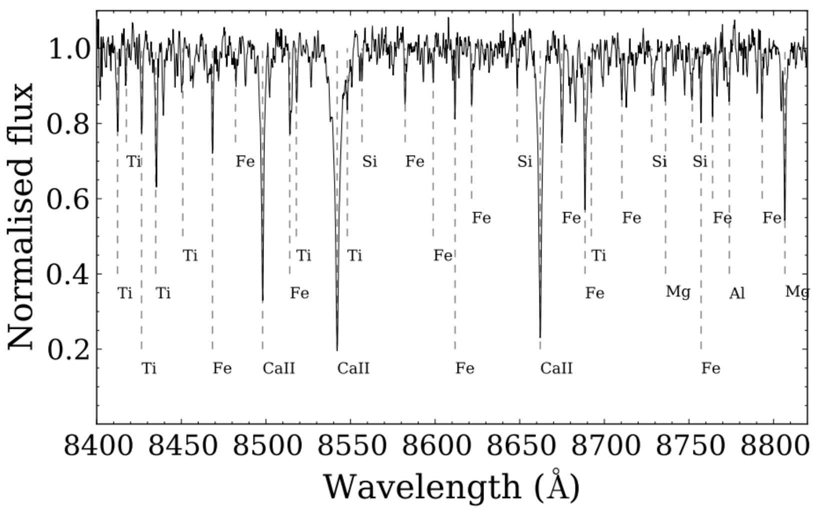

Figure 1.16: The continuum normalised spectrum in the Ca-triplet region of a red giant star taken with the AAOmega system on the Anglo-Australian Telescope. The star has T_{eff} = 4600 K, log(g) = 2.8 dex, and [Fe/H] = 0 dex. Figure taken from Freeman et al. (2012).

with position as can be see in Fig. 1.10 from Hayden et al. (2015). Through comparison of the [α/Fe]-[Fe/H] distribution in the Milky Way with those from Auriga Milky Way like galaxies Grand et al. (2018) concludes that the inner and outer disks have different star formation histories. In the inner disk there was an intense early period of star formation followed by a long period of quiescent star formation while in the outer disk there was an early period of star formation followed by a shrinking of the Galactic disk dropping the star formation rate. Lian et al. (2020b) presents a chemical evolution model that can reproduce the bulge's [α/Fe]-[Fe/H] distribution in which an initial early star burst is quickly quenched and followed by period of low-level star formation.

Measurement techniques

The deepest layers of a star's photosphere emit a bright continuous spectrum. Atoms in the photosphere's outer layers intercept this light and absorb photons to transition to higher orbitals. This creates absorption lines in the spectrum. The more atoms there are of a given element, the deeper the associated absorption lines become until they saturate. Thus, a star's elemental abundances are recorded in its spectrum. As an example, the continuum normalised spectrum in the Ca-triplet region of a red giant star with the elements producing important lines labeled is shown in Fig. 1.16.

The spectral intensity of each line, also called the equivalent width, is calculated by taking the area of the line under the continuum in the wavelength-intensity plane. A spectral line can broaden thereby increasing its equivalent width via main three processes each of which produces a unique line profile. The first, pressure broadening, dominates the wings of the line and results when collisions with neutral atoms or ions shift the orbitals of excited atoms. Due to pressure, a

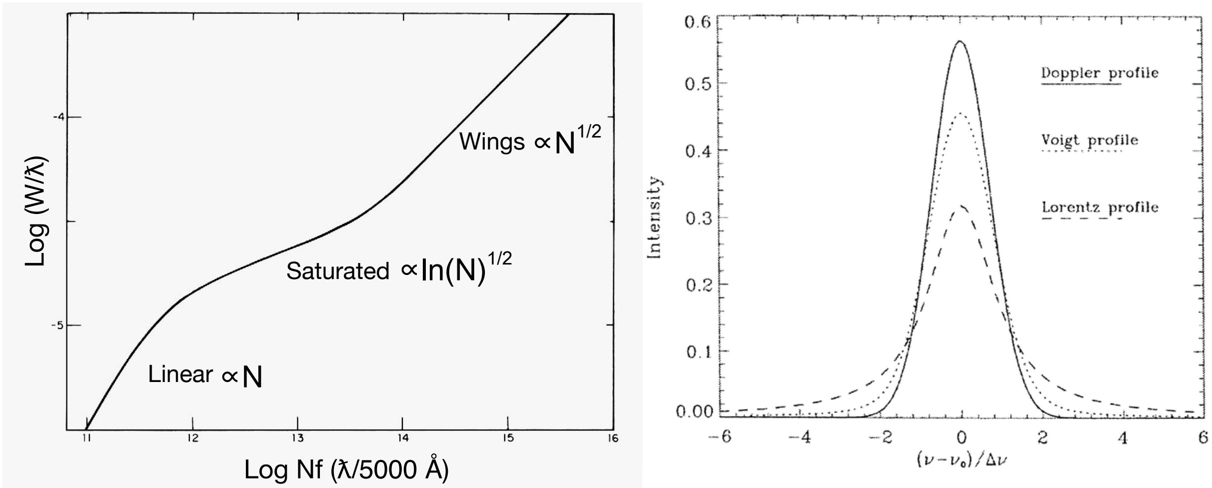

Figure 1.17: Left: The curve of growth. Figure adapted from Carroll and Ostlie, "An Introduction to Modern Astrophysics". Right: The normalized Doppler, Voigt, and Lorentz line profiles. Figure taken from Thomas & Stamnes (2002).

line broadens by:

$$\Delta\lambda \approx \frac{\lambda^2 \mathrm{n}\sigma}{\pi \mathrm{c}} \sqrt{\frac{2\mathrm{kT}}{\mathrm{m}}}, \tag{1.9}$$

and results in a line with a Lorentz profile (also called a damping profile), shown in the right plot of Fig. 1.17. The second type of broadening, Doppler broadening, dominates the centre of the line and is a result of the atoms moving. In thermal equilibrium, atoms within a gas will have velocities following the Maxwell-Boltzmann distribution. Their movement causes the absorbed/emitted light to be Doppler-shifted. Due to Doppler shifts, a line broadens by:

$$\Delta\lambda \approx \frac{2\lambda}{\mathrm{c}} \sqrt{\frac{2\mathrm{kT}}{\mathrm{m}}}, \tag{1.10}$$

and results in a line with a Doppler profile, shown in the right plot of Fig. 1.17. The last and weakest of the three main broadening types, natural broadening, is a result of the Heisenberg uncertainty principle: an excited electron occupies an orbital for some time and therefore its exact energy (wavelength) cannot be known. Due to natural broadening, a line broadens by:

$$\Delta\lambda \approx \frac{\lambda^2}{2\pi \mathrm{c}} \left(\frac{1}{\Delta t_i} + \frac{1}{\Delta t_f} \right), \tag{1.11}$$

where Δt_i and Δt_f are the lifetimes of the electron in the initial and final states respectively. The line profile created by natural broadening is also a Lorentz profile. The typical line profile comes from the combination of the pressure (dominates the wings) and Doppler profiles (dominates the core) and is called the Voigt profile, shown in the right plot of Fig. 1.17. Thus, the shape and strength of an absorption line is dependent upon the abundance of an element but also the temperature and density of the gas as well as the probabilities of the orbital transitions i.e. the oscillator strength.

The curve of growth, shown in the left plot of Fig 1.17, describes how the log of the equivalent width of a line changes with the log of the column density of the absorbing atoms. For weak lines (low density), the equivalent width grows linearly with density. As the density continues to increase, at some point the line saturates and the equivalent width is no long a good indicator of the number of atoms. Ultimately, if the density increases further, at some point the wings start to broaden again due to pressure broadening and the equivalent width becomes proportional to the square root of the number of atoms. Lines in this regime are called strong lines. Weak lines (first regime) are the easiest with which to obtain abundances. Using the curve of growth, one can use the measured equivalent width (y-axis left plot, Fig 1.17) to obtain the number of absorbing atoms per unit area (x-axis left plot, Fig 1.17). Then, using the Boltzmann and Saha equations, one can convert the number of absorbing atoms into the total number of atoms of the element in the photosphere. Errors can be reduced by performing this analysis for several lines of the same element. However, to obtain the correct curve of growth in the first place one must know the temperature and pressure of the star in question. There are multiple methods to obtain temperature and gravity. For example, using photometry, the color of a star can be used to obtain a star's temperature as bluer stars are hotter than redder stars. Spectroscopically, temperature can also be estimated by calculating the abundances from many lines of the same element over a range of excitation potentials and choosing the temperature that causes the abundance not to vary with excitation potential. Gravity can also be estimated spectroscopically. For a given star and element, the gravity can be estimated as the value that results in measured abundance being the same regardless if it was measured via neutral and single-ionized lines. For determining the temperature and gravity using spectroscopy, often iron lines are used since their are many of them over a wide wavelength range. For a review on stellar atmosphere please see Gray (2008).

With the advent of very large spectroscopic surveys automated analysis techniques are often necessary to obtain stellar abundances. Equivalent width methods can be used however they generally require high resolution spectra and a good line list (Smiljanic et al. 2014). Another technique is to compare the observed spectra with a grid of model spectra and assigning the stars the parameters/abundances of the spectra with the best χ^2 fit (García Pérez et al. 2016). This technique is quick and can work for lower resolution stars. However, a large spectral range is required to minimise degeneracies between temperature, gravity and metallicity. Furthermore, one must trust that the model spectra are accurate. To calculate model spectra, one generally requires a grid of model atmospheres (Kurucz 1979; Gustafsson et al. 2008; Mészáros et al. 2012), atomic and molecular line lists, physical equations like the Saha and energy transport equations, and the line profiles. Data driven methods are a relatively new way to determine abundances (Ness et al. 2015; Leung & Bovy 2019a). In this method, a set of reference objects with known labels (parameters/abundances) are used to train a model which relates the stellar flux at each wavelength to the labels. This model can then infer the labels of other stars in the survey. This technique has the advantage that it is fast and can transfer abundances from high to low resolution spectra. However, it is only as good as the reference set and the underlying physics is hidden (only clear in the reference set). This method is used in this work to re-calibrate the ARGOS survey, see Section 2.3 for a more detailed description.

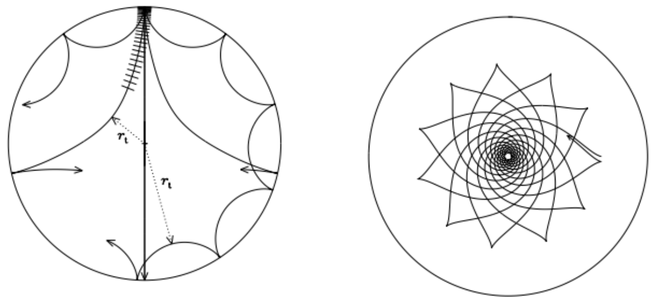

Figure 1.18: Figure taken from Di Mauro (2016) showing examples of pressure (left) and gravity (right) waves in a star.

Metals preferentially absorb blue light making stars redder. Metals increase the opacity of the gas by absorbing energy released from the interior of the star which causes the star to increase its radius, cooling it and resulting in it becoming redder. Thus, the metallicity of stars can also be estimated photometrically. The Johnson UVB filters (Johnson & Morgan 1953) can be used to estimate the metallicity of a star as the detection of an excess in the ultraviolet indicates lower metallicity as metals absorb ultraviolet light. Alternatively, the metallicities can be estimated by interpolating the de-reddened $(J - K)_0$ colors of red giant branch stars across globular cluster ridge lines as was done in Gonzalez et al. (2013) to create a metallicity map of the Galactic bulge.

Nomenclature

Unlike in chemistry, the word "metal" in astrophysics refers to all elements heavier than hydrogen and helium. The mass fraction of metals in a star is called the metallicity and is written as Z. By construction, $X + Y + Z = 1$ for a given star where X and Y are the mass fractions of hydrogen and helium. Often, the metallicity relative to that of the Sun is given and defined as $[M/H] = \log\left(\frac{Z}{Z_\odot}\right)$ where the Sun's metallicity is $Z_\odot = 0.0134$ (Asplund et al. 2009).

The metallicity of a star can be difficult to obtain as it requires all elemental abundances in a star to be measured. Instead, the iron abundance of a star, which is easy to measure, is often used as a proxy for its metallicity and is expressed as the ratio of iron to hydrogen atoms in the star with respect to the Sun: $[Fe/H] = \log\left(\frac{N_{Fe}}{N_H}\right) - \log\left(\frac{N_{Fe}}{N_H}\right)_\odot$. As this is a logarithmic scale, a star with $[Fe/H] = 0$ dex would have the same iron abundance as the Sun while a star with $[Fe/H] = -1$ dex would have 1/10th the iron abundance of the Sun. Often in literature, including this thesis, the word "metallicity" refers to the iron-abundance. Other abundances in a star are also commonly expressed as their number fraction to hydrogen with respect to the Sun. For example, $[Mg/H] = \log\left(\frac{N_{Mg}}{N_H}\right) - \log\left(\frac{N_{Mg}}{N_H}\right)_\odot$.

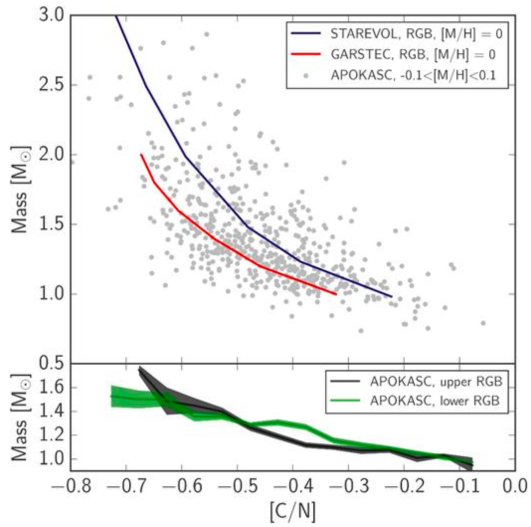

Figure 1.19: The top panel shows the relationship between stellar mass and [C/N] abundance of APOKASC stars (grey points) and that predicted by the stellar evolution models of Weiss & Schlattl (2008) (red) and Lagarde et al. (2012) (blue). The mean mass versus [C/N] of APOKASC stars on the upper and lower red giant branch is shown in the bottom panel. Figure taken from Martig et al. (2016).

1.3.3 Stellar ages

A variety of techniques with differing degrees of precision have been developed over the years to obtain stellar ages, the most difficult stellar parameter to measure.

The standard method to determine stellar ages is isochrone fitting which exploits the fact that a star's luminosity and color (or equivalently surface gravity and temperature) change with age. Because stars of higher masses evolve faster, they will be at a later stage of evolution as compared to a lower mass star with the same age. An isochrone is a track in the color magnitude diagram that connects stars with the same age but different masses and is obtained from stellar evolution models. Isochrone fitting involves comparing a star's luminosity and color with a grid of isochrones. Once the metallicity of a star is known, precise age estimates can be obtained for stars at certain evolutionary stages such as the main sequence turn-off and the sub-giant branch. Isochrone fitting works particularly well for stellar clusters which are composed of stars born from the same cloud and therefore are of roughly the same age and chemical compositions but of different masses/evolutionary stages. An isochrone can be fit to the distribution of the stellar cluster's stars in the color magnitude diagram and the age of its stars can be obtained, see Fig. 1.13 for an example of a cluster's color magnitude distribution. The age precision of isochrone fitting generally ranges from 20% for advanced main-sequence stars to 120% for zero-age main-sequence stars (Prada Moroni et al. 2016). Feuillet et al. (2016) estimated the ages of local giant stars observed with the APOGEE spectrograph and with known distances using Bayesian isochrone matching and obtained age uncertainties of ~ 0.2 dex in log(age).

Another method to determine stellar ages is asteroseismology. Similar to how geologists on

Earth can infer the Earth's internal structure through studying seismic waves, astronomers can infer the internal structures of stars, including our Sun, by studying their oscillations though photometric and radial velocity measurements. These oscillations are produced by the constructive interference of standing waves within a star which result in resonant modes. The waves can be classified into two types, pressure waves and gravity waves, shown in Fig. 1.18. The mass of a star can be estimated from maximum frequency ($\nu_{\rm max}$) and spacing in frequency of the oscillation modes of pressure waves ($\Delta\nu$) using the following relation:

$$\left(\frac{M}{M_\odot}\right) = \left(\frac{\nu_{\rm max}}{\nu_{\rm max\odot}}\right)^3 \left(\frac{\Delta\nu}{\Delta\nu\odot}\right)^{-4} \left(\frac{\rm T_{eff}}{\rm T_{eff\odot}}\right)^{3/2} \tag{1.12}$$

where $\Delta\nu\odot = 135.03\mu$Hz, $\nu_{\rm max}\odot = 3140\mu$Hz, and $\rm T_{eff} = 5777$K (Hekker et al. 2013). Ages with uncertainties of $\sim 30\%$ (Gai et al. 2011; Chaplin et al. 2014) can be derived though comparison of the seismic data with evolutionary models (Stello et al. 2009; Basu et al. 2010; Casagrande et al. 2014). This method only works for solar-type and giant stars and spectroscopy is required to obtain the temperatures and chemical compositions of the stars. Over the years, a number of space missions, such as COROT (COnvection, ROtation and planetary Transits Auvergne et al. 2009), Kepler (Gilliland et al. 2010), and TESS (Transiting Exoplanet Survey Satellite Ricker et al. 2015), have been designed to observe changes in stellar brightness and detect acoustical waves within stars.

A relatively new age determination method is to train a model on reference set with good ages that can take as input stellar parameters/abundances and output stellar ages. Once trained, this model can be applied to stars without age estimates to obtain their ages. Martig et al. (2016) trained a model that could predict the masses of APOGEE Dr12 stars to 14% fractional rms errors and ages to 40% rms errors from their photospheric carbon and nitrogen abundances and spectroscopic log(g), $\rm T_{eff}$, and [Fe/H] values. The [C/N] abundance observed in the envelope of a red giant star is related to its mass and therefore age because the [C/N] abundance in its core and the depth at which its convective envelope reaches during the dredge up phase (see Section 1.3.2) depends on the mass of a star. The relationship between mass and [C/N] abundance using APOKASC stars is shown in Fig. 1.19. APOKASC stars are APOGEE stars also observed by Kepler giving them accurate age estimates (Pinsonneault et al. 2018). Bovy et al. (2019) also created a catalog of ages for the APOGEE survey using a similar data driven method, however they trained the model on stars with known asteroseismic ages to predict the stellar ages directly from the spectra. They estimate that their catalog has a typical age precision of 30%. Their ability to obtain ages from the spectra likely is due to the presence of Carbon and Nitrogen molecular bands in the APOGEE spectra.

The ages of Galactic bulge stars have been measured using a variety techniques with a range of accuracies. Interestingly, as discussed in Section 1.2.2, different techniques have given conflicting answers. For example, CMD derived ages generally find that the bulge is predominately old with little presence of young populations (Ortolani et al. 1995; Kuijken & Rich 2002; Clarkson et al. 2008; Gennaro et al. 2015). On the other hand, a nonnegligible fraction of microlensed bulge dwarfs have been found to have ages (determined via isochrone fitting) less than 8 Gyr (Bensby et al. 2018). Data driven methods have also found young bulge stars (Hasselquist et al. 2020).

1.4 Goal and outline of the thesis

In this thesis we use the wealth of photometric, spectroscopic, and astrometric data available to us to investigate the current chemo-chronodynamical structure of the inner Milky Way, home of the nuclear stellar bulge, b/p bulge, and bar (Sections 1.2.2 and 1.2.2) but also of the inner regions of the disks and halo (Sections 1.2.2 and 1.2.2). Through constraining the Milky Way's current structure we infer its formation history.

Chapter 2 describes the current chemical structure of the inner Milky Way. Precise stellar distances (Section 1.3.1) and abundances (Section 1.3.2) from the A2A and APOGEE surveys are used to map in detail inner Milky Way's 3D chemical structure. Through comparison with theoretical predictions from N-body models the inner Milky Way is found to have had a multi-disc origin. Additionally in this chapter, the creation of the A2A catalog is described. Specifically, a data driven method (Section 1.3.2) is used to re-calibrate the ARGOS catalog parameters and abundances to the scale of the APOGEE catalog. The resulting A2A catalog is consistent with the APOGEE catalog.

Chapter 3 extends on Chapter 2, using the orbits of APOGEE stars to build detailed chemical (Section 1.3.2) and age (Section 1.3.3) maps of the inner Milky Way with a particular focus on the in-plane structures. As orbits fill a 3D volume, the coverage of the inner Milky Way is increased and Galactic structures become more apparent. A new Galactic structure encircling the Galactic bar (Section 1.2.2), a thick inner ring, is revealed. Through comparisons of the age distributions in the different structures, a lower limit for the formation time of the bar is estimated.

Chapter 4 describes the dissection of the bulge and bar region into the different components contributing to it using both APOGEE and A2A orbits. Evidence is found that while most of the magnesium-rich stars (Section 1.3.2) are part of the inner thick disk (Section 1.2.2), a significant fraction belong to the in-situ halo - a component previously detected in the solar neighborhood (Section 1.2.2). This finding makes the presence of a classical bulge (Section 1.2.2) even less likely as the available parameter space is decreased significantly.

Chapter 5 concludes this thesis, summarising its main findings and explaining what they mean in a larger context. Finally, a few potential future projects are described that both improve on the work described here but also will reveal new insights on the Milky Way's current and past structure.

Chapter 2

A2A: 21,000 bulge stars from the ARGOS survey with stellar parameters on the APOGEE scale

Original publication: Shola M. Linz-Wylie, Ortwin E. Gerhard, Melissa K. Ness, Jonathan P. Clarke, Kenneth C. Freeman, and Joss Bland-Hawthorn, 2021, A&A, 653, A143

Abstract

Spectroscopic surveys have by now collectively observed tens of thousands of stars in the bulge of our Galaxy. However, each of these surveys had unique observing and data processing strategies that led to distinct stellar parameter and abundance scales. Because of this, stellar samples from different surveys cannot be directly combined. Here we use the data-driven method, *The Cannon*, to bring 21,000 stars from the ARGOS bulge survey, including 10,000 red clump stars, onto the parameter and abundance scales of the cross-Galactic survey, APOGEE, obtaining rms precisions of 0.10 dex, 0.07 dex, 74 K, and 0.18 dex for [Fe/H], [Mg/Fe], $T_{\rm eff}$, and log(g), respectively. The re-calibrated ARGOS survey – which we refer to as the A2A survey – is combined with the APOGEE survey to investigate the abundance structure of the Galactic bulge. We find X-shaped [Fe/H] and [Mg/Fe] distributions in the bulge that are more pinched than the bulge density, a signature of its disk origin. The mean abundance along the major axis of the bar varies such that the stars are more [Fe/H]-poor and [Mg/Fe]-rich near the Galactic centre than in the outer bulge and the long bar region. The vertical [Fe/H] and [Mg/Fe] gradients vary between the inner bulge and the long bar, with the inner bulge showing a flattening near the plane that is absent in the long bar. The [Fe/H]-[Mg/Fe] distribution shows two main maxima, an '[Fe/H]-poor [Mg/Fe]- rich' maximum and an '[Fe/H]-rich [Mg/Fe]-poor' maximum, that vary in strength with position in the bulge. In particular, the outer long bar close to the Galactic plane is dominated by super-solar [Fe/H], [Mg/Fe]-normal stars. Stars composing the [Fe/H]-rich maximum show little kinematic dependence on [Fe/H], but for lower [Fe/H] the rotation and dispersion of the bulge increase slowly. Stars with [Fe/H] < -1 dex have a very different kinematic struc-

ture than stars with higher [Fe/H]. Comparing with recent models for the Galactic boxy-peanut bulge, the abundance gradients and distribution, and the relation between [Fe/H] and kinematics suggests that the stars comprising each maximum have separate disk origins with the '[Fe/H]-poor [Mg/Fe]-rich' stars originating from a thicker disk than the '[Fe/H]-rich [Mg/Fe]-poor' stars.

2.1 Introduction

The Milky Way bulge is notoriously difficult and expensive to observe due to the high extinction along our sight line to the Galactic centre (GC). Nevertheless, over the past two decades the number of spectroscopically observed bulge stars has increased from a few hundred to tens of thousands thanks to multiple spectroscopic stellar surveys, such as ARGOS (Freeman et al. 2012), *Gaia*-ESO (Gilmore et al. 2012), GIBS (Zoccali et al. 2014), APOGEE (Majewski 2016), and *Gaia* (Cropper et al. 2018).

The extensive coverage of these spectroscopic surveys has led to many novel discoveries and has vastly improved our understanding of bulge formation and evolution. We know from its wide, multi-peaked metallicity distribution function (MDF) that the bulge is composed of a mixture of stellar populations. This is further supported by the different populations, defined by their metallicities, exhibiting different kinematics (Hill et al. 2011; Ness et al. 2013b; Rojas-Arriagada et al. 2014, 2017; Zoccali et al. 2017). Through careful chemodynamical dissection, the bulge has been found to contain stars that are part of the bar, inner thin, and thick disks, as well as a pressure-supported component (Queiroz et al. 2021). Furthermore, there is evidence that the bulge also contains a remnant of a past accretion event, the inner Galaxy structure (Horta et al. 2021). Multiple age studies of the bulge have reported that while the bulge is mainly composed of old stars (~10 Gyr), it contains a non-negligible fraction of younger stars (Bensby et al. 2013, 2017; Schultheis et al. 2017; Bovy et al. 2019; Hasselquist et al. 2020).

While analysis of these surveys has greatly improved our understanding of the bulge, direct comparisons of studies that use different survey data, as well as combinations of the measurements of the stars from different survey pipelines, are problematic. This is because different surveys use different selection criteria, wavelength coverage, and spectral resolution. Furthermore, they employ different data analysis methods, assume different underlying stellar models, and make different approximations to derive stellar parameters and individual element abundances from their spectra (see Jofré et al. 2019 for a review).

Despite these inconsistencies, analyses that employ stars from different surveys are often compared, leading to uncertainty as to whether the results reflect intrinsic properties of the Galaxy or if they are simply due to different observing and data processing strategies. For example, Zoccali et al. (2017) and Rojas-Arriagada et al. (2017) find bi-modal bulge MDFs using data from the *Gaia*-ESO and GIBS surveys, Rojas-Arriagada et al. (2020) finds a three-component bulge MDF using data from the APOGEE survey, and Ness et al. (2013a) finds a five-component bulge MDF using data from the ARGOS survey. Because the stars in these surveys have not been observed and analysed in the exact same manner, it is unclear whether these differences in the bulge MDF arise because of different parameter and abundance scales or because of different selection functions.

In this paper we use the data-driven method, *The Cannon* (Ness et al. 2015), to put 21,000 stars from the Galactic bulge survey ARGOS onto the parameter and abundance scales of the cross-Galactic survey APOGEE. Of these 21,000 stars, there are roughly 10,000 red clump (RC) stars with accurate distances. By rectifying the scale differences between the two surveys, we can combine them and gain a deeper coverage of the Galactic bulge. We call the re-calibrated ARGOS catalogue the A2A catalogue as we are putting ARGOS stars onto the APOGEE scale. Then, using the combined A2A and APOGEE surveys, we investigate the chemodynamical structure of the bulge. Specifically, we examine how the iron abundance and magnesium enhancement vary over the bulge as well as their kinematic dependencies.

The paper is structured as follows: In Sect. 2.2 we describe the ARGOS and APOGEE surveys as well as highlight the inconsistencies between them that make directly combining them questionable. In Sect. 2.3 we summarise the technical background of *The Cannon*. In Sect. 2.4 we explain how we apply *The Cannon* to the ARGOS catalogue to create the A2A catalogue. In Sect. 2.4 we describe the three validation tests we performed to verify that the label transfer was successful. In Sect. 2.5 we discuss the selection functions of the A2A and APOGEE surveys. In Sect. 2.6 we use the A2A and APOGEE catalogues to examine the abundance structure of the Galactic bulge. In Sect. 2.7 we discuss the results of the paper in more detail, and, finally, in Sect. 2.8 we end the paper with our conclusions.

2.2 Data

In this section, we provide some background on the data used in this paper before discussing their main properties.

2.2.1 ARGOS

The Abundance and Radial Velocity Galactic Origin Survey (ARGOS; Freeman et al. (2012); Ness et al. (2013a,b)) is a medium resolution spectroscopic survey designed to observe RC stars in the Galactic bulge. Using the AAOmega fibre spectrometer on the Anglo-Australian Telescope, ARGOS observed nearly 28,000 stars located in 28 fields directed towards the bulge. The field locations are shown as green ellipses in Fig. 2.1. The observations were performed across a wavelength region of 840−885 nm at a resolution of R $= \lambda/\delta\lambda \simeq 11,000$, where $\delta\lambda$ is the spectral resolution element.

The ARGOS team determined the iron abundance ([Fe/H]), surface gravity (log(g)), and alpha enhancement ([α/Fe]) of each star in their catalogue using χ^2 minimisation to find the best fit between the observed spectra and a library of synthetic spectra. The local thermodynamic equilibrium stellar synthesis program MOOG (Sneden et al. 2012) was used to generate the library of spectra. The effective temperature ($T_{\rm eff}$) was determined from the stellar colours $(J - K_s)_0$ using the calibration by Bessell et al. (1998). For more information about the ARGOS parameter and abundance determination process see Freeman et al. (2012).

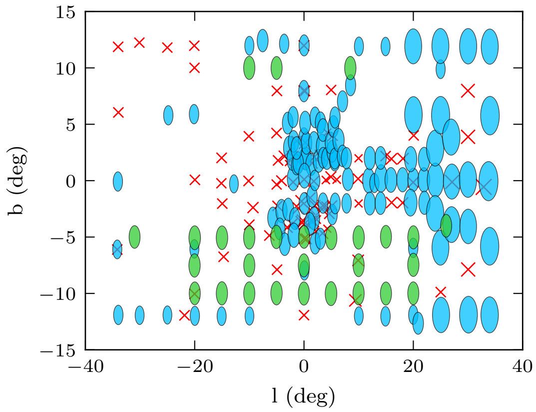

Figure 2.1: Locations of the APOGEE (blue ellipses and red crosses) and ARGOS (green ellipses) bulge fields. The red crosses indicate APOGEE fields that either have no or poor SSF estimates. The marker size indicates the field size.

The ARGOS catalogue used in this paper contains 25,712 stars and corresponding spectra from the original 28,000 observed. The missing stars were removed because they had a low signal-to-noise ratio (S/N) and poor quality spectra (Freeman et al. 2012). The number of pixels of each ARGOS flux array is 1697. To process the data, we re-normalised the remaining ARGOS spectra by dividing each by a Gaussian-smoothed version of itself, with the Calcium-triplet lines removed, using a smoothing kernel of 10 nm. We also transformed each spectrum to a common rest frame and masked out the diffuse interstellar band at 8621 nm. We also masked out the region around 8429 nm as we found that this region has a strong residual between the mean spectra of positive and negative velocity stars, indicating that it is systematically affected by the velocity shift.

2.2.2 APOGEE

The Apache Point Observatory Galactic Evolution Experiments (APOGEE; Majewski (2016)) is a programme in the Sloan Digital Sky Survey (SDSS) that was designed to obtain high resolution spectra of red giant stars located in all major components of the Galaxy. The survey operates two telescopes: one in each hemisphere, with identical spectrographs that observe in the near-infrared between 1.5μm to 1.7μm at a resolution of $R \simeq 22,500$. In this work, we use the latest data release, DR16 (Ahumada et al. 2019), which is the first data release to contain stars observed in the southern hemisphere. The locations of the APOGEE fields used in this work are shown in Fig. 2.1 as blue ellipses and red crosses.

Stellar parameters and abundances of the APOGEE stars used in this work were obtained from the APOGEE Stellar Parameters and Chemical Abundance Pipeline (ASPCAP; García Pérez et al. (2016); Holtzman et al. (2018); Jönsson et al. (2020)). This pipeline used the radiative transfer code Turbospectrum (Plez et al. 1992; Plez 2012) to build a grid of synthetic spectra. The parameters and abundances were determined using the code FERRE (Allende Prieto et al. 2006), which iteratively calculated the best-fit between the synthetic and observed spectra. The fundamental atmospheric parameters, such as log(g), T_{eff}, and the overall metallicity, were determined by fitting the entire APOGEE spectrum of a star. Individual elemental abundances were determined by fitting spectral windows within which the spectral features of a given element are dominant.

We obtained spectrophotometric distances for the APOGEE stars from the AstroNN catalogue (Leung & Bovy 2019b; Mackereth et al. 2019a), which derived them from a deep neural network trained on stars common to both APOGEE and *Gaia* (Gaia Collaboration et al. 2018).

In this work, we specifically focused on APOGEE stars located in fields directed towards the bulge with $|l_f| < 35°$ and $|b_f| < 13°$ where l_f and b_f are the Galactic longitude and latitude locations of the fields. We removed six fields that were designed to observe the core of Sagittarius. We required the stars to be part of the APOGEE main sample (MSp) by setting the APOGEE flag, EXTRATARG, to zero. We refer to this sample as the APOGEE bulge MSp. To ensure that the stars we use have trustworthy parameters and abundances, we also required the stars to have valid ASPCAP parameters and abundances, $S/N \geq 60$, $T_{eff} \geq 3200$ K, and no Star_Bad flag set (23rd bit of ASPCAPFLAG = 0). After applying these cuts, there are 172 remaining bulge fields containing 37, 313 stars. For reference, we refer to this sample as the HQ APOGEE bulge MSp.

In the analysis sections of this work, unless explicitly stated otherwise, we further restrict our APOGEE sample to only stars for which we can obtain good selection function estimates. This sample contains 23, 512 stars and we refer to it as the HQSSF APOGEE bulge MSp. (See Sect. 2.5.2 for further details on this sample.)

2.2.3 Survey inconsistencies

After the removal of potential binaries though visual inspection of individual spectra, we found 204 stars that were observed by both the APOGEE and ARGOS surveys. Using these stars we can determine whether the surveys are consistent by checking that they derive the same parameters and abundances for the same stars.

In Fig. 2.2 we compare the [Fe/H], α-enhancements, T_{eff}, and log(g) of the common stars. The ARGOS α-enhancement is the average of the individual α-elements over iron ([α/Fe]). For APOGEE stars, ASPCAP provides individual α-elements with respect to iron ([Mg/Fe], [O/Fe], [Ca/Fe], ...) as well as an average of the α-elements to metallicity ([α/M]). For our comparisons, we chose the ASPCAP magnesium enhancement ([Mg/Fe]) because magnesium is produced only by supernova-II with no contribution from supernova-Ia. The bias and rms of each distribution are given in the upper left hand corner of each plot. The bias was calculated by subtracting the APOGEE values from the ARGOS values and taking the mean of the differences.

The [Fe/H] comparison in the first plot of Fig. 2.2 shows that the surveys roughly agree between ~ -0.75 dex and ~0 dex (limits in APOGEE [Fe/H]) with a scatter of ~0.16 dex. However, beyond these limits, the deviation between the surveys increases, reaching up to ~0.4 dex. The α-enhancement magnesium-enhancement comparison in the second plot shows that the ARGOS [α/Fe] estimates are on average ~0.07 dex larger than the APOGEE [Mg/Fe] estimates. If we instead compare the ARGOS [α/Fe] estimates to the APOGEE [α/Fe] estimates, then the bias and rms of the distribution are larger at 0.12 dex and 0.15 dex, respectively. The T_{eff} comparison in the third plot shows that the ARGOS T_{eff} estimates are on average ~300 K hotter than the APOGEE T_{eff} estimates. Finally, while there is a lot of scatter, the log(g) comparison in the last plot shows that the ARGOS log(g) values are generally higher than the APOGEE log(g) values.

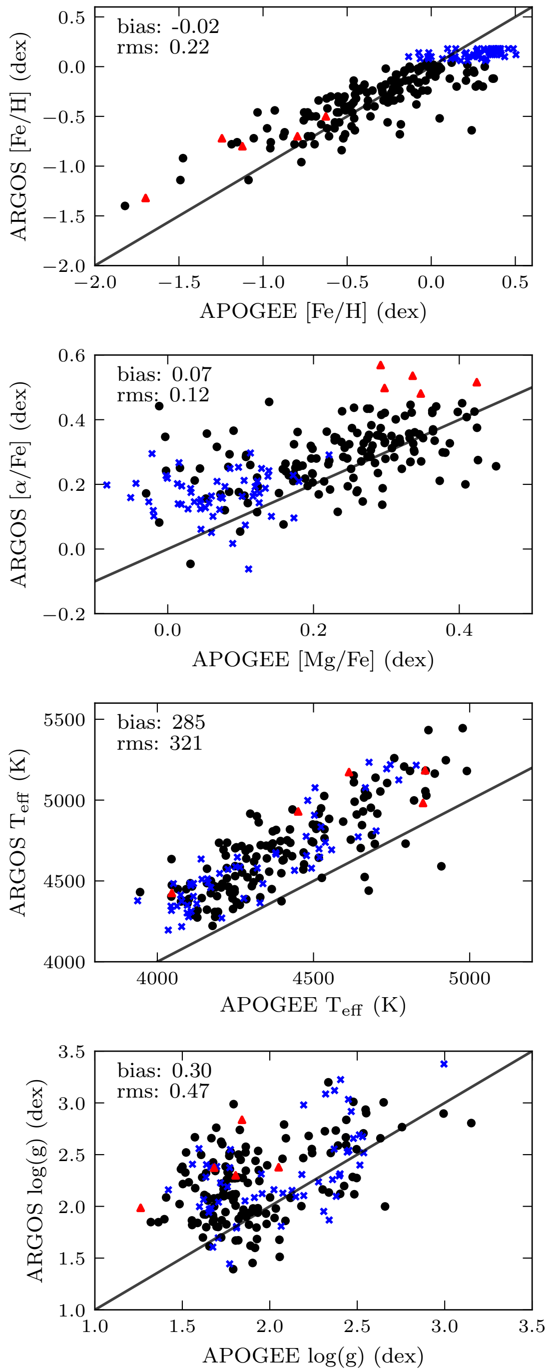

Figure 2.2: APOGEE-derived parameters (x axis) versus ARGOS derived parameters (y axis) for the 204 reference set stars observed by both surveys. The bias (mean of the differences) and rms of the distributions are given in the upper left hand corner of each plot. The reference set stars that are within one ARGOS observational error, 0.13 dex (0.1 dex), from the maximum [Fe/H] ([α/Fe]) value reached by the reference set are plotted as blue crosses (red triangles).

The parameter comparisons show that for most of the common stars, the APOGEE and ARGOS parameters differ significantly. This could be due to a number of factors, such as observing in different wavelength regions (e.g. optical in ARGOS versus infrared in APOGEE), their use of different data analysis methods (e.g. photometric temperatures in ARGOS versus spectroscopic temperatures in APOGEE), or their use of different stellar models. In the following sections, we use the data-driven method, *The Cannon*, and this set of common stars to bring the APOGEE and ARGOS surveys on to the same parameter and abundance scales, thereby correcting the deviations we see in Fig. 2.2.

2.3 The Cannon method

The Cannon is a data-driven method that can cross-calibrate spectroscopic surveys. It has the advantage that it is very fast, requires no direct spectral model, and has measurement accuracy comparable to physics based methods even at lower S/N. *The Cannon* has been previously used to put different surveys on the same parameter and abundance scales using common stars (Casey et al. 2017; Ho et al. 2017; Birky et al. 2020; Galgano et al. 2020; Wheeler et al. 2020).

The Cannon uses a set of reference objects with known labels (i.e. $T_{\rm eff}$, log(g), [Fe/H], [X/Fe] ...), which describe the spectral variability well, to build a model to predict the spectrum from the labels. This model is then used to re-label the remaining stars in the survey. The word 'label' is a machine learning term that we use here to refer to stellar parameters and abundances together with one term. The set of common stars used to build the model is called the reference set.

The Cannon is built on two main assumptions: (i) stars with the same set of labels have the same spectra and (ii) spectra vary smoothly with changing labels.

Consider two surveys, A and B, where we want to put the stars in survey A onto the label scales of survey B using *The Cannon*. Assume we also have the required set of common stars between the two surveys to form the reference set. To cross calibrate the surveys, *The Cannon* performs two main steps: the training step and the application step. During the training step, the spectra from survey A and the labels from survey B of the reference set stars are used to train a generative model. Then, given a set of labels, this model predicts the probability density function for the flux at each wavelength. During the application step, the spectra of a new set of survey A stars (not the reference set) are re-labelled by the trained model. We call this set of stars the application set. If the region of the spectra fit to carries the label information and the reference set well represents the application set, then the new labels of survey A's stars should be on survey B's label scales. The success of the re-calibration can be quantified with a cross-validation procedure, the pick-on-out test described in Sect. 2.4.2, which returns the systematic uncertainty with which labels can be inferred from the data, as well as a comparison of the generated model spectra to the observational spectra for individual stars, using a χ^2 metric.

In the next two subsections we describe the main steps of *The Cannon* in more detail.

2.3.1 The training step

During the training step, a generative model is trained such that it takes the labels as input and returns the flux at each wavelength of the spectrum. The functional form of the generative model, $f_{n\lambda}$, can be written as a matrix equation:

$$f_{n\lambda} = \theta_\lambda^T \cdot l_n + \sigma, \tag{2.1}$$

where θ_λ is a coefficient matrix, l_n is a label matrix, and σ is the noise. The subscript n indicates the reference set star while subscript λ indicates the wavelength.

The coefficient matrix, θ_λ, contains the coefficients that control how much each label affects the flux at each pixel. The coefficients are calculated during the training step.

Here the label matrix, l_n, is quadratic in the labels and for each star (each column in the matrix) has the form:

$$l_n \equiv [1,\ l_{(1...n)},\ l_{(1...n)} \cdot l_{(1...n)}]. \tag{2.2}$$

If, for example, the generative model is trained on the labels $\mathrm{T_{eff}}$ and log(g), then each column in the label matrix would be:

$$l_n \equiv [1,\ \mathrm{T_{eff}},\ \log(\mathrm{g}),\ \mathrm{T_{eff}} \cdot \mathrm{T_{eff}},\ \log(\mathrm{g}) \cdot \log(\mathrm{g}),\ \mathrm{T_{eff}} \cdot \log(\mathrm{g})]. \tag{2.3}$$

The noise, σ, is the rms combination of the uncertainty in the flux at each wavelength due to observational errors, $\sigma_{n\lambda}$, and the intrinsic scatter at each wavelength in the model, s_λ.

Equation 2.1 corresponds to the single-pixel log-likelihood function:

$$\ln p(f_{n\lambda}|\theta_\lambda^T, l_n, s_\lambda) = -\frac{1}{2}\frac{[f_{n\lambda} - \theta_\lambda^T \cdot l_n]^2}{s_\lambda^2 + \sigma_{n\lambda}^2} - \frac{1}{2}\ln(s_\lambda^2 + \sigma_{n\lambda}^2). \tag{2.4}$$

During the training step, the coefficient matrix θ_λ and the model scatter s_λ are determined by optimising the single-pixel log-likelihood in Eq. 2.4 for every pixel separately:

$$\theta_\lambda, s_\lambda \leftarrow \underset{\theta_\lambda, s_\lambda}{\operatorname{argmax}} \sum_{n=1}^{\mathrm{N_{stars}}} \ln p(f_{n\lambda}|\theta_\lambda^T, l_n, s_\lambda). \tag{2.5}$$

During this step *The Cannon* uses the reference set stars to provide the label matrix, l_n. The label matrix is held fixed while the coefficient matrix and model scatter are treated as free parameters.

2.3.2 The application step

In the training step, we have the label matrix, l_n, and we solve for the coefficient matrix θ_λ and the scatter s_λ. In the application step, we do the opposite: we have the coefficient matrix θ_λ and the scatter s_λ and we solve for a new label matrix, l_m. The subscript m is used in this step because the label matrix now corresponds to stars in the application set, not the reference set.

The label matrix, l_m, is solved for by optimising the same log-likelihood function as Eq. 2.4. However, here this optimisation is performed using a non-linear least squares fit over the whole spectrum, instead of per pixel:

$$l_m \leftarrow \underset{l_m}{\operatorname{argmax}} \sum_{\lambda=1}^{\mathrm{N_{pix}}} \ln p(f_{m\lambda}|\theta_\lambda^T, l_m, s_\lambda). \tag{2.6}$$

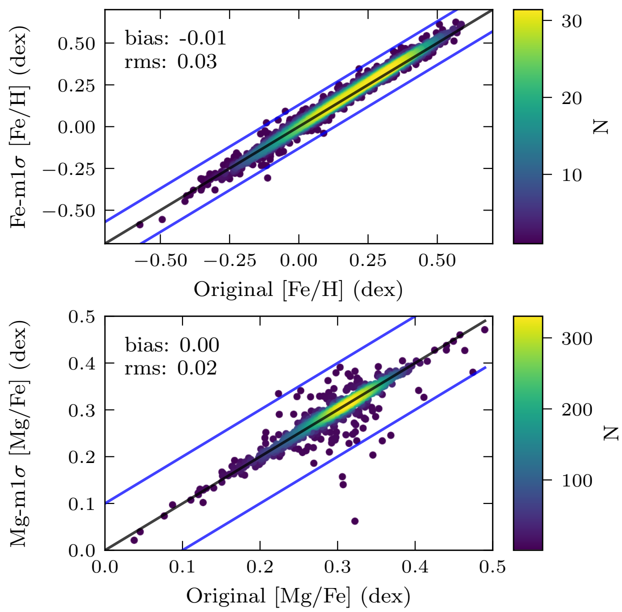

Figure 2.3: Comparison of the [Fe/H] (top) and [Mg/Fe] (bottom) labels generated by the original *Cannon* model (x axis) and the m1σ models (y axis). In the top plot, only stars with ARGOS $0.05 < \mathrm{[Fe/H]}\,(\mathrm{dex}) < 0.18$ are compared (the region in [Fe/H] spanned by the blue crosses in the top plot of Fig. 2.2). In the bottom plot, only stars with ARGOS $0.47 < [\alpha/\mathrm{Fe}]\,(\mathrm{dex}) < 0.57$ are compared (the region in $[\alpha/\mathrm{Fe}]$ spanned by the red triangles in the plot second from the top in Fig. 2.2). The points are coloured by the point density. The black lines are one-to-one lines, and blue lines indicate $\pm 1\sigma_{\mathrm{ARG}}$. The bias and rms of each distribution are given in the top left corner of each plot.

2.4 A2A catalogue

In this paper we use *The Cannon* to put the stars from the ARGOS survey onto the APOGEE survey's label scales for the following labels: [Fe/H], [Mg/Fe], T_{eff}, log(g), and K-band extinction (A_k). After applying *The Cannon* to the ARGOS survey, we obtain a new catalogue containing the same stars observed by the ARGOS survey but with new label values. Other labels, such as line-of-sight velocity or apparent magnitude, remain unchanged. We call this new catalogue the A2A catalogue. In this section, we describe the reference and application sets used to build the A2A catalogue and perform three validation tests to confirm that the A2A catalogue is on the APOGEE scale. Lastly, we compare the A2A catalogue to the ARGOS catalogue and explain how we extracted the A2A RC and corresponding distances.

2.4.1 Reference and application sets

A reference set of stars, which is used to train *The Cannon*'s model, is composed of the stars that are observed by both surveys. The labels for this reference set come from the survey with the desired label scale (in our case APOGEE), while the spectra are taken from the other (in our case

ARGOS). The model that is learned at training time should only be applied to stars that are well represented by the reference set. That is, applied to stars that span the label region of the training data, within which the model can interpolate but need not extrapolate. This can also be thought of as a selection in spectra. In our case, the 204 stars that are common to both the APOGEE and the ARGOS surveys (discussed in Sect. 2.2.3) formed the reference set for our *Cannon* model. The average S/N of the reference set is 46 for ARGOS and 107 for APOGEE.

These reference set stars are found in the following intervals in the ARGOS parameter space:

$$4195 \leq \mathrm{T_{eff}}\ (\mathrm{K}) \leq 5444, \quad (2.7a)$$

$$1.393 \leq \log(g)\ (\mathrm{dex}) \leq 3.376, \quad (2.7b)$$

$$-1.4 \leq [\mathrm{Fe/H}]\ (\mathrm{dex}) \leq 0.18, \quad (2.7c)$$

$$-0.062 \leq [\alpha/\mathrm{Fe}]\ (\mathrm{dex}) \leq 0.569. \quad (2.7d)$$

We ignore the limits in A_k as this label was only included to stabilise the fits to the other labels. As such, we do not use the learned A_k label for science.

There are 20,435 ARGOS stars (~79% of the ARGOS catalogue) within the 4D parameter space defined by intervals 2.7a to 2.7d. These stars are considered to be well represented by the reference set and normally would have formed our application set. However, there are many stars with parameter values close to but just outside of the reference set limits. For example, if we extend all the limits by $1\sigma_{\mathrm{ARG}}$, equal to the ARGOS observational error of each label, then we would include 2704 more stars in the application set (~10.5% more of the ARGOS catalogue). Because these stars are still close to the reference set stars, the labels returned by *The Cannon* for these stars may be correct to the first order. To test whether we could extend any of the limits we used the following procedure: (i) Remove reference set stars $1\sigma_{\mathrm{ARG}}$ from each limit. This decreases the number of reference set stars. (ii) Train a new *Cannon* model on the reduced reference set. For clarity, we refer to this model as the minus-one-sigma (m1σ) model. (iii) Reprocess ARGOS spectra using the m1σ model to obtain new *Cannon* parameters for each star. The application set remains the same as the one processed by the original *Cannon* model. (iv) Compare the new *Cannon* labels from the m1σ model to the labels given by the original *Cannon* model.

For reference, the ARGOS observational errors, σ_{ARG}, for [Fe/H], [α/Fe], $\mathrm{T_{eff}}$, and log(g) are: 0.13 dex, 0.1 dex, 100 K, and 0.3 dex, respectively.

We applied this test to each label limit separately and found that the extrapolation works best for the high [Fe/H] and high [α/Fe] limits. In Fig. 2.3, we compare the output labels produced by the original *Cannon* model against the output labels produced by the m1σ models trained on the reduced reference sets. The original *Cannon* model was trained on all 204 reference set stars, shown as the black, blue, and red markers in Fig. 2.2. The Fe-m1σ model (top plot) was trained on 149 reference set stars, shown as just the black and red markers in Fig. 2.2. The Mg-m1σ model (second plot) was trained on 199 reference set stars, shown as just the black and blue markers in Fig. 2.2. For each comparison (or plot) we only compare stars that have ARGOS parameter values in the $1\sigma_{\mathrm{ARG}}$ region we removed (regions occupied by the blue and red markers in Fig. 2.2). For both labels, fewer than 1% of stars have original *Cannon* model and m1σ model labels that differ by more than $1\sigma_{\mathrm{ARG}}$.

We also compared the labels produced by the original *Cannon* model to the labels produced by a *Cannon* model that was trained on a reference set that was simultaneously reduced by $1\sigma_{\rm ARG}$ in [Fe/H] and [Mg/Fe]. The reference set of this model consisted of only 144 stars, shown as the black markers in Fig. 2.2. We find that fewer than 1% of stars from this model have labels that differ from the original *Cannon* model by more than $1\sigma_{\rm ARG}$ in [Fe/H] and 2% in [Mg/Fe].

Because we found that we could accurately predict the [Fe/H] and [Mg/Fe] labels of stars in the $1\sigma_{\rm ARG}$ regions of the parameter space removed from the reference set, we made the assumption that we could apply the *Cannon* model trained on all 204 reference set stars to stars with ARGOS parameters $1\sigma_{\rm ARG}$ beyond the high [Fe/H] and [α/Fe] limits and still get approximately correct labels. Thus, we extended the limits of 2.7c and 2.7d to be:

$$-1.4 \leq [\mathrm{Fe/H}]\ (\mathrm{dex}) \leq 0.31, \tag{2.8a}$$

$$-0.062 \leq [\alpha/\mathrm{Fe}]\ (\mathrm{dex}) \leq 0.669. \tag{2.8b}$$

Limits 2.7a,2.7b, 2.8a, and 2.8b enabled us to process 85% of the ARGOS catalogue, or 21,577 stars. This increased the number of stars in the A2A catalogue with [Fe/H] above 0.5 dex by roughly 45%, the number of stars with [Fe/H] between 0 dex and 0.5 dex by roughly 23%, and the stars with [Fe/H] below -1 dex by roughly 10%.

In Sect. 2.5.1 we define our A2A catalogue used for the bulge analysis. This final catalogue has an additional colour cut applied (Eq. 2.12), which removes an additional 252 stars, leaving 21,325 stars in the final catalogue. If the same colour cut is applied to the original ARGOS catalogue then the ARGOS catalogue would contain 23,487 stars. The final colour cut A2A catalogue is then 91% complete compared to the colour cut ARGOS catalogue. The parameter and abundance errors of the colour cut A2A catalogue are calculated in Sect. 2.4.2. For [Fe/H], [Mg/Fe], $T_{\rm eff}$, and log(g), the rms of the errors, $\sigma_{\rm A2A}$, are 0.10 dex, 0.07 dex, 74 K, and 0.18 dex, respectively.

2.4.2 Validation tests

Given a reference set and an application set, *The Cannon* will always return new labels for the stars in the application set. However, if one is not careful, the returned labels can have large errors. In this section, we describe three validation tests we performed to verify that the labels returned by *The Cannon* are reasonable.

The first validation test we performed is a common machine learning test called the pick-one-out test. In this test, we created 204 models, each of which was trained on 203 stars from the reference set. The single star that was left out from the reference set changed between each model. Every model was then applied to the spectra of the respective left out star to obtain a new set of labels for it. How similar the new set of labels are to the original APOGEE labels indicates how well *The Cannon* can learn the APOGEE labels given the reference set. In Fig. 2.4 we compare the new *Cannon* labels of these stars to their APOGEE labels. For all four labels, the bias and rms, given in the upper left hand corner of each plot, are much lower than those from the ARGOS-APOGEE comparisons in Fig. 2.2. The strong agreement indicates that *The Cannon* can successfully learn the APOGEE labels from the ARGOS spectra using the reference set composed of the 204 common stars. The error on each parameter for each star in the A2A catalogue was calculated by adding

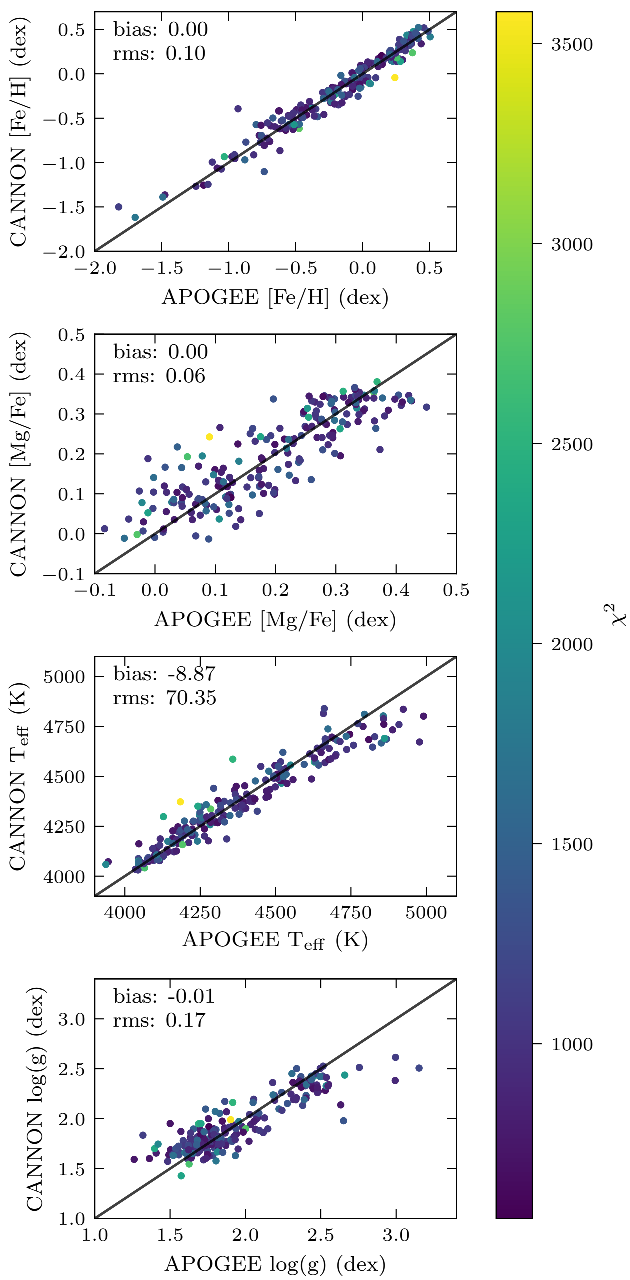

Figure 2.4: Pick-one-out test. For each plot, each point represents a different reference set star. For a given point in a plot, the x axis value is the APOGEE-derived label and the y axis value is the label prediction from a *Cannon* model trained on all other (203) reference set stars. Therefore, for each point in each plot, the applied *Cannon* model is different than that of every other point. The points are coloured by their model χ^2 values. The bias and rms of each distribution are given in the top left corner of each plot.

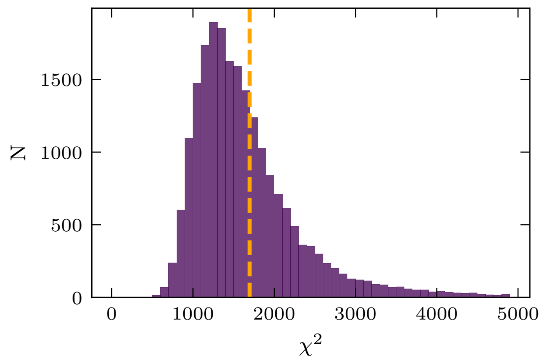

Figure 2.5: Model χ^2 distribution of A2A stars. The dashed orange line gives the number of pixels in each ARGOS spectrum.

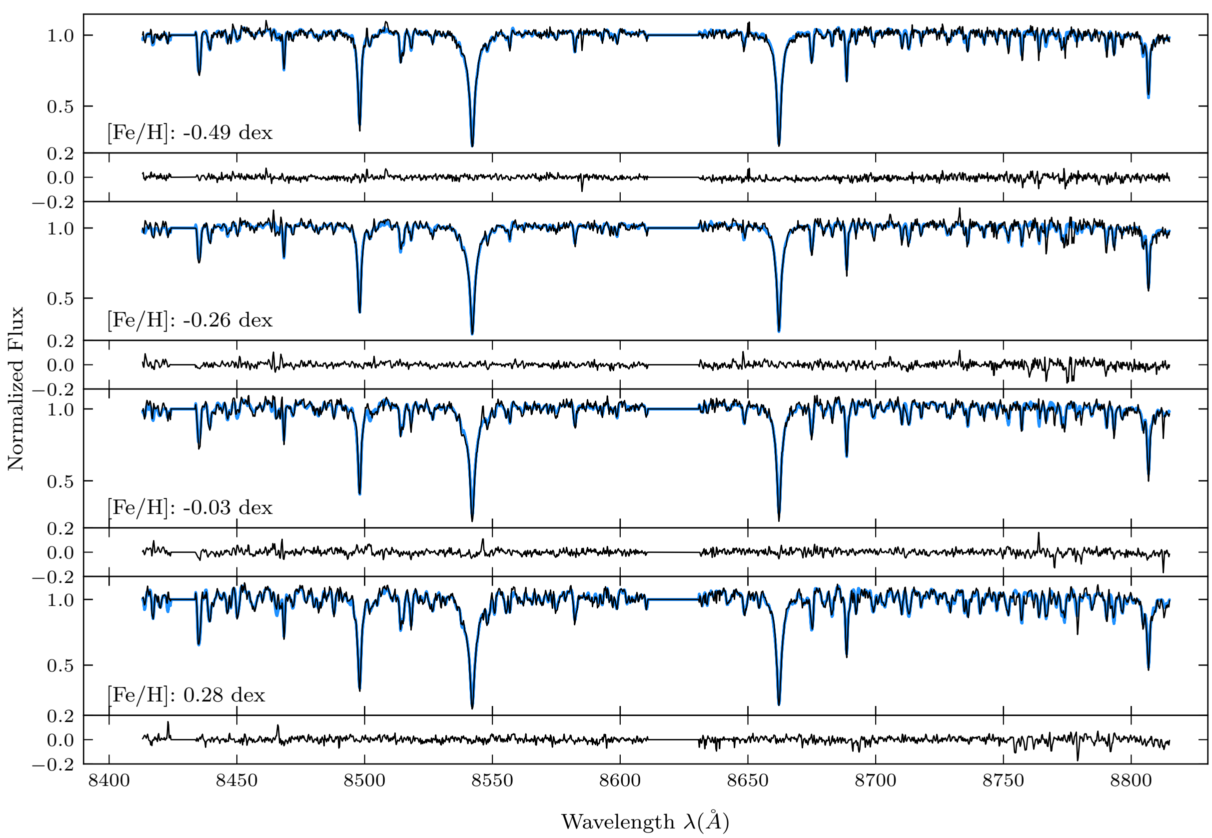

Figure 2.6: Normalised ARGOS spectra (black) versus the normalised model spectra (blue) generated by *The Cannon* for A2A stars with [Fe/H] values between $-0.5 \lesssim$ [Fe/H] $\lesssim 0.25$. The plotted line thicknesses of the model spectra indicate the scatter of each fit by *The Cannon*. The residuals between the normalised ARGOS spectra and normalised model spectra are also shown in the panels below the spectra.

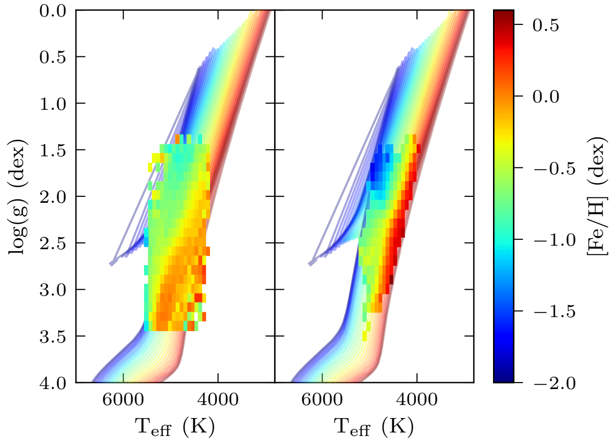

Figure 2.7: T_{eff}-log(g) distribution of ARGOS (left) and A2A (right) stars coloured by mean [Fe/H]. 10 Gyr PARSEC isochrones with $-2 <$ [Fe/H] (dex) < 0.6 are plotted beneath. We note that the isochrones are plotted at 35% transparency in order to visually differentiate them from the 2D histograms.

in quadrature the rms value from the pick-one-out test and the small error that is output by the optimiser of *The Cannon* (see Sect. 2.3).

As a second validation test we compared the model and observational spectra. The shape of the spectrum of a star can be affected by many different stellar parameters and abundances. Ideally, when training a model to describe a stellar spectrum with labels one would like to include all stellar labels that affect the spectrum's shape. However, this would require a huge number of reference set stars, which we do not have. Instead, we made the approximation that the ARGOS spectra (8400 Å - 8800 Å) could be well described by the five labels: [Fe/H], [Mg/Fe], T_{eff}, log(g), and A_k. To test this, we compared the model spectra generated by *The Cannon* against the true observational spectra. This could be done because *The Cannon* trained model returns the flux at each pixel when given the labels (Eq. 2.1). In Fig. 2.6 we plot the ARGOS spectra of a few example stars with a range of [Fe/H] values and cumulative χ^2 values (sum of the pixel χ^2 values) around the ARGOS pixel number (1697, see Fig. 2.5) versus their model spectra generated by *The Cannon*. For the model spectra, line thicknesses show the scatter of the fit by *The Cannon* at each wavelength. Figure 2.6 shows that the model spectra closely reproduce the true observational spectra. The overall good fit between the model spectra and the true spectra indicates that the spectra of the ARGOS stars can be well described by the variation in the five labels.

The third test we did was comparing the T_{eff}-log(g)-[Fe/H] distribution of A2A stars to theoretical distributions. In the right hand plot of Fig. 2.7, we show the T_{eff}-log(g) distribution of A2A stars coloured by mean [Fe/H] on top of 10 Gyr PARSEC isochrones with metallicities ranging from -2 dex to 0.6 dex (Tang et al. 2014; Chen et al. 2014, 2015; Bressan et al. 2012). The A2A stars tightly follow the PARSEC isochrones. Furthermore, even though no isochrone information was input into *The Cannon*, there are no A2A stars in non-physical regions of the diagram. The close fit of the A2A stars to the PARSEC isochrones supports that the label transfer

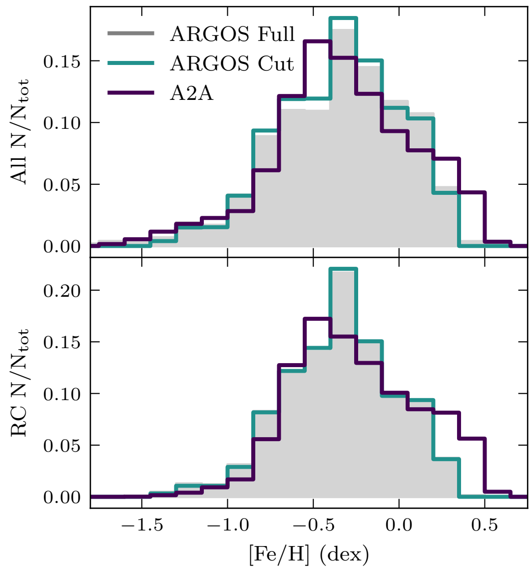

Figure 2.8: Normalised ARGOS and A2A MDFs of all stars (top) and RC stars (bottom). The grey histogram includes stars from the full ARGOS catalogue, while the teal histogram includes only ARGOS stars that could be processed by *The Cannon* (same stars as in the A2A catalogue but with their old ARGOS labels).

was successful.

The success of these three tests shows that it is possible to train a *Cannon* model on a moderate number (204) of common stars and still obtain a set of labels with good precisions (see Sect. 2.4.1).

2.4.3 A2A versus ARGOS

In this section we compare the A2A catalogue to the ARGOS catalogue. In Fig. 2.7 we show the T_{eff}-log(g)-[Fe/H] distributions of ARGOS stars (left) and A2A stars (right) on top of 10 Gyr PARSEC isochrones. The ARGOS stars very roughly follow the PARSEC isochrones. Many ARGOS stars also fall in non-physical regions of the parameter space. As discussed in the previous section, A2A stars have a much tighter alignment with the PARSEC isochrones with no stars falling in non-physical regions.

In Fig. 2.8 we show the ARGOS and A2A MDFs of all stars (top) and only RC stars (bottom). The most prominent difference between the MDFs of the surveys is that A2A obtains more very [Fe/H]-rich stars than ARGOS for all stars as well as when we restrict to only the RC. ARGOS has more solar to sub-solar stars until ~ -0.5 dex where A2A has more stars. Between ~ -1 and ~ -0.7 dex ARGOS has more stars for all stars and the RC. Below ~ -1 dex, the difference between ARGOS and A2A is small.

2.4.4 Red clump extraction and A2A distances

We statistically extracted RC stars from the A2A catalogue using the following probabilistic method: First, we determined the spectroscopic magnitudes, M_{K_s}, of each A2A star by fitting their log(g), T_{eff}, and [Fe/H] parameters to theoretical isochrones. Then, using the spectroscopic magnitudes, we calculated a weight for each star that gives the probability that it is part of the RC. The functional form of this weight is a Gaussian:

$$\omega_{rc}(M_{K_s}) = \frac{1}{\sigma_{M_{K_s}}\sqrt{2\pi}}\exp\left(-\frac{1}{2}\frac{(M_{K_s}-M_{rc})^2}{\sigma^2_{M_{K_s}}}\right), \tag{2.9}$$

where $M_{rc} = -1.61 \pm 0.22$ mag is the intrinsic magnitude of the RC (Alves 2000). We found that for 10 Gyr old PARSEC isochrones (Tang et al. 2014; Chen et al. 2014, 2015; Bressan et al. 2012) the spectroscopic magnitude varies with log(g) as $dM_{K_s}/d(\log g) = 2.33$. The average A2A log(g) error is 0.18 dex, giving an average magnitude error of 0.42 mag. We added this in quadrature with the intrinsic width of the RC magnitude to obtain a total magnitude error of 0.47 mag for our RC sample. This is $\sigma_{M_{K_s}}$ in Eq. 2.9. This magnitude-dependent weighing method extracts the RC from A2A by giving higher weights to stars that are likely to be part of the RC and lower weights to stars that are unlikely to be part of the RC.

To obtain distances for the A2A stars, we first treated each star as a RC star and assumed their absolute magnitudes were that of the RC (−1.61 mag). We then compared the RC absolute magnitude to the de-reddened apparent magnitude of each star, which we obtained using the Schlegel et al. (1998) extinction maps re-calibrated by Schlafly & Finkbeiner (2011). This method gave us the distance of each star assuming that it was a RC star. To account for the fact that not every A2A star is a RC star, we weighed the stars by how likely they were to be RC stars using the weight in Eq. 2.9. By weighing the stars in this manner, we treated all stars as RC stars but effectively removed the stars that were unlikely to be part of the RC by strongly de-weighting them.

The A2A catalogue contains 10,357 RC stars. We obtained this number by summing the RC weights (Eq. 2.9).

2.5 Selection functions

The probability that any given star in the Galaxy is observed by a large survey programme is called the survey selection function (SSF); see Sharma et al. (2011) for a detailed discussion. In order to obtain unbiased parameter and abundance distributions of the Galactic bulge using the A2A and APOGEE surveys we must correct for their SSFs. Otherwise, it would not be clear if the distributions we obtain are the true distributions of the Galactic bulge, or whether they are biased by the selection choices of the surveys. In the next two sections, we discuss the A2A and APOGEE SSFs.

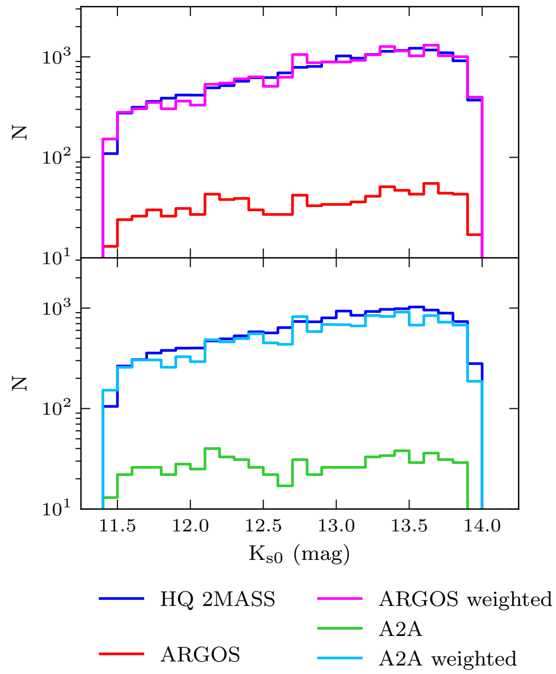

Figure 2.9: Original and weighted K_{s0}-band LFs of ARGOS (top) and A2A (bottom) stars in the field $(l, b) = (-10°, -10°)$. The HQ 2MASS LF is also plotted. The colour limits $0.45 \leq (J - K_s)_0$ (mag) ≤ 0.86 are applied to the LFs in the bottom plot. The A2A LF is slightly below the HQ 2MASS LF due to the parametric limits applied during the creation of the A2A catalogue.

2.5.1 A2A selection function

The stars composing the A2A catalogue were selected from the ARGOS catalogue, which, in turn, was selected from a high quality (HQ) subset of the Two Micron All Sky Survey (2MASS; (Skrutskie et al. 2006)). In the following subsections we discuss the selection of the ARGOS survey from the HQ 2MASS subset and the selection of the A2A survey from the ARGOS survey.

Selection of ARGOS from HQ 2MASS

The ARGOS stars were selected from a HQ sub-sample of the 2MASS survey, requiring the stars to have high photometric quality flags (see Freeman et al. (2012)), magnitudes between $11.5 \leq K_s$ (mag) ≤ 14.0, and colours $(J - K_s)_0 \geq 0.38$ mag. For each 2MASS star that met these requirements, its I_0-band magnitude was estimated using the equation:

$$I_0 = K_s + 2.095(J - K_s) + 0.421E(B - V). \tag{2.10}$$

Then, for each field, the ARGOS team randomly selected approximately 1000 stars roughly evenly distributed among the I_0-band bins: 13-14 mag, 14-15 mag, and 15-16 mag. This was done in order to sample a roughly equal number of stars from the front, middle, and back regions of the bulge.

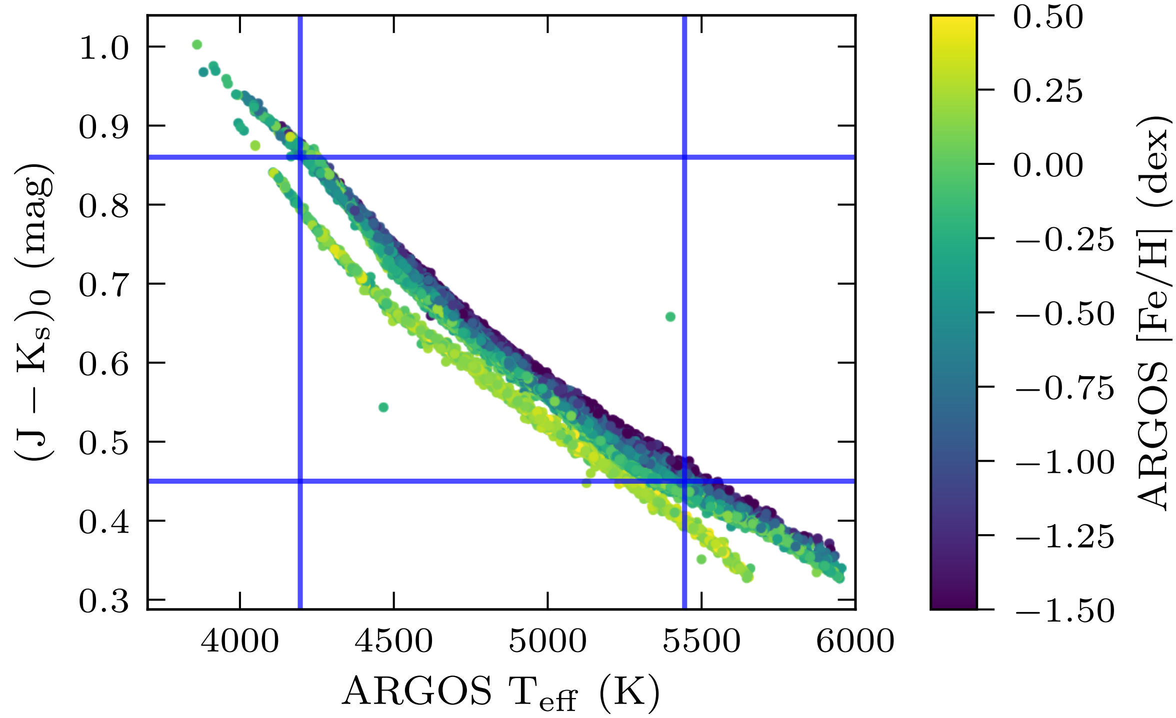

Figure 2.10: ARGOS T_{eff} versus de-reddened colour distribution of the full ARGOS catalogue. The point colour indicates the ARGOS [Fe/H]. The blue vertical lines show the reference set T_{eff} limits (2.7a). The blue horizontal lines show the colour limits (2.12) used to approximate the T_{eff} limits.

We used the following procedure to correct for the I_0-band selection (similar to Portail et al. (2017a), their Sect. 5.1.1). First we took all 2MASS stars in a given field and applied the colour, magnitude, and quality cuts described above. Then, we estimated the I_0-band magnitude of each remaining 2MASS star as well as of each ARGOS star using Eq. 2.10. We could then correct for the I_0-band selection by weighing each ARGOS star by the ratio of the number of HQ 2MASS stars to the number of ARGOS stars in each I_0-band bin and field:

$$\omega_{\mathrm{f,I_0}} = \mathrm{N}_{\mathrm{f,I_0}}^{\mathrm{HQ\ 2MASS}} / \mathrm{N}_{\mathrm{f,I_0}}^{\mathrm{ARGOS}}. \tag{2.11}$$

After the application of the weights in Eq. 2.11 to the ARGOS luminosity function (LF), we statistically recover the HQ 2MASS LF within the respective colour and magnitude limits. The upper plot of Fig. 2.9 shows this for the field $(l, b) = (-10°, -10°)$.

Selection of A2A from ARGOS

As the A2A stars were selected from the ARGOS catalogue, we also similarly corrected the A2A catalogue for the I_0-band selection using the weights from Eq. 2.11. However, the weighted A2A LFs are systematically below the HQ 2MASS LFs because of the A2A selection from the ARGOS catalogue, which removed 4, 135 stars. These stars were removed because their spectra could not be processed by *The Cannon* (did not satisfy limits 2.7a, 2.7b, 2.8a, and 2.8b). Because of this, we know the label values of these stars on the ARGOS scale but only have approximate knowledge of where they are on the APOGEE scale. To replicate this selection, we examined if the limits that removed these stars could be described using parameters that did not change during the label transfer.

The T_{eff} limits (see 2.7a) are simple to approximate as there is a near linear relationship between ARGOS T_{eff} and colour, shown in Fig. 2.10. However, this substitution is not perfect and the colour limits must be chosen carefully as the T_{eff}-colour distribution has some spread due to variations in the other labels. For example, stars with lower ARGOS [Fe/H] are hotter for constant colour (see the point colour in Fig. 2.10). If chosen incorrectly, the colour limits can remove many stars that satisfy limits 2.7a,2.7b, 2.8a, and 2.8b. We found that the T_{eff} limits are well approximated by the colour limits:

$$0.45 \leq (\mathrm{J} - \mathrm{K_s})_0 \text{ (mag)} \leq 0.86. \tag{2.12}$$

We show in the lower plot of Fig. 2.9 the weighted A2A and HQ 2MASS LFs in the field $(l, b) = (-10°, -10°)$; both of which have the colour cut in Eq. 2.12 applied. While the two LFs are close, there is still a slight deviation due to the other parametric limits.

Unfortunately, the other parametric limits are not as easily replaced using alternative parameters that remain constant during the label transfer. We take the final A2A catalogue to include all stars processed by *The Cannon* that: (i) have model χ^2 values below 5000 (see Fig. 2.5), (ii) satisfy the limits 2.7a,2.7b, 2.8a, and 2.8b, and (iii) are within the colour limits in Eq. 2.12.

Within these conditions, the A2A catalogue contains 21,325 stars. If we apply the colour cut (Eq. 2.12) to the ARGOS catalogue then the ARGOS catalogue would contain 23,487 stars. Thus, the colour cut A2A catalogue is 91% complete compared to the colour cut ARGOS catalogue.

In the subsequent analysis of the bulge's chemodynamical structure, we often select and plot A2A RC stars to obtain good distance estimates (see Sect. 2.4.4 for a discussion on RC extraction). We make the assumption that the reference set limits affect RC and red giant branch stars equally such that the A2A RC catalogue is also ~91% complete. We test this assumption in Appendix A.

2.5.2 APOGEE selection function

The APOGEE sample we used for most of this work's analysis is the HQSSF APOGEE bulge MSp. It is a sub-sample of the full APOGEE bulge MSp in that we also required the stars to have high quality ASPCAP parameters and abundances (see Sect. 2.2.2) and good SSF estimates. In this sample, only stars that are part of complete cohorts (i.e. groups of stars observed together during the same visits) have SSF estimates. Estimating the SSF for this sample proceeded in two steps. First, to account for the selection of the APOGEE bulge MSp from the HQ 2MASS subset, we used the publicly available python package *APOGEE* (Bovy et al. 2014; Bovy 2016; Mackereth & Bovy 2020). For each complete cohort, the program returned the ratio of the number of APOGEE MSp stars to the number of HQ 2MASS stars within the respective colour and magnitude limits of

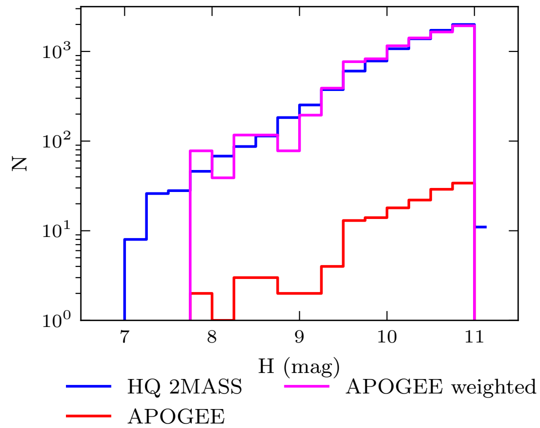

Figure 2.11: Original and weighted APOGEE H-band LFs of the HQSSF bulge MSp for a cohort in the field $(l, b) = (-2°, 0°)$. The HQ 2MASS LF is also plotted.

the cohort[1]. Then, we weighted each star in each cohort, c_i, by the inverse of this ratio:

$$\omega_{c_i} = N_{c_i}^{\mathrm{HQ\ 2MASS}} / N_{c_i}^{\mathrm{APOGEE\ MSp}}. \tag{2.13}$$

Second, restricting our sample to APOGEE stars with HQ ASPCAP parameters and abundances (Sect. 2.2.2) removed ~14% of the APOGEE bulge MSp. To correct for this selection we binned all APOGEE bulge MSp stars (including the stars with poor ASPCAP estimates) and all HQ ASPCAP MSp stars in magnitude, colour, and cohort. Then, we weighted each HQ ASPCAP MSp star by the ratio of the number of MSp stars to the number of HQ ASPCAP MSp stars in the colour and magnitude bin in which it fell:

$$\omega_{c_i,H,(J-K_s)_0} = N_{c_i,H,(J-K_s)_0}^{\mathrm{APOGEE\ MSp}} / N_{c_i,H,(J-K_s)_0}^{\mathrm{HQ\ ASPCAP}}. \tag{2.14}$$

Figure 2.11 shows the result of the application of the weights in Eqs. 2.13 and 2.14 to the H-band LF of a cohort in the field $(l, b) = (-2°, 0°)$. We see that after the application of the weights, the LFs of the HQSSF APOGEE bulge MSp and HQ 2MASS subset approximately match.

In Fig. 2.1, the red crosses indicate APOGEE field locations for which we could not use the *APOGEE* python package to obtain good SSF estimates of the observed stars. This occurred either because the cohorts composing the fields were not complete or because they did not contain any MSp stars. Removing these fields, as well as a few cohorts for which the weighted LF poorly reproduced the LF of its HQ 2MASS parent sample, leaves 23, 512 stars in the HQSSF APOGEE bulge MSp.

In the subsequent analysis we restrict the HQSSF APOGEE bulge MSp further by requiring stars to have AstroNN distance errors of less than 20%. This roughly removes 5% of the HQSSF APOGEE bulge MSp leaving 22, 340 APOGEE stars.

[1]Cohort magnitude limits were set depending on the planned number of visits. Most cohorts used in this work have the magnitude limits $7 < H_0$ (mag) < 11, $7 < H_0$ (mag) < 12.2, or $7 < H_0$ (mag) < 12.8, although some have fainter limits. The colour limits of the cohorts are $(J-K_s)_0 \geq 0.5$ mag in bulge and APOGEE-1 disk fields, and $0.5 \leq (J-K_s)_0$ (mag) ≤ 0.8 and $(J-K_s)_0 > 0.8$ mag in APOGEE-2 disk fields; see Zasowski et al. (2017).

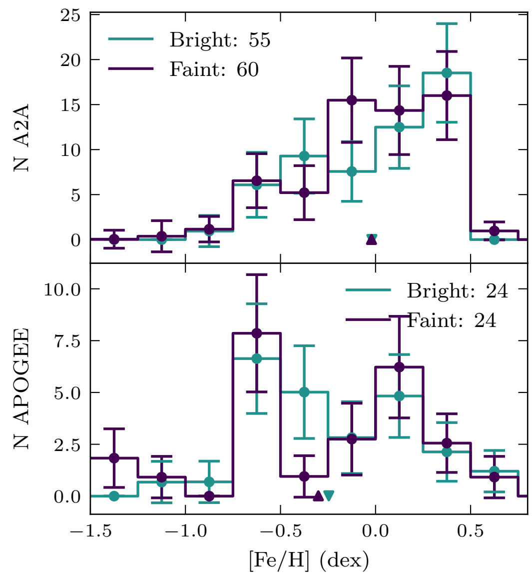

Figure 2.12: MDFs of bright and faint stars in the same distance bins. Top: A2A RC stars from the field $(l, b) = (0°, -5°)$ and the distance bin 6 to 8 kpc with the weights from Eq. 2.11 applied. Bottom: APOGEE stars from the field $(l, b) = (0°, -2°)$ and the distance bin 6 to 8 kpc with the weights from Eqs. 2.13 and 2.14 applied. The number of stars in each MDF is given in the legend of each plot. The means of each histogram are given by the triangular markers.

2.5.3 Selection of HQ 2MASS catalogues

So far we have described the A2A and APOGEE SSFs as well as the corresponding weights that were needed to statistically correct each survey to the magnitude and colour distributions of their respective HQ 2MASS parent samples. This is similar to the procedure done by Rojas-Arriagada et al. (2020), who used simple stellar populations to determine the fraction of giants with fixed distance modulus and metallicity that fall with in the APOGEE magnitude and colour ranges. Then using these fractions, they re-weighted the observed stars to the weights they had in the survey input sample. However, the input HQ 2MASS sample of each survey itself has a SSF relative to the real Galaxy (in practice, the current deepest photometric survey, VVV (Minniti et al. 2010; Surot et al. 2019)) due to photometric criteria, crowding, and extinction. The 2MASS SSF is strongest at low latitudes and is illustrated in Portail et al. (2017a, their Sect. 5.1.1). This SSF would be additionally required when comparing (or weighting by) the relative number densities of stars in different fields, especially those with different latitudes.

In this paper, we confine our analysis to small spatial bins, making use of RC distances for A2A and AstroNN distances for APOGEE. When we do this, the observed stars in a given bin are representative of the stellar population at that distance making further corrections of the HQ 2MASS survey magnitude distribution unnecessary. However, in practice, the bins we use have sizes ~2 kpc, thus if there is a line-of-sight abundance gradient in a field, the fainter stars in a given bin could have a slightly different abundance distribution than the brighter stars as they trace somewhat larger distance. Figure 2.12 shows, for example bins, that no such effect is seen within the errors in either survey.

An additional effect could arise due to fields at different latitudes/heights contributing stars to the same distance bins. Specifically, lower latitude fields are generally more [Fe/H]-rich and have higher crowding than higher latitude fields due to the [Fe/H] and density gradients in the bulge. In such cases, by not correcting for the HQ 2MASS SSF we may introduce a slight bias against the lower latitude, higher [Fe/H] stars in each spatial bin. However, the effects of field mixing would be small in A2A as its fields are well separated and generally located at latitudes with low crowding ($|b| \geq 5°$). Whereas for APOGEE, the effects of field mixing would also be small because at low latitudes ($|b| < 4°$), where the incompleteness of the HQ 2MASS catalogue is largest, the [Fe/H] gradient is nearly flat (Rich et al. 2012; Ness et al. 2016), and at high latitudes ($|b| > 4°$), where the [Fe/H] gradient is negative, the incompleteness of the HQ 2MASS catalogue is small. When we vary the width of our distance bins in $|Z|$, we do not find significant changes in the bulge [Fe/H] gradient. Therefore, we neglect field mixing effects in this paper.

2.5.4 Application of the SSF corrections

Here we illustrate the effect of the different spatial selections of the two surveys in the inner Galaxy, and then compare their SSF-corrected MDFs and [Mg/Fe] distribution functions (Mg-DFs) in regions of spatial overlap.

The first two plots in the top row of Fig. 2.13 show the APOGEE and A2A MDFs and Mg-DFs of all stars (RC for A2A) in each catalogue. APOGEE observes many stars near the Galactic plane and in the nearby disk that A2A misses, as illustrated in the right two plots of this row. These stars tend to be more [Fe/H]-rich and [Mg/Fe]-poor than stars at larger heights, causing much stronger [Fe/H]-rich and [Mg/Fe]-poor peaks in the APOGEE histograms than in A2A. In the second row of Fig. 2.13, the samples are restricted to smaller regions of overlap between the surveys, demanding $|Z| \geq 0.5$ kpc and distances from the Sun between 4 and 12 kpc, and thereby removing many of the in-plane [Fe/H]-rich [Mg/Fe]-poor stars in the APOGEE catalogue. This causes the [Fe/H]-rich and [Mg/Fe]-poor peaks in the APOGEE MDF and Mg-DF to decrease, leading to better agreement with A2A. Some differences in the MDF and Mg-DF shapes are still expected, due to differences both in detailed coverage and in number density along the line-of-sight, as we did not correct each survey past the HQ 2MASS catalogues they were selected from.

However, if we restrict the sample to a smaller distance bin as shown in the third row of Fig. 2.13, such effects are significantly weakened. Now the MDFs and Mg-DFs agree within the errors except for the most [Fe/H]-poor bin in the MDF and the most [Mg/Fe]-rich bin (> 0.35 dex) in the Mg-DF where APOGEE observes a larger fraction of stars.

2.5.5 The high [Mg/Fe] and low [Fe/H] stars

In the following sections we see that the discrepancy seen in Fig. 2.13 at the high [Mg/Fe] end is widespread in the bulge occurring in both the inner and outer bulge and at various heights from the plane, even after the SSF corrections are applied. We believe that this discrepancy can be at least partially explained by the limited T_{eff} range spanned by the reference set (see Fig. B.2) coupled with systematic trends between the ASPCAP T_{eff} and abundances of the APOGEE stars

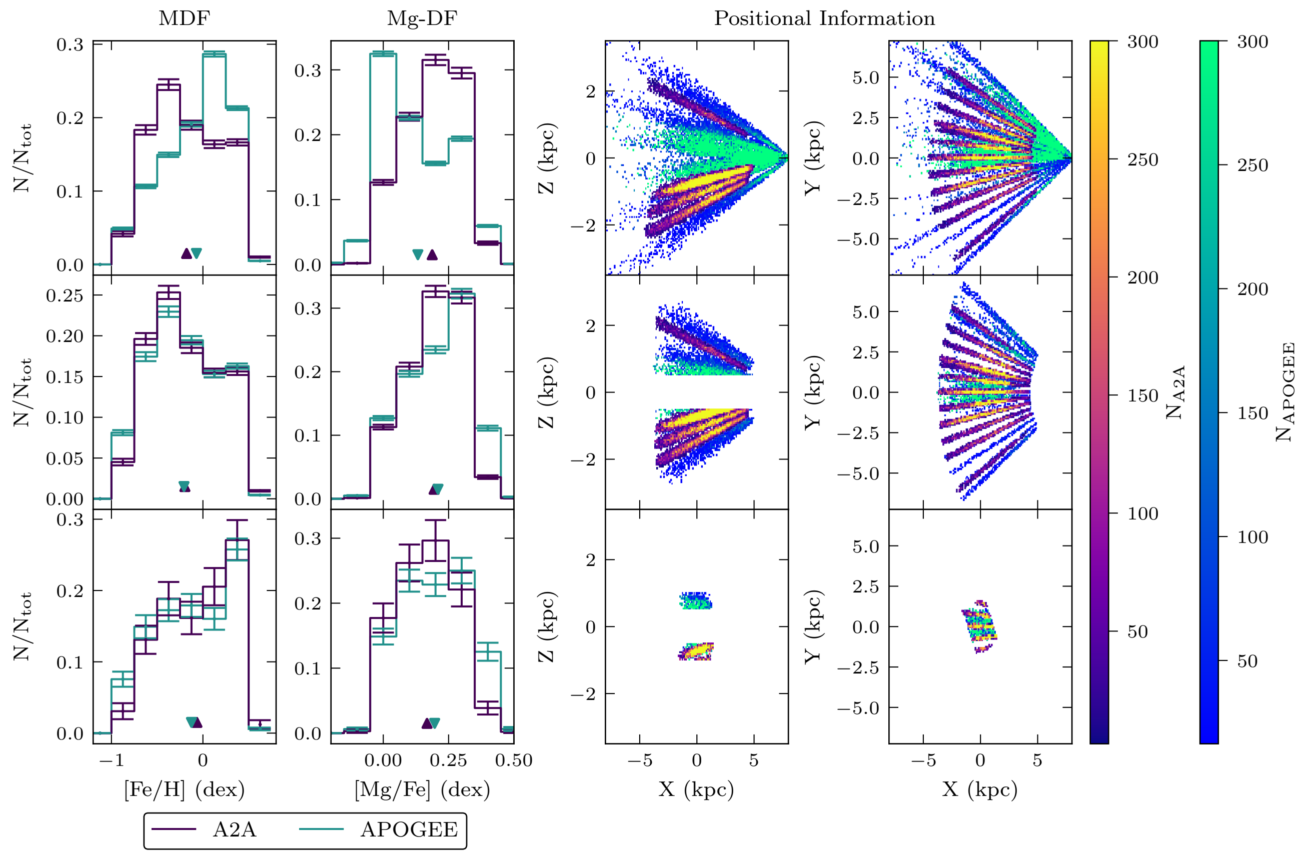

Figure 2.13: SSF-corrected MDFs (first column), Mg-DFs (second column), and their respective positional information (third and fourth columns) of A2A and APOGEE stars with [Fe/H] > −1 dex. The top row includes all stars in each catalogue, while the stars in the second and third rows are restricted to successively smaller areas. The A2A stars are restricted to RC stars. The mean [Fe/H] and [Mg/Fe] values of each MDF and Mg-DF are shown by the triangular markers in each plot.

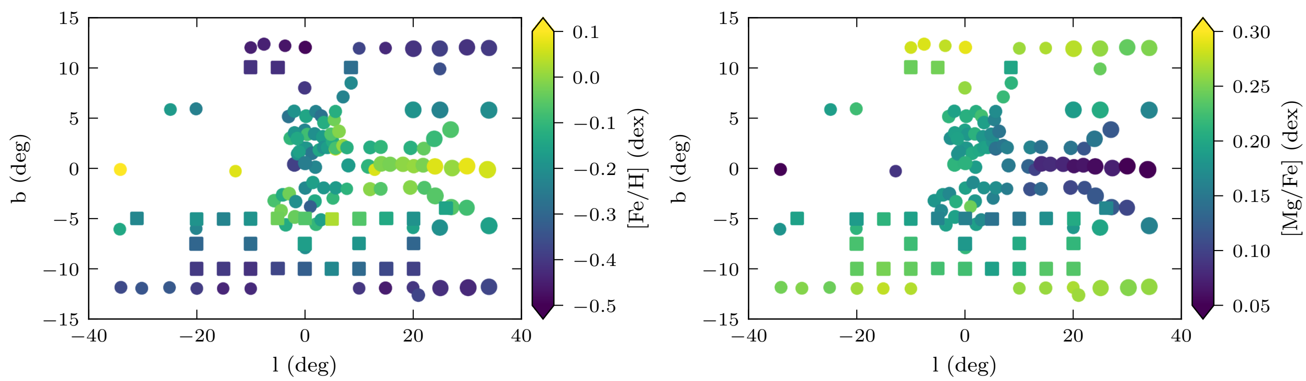

Figure 2.14: SSF-corrected mean [Fe/H] (left) and [Mg/Fe] (right) in APOGEE (circles) and A2A (squares) fields for stars with [Fe/H] > −1 dex and distances from the Sun between 4 and 12 kpc.

(Jönsson et al. 2018; Jofré et al. 2019). Figure B.1 in Appendix B shows the trends between ASPCAP $T_{\rm eff}$ and [Mg/Fe] in the APOGEE bulge sample for a range of [Fe/H] bins and roughly fixed stellar distance, height from the plane, and S/N. From this figure, we can see that regardless of [Fe/H], the average [Mg/Fe] of the APOGEE stars generally increases with increasing $T_{\rm eff}$ until ~4000 K, after which it decreases with increasing $T_{\rm eff}$. The $T_{\rm eff}$ range of the reference set, shown by the blue shaded region in Fig. B.1, does not reach below ~4000 K. Because of this, *The Cannon* cannot learn the trends between $T_{\rm eff}$ and the abundances in ASPCAP that exist below ~4000 K. Furthermore, this $T_{\rm eff}$ cut means that the A2A catalogue would not contain many of these [Mg/Fe]-rich stars with $T_{\rm eff}$ values just below ~4000 K. Together, this could explain why the APOGEE and A2A Mg-DFs disagree at the high [Mg/Fe] end. As we will see in Sect. 2.6.4, [Mg/Fe]-rich stars are typically also [Fe/H]-poor. This could then explain why A2A also observes fewer [Fe/H]-poor stars as compared to APOGEE.

We cannot currently be sure whether the trends we observe between ASPCAP $T_{\rm eff}$ and [Mg/Fe] are physical or systematic and therefore whether the lack of these trends in A2A is problematic or not.

2.6 Abundance structure of the bulge

We now present how the abundances and kinematics vary over the Galactic bulge using the combined APOGEE and A2A catalogues.

For all figures in this section, we restrict the A2A stars to RC stars and require the APOGEE stars to have AstroNN distance errors less than 20%. Unless mentioned otherwise, we use the HQSSF APOGEE bulge MSp and, correct each survey to the HQ 2MASS catalogue they were selected from, and limit stars to [Fe/H] > -1 dex. Furthermore, when combining stars from different spatial bins, we weight the stars in each distance bin to correct for the SSF effects on the abundance distributions but then in each bin we re-weight both surveys such that the sum of their weights is equal to the number of stars (RC for A2A) contributed by each survey.

2.6.1 Mean abundance maps

We first examine the overall variation in [Fe/H] and [Mg/Fe] with position in the Galactic bulge. Figure 2.14 shows the mean [Fe/H] and [Mg/Fe] values in each field of stars with distances from the Sun between 4 and 12 kpc. The APOGEE and A2A surveys generally agree on the overall [Fe/H] and [Mg/Fe] trends with Galactic longitude and latitude. As expected, the high latitude fields are more [Fe/H]-poor and [Mg/Fe]-rich than the low latitude fields. Additionally, at low latitudes, the stars are more [Fe/H]-poor and [Mg/Fe]-rich near the GC than they are in the long bar and disk. Because of this, the vertical abundance gradients at large absolute longitudes are steeper near the plane than at small absolute longitudes. Similar abundance trends with Galactic longitude and latitude were seen by Ness et al. (2016) using APOGEE DR12 data.

Figure 2.15 shows illustrative mean X-Z and X-Y [Fe/H] maps built using A2A and APOGEE stars separately and combined. Here we use a Galactocentric left-handed coordinate system with positive X directed towards the Sun, Y along positive longitude (l), and Z along positive latitude

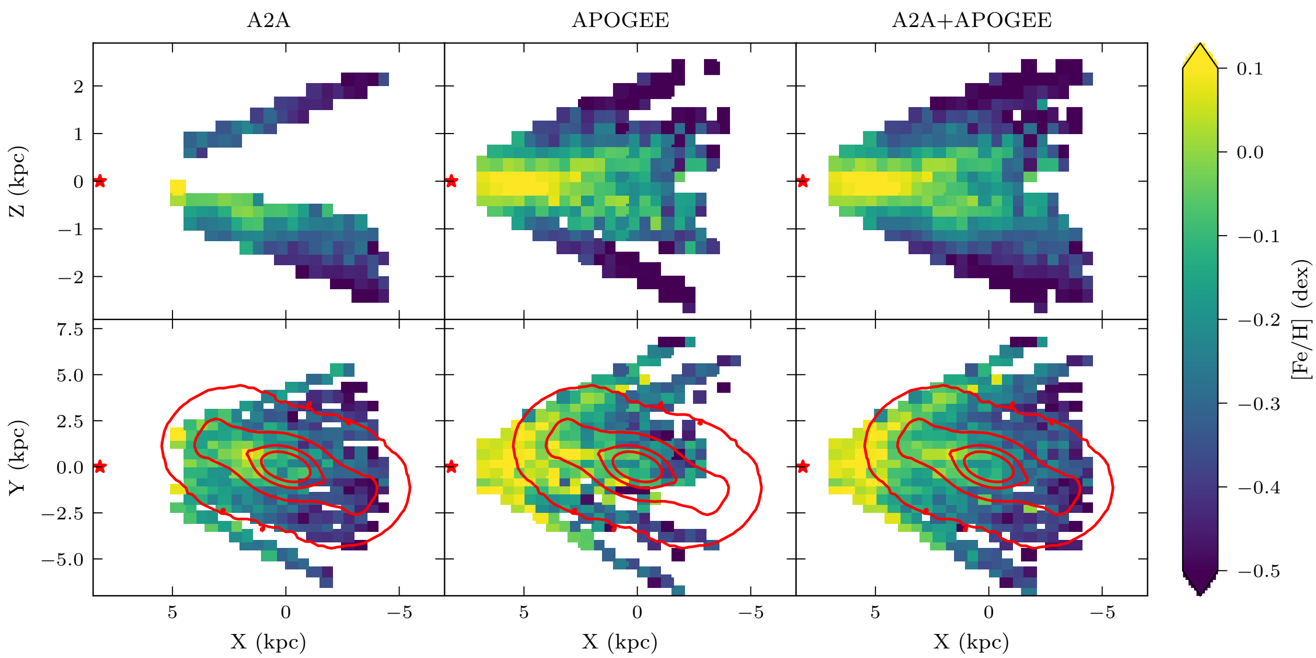

Figure 2.15: SSF-corrected mean [Fe/H] distributions in the X-Z plane (top row) and X-Y plane (bottom row) of A2A (left column), APOGEE (middle column), and combined (right column) stars with [Fe/H] > -1 dex. The red lines trace the density distribution of the Milky Way's bar obtained from a Portail et al. (2017a) bulge-bar model. The red star in each plot marks the position of the Sun.

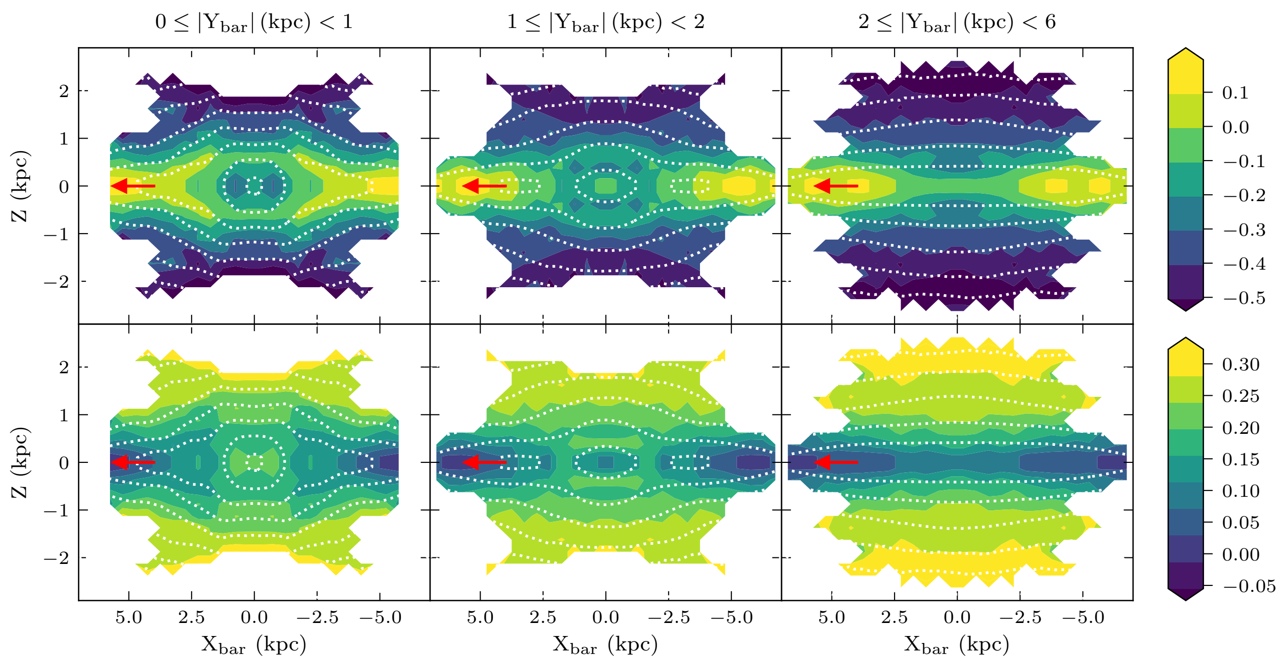

Figure 2.16: SSF-corrected symmetrised mean [Fe/H] (top row) and [Mg/Fe] (bottom row) distribution in the X_{bar}-Z plane for combined A2A and APOGEE stars with [Fe/H] > -1 dex in slices of $|Y_{bar}|$. The dotted white lines trace the density distribution obtained from a Portail et al. (2017a) bulge-bar model. The red arrow points in the direction of the Sun.

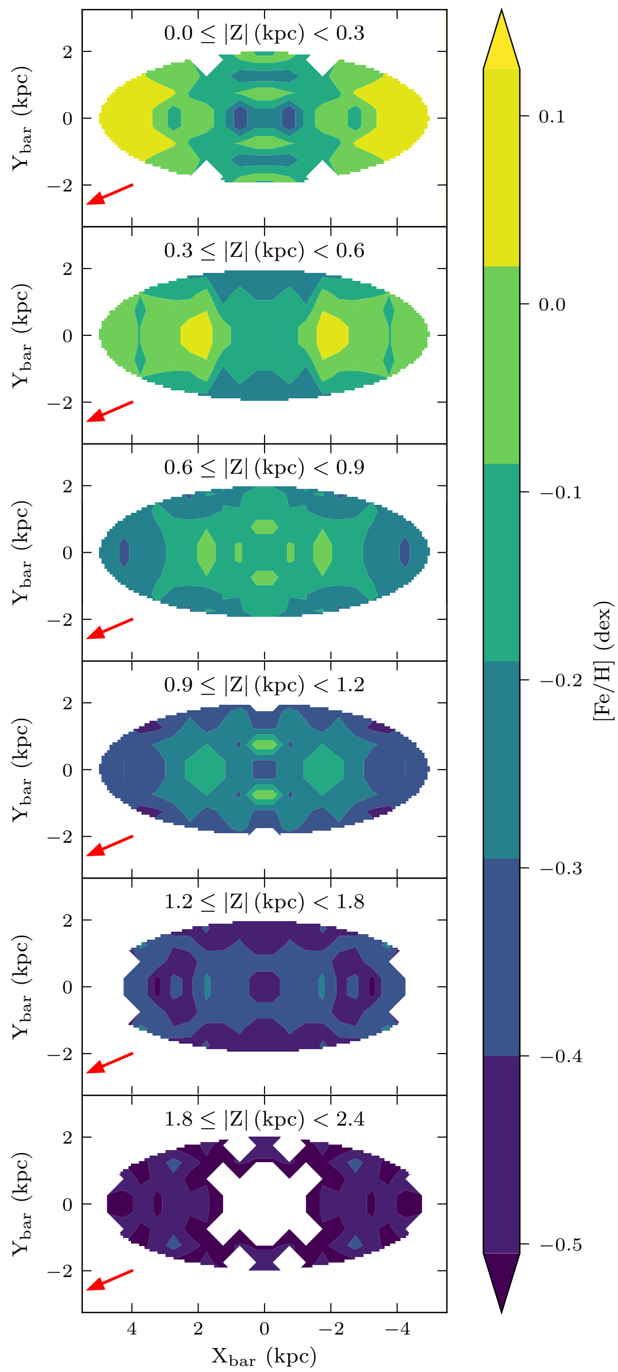

Figure 2.17: SSF-corrected symmetrised mean [Fe/H] distribution in vertical slices along the Galactic bar for combined A2A and APOGEE stars with [Fe/H] > −1 dex. The red arrow points in the direction of the Sun.

(*b*). The assumed value of the solar distance is $R_0 = 8.2$ kpc (Bland-Hawthorn & Gerhard 2016). In order to show all our data, we do not restrict the third dimension in each plot. From the X-Z plots in the top row, we see that the stars from both surveys become more [Fe/H]-rich towards the plane. Additionally, both the individual and combined maps show that the more [Fe/H]-rich stars dominate at larger |Z| at small |X| than they do at larger |X|. Lastly, the stars at the GC are more [Fe/H]-poor than their immediate surroundings.

In the bottom row of Fig. 2.15, on top of the X-Y [Fe/H] maps, we plot the bulge's density distribution obtained from one of the Portail et al. (2017a) bulge-bar models. These models were fit to the RC density of VVV, UKIDSS, and 2MASS and to the stellar kinematics of BRAVA, OGLE, and ARGOS. The model we use has a pattern speed of $\Omega_b = 37.5\,\mathrm{km\,s^{-1}\,kpc^{-1}}$ as that was found to give the best visual match to the VIRAC proper motion data (Clarke et al. 2019a). In both the separate and combined X-Y maps, the near side of the bulge appears to be more [Fe/H]-rich than the far side. This is an effect of the field viewing angles, which cause the nearer stars to be preferentially sampled closer to the plane than the farther stars.

Because we do not restrict the surveys to small bins in the projection direction in Fig. 2.15, the relative weighting by number density is incorrect, especially at low heights in the face-on view (see Sect. 5). In the following plots of this section, we restrict the abundance maps to smaller bins in vertical height and distance in order to minimise this effect.

The bar causes an asymmetry in the spatial maps. To remove this asymmetry, we reorient the following plots to the bar reference system taking the bar angle to be 25° (Bovy et al. 2019). The coordinate system is: the bar long axis (X_{bar}), the bar short axis (Y_{bar}), and the height from the Galactic plane (Z). For these figures we also symmetrise the distribution of stars in order to fill in gaps in our spatial coverage as well as increase the statistics. The symmetrisation is done by reflecting each star into each projected quadrant.

The top row of Fig. 2.16 shows the symmetrised mean [Fe/H] maps in the $|X_{bar}|$-|Z| plane for different slices in $|Y_{bar}|$ using stars from both APOGEE and A2A. On top of the map, we plot the bulge density distribution (white dotted lines) obtained from the Portail et al. (2017a) model. In all $|Y_{bar}|$ slices, the mean [Fe/H] generally increases towards the plane. However, for $|Y_{bar}| < 1$ kpc and $|X_{bar}| < 1$ kpc, the mean [Fe/H] increases rapidly towards the plane, then remains roughly constant between $0.3 \lesssim |Z|\,(\mathrm{kpc}) \lesssim 0.7$, and finally decreases within the inner few 100 pc. This is not the case well outside the boxy-peanut (b/p) bulge lobes ($|X_{bar}| > 3$ kpc) where, within 1 kpc from the Galactic plane, the mean [Fe/H] values increase rapidly towards the plane with no large regions of constant mean [Fe/H] or inversions of the [Fe/H] gradient. Furthermore, the [Fe/H] structure in the $|Y_{bar}| < 1$ kpc slice (top left panel of Fig. 2.16) is puffed up and X-shaped with the more [Fe/H]-rich stars dominating at large |Z| inside the b/p bulge lobes ($|X_{bar}|{\sim}2$ kpc). The X-shape is seen in mean [Fe/H] values between 0 dex and −0.4 dex. For $|Y_{bar}| > 1$ kpc, the mean [Fe/H] structure becomes increasingly flat with increasing $|Y_{bar}|$ and the difference between large and small $|X_{bar}|$ decreases. In the $1 \leq |Y_{bar}|\,(\mathrm{kpc}) < 2$ slice (middle panel of Fig. 2.16), one still sees a slight pinching/X-shape in the [Fe/H] distribution at mean [Fe/H] values of ~ -0.25 dex.

The bottom row of Fig. 2.16 shows the symmetrised mean [Mg/Fe] distribution for APOGEE and A2A stars in the $|X_{bar}|$-|Z| plane in slices of $|Y_{bar}|$. The [Mg/Fe] maps mirror the [Fe/H] maps. The mean [Mg/Fe] generally decreases towards the plane in all $|Y_{bar}|$ slices. For $|Y_{bar}| < 1$ kpc (bottom left panel of Fig. 2.16) and $|X_{bar}| < 1$ kpc, the rate of decrease of the mean [Mg/Fe] is slower and the gradient inverts at small |Z| such that the inner bulge is slightly more [Mg/Fe]-rich than its immediate surroundings. A clear X-shape is seen in the mean [Mg/Fe] distribution at roughly [Mg/Fe] ≈ 0.175 dex in the $|Y_{bar}| < 1$ kpc slice. In the region of the X-shape, the [Mg/Fe]-poor stars dominate at larger |Z| than they do at larger $|X_{bar}|$ or larger $|Y_{bar}|$. For larger $|Y_{bar}|$, the mean [Mg/Fe] distribution becomes increasingly flat.

The [Fe/H] and [Mg/Fe] distributions are more strongly pinched than the density distribution in the $|Y_{bar}| < 1$ kpc slice (left panels of Fig. 2.16). At larger $|Y_{bar}|$, the density contours and the [Fe/H] and [Mg/Fe] contours are in better agreement.

Figure 2.17 shows the symmetrised mean [Fe/H] maps in the $|X_{bar}|$-$|Y_{bar}|$ plane for different slices in |Z|. The stars are restricted to the bar region, which we approximate as an ellipse with a semi-major axis and axis ratio of 5 kpc and 0.4, respectively (see Fig. 2.15). For $|Z| < 0.3$ kpc, the centre of the bar is more [Fe/H]-poor than the bar ends. As the distance from the plane increases, this reverses at ~0.75 kpc. At greater heights, we again see that the centre of the bar is more [Fe/H]-poor than the bar ends.

In near infrared star counts, the Galactic bar has a half length of ~5 kpc (Wegg et al. 2015). The b/p bulge extends out to ~2 kpc from the GC. The bar region that extends outside the b/p bulge is known as the long bar. Wegg et al. (2015) shows that the long bar is composed of two bar components, the thin bar with a scale height of 180 pc, extending to ~4.6 kpc, and the super thin bar with a scale height of 45 pc, reaching ~5 kpc. We do not have the resolution to detect an [Fe/H] or a [Mg/Fe] signature of the super thin bar; however, the top panel of Fig. 2.17 extents to roughly 1.7 thin bar scale heights above the plane. From this, we can approximately say that the combined long bar is super solar in [Fe/H] (also seen in the top left panel of Fig. 2.16). The lower left panel of Fig. 2.16 also shows that the region occupied by the long bar is nearly solar in [Mg/Fe]. This is in contrast to the inner region of the b/p bulge, which has a mean sub-solar [Fe/H] value and is more [Mg/Fe]-rich.

2.6.2 Abundance gradients

Having shown how [Fe/H] and [Mg/Fe] vary over the bulge, we now quantify the vertical and horizontal abundance gradients in the various bulge regions. In Fig. 2.18, we present the mean [Fe/H] and [Mg/Fe] profiles for A2A and APOGEE stars in the inner bulge (left column) and long bar-outer bulge region (right column) as a function of |Z|. We take the inner bulge to be the region within $|X_{bar}| < 2$ kpc and $|Y_{bar}| < 1$ kpc and the long bar-outer bulge region to be the region within $2.5 \leq |X_{bar}|\,(\mathrm{kpc}) < 4.5$ kpc and $|Y_{bar}| < 1$ kpc.

The APOGEE and A2A [Fe/H] and [Mg/Fe] gradients agree within the errors in both regions of the bulge. However, the [Fe/H] and [Mg/Fe] profiles in the inner bulge are offset by roughly 0.1 dex and 0.05 dex, respectively. These offsets are at least partially due to missing [Fe/H]-poor, [Mg/Fe]-rich stars in A2A as discussed in Sect. 2.5.5.

The inner bulge has a different vertical [Fe/H] profile than the long bar-outer bulge region. For $0.7 \lesssim |Z|\,(\mathrm{kpc}) \lesssim 2$, the inner bulge [Fe/H] gradient is ~ − 0.41 dex/kpc; at lower heights, between $0.3 \lesssim |Z|\,(\mathrm{kpc}) \lesssim 0.7$ it flattens at [Fe/H] ≈ −0.12 dex. This flattening of the [Fe/H] gradient is only clear in the APOGEE data (the A2A coverage is too sparse in this area), but was

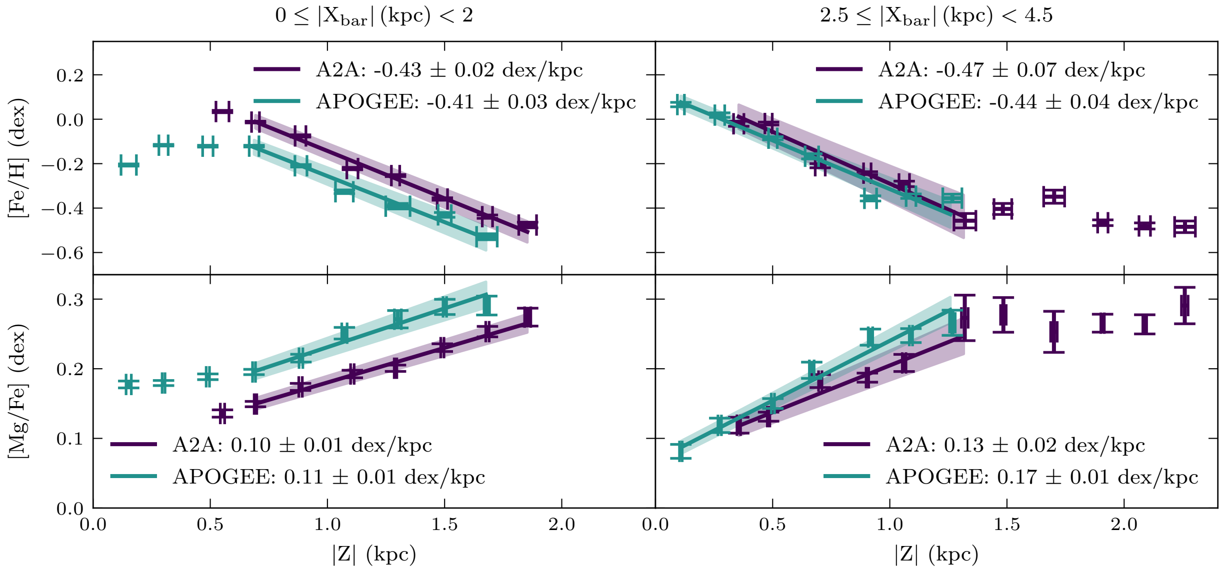

Figure 2.18: SSF-corrected mean [Fe/H] (top row) and [Mg/Fe] (bottom row) vertical abundance profiles for A2A and APOGEE stars in the inner b/p bulge ($|X_{bar}| < 2$ kpc, $|Y_{bar}| < 1$ kpc; left) and long bar-outer bulge regions (2.5 kpc $| \leq X_{bar}| < 4.5$kpc, $|Y_{bar}| < 1$ kpc; right). The A2A and APOGEE gradients of the regions shown by the teal and purple lines are given in the legend of each diagram; error ranges of the linear fits are shown by the shaded regions. For all plots, we require the stars to have [Fe/H] > -1 dex.

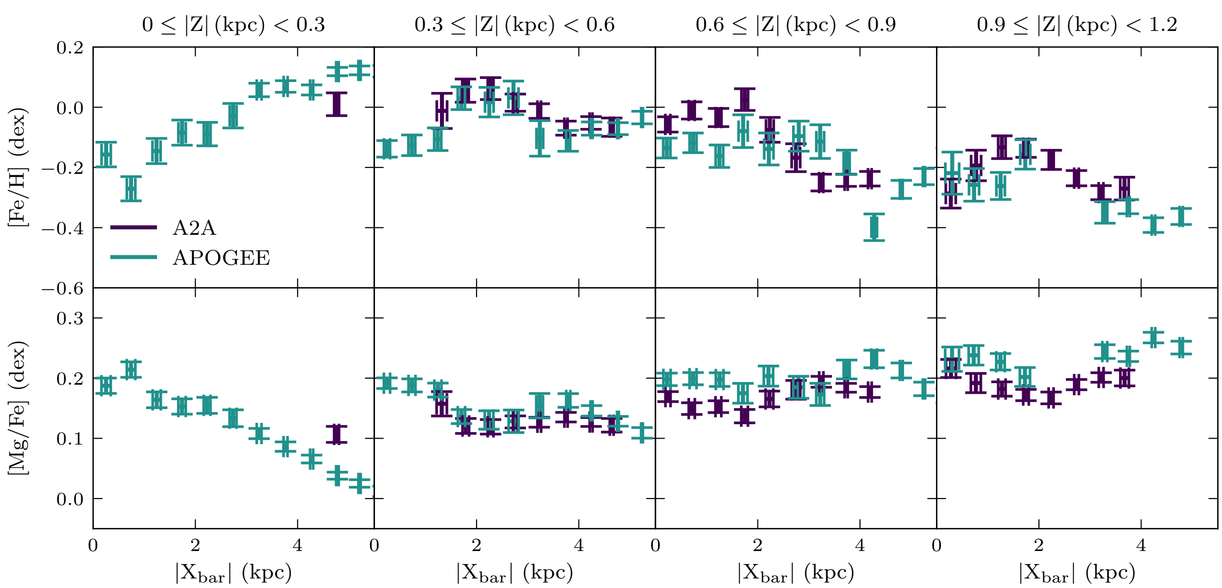

Figure 2.19: SSF-corrected mean [Fe/H] (top row) and [Mg/Fe] (bottom row) horizontal abundance profiles of A2A and APOGEE stars along the bar and at different heights above the Galactic plane. For all plots, we require the stars to have [Fe/H] > -1 dex and $|Y_{bar}| < 1$ kpc.

previously seen also by Rich et al. (2012, 2007) and Ness et al. (2016). Below 0.3 kpc the mean [Fe/H] slightly decreases. This inversion of the mean [Fe/H] gradient was also seen in Fig. 2.16.

The [Fe/H] gradient of the long bar-outer bulge region is roughly flat between $1.25 \lesssim |Z|\,(\mathrm{kpc}) \lesssim 2.25$ at a value of ~ -0.44 dex. For $|Z| \lesssim 1.25$ kpc, the gradient is ~ -0.44 dex/kpc and has no inner flattening.

Using stars with $|l| < 11°$, Rojas-Arriagada et al. (2020) finds the bulge vertical metallicity gradient to be -0.09 dex/kpc for $|Z| < 0.7$ kpc and -0.44 dex/kpc for $0.7 < |Z|\,(\mathrm{kpc}) < 1.2$. Beyond $|Z| > 1.2$ kpc, Rojas-Arriagada et al. (2020) finds a noisy but flat profile. Assuming the bar is at an angle of 25° with respect to the Sun, the 11° limit in Galactic longitude restricts their sample to $\lesssim 2.7$ kpc along the bar, or roughly the region we refer to as the inner bulge. Thus, their vertical metallicity gradient is consistent with our inner bulge vertical metallicity gradient. However, our increased Galactic longitude range allows us to see that the flattening at small $|Z|$ only occurs in the inner bulge and not in the long bar-outer bulge region.

The [Mg/Fe] profiles mirror the [Fe/H] profiles. For the inner bulge, the [Mg/Fe] profile is roughly flat for $|Z| \lesssim 0.7$ kpc at $[\mathrm{Mg/Fe}] \approx 0.19$ dex. For $|Z| \gtrsim 0.7$ kpc, the [Mg/Fe] gradient is ~0.11 dex/kpc. In the long bar-outer bulge region, the [Mg/Fe] gradient is ~0.17 dex/kpc in APOGEE and ~0.13 dex/kpc in A2A between $0 \lesssim |Z|\,(\mathrm{kpc}) \lesssim 1.25$. For $|Z| \gtrsim 1.25$ kpc the [Mg/Fe] profile flattens at ~0.27 dex.

The top row of Fig. 2.19 shows the horizontal mean [Fe/H] profile of A2A and APOGEE stars along the Galactic bar at different heights above the plane. For $|Z| \lesssim 0.3$ kpc, the radial [Fe/H] gradient is steep and positive. However, the stars at $|X_{\mathrm{bar}}| \gtrsim 2-3$ kpc from both surveys strongly decrease in [Fe/H] with increasing height from the plane. For stars at $|X_{\mathrm{bar}}| \lesssim 2-3$ kpc this effect is less pronounced. For A2A, this decrease in mean [Fe/H] within $|X_{\mathrm{bar}}| \lesssim 2-3$ kpc is stronger at smaller $|X_{\mathrm{bar}}|$. This reflects the transitions between the relatively [Fe/H]-poor central bulge, the [Fe/H]-rich long bar near the Galactic plane, the region of enhanced [Fe/H] in the b/p bulge, and the [Fe/H]-poor region above the long bar in Fig. 2.16.

The [Mg/Fe] horizontal profiles of both surveys are shown in the bottom row of Fig. 2.19. For $|Z| \lesssim 0.3$ kpc, the mean radial [Mg/Fe] gradient is steep and negative. However, as the distance from the plane increases the stars at large $|X_{\mathrm{bar}}|$ increase in [Mg/Fe], causing the profile to flatten. At large $|Z|$, a minimum in [Mg/Fe] is seen around $|X_{\mathrm{bar}}| \approx 2$ kpc. This profile is due to the lobes of the b/p bulge.

As was the case for the vertical gradients, there are clear offsets between the APOGEE and A2A horizontal profiles in [Fe/H] and [Mg/Fe], especially for $|X_{\mathrm{bar}}| < 2$ kpc. This could at least in part be due to the limited T_{eff} range of the reference set (see Sect. 2.5.5).

2.6.3 Shape of bulge abundance distribution functions

So far we have only examined how the mean [Fe/H] and [Mg/Fe] vary with position in the bulge. In this section, we illustrate how the MDFs and Mg-DFs change with position in the bulge.

In Fig. 2.20 we plot the generalised MDFs and Mg-DFs of A2A (RC) and APOGEE stars in the inner bulge for $0 < |Z|\,(\mathrm{kpc}) < 1.8$ in bins of width 0.3 kpc. The bins are chosen such that they each contain at least 100 distinct stars. The Gaussian smoothing of each stars is 0.1 dex in the MDFs and 0.033 dex in the Mg-DFs. We see that, while there are some deviations, both surveys

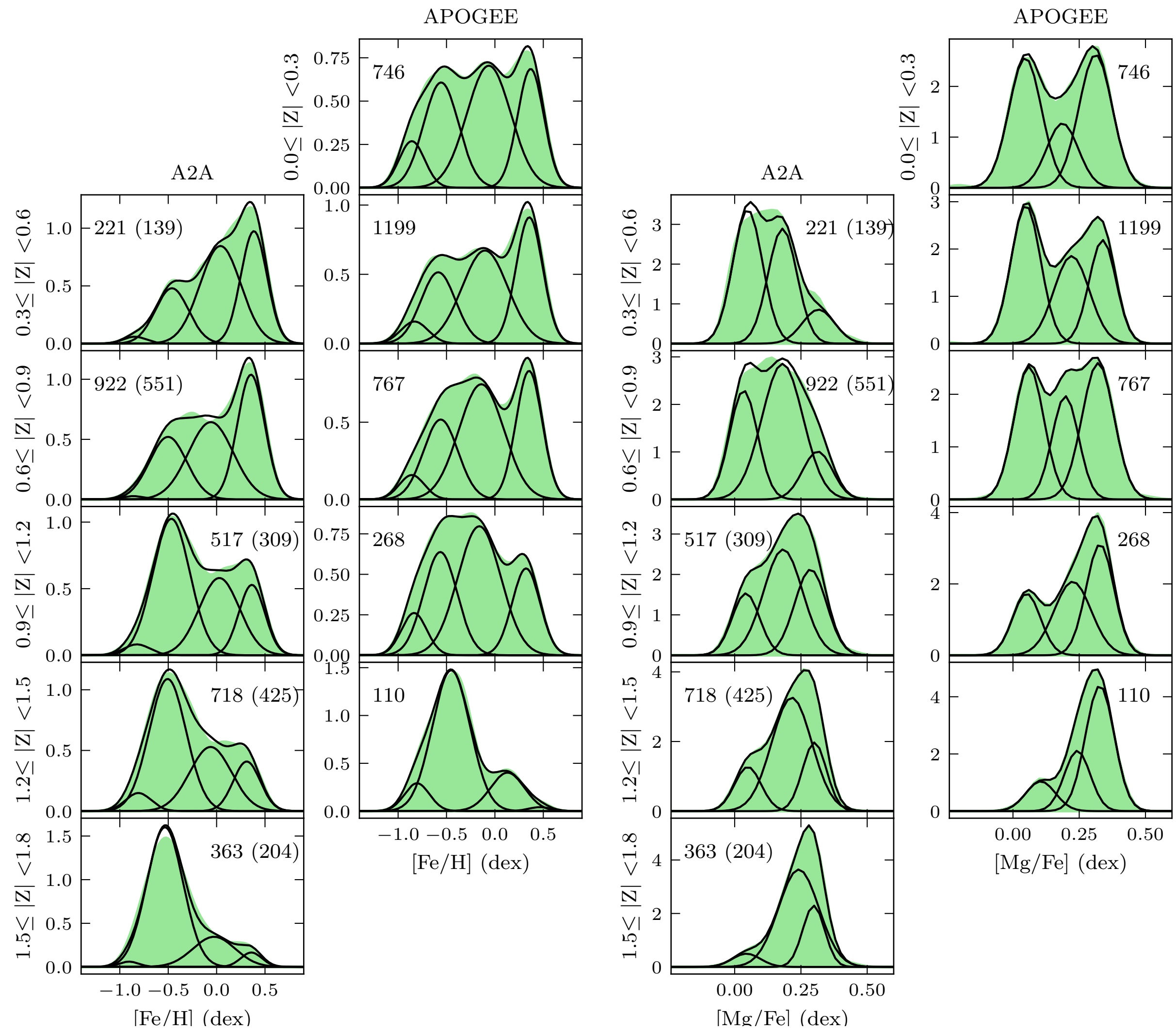

Figure 2.20: Generalised MDFs (left two columns) and Mg-DFs (right two columns) of A2A (RC) and APOGEE stars at different absolute heights above the plane in the inner bulge, shown as filled distributions in green. The stars are required to have $|X_{bar}| < 2$ kpc, $|Y_{bar}| < 1$ kpc, and [Fe/H] > -1 dex. Gaussian mixture decompositions at each height are also shown, in black (individual Gaussians and sums). The number of distinct stars composing each distribution is given in each plot. The number in brackets in the A2A plots gives the number (total weight) of A2A RC stars.

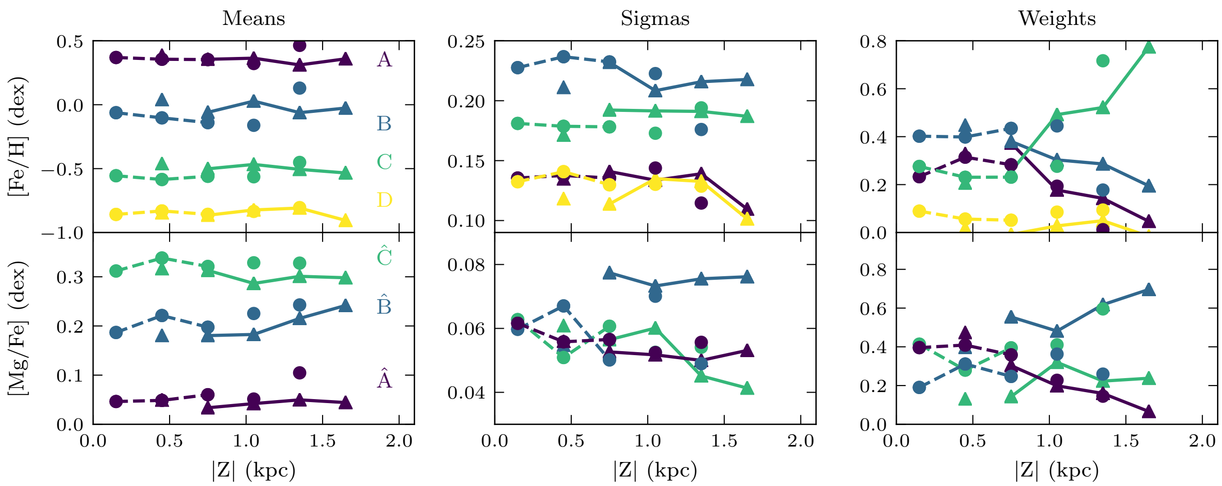

Figure 2.21: Variation in the Gaussian parameters with height from the Galactic plane (|Z|) for the inner bulge. Top row: Parameters from the MDF decompositions. Bottom row: Parameters from the Mg-DF decompositions. The lines connect points with at least 300 distinct stars. Triangular markers and solid lines show the A2A decompositions. Circular markers and dashed lines show the APOGEE decompositions.

show similar trends in their MDFs with |Z|. Far from the plane, the MDFs of both surveys are dominated by a strong peak at ~ -0.4- ~ -0.5 dex. As the distance from the plane decreases, a solar and super solar peak in [Fe/H] grow and become prominent. The surveys show a stronger difference in their Mg-DFs. In APOGEE, far from the plane the Mg-DF is dominated by a single peak at ~0.3 dex. As the distance from the plane decreases, a second peak at ~0.05 dex increases in strength, such that near the Galactic plane, the two peaks are nearly equal in strength. In A2A, the Mg-DF far from the plane is also dominated by a single peak at ~0.3 dex. However, as the distance from the plane decreases, the strength of the high [Mg/Fe] peak decreases and the stars below ~0.25 dex increase in strength. The peak at ~0.3 dex, seen in the APOGEE Mg-DF, is not prominent in the A2A Mg-DFs near the plane.

Using the affine-invariant Markov chain Monte Carlo sampler *emcee* (Foreman-Mackey et al. 2013), we fit a four-component Gaussian mixture model (GMM) to each generalised MDF and a three-component GMM to each generalised Mg-DF. The Gaussians and their sums are plotted on top of the generalised MDFs and Mg-DFs in Fig. 2.20. To see the variation in the MDF and the Mg-DF Gaussian parameters clearly, we plot the Gaussian means, sigmas, and weights against |Z| in Fig. 2.21. To minimise the effects of noise, we only connect points in Fig. 2.21 with at least 300 distinct stars.

The top left plot of Fig. 2.21 shows the variation in the MDF Gaussian means with |Z|. Both the A2A and APOGEE MDFs are well fit by a super solar [Fe/H] Gaussian (A), an intermediate [Fe/H] Gaussian (B), an [Fe/H]-poor Gaussian (C), and a very [Fe/H]-poor Gaussian (D). The overall variation in the [Fe/H] means with latitude is not substantial. The top middle plot shows the MDF sigma variations with |Z|. Gaussian B generally has the largest sigma closely followed

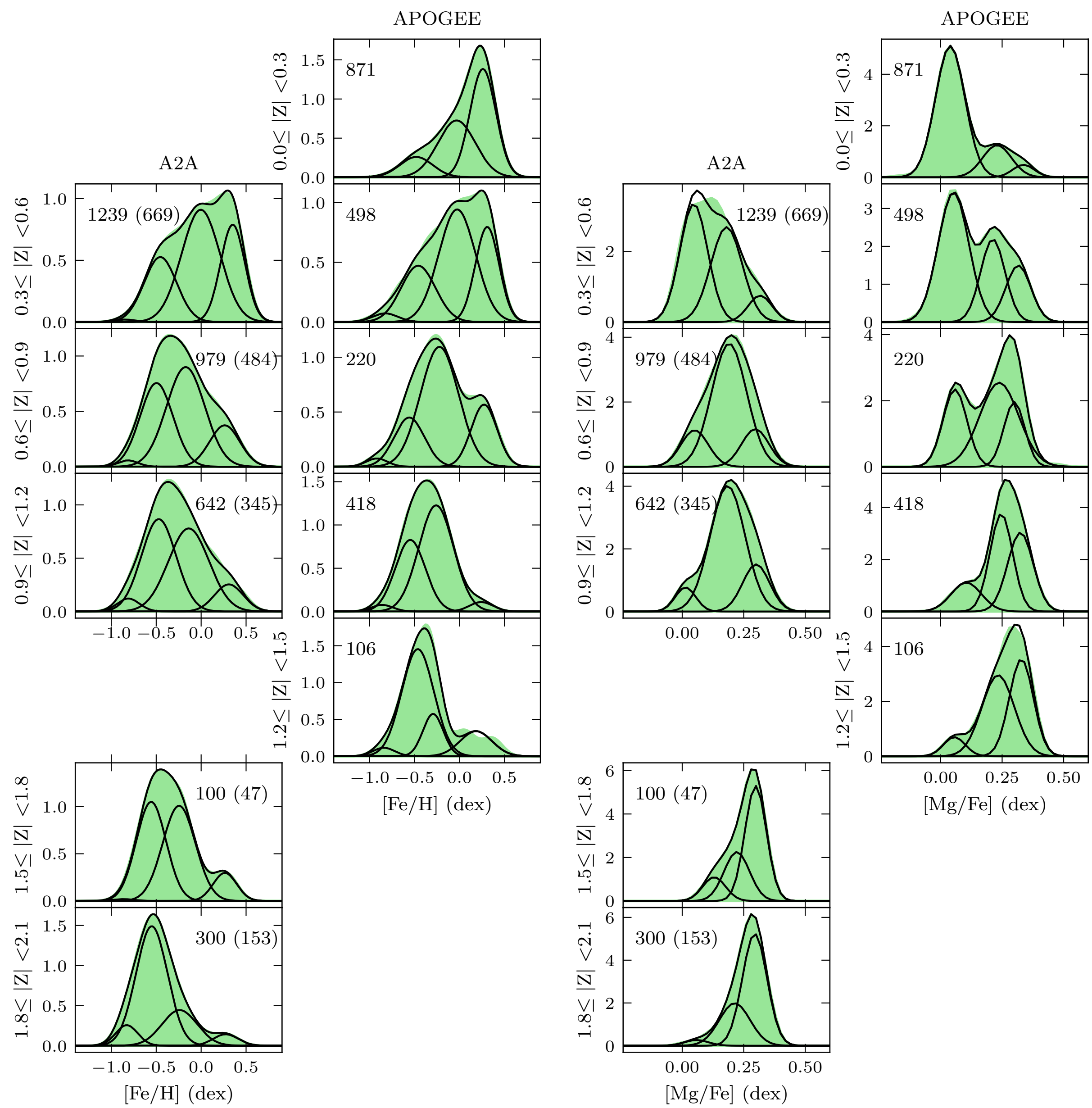

Figure 2.22: Same as Fig. 2.20 except for the long bar-outer bulge region.The stars are required to have 2.5 kpc ≤ $|X_{bar}|$ < 4.5 kpc, $|Y_{bar}|$ < 1 kpc, and [Fe/H] > −1 dex.

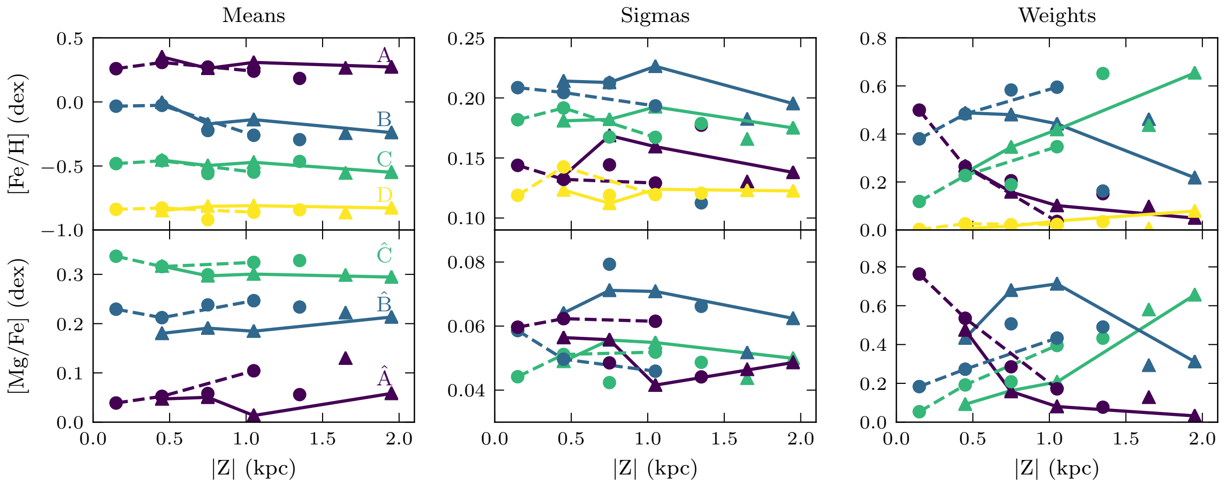

Figure 2.23: Same as Fig. 2.21 except for the long bar-outer bulge region.

by C, and then A and D, which are nearly equal in sigma. The top right plot shows the MDF weight variations with |Z|. The weights of all Gaussians are roughly constant below $|Z| \approx 0.7$ kpc, with B having marginally the largest weight. For $|Z| \gtrsim 0.7$ kpc, the most significant metal-poor Gaussian C increases, while the other two decrease such that C becomes the most dominant at large |Z|. Gaussian D is the weakest component at all heights as it never reaches over 10% in weight.

The variation in the Gaussian parameters from the three Gaussians fit to the Mg-DFs in the inner bulge is shown in the bottom row of Fig. 2.21. The bottom left plot shows the variation in the Gaussian means with |Z|. The Mg-DFs of both surveys are well fit by a [Mg/Fe]-normal Gaussian (Â), an intermediate [Mg/Fe] Gaussian (B̂), and a [Mg/Fe]-rich Gaussian (Ĉ). The bottom middle plot shows the sigma variation in the Gaussians with |Z|. The A2A Gaussian B̂ generally has the highest sigma by ~0.025 dex. The rest of the Gaussians have nearly equal sigma values. The bottom left plot shows the variations in the weights with |Z|. The Gaussian weights are constant below ~0.7 kpc and nearly equal in weight. Above ~0.7 kpc, the weight of Gaussian Â decreases with increasing |Z| such that at ~1.7 kpc its weight is nearly zero. Above ~0.7 kpc, the behaviours of Gaussians B̂ and Ĉ strongly differ between the A2A and APOGEE surveys. As |Z| increases, the APOGEE weights of Gaussians Ĉ and B̂ increase and remain roughly constant, respectively, while the A2A weights of Gaussians Ĉ and B̂ remain constant and increase, respectively.

In Fig. 2.22 we perform a similar procedure as in Fig. 2.20 but on the long bar-outer bulge region. Using both surveys, we obtain generalised MDFs and Mg-DFs with smoothings of ~0.1 dex and ~0.033 dex, respectively, and their Gaussian decompositions in |Z| bins of width 0.3 kpc between $0 < |Z|\,(\mathrm{kpc}) < 2.1$. As was the case with the inner bulge, the more [Fe/H]-poor [Mg/Fe]-rich stars dominate far from the plane while the more [Fe/H]-rich [Mg/Fe]-poor stars dominate close to the plane.

The variations in the MDF Gaussian parameters with |Z| are shown in the top row of Fig.

2.23. We only connect points with at least 300 distinct stars to minimise noise. Similarly to the inner bulge, the top left plot shows that the long bar-outer bulge region is well fit by a super solar [Fe/H] Gaussian (A), an intermediate [Fe/H] Gaussian (B), an [Fe/H]-poor Gaussian (C), and a very [Fe/H]-poor Gaussian (D). The sigma variations are shown in the top middle plot. Gaussian B has the largest sigma value, sequentially followed by Gaussians C, A and D. The variations of the MDF Gaussian weights are shown in the top right plot. At $|Z| \gtrsim 1$ kpc, the weights of the Gaussians are similar to those of the inner bulge, with C dominating over B and A. At low |Z| the weight of the most metal-rich Gaussian A is higher than weight of C, the most significant metal-poor Gaussian. The transition in weight occurs at lower |Z| than in the inner bulge. Furthermore, for $|Z| \lesssim 0.7$ kpc, the weight profiles of A and C are not constant, but continue to increase and decrease towards the Galactic plane, respectively. This is consistent with the profiles in Fig. 2.18. The weight of Gaussian D is weak at all heights, never rising above 10%.

In the bottom row of Fig. 2.23 we plot the variation of the Mg-DFs Gaussian parameters. The left most plot shows the variation in the Gaussian means. The Mg-DFs of both surveys are well fit by a [Mg/Fe]-normal Gaussian ($\hat{A}$), an intermediate [Mg/Fe] Gaussian ($\hat{B}$), and a [Mg/Fe]-rich Gaussian ($\hat{C}$). We see a significant offset between the Gaussian $\hat{B}$ means from both surveys. Furthermore, at $|Z| \approx 1$ kpc the Gaussians $\hat{A}$ means have a large offset. The bottom right plot shows the Gaussian weight variations with |Z|. For both surveys, the [Mg/Fe]-rich Gaussian $\hat{C}$ is strong at high |Z| and decreases in weight with decreasing |Z|, while the [Mg/Fe]-normal Gaussian $\hat{A}$ is very weak at high |Z| and increases in weight with decreasing |Z|. Because of these trends, close to the plane, Gaussian $\hat{A}$ dominates and Gaussian $\hat{C}$ is near zero in weight. At most heights, the Gaussian $\hat{B}$ weight behaviour from both surveys deviates with the weight of Gaussian $\hat{B}$ from A2A being much larger than the weight of Gaussian $\hat{B}$ from APOGEE. Accordingly, the weight of Gaussian $\hat{C}$ from A2A is lower than the weight of the correspondingly [Mg/Fe]-rich Gaussian $\hat{C}$ from APOGEE at most heights.

By comparing the APOGEE weight behaviour of the MDF and Mg-DF Gaussians in both regions of the bulge, it is clear that Gaussians A, B, and C from the MDF decomposition roughly correspond to Gaussians $\hat{A}$, $\hat{B}$, and $\hat{C}$ from the Mg-DF decomposition. However, in the outer bulge, Gaussian $\hat{A}$ is higher in weight than Gaussian A, while Gaussian B is higher in weight than Gaussian $\hat{B}$. Therefore, there is mixing between the Gaussians with some stars that compose Gaussians A and B in APOGEE being part of Gaussians $\hat{B}$ and $\hat{A}$, respectively. For A2A, Gaussian A corresponds to Gaussian $\hat{A}$. However, the behaviours of Gaussians B and C from A2A from the MDF decomposition differ strongly from the behaviours of Gaussians $\hat{B}$ and $\hat{C}$ from the Mg-DF decomposition. This deviation in Gaussian weight behaviour is much stronger in the inner bulge than in the outer bulge.

Overall, it appears that the A2A stars do not reach as high in [Mg/Fe] as the APOGEE stars do. Because of this, the APOGEE and A2A Mg-DFs deviate in shape at the [Mg/Fe]-rich end. We suspect that this may be due to the limited $T_{\rm eff}$ range of the reference set used to train *The Cannon* model for the A2A catalogue (see Sect. 2.5.5 for a more detailed discussion on this).

Multiple other surveys (Rojas-Arriagada et al. 2017; Zoccali et al. 2017; Hill et al. 2011; Schultheis et al. 2017; Uttenthaler et al. 2012) report the bulge MDF to be bi-modal. The [Fe/H]-rich Gaussians in many of these surveys have a mean value of ~0.3 dex, similar to the mean of our most [Fe/H]-rich Gaussian in both the inner and outer bulge. Recently, Rojas-Arriagada et al. (2020) analysed the bulge MDF using a larger sample from APOGEE DR16 data and reported that the bulge is best represented by the superposition of three Gaussian components with nearly constant means at 0.32 dex, −0.17 dex, and −0.66 dex. While we find that the bulge is best fit by four Gaussians, the fourth most [Fe/H]-poor Gaussian is not very significant and we mainly include it to improve the fit. In the inner bulge, the mean values of Gaussian A are similar to that of the most [Fe/H]-rich Gaussian of Rojas-Arriagada et al. (2020). However, in the inner bulge the means of Gaussians B and C are generally more [Fe/H]-rich than their two most [Fe/H]-poor Gaussians. This is likely due to the inclusion of the fourth [Fe/H]-poor Gaussian. Alternatively, the difference may arise from differing SSF-correcting methods or differing distance criteria. Thus, we do not believe that our results significantly differ from those of Rojas-Arriagada et al. (2020).

2.6.4 [Mg/Fe]-[Fe/H] distribution

In this section we present how the [Mg/Fe]-[Fe/H] distribution changes along the Galactic bar using a similar method to Hayden et al. (2015) and Queiroz et al. (2020).

In Fig. 2.24, using stars from both the A2A and APOGEE, we plot the [Mg/Fe]-[Fe/H] distribution along the bar in bins of $|Z|$ and $|X_{bar}|$, requiring $|Y_{bar}| < 1$ kpc. We colour the points by the Gaussian kernel-density estimation using band-widths that obey Scott's rule (Scott 1992).

Figure 2.24 shows that the [Mg/Fe]-[Fe/H] distribution of the bulge and bar has two main maxima, an '[Fe/H] rich-[Mg/Fe] poor' maximum and an '[Fe/H] poor-[Mg/Fe] rich' maximum. These maxima vary in strength with position along the bar. The '[Fe/H] poor-[Mg/Fe] rich' stars dominate away from the plane while the '[Fe/H] rich-[Mg/Fe] poor' stars dominate close to the plane. This trend is weaker at smaller $|X_{bar}|$.

Hayden et al. (2015) concluded using data from APOGEE DR12 (Alam et al. 2015) that the [α/Fe]-[Fe/H] distribution of the outer bulge appeared to be a single sequence with 'high [α/Fe]-low [Fe/H]' stars dominating far from the plane and 'low [α/Fe]-high [Fe/H]' stars dominating close to the plane. Conversely, Rojas-Arriagada et al. (2019a) concluded using data from APOGEE DR14 that the inner bulge [Mg/Fe]-[Fe/H] distribution was composed of two sequences, a 'high [Mg/Fe]-low [Fe/H]' sequence and a 'low [Mg/Fe]-high [Fe/H]' sequence, that merge above [Fe/H] = 0.15 dex. The division of the distribution into two sequences was based on there being relatively few stars around $([\mathrm{Fe/H}], [\mathrm{Mg/Fe}]) = (0.1\,\mathrm{dex}, 0.15\,\mathrm{dex})$, which distorted the contours. Most recently, Queiroz et al. (2020) concluded using data from APOGEE DR16, that the inner bulge [α/Fe]-[Fe/H] distribution consists of two sequences that, unlike what was found by Rojas-Arriagada et al. (2019a), do not merge. Both sequences extend towards each other in [Fe/H], but the transition between them is steep and contains very few stars. From Fig. 2.24 it is not clear if the two maxima compose two separate sequences (as is the case in the solar neighbourhood) or if they are simply the two maxima of a single sequence. Queiroz et al. (2021) finds, from examining the inner bulge [α/Fe]-[Fe/H] and [Mg/Fe]-[Fe/H] distributions using APOGEE DR16 data that, while a discontinuity is visible in the [Mg/Fe]-[Fe/H] distribution, it is much stronger and steeper in the [α/Fe]-[Fe/H] distribution. Because we use [Mg/Fe], it may be harder for us to differentiate whether our data show two merging sequences or a single sequence with two maxima. While we cannot claim separate sequences, our data are consistent with the

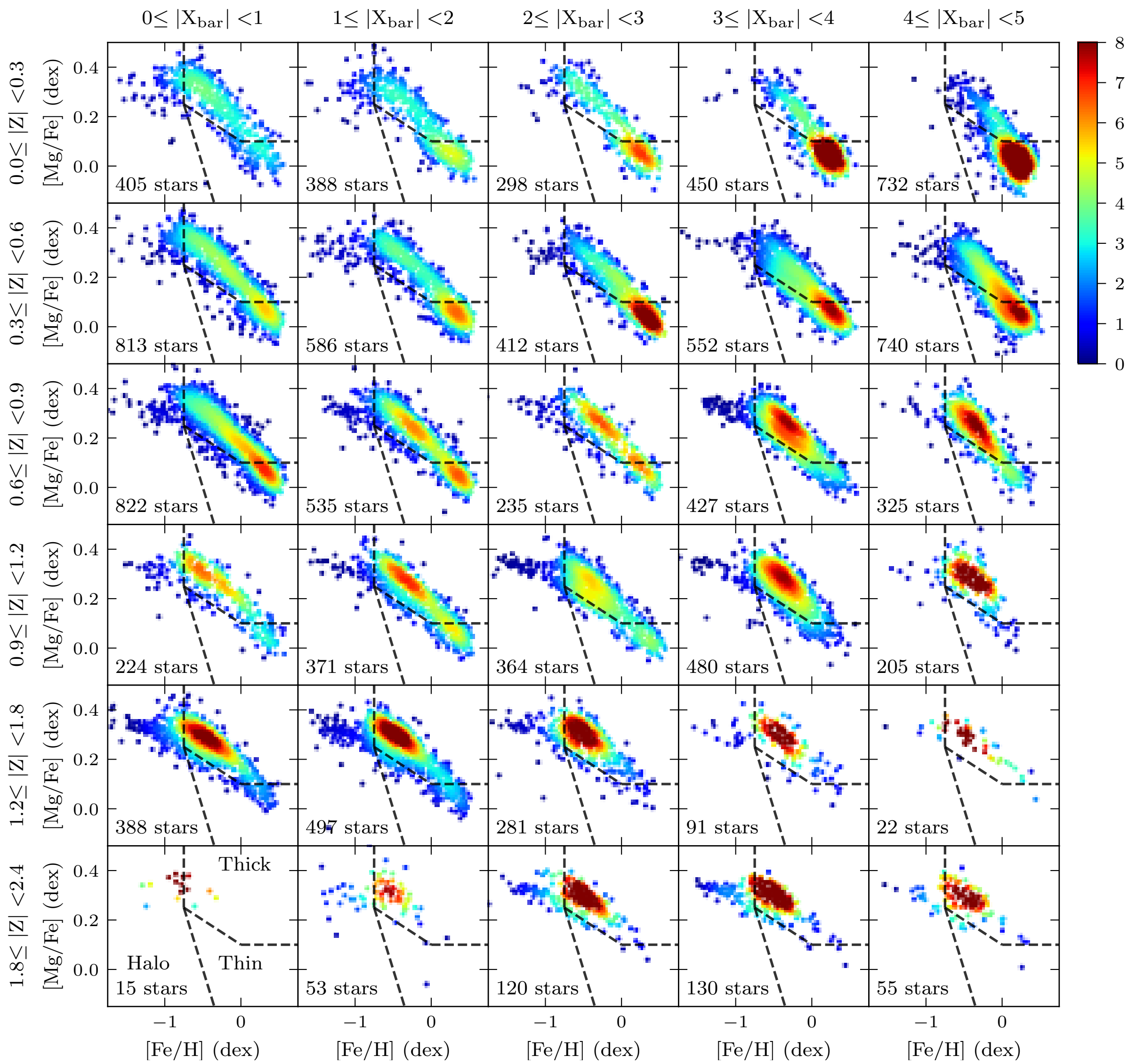

Figure 2.24: [Mg/Fe]-[Fe/H] distribution of A2A and APOGEE stars in intervals of height from the plane (|Z|, kpc) and distance along the bar ($|X_{bar}|$, kpc). The stars are required to have $|Y_{bar}| < 1$ kpc. The point colour gives the Gaussian kernel density estimate. The dashed lines separate the different regions in the parameter space generally populated by the halo, thin disk, and thick disk (defined in the lower-leftmost plot; see text). The number of stars composing each plot (A2A RC stars + APOGEE stars) is given in the lower left corner of each plot.

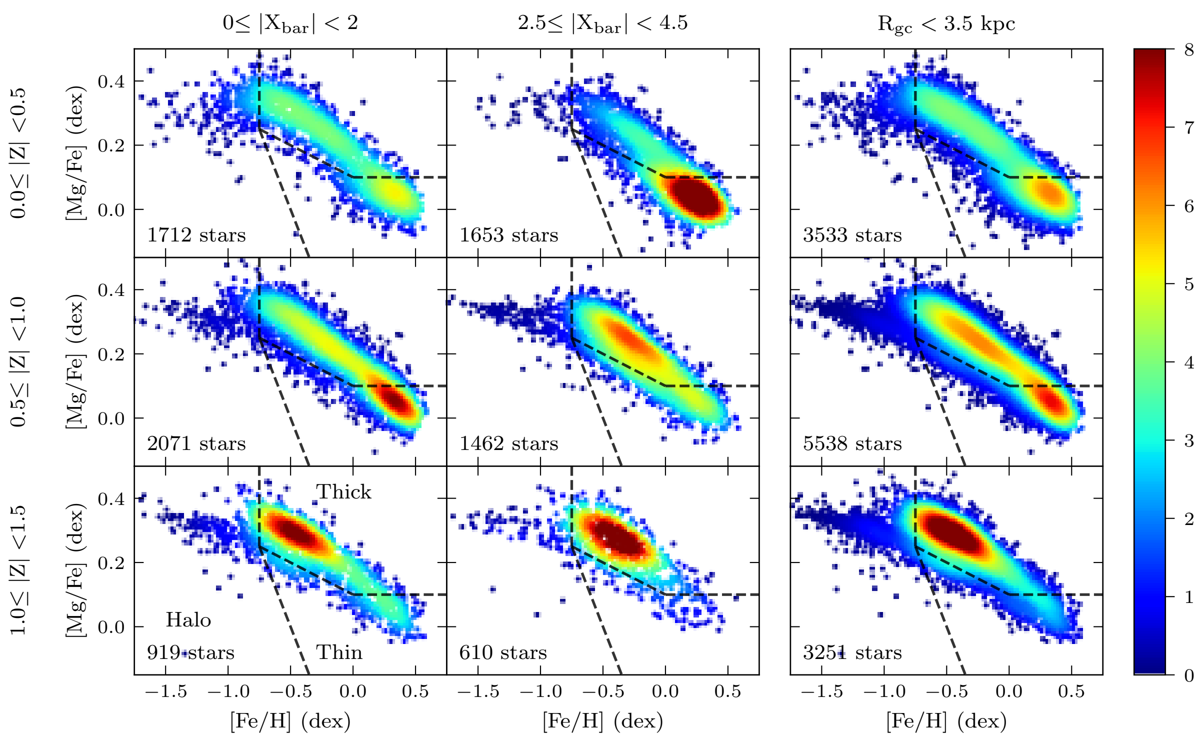

Figure 2.25: [Mg/Fe]-[Fe/H] distribution for A2A and APOGEE stars in intervals of vertical height (in kpc), for the inner bulge (left column), long bar-outer bulge region (middle column), and within a galactocentric radius of 3.5 kpc (right column). The stars in the first two columns are required to have $|Y_{\rm bar}| < 1$ kpc. For plot specifics, see the caption of Fig. 2.24.

suggested bi-modality.

Figure 2.25 is similar to Fig. 2.24; however, the distance bins have been expanded. The first two columns give the [Mg/Fe]-[Fe/H] distributions as a function of |Z| in the inner bulge and long bar-outer bulge region. The third column gives the [Mg/Fe]-[Fe/H] distributions of stars with galactocentric radii (R_{gc}) less than 3.5 kpc. Presenting the distribution in these bins has three advantages: it increases number of stars leading to better statistics, allows us to easily compare the inner bulge and long bar-outer bulge [Mg/Fe]-[Fe/H] distributions, and the bins are comparable to those used in Rojas-Arriagada et al. (2019a) and Queiroz et al. (2020). In the first two columns in Fig. 2.25, it is only the first panel containing the inner bulge stars closest to the plane that shows a bi-modal distribution with a gap around ([Fe/H], [Mg/Fe]) = (0.1 dex, 0.15 dex). No other panel shows a clear bi-modal distribution. Close to the plane, the [Mg/Fe]-[Fe/H] distribution of the long bar-outer bulge region differs significantly from that of the inner bulge with most stars residing in the '[Fe/H] rich-[Mg/Fe] poor' maximum.

In fact, we see that while the '[Fe/H] rich-[Mg/Fe] poor' stars tend to dominate close to the plane and the '[Fe/H] poor-[Mg/Fe] rich' stars tend to dominate far from the plane, these trends are weaker in the inner bulge than in the long bar-outer bulge region. Instead, in the inner bulge, the '[Fe/H] poor-[Mg/Fe] rich' stars extend lower into the plane and the '[Fe/H] rich-[Mg/Fe] poor' stars extend higher out of the plane than they do in the long bar-outer bulge. This is similar to what we saw in Fig. 2.24, although now we see it with greater statistics. Many authors take the bulge to be within $R_{gc} < 3.5$ kpc. When we apply this distance cut in the third column of Fig. 2.25 we again see that the '[Fe/H] rich-[Mg/Fe] poor' stars dominate close to the plane while the "[Fe/H] poor-[Mg/Fe] rich" stars dominate far from the plane. Additionally, there is a clear bi-modality for stars with $|Z| < 0.5$ kpc and $0.5 < |Z|\,(\mathrm{kpc}) < 1$. We confirm the clear bi-modality in the [Fe/H]-[Mg/Fe] distribution in the bulge seen by other authors. However, by dividing the bulge into inner bulge and long bar-outer bulge we see that the bi-modal distribution only occurs in the inner bulge. From Fig. 2.25 we still cannot claim that the two maxima we observe originate from different sequences.

A large fraction of the stars in the inner galaxy are likely contributed by the thin and thick disks. Additionally, a significant fraction of the halo's stellar mass is thought to reside in the inner galaxy. In Figs. 2.24 and 2.25 we draw lines that differentiate regions of the [Mg/Fe]-[Fe/H] space generally populated by the halo, thin disk, and thick disk. These lines are drawn by eye and are similar to those in Adibekyan et al. (2011); Mackereth et al. (2019b); Beraldo e Silva et al. (2021). From examining the stars relative to the lines, we see that stars with abundances similar to the thin disk generally dominate close to the plane while stars with abundances similar to the thick disk generally dominate far from the plane. For small $|X_{bar}|$, the '[Mg/Fe] poor-[Fe/H] rich' stars associated with the thin disk dominate at larger |Z| than they do at larger $|X_{bar}|$. This could be a result of the thin disk stars being more efficiently mapped to larger |Z| during the buckling episodes that built the b/p bulge. We also see that the stars in the very inner bulge ($|X_{bar}| < 1$ kpc and $|Z| < 0.3$ kpc) are more [Fe/H]-poor and [Mg/Fe]-rich than stars in the neighbouring bins. As these stars reside mainly in the thick disk region, these stars could be thick disk stars. The thick disk is more centrally concentrated than the thin disk and therefore could dominate over the thin disk in the very centre.

Lastly, we want to determine how the Gaussian fits in Sect. 2.6.3 correspond to the two max-

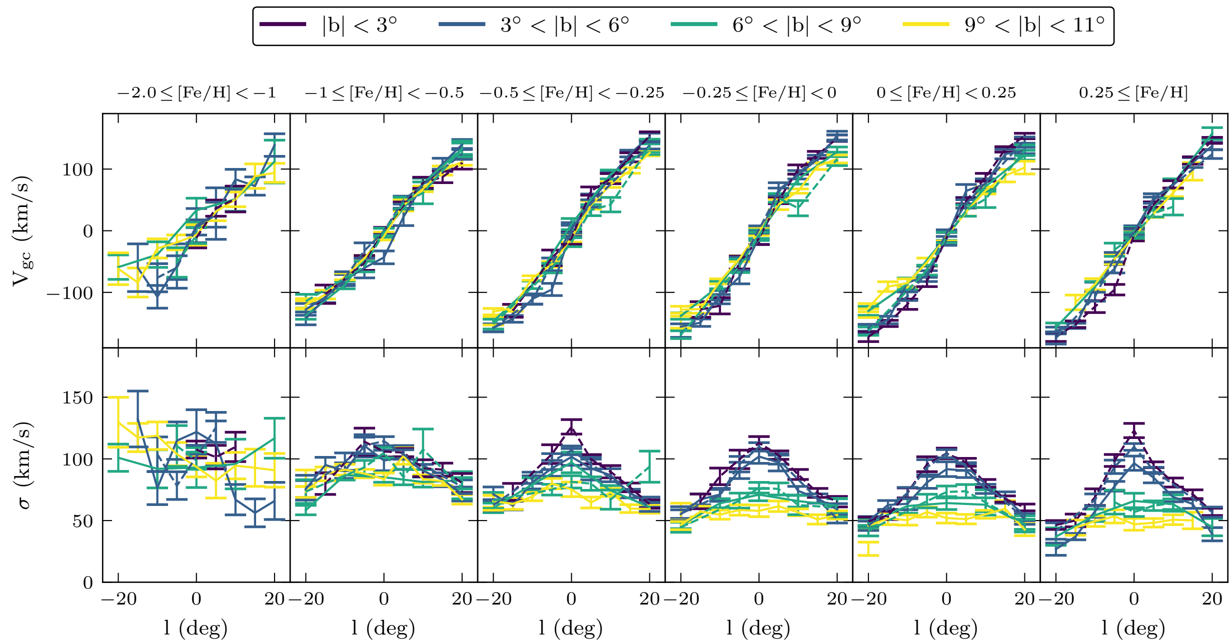

Figure 2.26: Mean radial velocity (top) and velocity dispersion (bottom) versus longitude and latitude in different [Fe/H] bins. The line colour indicates the latitude range. Dashed lines connect APOGEE fields, and solid lines connect A2A fields. All stars are required to have R_{gc} < 4.5 kpc.

ima we see in the [Fe/H]-[Mg/Fe] plane. It is clear from their weight behaviour with position, mean [Fe/H] values, and their correlations to the Mg-DF Gaussians that the MDF Gaussians A and C mainly populate the '[Fe/H] rich-[Mg/Fe] poor' and '[Fe/H] poor-[Mg/Fe] rich' maxima, respectively. Gaussian B from the MDF decomposition appears to be a separate component with strong contamination by the wings of the others.

2.6.5 Bulge chemo-kinematics

In this section we look at how the radial velocity and dispersion vary with [Fe/H] and field position.

In Fig. 2.26, we plot the mean velocity (top row) and velocity dispersion (bottom row) of stars against longitude and latitude in different [Fe/H] intervals. In order to increase the number of APOGEE stars at negative longitudes, we use the HQ APOGEE bulge MSp for this analysis, no longer requiring the APOGEE stars to have good SSF estimates. Thus, we include APOGEE stars from fields represented by both the blue ellipses and red crosses in Fig. 2.1 out to longitudes of ±22°. Because we are including APOGEE stars with no SSF estimates, we do not correct the APOGEE catalogue to the HQ 2MASS catalogue. However, we still correct the A2A catalogue to the HQ 2MASS catalogue it was selected from. Lastly, we restrict the stars to the bulge region by requiring them to have R_{gc} ≤ 4.5 kpc. The error bars in Fig. 2.26 were determined using bootstrapping.

We see from Fig. 2.26 that for stars with [Fe/H] > −1 dex, the mean velocity profiles do not significantly vary with [Fe/H] and that stars in the bulge rotate cylindrically regardless of [Fe/H]. There is a weak trend with latitude where stars located closer to the Galactic plane tend to rotate slightly faster than stars located farther from the Galactic plane. Other studies have observed cylindrical rotation in the bulge (Howard et al. 2009; Kunder et al. 2012; Zoccali et al. 2014) and it is a known property of b/p bulges from N-body simulations (e.g. Athanassoula & Misiriotis 2002; Saha & Gerhard 2013). Below −0.5 dex, the stars rotate more slowly with decreasing [Fe/H]. The stars with [Fe/H] < −1 dex rotate significantly slower than the more [Fe/H]-rich stars.

The velocity dispersion profiles, shown in bottom row of Fig. 2.26, behave differently with [Fe/H]. Far from the Galactic plane, the shapes of the velocity dispersion profiles are flat for [Fe/H] > −1 dex but the amplitudes increase with decreasing [Fe/H] for −1 < [Fe/H] (dex) < 0. Near the Galactic plane and for [Fe/H] > −0.5 dex, the shapes of the velocity dispersion profiles are high and peaked around |l| = 0°, but the change in amplitude becomes less significant with decreasing [Fe/H]. For stars with [Fe/H] > 0 dex, the dispersion does not change significantly with [Fe/H]. Thus contrary to the velocity profiles, the velocity dispersion profiles of stars with [Fe/H] < 0 dex, do show a clear [Fe/H] dependence.

The dispersion profile of stars with −1 < [Fe/H] (dex) < −0.5 differs from those with [Fe/H] > −0.5 dex as the separation between latitudes in the inner longitudes is much weaker and the profiles of stars closer to the plane are flatter. However, we see that, as is the case for the more [Fe/H]-rich stars, the increase in dispersion is stronger for the stars at latitudes farther from the plane (|b| > 7.5°). Furthermore, while the dispersion profiles of the stars closer to the plane are flatter than their [Fe/H]-rich counterparts, the distributions of these stars are still peaked around the central longitudes. Therefore, we conclude that the dispersion profiles of stars with −1 < [Fe/H] (dex) < −0.5 are higher dispersion, slightly flatter versions of the profiles of the stars with [Fe/H] > −0.5 dex.

We find that the stars with −2 < [Fe/H] (dex) < −1 have different dispersion profiles than the more [Fe/H]-rich stars. Apart from the A2A stars between 3° < |b| < 6°, the dispersion profiles of the low latitude stars are not peaked towards the central longitudes. Furthermore, the dispersion of the stars at large absolute longitudes varies significantly between the different latitudes. The range of [Fe/H], the lower rotation, and higher dispersion is consistent with these stars being part of the halo or very [Fe/H]-poor old thick disk.

We examined the velocity and velocity dispersion profiles of APOGEE stars in the HQSSF APOGEE bulge MSp corrected to the HQ 2MASS catalogue. We find that while the data are noisier due to the lower number of stars and fields, we see similar trends between [Fe/H], kinematics, and positions as in the case when we do not correct for the SSF. Therefore, we believe that the longitude and latitude bins we have chosen are small enough that the effects of the SSF are minimal. As a further check of the effect of the SSF, we compared out results to those of Rojas-Arriagada et al. (2020), who finds using APOGEE DR16 data that the dispersion profiles of the more metal-poor stars with −1.2 < [Fe/H] (dex) < −0.5 in the bulge ($R_{gc} \leq 3.5$ kpc) are flat even for the stars at latitudes close to the plane. We find that we can reproduce the trends they find, especially those at low metallicities, if we use their metallicity, longitude, and latitude bins. However, using their bins, we find that the dispersion of the very [Fe/H]-rich stars that are close to the plane and near |l| = 0° is lower than what they report. We suspect that this is due to discrepancies on how we correct for the APOGEE SSF. However, this difference is small and we still observe similar trends as Rojas-Arriagada et al. (2020) at the high [Fe/H] end and therefore do not believe the lack of correction for the SSF will significantly affect the main trends we see or the interpretation of our results. Furthermore, the strong agreement we see between the APOGEE and A2A profiles also supports that the effect of the APOGEE SSF is minor.

2.7 Discussion

Several authors have shown evidence that the presence of a classical bulge in the Milky Way is at most minimal (Shen et al. 2010; Di Matteo et al. 2014; Portail et al. 2017b; Clarke et al. 2019a; Queiroz et al. 2021). Instead, the Milky Way's bulge is likely to be of mainly disk origin. However, whether the bulge formed from an evolving thin disk, a combination of distinct thin and thick disks, or a disk-continuum is currently debated. N-body models of b/p bulges built from single thin disks with inside-out population gradients have reproduced several characteristics observed in the Milky Way's b/p bulge, such as cylindrical rotation (Shen et al. 2010) or the vertical metallicity gradient (Martinez-Valpuesta & Gerhard 2011). However, these models also miss many of the finer chemo-kinematic properties seen in the bulge (Di Matteo et al. 2015; Fragkoudi et al. 2017; Di Matteo et al. 2019).

To put further constraints on the formation of the Galactic bulge, we compare the predictions from a number of models exploring different evolutionary scenarios to our principal results.

Bulge iso-[Fe/H] contours: The bulge's iso-[Fe/H] and iso-[Mg/Fe] contours are X-shaped and exhibit stronger "pinching" than the bulge's density distribution (see Fig. 2.16).

Debattista et al. (2017, DB17) presents an evolving single disk model with continuous star formation that evolved to form a bar, which subsequently buckled, forming a b/p bulge. The iso-[Fe/H] contours of the resulting b/p bulge are X-shaped and more pinched than its density distribution. DB17 argues that the stronger pinching of the [Fe/H] distribution in their model is the result of kinematic fractionation, which they define as the separation of stellar populations by the bar due to their different initial radial kinematics. However, Di Matteo et al. (2019, DM19) shows that separation due to differences in vertical dispersion and scale height is similarly important. They created two N-body b/p bulge models using three disks, which either differed in their radial dispersions or in their vertical dispersions and scale heights, but always had the same radial scale lengths. Both models produced b/p bulges with iso-[Fe/H] contours that are X-shaped and more pinched than their density distributions (see their Fig. 5). Lastly, Fragkoudi et al. (2018, F18) built an N-body b/p bulge model initialised from three co-spatial disks each with different kinematics, scale heights, scale lengths, and abundance distributions. The iso-[Fe/H] contours of their final model are also X-shaped and more strongly pinched than the density distribution.

Therefore, we cannot use our result at current resolution to differentiate between the models. However, the stronger pinching of the iso-[Fe/H] contours with respect to the density distribution further verifies that the bulge has a mainly disk origin.

Bulge radial gradient: In the Galactic plane, the Milky Way's bulge has clear radial gradients in [Fe/H] and [Mg/Fe], such that close to the plane, the inner bulge is more [Fe/H]-poor and [Mg/Fe]-rich than the long bar-outer bulge region; see Figs. 2.14-2.17 and Fig. 2.19.

N-body models initialised as a single disk with a strong negative radial metallicity gradient, such as to reproduce the observed vertical gradient in the bulge after bar evolution, inevitably also show a steep radially inward rise in [Fe/H] (Di Matteo et al. 2015; Fragkoudi et al. 2017). Unlike these models, the longitudinal abundance gradient of the multi-disk model of F18 closely matches the gradients we see in Fig. 2.14 (see their Figs. 9 and 13; already matched to APOGEE DR13 data). This model can reproduce the bulge's final radial [Fe/H] gradient because the [Fe/H]-poor and [α/Fe]-rich initial disks dominate in the central regions, due to their scale lengths being shorter than that of the [Fe/H]-rich and [α/Fe]-poor disk. On the other hand, the three-disk models of DM19, where all disks were initialised with the same radial scale lengths, show similar or larger final [Fe/H] in their centres than in their in-plane bar regions (see Fig. 5 of DM19). In the star-forming, evolving disk model of DB17, the highest metallicities occur in the centre of the final b/p bulge (see their Figs. 11, 24, 26). While this model was built from a single disk, before the bar formed the older populations had lower metallicities, as well as larger radial and vertical velocity dispersions and scale heights, than the younger populations, which end up with the largest central concentration.

Thus it appears that the critical ingredient in these models for explaining the radial [Fe/H] gradient in the bulge and bar is the shorter radial scale length of the initial [Fe/H]-poor disk. However, the F18 model assumes a thin disk radial scale length of 4.8 kpc, significantly larger than in current observations (Bland-Hawthorn & Gerhard 2016), and more than twice the thick disk scale length. This suggests other factors are at play as well.

Bovy et al. (2019) and Hasselquist et al. (2020) show age maps for bulge and long bar stars from APOGEE DR16. These maps indicate a significant fraction of younger stars in the long bar and surrounding disk for R_{gc} > 3.5 kpc and close to the Galactic plane, which are not prominent at smaller radii and at heights above a few 100 pc. This suggests that after the formation of the bulge, the Galactic bar either experienced substantial additional gas inflow and star formation or captured a significant population of disk stars, by slowing its pattern rotation and increasing in size. Capturing disk stars could have happened both intermittently, if indeed the bar regularly changes its pattern speed on dynamical timescales, due to interaction with spiral arms (Hilmi et al. 2020), or secularly by angular momentum transfer to the halo (Chiba & Schönrich 2021). Both mechanisms would be consistent with the dominance of the super-thin bar (Wegg et al. 2015) at these radii. Using the stellar ages from Mackereth et al. (2019a), and restricting the APOGEE sample to ages $>$ 6 Gyr or $>$ 8 Gyr, we still find a horizontal gradient near the disk plane in the remaining bulge sample, but considerably milder. This could be built by a less extreme version of the F18 model, with thin and thick disk scale lengths closer to standard values.

Outer bulge vertical gradient: The vertical [Fe/H] and [Mg/Fe] gradients in the long bar-outer bulge region are ∼ − 0.44 dex/kpc and ~0.13~0.17 dex/kpc, respectively (see Figs. 2.16 and 2.18). In this region, there is no inner flattening of the vertical gradient near the plane as is the case in the inner bulge.

For their three-disk models DM19 shows that while both produce b/p bulges, the region beyond the lobes of the b/p bulge in the model formed from the disks with different radial dispersion has no vertical metallicity gradient (see Fig. 6 in DM19). However, in the model built from disks with different vertical scale heights, a vertical gradient remains in the outer bar. The DM19 models are not realistic and are instead designed to represent extreme cases. In reality, the in-plane and vertical dispersions of a disk should be correlated such that a disk with higher (lower) radial dispersion should also have higher (lower) vertical dispersion and therefore a larger (smaller) scale height. The F18 model is more realistic in that the disks with higher dispersions, which are designed to be more [Fe/H]-poor, have larger scale heights. Due to the interplay with the disks' scale lengths, the F18 model shows a strong vertical gradient in the disk regions.

The single-disk model of Fragkoudi et al. (2017) with an initial radial [Fe/H] gradient does not lead to such a vertical gradient in the outer bar. The evolving disk model, DB17, does show a vertical gradient in the disk. In this model the older populations, which tend to be more metal poor, have larger scale heights than the younger populations, which tend to be metal rich.

This comparison supports a multi-disk formation scenario where the disks that form the bulge must differ in vertical velocity dispersion, and therefore scale height, in order to produce a bulge where the region outside the b/p bulge lobes has strong vertical [Fe/H] and [Mg/Fe] gradients.

The [Fe/H]-[Mg/Fe] distribution: The [Fe/H]-[Mg/Fe] distribution along the bar is roughly linear and composed of two maxima: an '[Fe/H] rich-[Mg/Fe] poor' maximum and an '[Fe/H] poor-[Mg/Fe] rich' maximum. These two maxima vary in strength with position in the bulge such that the [Fe/H]-rich maximum dominates near the plane while the [Fe/H]-poor maximum dominates far from the plane (see Figs. 2.24 and 2.25). At small $|X_{bar}|$, this trend is also present, although weaker than at larger $|X_{bar}|$. There is no clear evidence for two distinct sequences in Figs. 2.24 and 2.25 (but see also Queiroz et al. 2021).

The stronger bi-modality in the [Fe/H]-[α/Fe] distribution is often interpreted as two distinct star formation episodes well separated by a period of quenched star formation (Chiappini et al. 1997; Haywood et al. 2018a). The APOGEE DR16 [Fe/H]-[Mg/Fe] distribution of the bulge (R_{gc} < 3 kpc and $|Z|$ < 0.5 kpc) was recently modelled by Lian et al. (2020b) using a chemical evolution model with an early period of high star formation, which formed the high [Mg/Fe] stars, followed by a quick star formation quenching episode and a long lived period of low star formation, which formed the low [Mg/Fe] stars. This model reproduces the [Fe/H]-[Mg/Fe] distribution of the inner bulge (see Fig. 2.25) and the bi-modal Mg-DFs of the inner bulge seen in APOGEE (Fig. 2.20) (see also Matteucci et al. 2019).

Kinematics with metallicity along the [Fe/H]-[Mg/Fe] distribution: The stars composing the two maxima in the [Fe/H]-[Mg/Fe] distribution display different kinematics. Specifically, the stars in the [Fe/H]-rich maximum (mainly [Fe/H] > 0 dex) are kinematically colder than the stars in the [Fe/H]-poor maximum (mainly $-1 <$ [Fe/H] (dex) < -0.25). Furthermore, the stars composing the [Fe/H]-rich maximum have little kinematic-[Fe/H] dependence while the stars composing the [Fe/H]-poor maximum rotate slightly slower and increase in dispersion with decreasing [Fe/H] (see Fig. 2.26).

Di Matteo et al. (2015) shows using an N-body model that if the origin of a b/p bulge is a single disk with a strong negative radial [Fe/H] gradient, then the [Fe/H]-poor stars should rotate faster than, and have warmer, although similarly shaped, velocity dispersion profiles to the [Fe/H]-rich stars as in this scenario the [Fe/H]-poor stars originate from larger disk radii. The lack of kinematic dependence on [Fe/H] of the stars in the [Fe/H]-rich maximum and the decrease in mean velocity with decreasing [Fe/H] in the [Fe/H]-poor maximum indicates that the origin of the Galactic bulge cannot be a single disk with a strong negative radial [Fe/H] gradient. Instead, kinematic and spatial differences of the maxima support a scenario where the stars composing the maxima originate from at least two separate disks, with the stars composing the [Fe/H]-rich maximum originating from a colder disk with little to no radial [Fe/H] gradient and the stars composing the [Fe/H]-poor maximum originating from a hotter disk.

DB17 finds that in order for the stars with [Fe/H] < -0.5 dex in their model to have the high, flat, and largely latitude-independent dispersion profiles observed in Ness et al. (2013b), they need to add a slowly rotating, low mass (5% central Milky Way mass), high dispersion component to their model. They associated this component with the stellar halo (see their Fig. 21). From our data, the slower rotation and increased dispersion of the stars with $-1 <$ [Fe/H] (dex) < -0.5 as compared to the stars with $-0.5 <$ [Fe/H] (dex) < -0.25 may be the result of contamination by the high dispersion component dominating below -1 dex. As the stars in the [Fe/H]-poor tail are slowly rotating, kinematically hot, and [Mg/Fe]-rich, we tentatively associate them with the stellar halo. A contamination by halo stars is further supported by Lucey et al. (2021) who, from examining the chemo-kinematics of metal-poor bulge stars, finds that the fraction of halo interlopers in the bulge increases with decreasing metallicity between $-3 <$ [Fe/H] (dex) < 0.5.

In all, our data paints a consistent picture for the origin of the b/p bulge: at least two initial disks with differing dispersions, scale heights, and scale lengths underwent spatial and kinematic fractionation resulting in the b/p bulge of the Milky Way that we observe today. Due to their kinematics as well as their [Fe/H]-[Mg/Fe] distributions, we associate these disks with the thin and thick disks. We also associate the very [Fe/H]-poor, [Mg/Fe]-rich, kinematically hot tail of the bulge stars with the stellar halo.

2.8 Summary and conclusions

In this work we used the data-driven method *The Cannon* to put stars from the ARGOS survey onto the parameter and abundance scales of the APOGEE survey. After doing so, we were able to directly combine the two surveys and gain a deeper and more reliable coverage of the Galactic bulge.

In the first half of the paper, we described how we applied *The Cannon* to the ARGOS stars to obtain the A2A survey. To show that we have successfully placed the A2A stars on the APOGEE label scales, we performed three validation tests: the pick-one-out test (Fig. 2.4), spectrum reconstruction (Fig. 2.6), and stellar $T_{\rm eff}$-log(g) distribution (Fig. 2.7). These tests show that it is possible to perform *The Cannon* label transfer using a moderate number (204) of reference set stars and still obtain labels with good precisions. After performing the validation tests, we accounted for the SSF of each survey such that, after it was corrected for, we statistically obtained the HQ 2MASS catalogues they were selected from. After this, we compared the SSF-corrected MDFs and Mg-DFs of the APOGEE and A2A surveys and found that the different spatial regions probed by each survey cause a clear spatial bias; however, when the distribution functions were compared in fixed distance bins, the MDFs and Mg-DFs agreed except at the high [Mg/Fe] and low [Fe/H] ends, where APOGEE observes more stars. This may be due to trends between T_{eff} and the abundances in APOGEE and the fact that the reference set only covers a limited T_{eff} range on the APOGEE scale.

In the second half of the paper, we used stars from both the A2A and APOGEE surveys to investigate the abundance structure of the bulge. The results we found include:

(i) The [Fe/H] and [Mg/Fe] maps built using APOGEE and A2A data show strong X-shapes that are more pinched than the density distribution given by the currently best dynamical model of the Milky Way's bulge and bar from Portail et al. (2017a). The stronger pinching in the [Fe/H] and [Mg/Fe] maps than in the density map supports a mainly disk origin for the Galactic bulge.

(ii) The inner bulge and long bar-outer bulge region have different chemical properties. While the inner bulge [Fe/H] and [Mg/Fe] profiles are nearly flat within 0.7 kpc of the Galactic plane and then steepen to ~ -0.41 dex/kpc and ~0.11 dex/kpc, respectively, the vertical [Fe/H] and [Mg/Fe] profiles of the long bar-outer bulge region are steep near the plane at ~ -0.44 dex/kpc and ~0.13~0.17 dex/kpc, respectively, with a flat distribution for $|Z| > 1.25$ kpc. Close to the plane the inner bulge is sub-solar in [Fe/H] and [Mg/Fe]-rich, while the flat bar is nearly solar in [Fe/H] and [Mg/Fe]-normal.

(iii) The [Fe/H]-[Mg/Fe] distributions in the bulge and long bar have two main maxima, an '[Fe/H] rich-[Mg/Fe] poor' maximum and an '[Fe/H] poor-[Mg/Fe] rich' maximum. The '[Fe/H] rich-[Mg/Fe] poor' maximum dominates close to the plane, has a lower dispersion, and shows no significant mean radial velocity dependence on [Fe/H]. The '[Fe/H] poor-[Mg/Fe] rich' maximum dominates far from the plane, has a higher dispersion, and its [Fe/H]-poorer stars rotate slightly more slowly on average than its [Fe/H]-richer stars.

(iv) The most [Fe/H]-poor stars ([Fe/H] < -1 dex) rotate slowly and have high flat dispersion profiles. We associate these stars with the stellar halo. This is also supported by the distribution of these [Fe/H]-poor stars in the [Fe/H]-[Mg/Fe] plane in Fig. 2.24.

The positive horizontal [Fe/H] gradient in the bulge close to the Galactic plane and the negative vertical [Fe/H] gradient in the long bar region favour models in which the bulge and bar formed from initial thin and thick disks with different vertical and radial scale lengths (Fragkoudi et al. 2018). This multi-disk origin is further supported by the higher pinching of the abundance distributions in the bulge as compared to the density distributions and the differing kinematics of the low and high [Fe/H] stars. However, the large thin-disk scale lengths required by these models, together with younger estimated mean ages in the outer bar (Bovy et al. 2019; Hasselquist et al. 2020), suggest that the Galactic bar may have captured younger, more metal-rich stars well after its formation.

Chapter 3

The Milky Way's middle-aged inner ring

Original publication: Shola M. Linz-Wylie, Jonathan P. Clarke, and Ortwin E. Gerhard, 2022, A&A, 659, A80

Abstract

We investigate the metallicity, age, and orbital anatomy of the inner Milky Way, specifically focussing on the outer bar region. We integrated a sample of APOGEE DR16 inner Galaxy stars in a state of the art bar-bulge potential with a slow pattern speed and investigated the link between the resulting orbits and their [Fe/H] and ages. By superimposing the orbits, we built density, [Fe/H], and age maps of the inner Milky Way, which we divided further using the orbital parameters eccentricity, $|X_{max}|$, and $|Z_{max}|$. We find that at low heights from the Galactic plane, the Galactic bar gradually transitions into a radially thick, vertically thin, elongated inner ring with average solar [Fe/H]. This inner ring is mainly composed of stars with AstroNN ages between 4 and 9 Gyr with a peak in age between 6 and 8 Gyr, making the average age of the ring ~6 Gyr. The vertical thickness of the ring decreases markedly towards younger ages. We also find very large L4 Lagrange orbits that have average solar to super-solar metallicities and intermediate ages. Lastly, we confirm a clear X-shape in the [Fe/H] and density distributions at large Galactic heights. The orbital structure obtained for the APOGEE stars reveals that the Milky Way hosts an inner ring-like structure between the planar bar and corotation. This structure is on average metal rich, intermediately aged, and enhances the horizontal metallicity gradient along the bar's major axis.

3.1 Introduction

From previous Galactic bulge studies, we know that the stars in the outer regions of the Galactic bar are on average more metal rich and younger in comparison to the stars in the central bulge (Bovy et al. 2019; Hasselquist et al. 2020; Queiroz et al. 2021). This difference leads to a pronounced horizontal metallicity gradient along the bar's major axis (Wylie et al. 2021). The Milky Way (MW) is not unique in this structure; bars with ends that are more metal rich and/or younger than their central regions have been observed in a few other galaxies as well (Seidel et al. 2016), including M31 (Gajda et al. 2021).

This gradient structure has several possible origins, one of which is that the bulge and bar were formed from dynamical instabilities of coexisting discs with differing scale lengths and metallicities (Fragkoudi et al. 2018; Wylie et al. 2021). In this scenario, the most metal-poor discs dominate in the very central regions due to their shorter scale lengths, while the more metal-rich discs dominate in the outer regions, resulting in a positive horizontal metallicity gradient. However the MW's horizontal gradient is likely too steep to be fully explained by this scenario, suggesting that additional mechanisms are at work. To investigate this further, we built density, [Fe/H], and age orbital maps for a sample of inner Galaxy stars from APOGEE[1] DR16, for which these parameters along with their positional and 3D kinematic information are available from the ASPCAP[2], AstroNN, and Gaia DR2 catalogues (García Pérez et al. 2016; Gaia Collaboration et al. 2018; Leung & Bovy 2019b; Mackereth et al. 2019a). We integrated the orbits of these stars in a realistic MW bar-bulge potential from Portail et al. (2017a, hereafter P17) which was fit to MW star count data derived from the VVV, UKIDSS, and 2MASS surveys[3] (Saito et al. 2012; Lucas et al. 2008; Skrutskie et al. 2006) by Wegg & Gerhard (2013) and Wegg et al. (2015), and to kinematic data from the BRAVA, ARGOS, and OGLE[4] surveys (Kunder et al. 2012; Ness et al. 2013b; Rattenbury et al. 2007). The favoured model from P17 had a slow pattern speed of $\Omega_b = 39 \pm 3.5\,\mathrm{km\,s^{-1}\,kpc^{-1}}$ which puts the corotation radius of the bar at slightly over 6 kpc. More recent dynamical studies of both the stellar kinematics in the bar and resonant stars in the solar neighbourhood have found similar or slightly slower values of Ω_b (e.g. Bovy et al. 2019; Binney 2020; Chiba & Schönrich 2021; Li et al. 2022; Clarke & Gerhard 2021).

As we later see, a mechanism to enhance the horizontal gradient in the bar is an inner ring between 4-6 kpc along the bar's major axis. This has also been seen in some galaxy models in cosmological simulations (Fragkoudi et al. 2020). Inner rings are observed in a substantial fraction of barred disc galaxies (Kormendy 1979; Buta & Combes 1996; Comerón et al. 2014) and tend to be preferentially aligned with the bar. Inner rings observed at optical wavelengths generally contain star-forming regions (Buta 1995) and are thought to form from the collection of gas around the bar's 4:1 resonance (Schwarz 1984; Buta & Combes 1996). Passive rings which no longer form stars can be thicker than active rings, but they are generally seen in earlier type galaxies ($\geq$ Sab, Comerón 2013).

This paper is structured as follows: In Sect.3.2 we explain, in more detail, the sample of stars we used, the potential we integrated them in, and the assumptions we made. We also compare the distributions of the APOGEE stars in heliocentric velocity space to predictions from the dynamical model used to generate the potential to check that they are consistent. In Sect.3.3 we show density maps for the model and the APOGEE stellar orbits, and [Fe/H] and age maps for the APOGEE orbits selected using spatial symmetry and orbital eccentricity criteria. We end in Sect.3.4 with a discussion of our results and our conclusions.

[1] Apache Point Observatory Galactic Evolution Experiment

[2] APOGEE Stellar Parameter and Chemical Abundance Pipeline

[3] Vista Variables in the Via Lactea, UKIRT Infrared Deep Sky Survey, Two Micron All Sky Survey

[4] Bulge Radial Velocity Assay, Abundances and Radial velocity Galactic Origins Survey, Optical Gravitational Lensing Experiment

3.2 Data and methods

In this work we used stars from the APOGEE DR16 catalogue (Majewski 2016). For each star, we obtained its [Fe/H] and line-of-sight velocity from the ASPCAP pipeline (García Pérez et al. 2016; Holtzman et al. 2018; Jönsson et al. 2020) and its RA and Dec proper motions from the Gaia DR2 Catalogue (Gaia Collaboration et al. 2018). Additionally, we obtained a spectrophotometric distance and age for each star from the AstroNN catalogue (Leung & Bovy 2019b; Mackereth et al. 2019a). We restricted the sample of stars to those in the APOGEE main sample (EXTRATARG flag= 0) with valid ASPCAP [Fe/H], effective temperatures ($T_{\rm eff}$), surface gravities (log(g)), and [Mg/Fe]. As quality cuts, we also required S/N> 60, ASPCAP $T_{\rm eff} > 3200$ K, AstroNN distance errors less than 20%, $0 \leq$ AstroNN age (Gyr) < 12, and no Star_Bad flag set (23rd bit of ASPCAPFLAG = 0). For the analysis of this work requiring the AstroNN ages, we restricted the stars to only those with AstroNN log(g) errors <0.2 dex to remove dwarf stars and AstroNN [Fe/H] > -0.5 dex as recommend by Bovy et al. (2019). Lastly, to focus on the inner MW, we made a spatial cut, requiring the stars to have cylindrical distances from the Galactic centre (GC) $R_{\rm GC} < 7$ kpc and absolute latitudes (|b|) $< 13°$. This leaves 32, 536 stars in our sample (26,416 in the age sample). We found that when we restricted our sample further by requiring the stars to have RA and Dec proper motion errors less than 0.5 mas yr^{-1} and distance errors less than 10% (removes ~9, 000 stars), our main results essentially remained unchanged.

We integrated the orbits of our APOGEE sample in the rotating potential of one of the P17 dynamical bar models. P17 adapted these models using the made-to-measure method, such that they fitted the red clump density from the VVV, UKIDSS, and 2MASS surveys and the stellar kinematics from the BRAVA, OGLE, and ARGOS surveys. They assumed a bar angle $\phi_\odot = 28°$ and the Sun's distance from the GC $R_0 = 8.2$ kpc. The dark matter potential was also adapted during these fits. For the results of the work here, we used the P17 model with a pattern speed $\Omega_b = 37.5\,{\rm km\,s^{-1}\,kpc^{-1}}$, their central disc mass $M_c = 2 \times 10^9$ $M_\odot$, and mass to red clump star number of 1000 $M_\odot$, as it has provided a good match to both the bulge proper motions (Clarke et al. 2019b) and inner Galaxy gas flows (Li et al. 2022). As a test, we also integrated the APOGEE stars in P17 models with $\Omega_b = 35\,{\rm km\,s^{-1}\,kpc^{-1}}$ and $\Omega_b = 40\,{\rm km\,s^{-1}\,kpc^{-1}}$, finding that a change in the pattern speed results in quantitative changes to the shapes of the structures we found; however, the main results of the paper remain unchanged.

For the orbit integration, we used the inbuilt leap frog integration algorithm (drift-kick-drift with an adaptive time step) of the NMAGIC code (de Lorenzi et al. 2007a), integrating our APOGEE sample for 2 Gyr and saving each orbit's trajectory every 1 Myr. When transforming the APOGEE stars to the bar frame and the model to the heliocentric frame, we took $\phi_\odot = 28°$ and the Sun's position and 3D velocities to be ($R_{\rm GC}$, $Z_\odot$)=(8.178 kpc, 20.8 pc) and ($V_{\phi,\odot}$, $V_{r,\odot}$, $V_{z,\odot}$) = (248.54km s^{-1}, 11.1km s^{-1}, 7.25km s^{-1}), respectively (Schönrich et al. 2010; Bennett & Bovy 2019; Gravity Collaboration et al. 2019; Reid & Brunthaler 2020). We define the bar frame such that X and Y are along the major and minor axes of the bar, respectively, with the Sun at negative X and Y (see red star in the top plot of Fig.3.1). As an additional test, we transformed the APOGEE stars to the bar frame assuming $\phi_\odot = 25°$ and reran the orbit integration. We found that while there were minor differences in the details, there were no major differences in our results.

In the top plot of Fig.3.1, we show the bar frame density distributions of the model particles

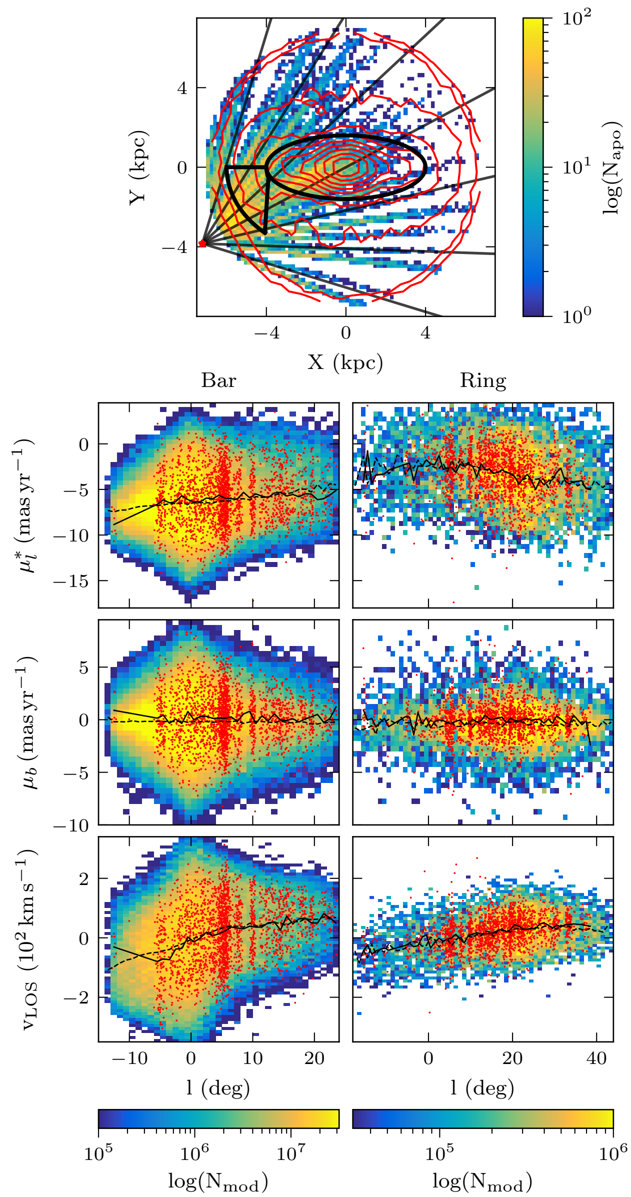

Figure 3.1: Comparisons of the model particles and APOGEE stars. Top: Bar frame density distributions of the model particles (red contours) and APOGEE stars, both restricted to $|b| < 13°$ and $R_{GC} < 7$ kpc. The straight grey lines mark sight lines at longitudes of 0°, ±15°, ±30°, and ±45° and the red star shows the Sun's position. Bottom: Comparison of the heliocentric velocity distributions of model particles (2D histograms) and APOGEE stars (red points) with $|b| < 3°$ in the bar region (left column, black ellipse in the top plot) and in a nearby section of a ring around the bar (right column, black arc in the top plot). Dashed and solid lines give the running means of the model and APOGEE distributions, respectively.

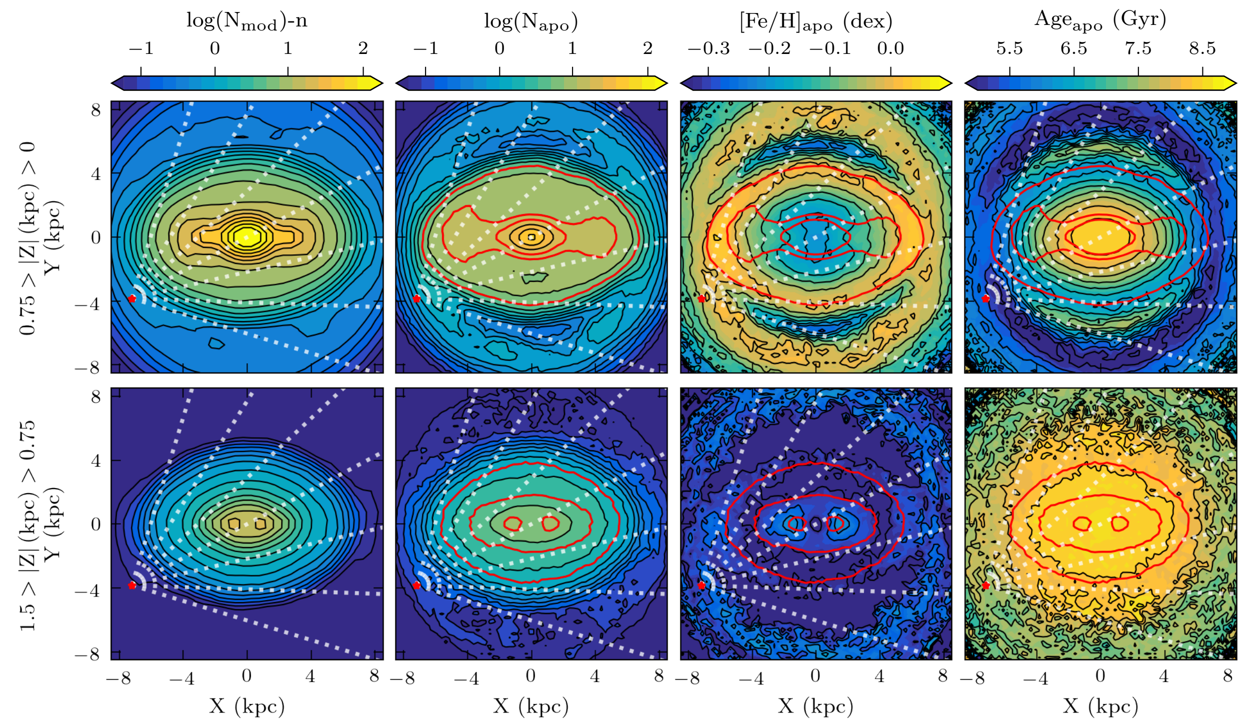

Figure 3.2: Orbital maps of the model and the APOGEE stars at different heights above the plane, using only Y-symmetric orbits with $-1 \leq$ [Fe/H] (dex) < 0.5. Left two columns: Density maps built from the superposition of the model (left) and APOGEE stellar (right) orbits. The model density map has been normalised to a similar scale as the APOGEE density map using the factor n. Right two columns: Mean [Fe/H] (left) and AstroNN age (right) APOGEE orbital maps. The top panels show the orbital maps of the stars closer to the plane. In all plots, the red star marks the position of the Sun, while the white dashed lines mark sight lines at the following longitudes: 0°, ±15°, ±30°, and ±45°. The red contours in the APOGEE maps show the specific density levels that were chosen to highlight important features and to guide the eye. The APOGEE SF has not been corrected for.

and all APOGEE stars used in this work. The APOGEE survey's spatial selection function (SF) is clearly visible. We therefore checked that the heliocentric velocity distributions, that is the longitude and latitude proper motion (μ_l^* and μ_b) and line-of-sight velocity (v_{LOS}) distributions, are consistent for APOGEE stars and model particles selected from similar spatial regions in the bar frame. The bottom plots of Fig.3.1 show this comparison for stars with |b| < 3° in the bar and an adjacent section of a ring around the bar, respectively. Here we define the bar as an ellipse orientated along X in the bar frame, with a major axis length and an axis ratio of 4 kpc and 0.4, respectively. The ring section is defined as the region between two ellipses with major axes of 4 and 6 kpc and with $X < -4$ kpc and $Y < 0$ kpc (see the top plot of Fig.3.1). This region is well populated by APOGEE stars. Fig.3.1 shows that the model particles and APOGEE stars generally overlap in heliocentric phase space when selected from similar bar frame spatial regions, and that their mean velocities at each longitude, when well populated, also generally agree (also see Fig. 19 of P17 comparing APOGEE DR12 with a similar model). The model's standard deviations of the three heliocentric velocities at each longitude agree with those of APOGEE in the bar region, and they are hotter by about 20% in the ring region. We note that the model was not fit to kinematic data in the planar bar region.

3.3 Results

In Fig.3.2 we show the orbital maps built for the model particles and the APOGEE stars. We restricted the orbits in Fig.3.2 to those that are Y-symmetric (i.e. that spend near-equal amounts of time on both sides of the Y-axis.) This cut mainly removed L4 and L5 Lagrange orbits, centred at (X, Y) = (0, ∼ ± 6) kpc, which are strongly affected by the APOGEE spatial SF (discussed later). In the left two columns of Fig.3.2, we reconstructed the density distributions at low and high |Z| (top and bottom rows, respectively), traced by the model particles (first column) and APOGEE stars (second column), by superimposing the orbits of each in the model potential and treating the orbital time steps as individual stars.

Close to the plane, we see a bar that is roughly 4-5.5 kpc long in both density distributions. As is expected, due to the lack of SF corrections to the APOGEE data and to likely residual differences between the model and the MW, the two bars do not completely agree. The APOGEE orbital bar has shallower density gradients along its major and minor axes and ansae that are not seen in the model. Interestingly, the APOGEE orbital bar appears to have a similar structure to that of the metal-rich stars in the Portail et al. (2017c) chemodynamical model (same potential as the P17 model with $\Omega_b = 40\,\mathrm{km\,s^{-1}\,kpc^{-1}}$), while our model's orbital bar looks very similar to their model's full face on projection (shown in their Figs. 1 and 8). At larger heights from the plane, the bars in the model and from the APOGEE orbits both become more elliptical and in better agreement with each other. The X-shape of the bulge is visible in both density maps as two peaks in the density along the bar's major axis. These plots show that the model and the APOGEE orbits generally agree on the structure of the bar-bulge region, differing only in part of the detailed substructure.

The right two columns of Fig.3.2 show the bulge's [Fe/H] and AstroNN age distributions built from the superposition of the APOGEE orbits weighted by their respective densities in each bin. Close to the plane, and in both the [Fe/H] and age maps, clear gradients are seen along

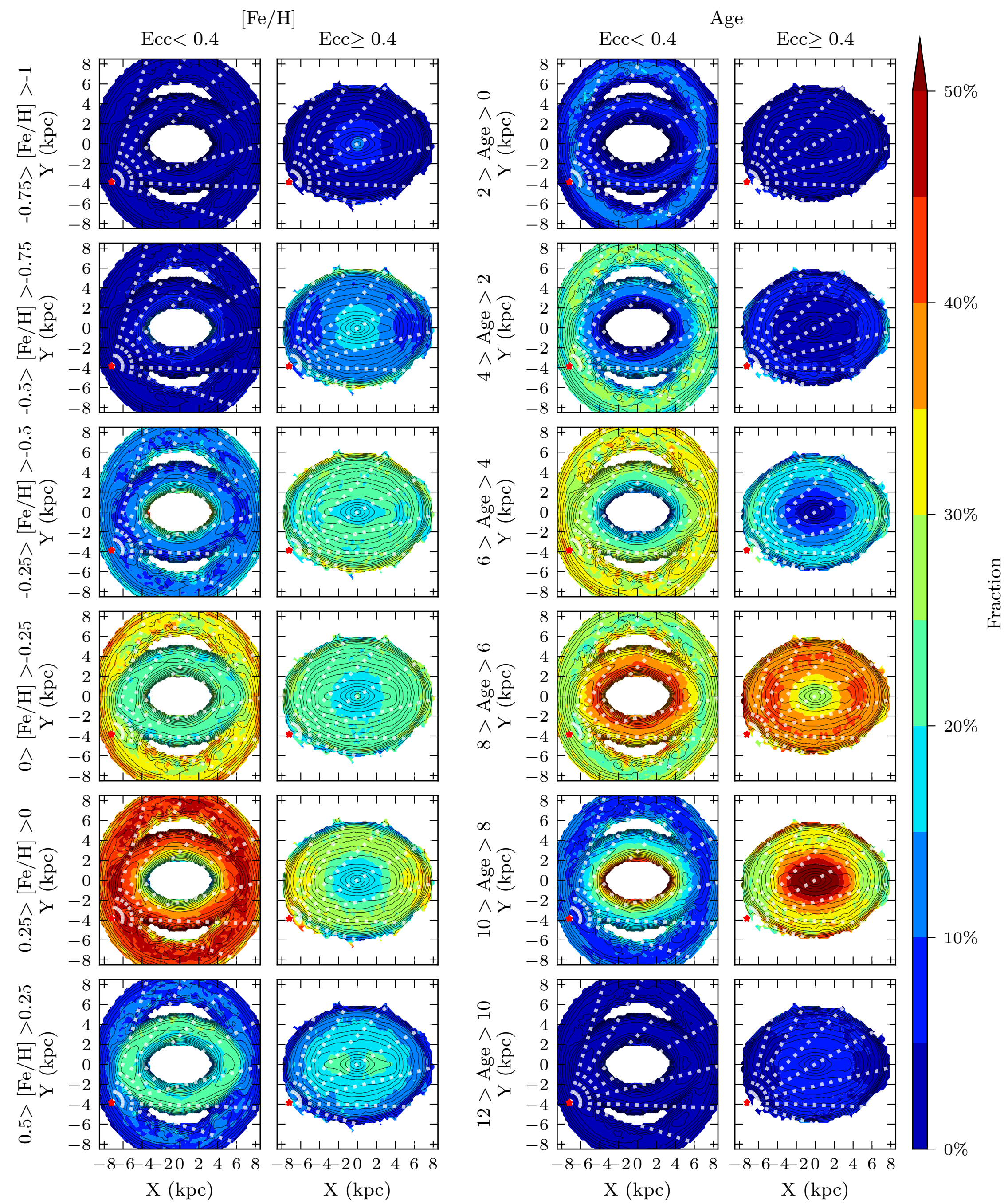

Figure 3.3: Fraction of stars (orbital time steps) along Y-symmetric APOGEE orbits with $|Z| < 0.75$ kpc, in different [Fe/H] and age bins that constitute the disc, ring, and bar. The black curves show the orbital density maps built from all disc and ring stars (Ecc < 0.4) and all bar stars (Ecc ≥ 0.4). The fraction at each position of stars in each [Fe/H] and age bin (rows) composing each structure is shown by the colour. For other plot details see Fig.3.2.

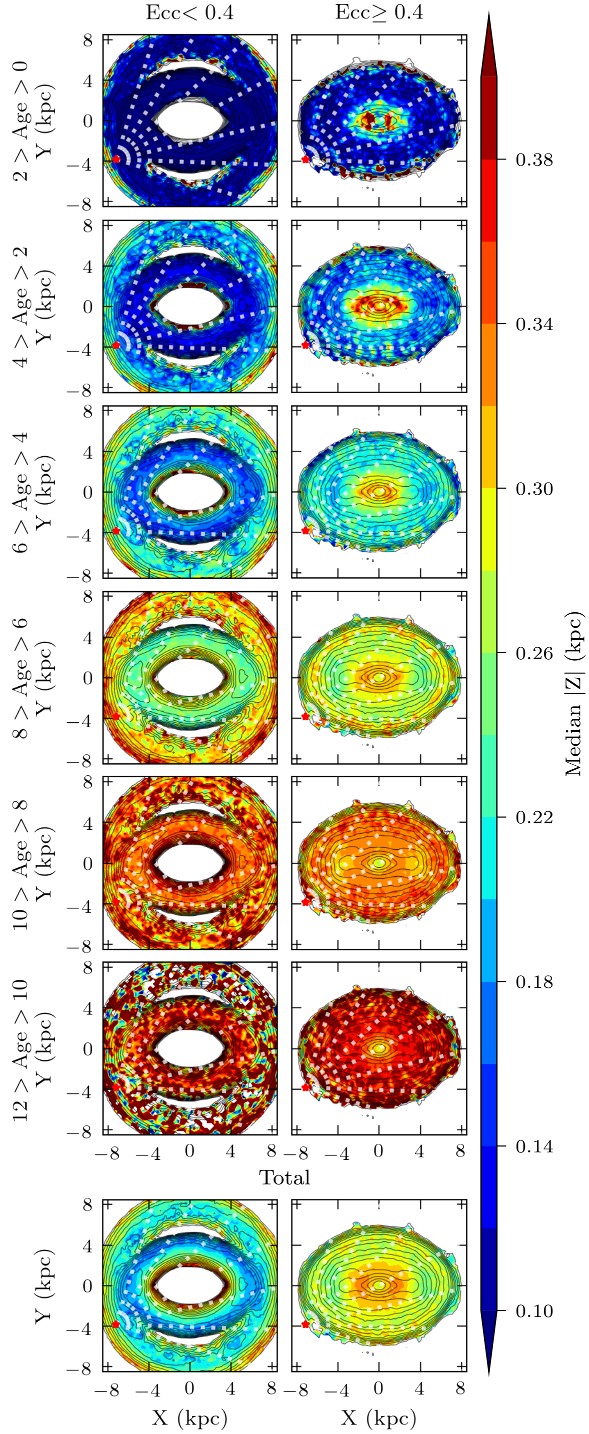

Figure 3.4: Median |Z| of the stars (orbital time steps) along Y-symmetric APOGEE orbits with $|Z| < 0.75$ kpc in the ring and disc (left; Ecc < 0.4) and bar (right; Ecc ≥ 0.4). The top six rows show the median |Z| of the stars in different age bins, while the last row shows the median |Z| of the total. The black curves show the orbital density maps built from all disc and ring stars and all bar stars. For other plot details see Fig.3.2.

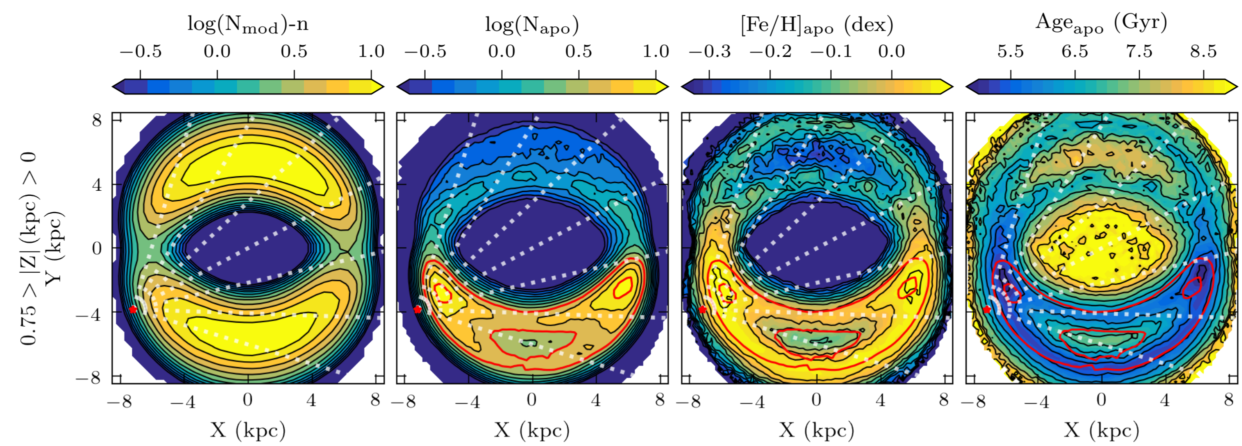

Figure 3.5: Orbital maps of the Y-asymmetric orbits with $|Z| < 0.75$ kpc and $-1 <$ [Fe/H] (dex) $<$ 0.5. Left two plots: Density maps built by superposing of model (left) and APOGEE stellar (right) Y-asymmetric orbits. The model density map has been normalised to a similar scale as the APOGEE density map using the factor n. Right two plots: Mean [Fe/H] (left) and age (right) maps built from the Y-asymmetric APOGEE stellar orbits. The red contours in the APOGEE maps show specific density levels to guide the eye. For other plot details see Fig.3.2.

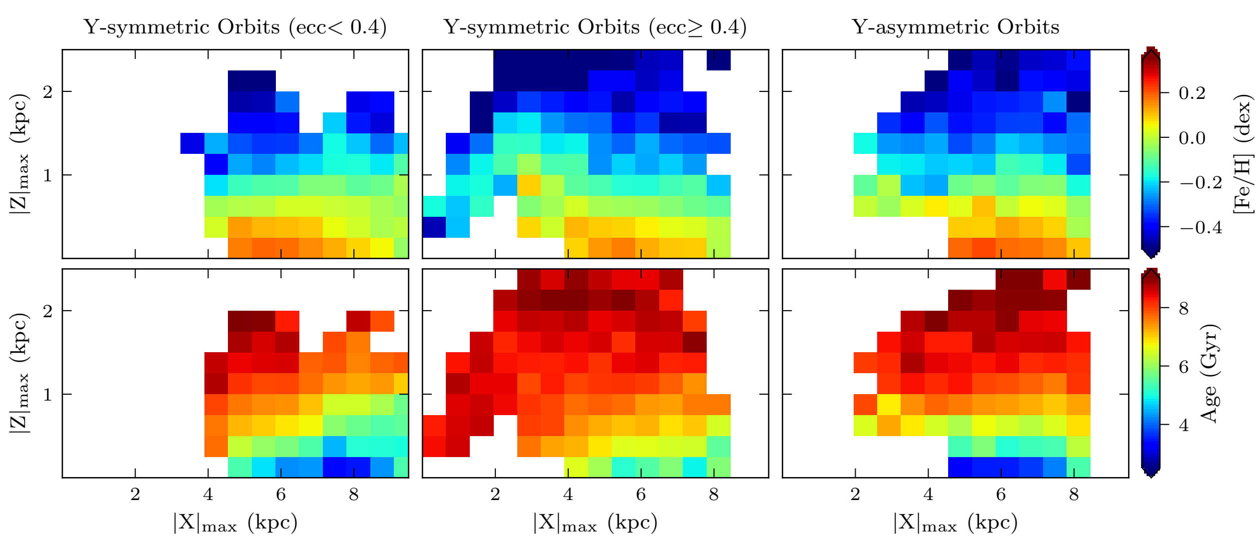

Figure 3.6: $|X|_{max}$-$|Z|_{max}$ distributions for the Y-symmetric low eccentricity (left), Y-symmetric high eccentricity (middle), and Y-asymmetric (right) APOGEE orbits, coloured by mean [Fe/H] (top) and AstroNN age (bottom). The white areas are regions with less than ten stars per bin.

the major axis of the bar. In [Fe/H], there is a positive horizontal gradient ($\sim$0.041 dex kpc^{-1}) at low |Z| along the bar's major axis such that the GC is more [Fe/H] poor than the bar ends, illustrating, in terms of the orbits, the horizontal gradient measured by Wylie et al. (2021, their Fig.19). The age gradient along the major axis is negative such that the stars at the ends of the bar are on average younger than the stars at the GC.

In both parameter maps, we see an elliptical 'inner' ring around the bar at low |Z| (and weakly at higher |Z| in [Fe/H]). This ring is solar in mean [Fe/H] and has a mean age of approximately 6 Gyr. At larger heights the stars become, on average, more [Fe/H] poor and older due to the vertical gradients in the bulge. In the [Fe/H] map, we see two peaks in [Fe/H] along the bar's major axis at ±1.5 kpc. These peaks are due to the X-shape of the boxy/peanut (b/p) bulge (readers are invited to compare also Figs. 16 and 17 in Wylie et al. 2021).

To investigate the structures seen in Fig.3.2 further, we divided the orbits into bins of [Fe/H] and age, and by low and high cylindrical eccentricity, defined as follows:

$$\mathrm{Ecc} = \frac{\max(\mathrm{R_{GC}}) - \min(\mathrm{R_{GC}})}{\max(\mathrm{R_{GC}}) + \min(\mathrm{R_{GC}})}. \tag{3.1}$$

While the exact eccentricity cut is somewhat arbitrary, we have chosen it at Ecc=0.4 such that it approximately extracts the [Fe/H] rich ring that we see in Fig.3.2. The density distributions of the resulting low (< 0.4) and high (≥ 0.4) eccentricity orbits are shown as black contours in Fig.3.3. The ring and the disc are clearly visible in the low eccentricity distribution. The ring is aligned with the bar and has its highest densities along the bar's major axis. It is composed of orbits whose time-averaged density distributions are roughly elliptical with an average major to minor aspect ratio of $\sim$0.7. These orbits are generally confined to small |Z| (see below) and they have many loops that are more densely spaced near the major axis causing the increase in density there. We also find that, in contrast to the ring, the disc is slightly elongated along the Y-axis.

We see the bar at larger eccentricities. The ansae are no longer present as they are largely caused by the high density regions of the ring along the bar's major axis. The majority of the high eccentricity orbits in the planar bar have X_{max} greater than Y_{max} by roughly 1 kpc; however, in the mean, the axis ratio is approximately 2:1. We also find that a fraction of the high eccentricity orbits in the planar bar are ring-like. This indicates that a more sophisticated parameter than eccentricity may be required to fully separate the ring from the planar bar. We plan to investigate the orbit structure of the planar bar more thoroughly in the future.

In Fig.3.3 the orbits composing the low and high eccentricity structures are divided into bins of [Fe/H] and age, and each bin's fractional contribution to each structure is shown. From these fractional maps, we see that the ring and the disc have a relatively narrow range in [Fe/H], mainly solar to slightly super-solar stars, but a wider range in age ($\sim$4-9 Gyr). The ring is slightly more super-solar in [Fe/H] than the disc. In contrast to the ring and disc, the inner bulge and bar are mainly composed of older stars with a wide range in [Fe/H]. Interestingly, both the planar bar and the ring peak in age between 6 and 8 Gyr. The peak in age for the inner bulge is older, between 8 and 10 Gyr.

The young ages of the ring stars indicate that they would be quite concentrated in the Galactic plane. Thus in Fig.3.4 we show median |Z| maps of all stars with $|Z| < 0.75$ kpc and on Y-symmetric orbits, dividing them into low and high eccentricity as before. The first six rows show the median |Z| distributions of the stars divided into different age bins, while the last row shows the total. Median |Z| is a useful measurement as it is indicative of how concentrated the bulk of the stars are in the plane without being overly weighted by outliers. From this plot we see that the distribution of the oldest stars in the ring and disc is ~3 thicker than that of the youngest stars. In the total map, the outer ring is thinner than the disc or its inner region, despite the disc being younger on average (Fig.3.3).

In the high eccentricity orbital maps, the inner bulge is thicker than the planar bar at all ages except for the very inner bulge (<1kpc), which is thinner than its immediate surroundings. The thick structure persisting to low ages is likely related to the X-shape of the b/p bulge. The planar bar gets thinner with decreasing age. Comparing the low and high eccentricity orbits, we see that the planar bar is of similar to only a slightly greater thickness than the ring in the regions where they spatially overlap and each have a significant number of stars.

We now extend the analysis to Y-asymmetric orbits; in Fig.3.5 we show the density, [Fe/H], and age maps of these orbits for the APOGEE stars compared to the density map of the model. In both cases, the majority of the asymmetric orbits are Lagrange orbits trapped in resonance at corotation ($R_{cr} \approx 6$ kpc). Interestingly, there are very large Lagrange orbits with mean ages of ~6 Gyr and solar to super-solar mean [Fe/H] that almost reach the solar radius. While both the model and APOGEE agree that these very large Lagrange orbits are populated, Fig.3.5 shows that the total density distributions of all Y-asymmetric orbits disagree; specifically, the APOGEE map has a minimum at L4, while the model's map has a maximum at L4. This density minimum in the APOGEE map also coincides with a minimum in the [Fe/H] map and a maximum in the age map. The density difference as well as the observed [Fe/H] and age gradients are likely artefacts of the APOGEE spatial SF. The small Lagrange orbits are more distant than the large Lagrange orbits, causing there to be fewer of them in the observed sample. Furthermore, there are gaps in the spatial distribution of the APOGEE fields (see the top plot of Fig.3.1) near the locations of L4 and L5. The few stars that are observed there are biased towards larger heights from the plane due the rise of the APOGEE sight lines with distance. This causes the small Lagrange orbits in the observed APOGEE sample to be biased towards lower [Fe/H] and older ages and result in the observed parameter gradients. We see in the next paragraph that these gradients disappear when the stars are restricted in maximum extent from the plane.

In Fig.3.6 we divided the APOGEE orbits by eccentricity and Y-symmetry and show their $|X|_{max}$-$|Z|_{max}$ distributions coloured by mean [Fe/H] and AstroNN age. For all three orbital types, orbits with $X_{max} > 3$ kpc and confined near the plane are, on average, younger and more [Fe/H] rich than those that can reach larger heights. Larger differences appear between the orbital types in their horizontal profiles. For the distributions of the inner ring and disc orbits (first column), the horizontal in-plane [Fe/H] gradient is slightly negative, such that the ring is more [Fe/H] rich than the disc. The age profile differs with the mean age decreasing with increasing $|X_{max}|$ until $7 - 8.5$ kpc after which it increases again.

Stars on the more eccentric bar and bulge orbits (middle column) have roughly a constant mean [Fe/H] and age out to 7 kpc, from whereon both [Fe/H] and age decrease. The gradients of the eccentric orbits change for $X_{max} < 3$ kpc. There the stars also become more [Fe/H] rich towards the plane until 0.5-0.75 kpc, below which they start to become more [Fe/H] poor again. Thus the inner bulge is more [Fe/H] poor than the bar. We also again see that the inner bulge is older than the bar. These trends indicate that the gradients we see in Figs.3.2 and 3.3 along the bar's major axis are real and not the result of the APOGEE spatial SF.

In the last column which shows the distributions of the Lagrange orbits, the stars are consistent with having a constant mean [Fe/H] and a constant or slightly younger mean age with decreasing extent in X_{max}. This figure confirms that the gradients in Fig.3.5 are the result of the APOGEE spatial SF. The trends seen in this figure do not clearly support the trend measured by Chiba & Schönrich (2021), but more data close to the L4 point would be needed to be sure.

3.4 Discussion and conclusions

In order to understand better the structure of the MW's bar and the horizontal metallicity and age gradients seen in the APOGEE data, we integrated the orbits of 32, 536 APOGEE stars in the gravitational potential of a realistic dynamical model of the inner Galaxy which was fitted to star counts and line-of-sight velocities (P17; see Sect.3.2). We find that stellar orbits in the outer parts of the planar bar trace a radially thick, vertically thin, elongated, stellar ring of low-eccentricity orbits, with a face-on width of ~2-3 kpc and an axis ratio of ~0.7. This ring is seen outwards of a major axis distance of X~4 kpc, while the remaining planar bar reaches X~4.5 kpc. Both components together make up a shallow outer long bar similar to that seen in the dynamical model. While there are quantitative variations with the bar model, this basic structure is robust for similar dynamical models with pattern speeds in the range 35-40 $\mathrm{km\,s^{-1}\,kpc^{-1}}$ favoured by recent studies, as mentioned in Sec. 3.1.

Colouring the orbits by their ASPCAP [Fe/H] and AstroNN ages, we find that the stellar ring is dominated by stars with solar to slightly super-solar metallicities ([Fe/H] = 0.125 ± 0.25 dex), and ages in the range 4−9 Gyr with a peak at 7 Gyr and a long tail towards younger ages. Ring stars with young ages are highly concentrated towards the plane. The eccentric planar bar is more metal-poor with a wider range of metallicities and is more concentrated in age around 6−9 Gyr with a peak at 8 Gyr. The bar ends are, on average, younger and more [Fe/H] rich than the b/p bulge, illustrating the horizontal gradients seen previously. The bulge's X-shape is clearly visible in [Fe/H] and density.

Sevenster (1999) previously suggested that the 3 kpc arm of the MW could actually be an inner ring and, more recently, from their study of the gas dynamics of the inner MW, Li et al. (2022) suggest that the 3 kpc arm along with the Norma arm and the bar-spiral interfaces compose an inner gas ring. Furthermore, Kormendy & Bender (2019) find that two MW analogues, NGC 4565 and NGC 5746, host inner rings.

In Sbc galaxies, such as the MW, a close connection between inner rings and spiral arms is common. Buta et al. (2015) find that of the 45% of the S4G Sbc galaxies that host inner rings, most tend to be ring spirals as opposed to pure rings or ring lenses, which are more common in early types. The model from which we generated the potential does not include spiral arms, making it impossible for us to see a connection between the inner stellar ring and the spiral arms that might exist in the MW. To understand better whether this structure in the MW is a ring or ring-spiral, the model must be augmented to include a realistic spiral arm potential.

The in-plane thickness of the inner ring is somewhat surprising as inner rings are generally thinner. Passive rings, which are rings that are no longer forming stars, can be thicker; however, they are only seen in earlier type galaxies (≥ Sab, Comerón 2013). It is possible that the MW also hosts a thin star-forming ring, but due to observing in the infrared, we can only see its older part which has spread out over time (as may be the case for NGC 7702, Buta 1991). Alternatively, the ring could actually be a lens such that the MW hosts both a lens and a bar. Lenses are characterised by a sharp edge encircling a shallow brightness gradient. However, further work is required to better understand the sharpness of the transition from the ring to the surrounding disc, and as discussed earlier, a lens would be unusual for a galaxy as late-type as the MW (Buta et al. 2015).

The question of whether the stellar inner ring is a separate structure from the long bar is not easily answered and may depend on how both structures are defined. The figures above show that the metallicity distribution function of the ring is shifted to higher metallicities than that of the bar, with a strong peak at super-solar metallicities, and the age distribution function to ~1 Gyr lower mean age, with a long tail towards younger ages. This leads to clear outward metallicity and age gradients in the bar region. In the orbit distribution, the ring has its highest density on lower eccentricity orbits close to corotation. Increasing the threshold in eccentricity to 0.5 results in a slightly thicker ring and shorter bar. However, some high-eccentricity orbits in the bar are still ring-like in appearance; there are high-metallicity and intermediate-age orbits in the bar as well as old stars on resonant ring orbits; and both components together make up a shallow outer long bar in the rotating potential. That is, in many variables, the distributions overlap, suggesting that the ring and bar are not easily separable, discrete components. The highly flattened, young components in both the ring and the bar were probably formed from gas and added to the old metal-poor central bulge and bar recently. The late addition of stars causes the overall potential and orbit structure of the system to evolve, further complicating matters. In all, this warrants a more careful study of the bar-ring connection.

The spatial transition between the ring and planar bar occurs at around ~ 4 kpc. Comparing this scale with the transition reported in Wegg et al. (2015) between their 'thin' and 'superthin' bars suggests that the superthin bar, which dominates outside X = 4.5kpc, might be identifiable with the young and thin part of the stellar ring in the APOGEE orbits. This also requires further study.

In the orbit maps, we also find very large Lagrange orbits that almost reach the solar radius and have a solar to super-solar mean metallicity and intermediate age (~6 Gyr). The small Lagrange orbits are not well sampled by APOGEE due to its spatial SF, but some can be found by dividing orbits in terms of their |X| and |Z| maxima. These suggest that stars closer to the core of the resonance have similar [Fe/H] and ages as the outer Lagrange orbits. This does not clearly support the trend measured by Chiba & Schönrich (2021), but further investigation with more data close to the L4 point is needed.

In the two barred galaxy models with a metal-rich inner ring in the Auriga cosmological simulations, the ring continues to form stars from gas driven inside corotation after the formation of the bar while the star formation in the bar drops more rapidly (Fragkoudi et al. 2020). They argue that the time when the star formation in the bar starts quenching may be used to estimate a lower limit to the age of the bar. In the AstroNN age distributions for the APOGEE stars, the peak for the fraction of stars in the inner ring occurs at age $\simeq$ 7 Gyr; whereas for the stars in the remaining planar bar outside the bulge, it occurs at $\simeq 8$ Gyr. After age $\simeq 7$ Gyr, the fraction of newly formed bar stars drops more rapidly than for the ring stars; therefore, we used this to estimate that the Galactic bar formed at least 7 Gyr ago.

In conclusion, by studying the orbits of APOGEE stars in the gravitational potential of a dynamical bar model for the MW with a slow Ω_b as measured recently, we find that (i) the MW hosts a radially thick, vertically thin elongated inner ring; (ii) the ring is dominated by stars with solar to super-solar metallicities and with ages between 4 and 9 Gyr; and (iii) the ring explains the steep horizontal metallicity gradient along the Galactic bar's major axis. From the distribution of ages in the ring and planar bar, we estimate a lower limit of 7 Gyr to the time since the formation of the bar.

Chapter 4

The inner Milky Way dissected into high and low [Mg/Fe]

Abstract

Using a large sample of A2A and APOGEE stars, we dissect the inner Milky Way into its principle components using strategic cuts in [Fe/H] and [Mg/Fe] and a careful analysis of the orbital kinematics. We integrate a sample of inner Milky Ways stars from the A2A and APOGEE surveys in a realistic bar-bulge potential with a slow pattern speed. We then correct for each survey's selection function and investigate the dependence of the stellar kinematics, orbital properties, and spatial distributions on [Fe/H] and [Mg/Fe]. We find evidence that the [Mg/Fe]-rich [Fe/H]-poor stars of the inner Milky Way are spheroidally distributed and argue that some of these stars are part of the in-situ halo component, the so called Splash. We also show that it is the [Mg/Fe]-poor stars that mainly support the Milky Way's boxy-peanut bulge. While the inner Milky Way hosts all major Galactic components, the individual components can be extracted though careful selection. The Splash, previously only seen near the Sun, is present in the inner Milky Way at even higher stellar densities.

4.1 Introduction

In the last years, state-of-the-art large-scale photometric, spectroscopic, and astrometric surveys such as the *Gaia*-ESO (Gilmore et al. 2012), APOGEE (Majewski 2016), VVV (Minniti et al. 2010; Surot et al. 2019), and *Gaia* (Cropper et al. 2018) surveys have significantly improved our understanding of the inner Milky Way (MW). The picture that has emerged shows a complex bulge with a two-fold nature: a metal rich component and a metal poor component with differing kinematic (Babusiaux et al. 2010; Zasowski et al. 2016; Rojas-Arriagada et al. 2020), [α/Fe] (Rojas-Arriagada et al. 2017; Rojas-Arriagada et al. 2019b; Wylie et al. 2021), and age distributions (Bensby et al. 2017; Hasselquist et al. 2020). Debate over the origin of the metal rich component has diminished with most agreeing that it is the result of secular evolution of the early thin disk which formed a bar and subsequently a b/p bulge though the redistribution of angular momentum. Conversely, the nature of the metal-poor bulge is still hotly debated. Some argue that it is the result of early, intense star formation (Hill et al. 2011; Rojas-Arriagada et al. 2014; Queiroz et al. 2021) while others argue that it is the inner thick disk (Debattista et al. 2017; Fragkoudi et al. 2018).

Using Gaia DR2 data, Haywood et al. (2018b) found that the low and high [α/Fe] stars of the kinematically identified halo near the Sun preferentially populate blue and red main sequences respectively on the color-magnitude diagram. They conclude that the recently discovered debris from the "Gaia-Enceladus-Sausage" (GES, Belokurov et al. 2018), a satellite galaxy that was accreted $\sim$ 10 Gyr ago (Helmi et al. 2018), is the main contributor to the blue sequence. These stars have high total orbital energy and no rotation/exhibit counter rotation (Koppelman et al. 2018). On the other hand, Haywood et al. (2018b) suggest that the red sequence is composed of stars formed in-situ i.e. the low rotation tail of the merger heated thick disk. Gallart et al. (2019) analysed the two halo populations finding that the redder population was of similar age to the bluer population but was more metal rich. Through comparisons with simulations, they suggest that the blue population is likely debris from GES and the red population is an in-situ population of MW proto-disc stars who were heated during the GES merger. Belokurov et al. (2020) analysed the chemistry, ages, kinematics of nearby bright stars and found evidence in the V_ϕ − [Fe/H] plane of three different components with [Fe/H] > -0.7: the thin disc, the thick disc, and a third component which smoothly transitions from the thick disk and has many retrograde stars. They designate this third component as the "Splash". From comparisons with simulations, they find that the Splash is likely the merger heated proto-disc of the MW i.e. the in-situ halo. From Aurgia simulations of MW like galaxies, Grand et al. (2020) find that the Splash components in these galaxies are more spherically distributed than the accreated halo or disks and have their highest densities near the Galactic centre.

In this work, we dissect the inner MW using cuts in [Fe/H], [Mg/Fe], and orbital kinematics. We find evidence of the Splash halo component in the inner MW along with evidence that the b/p bulge is mainly composed of [Mg/Fe]-poor stars. In Section 4.2 we discuss the observational data we use, specifically the A2A and APOGEE surveys, as well as how we correct each survey for their survey selection function (SSF). In this section we also discuss the methods we used to integrate the stars and obtain their orbits. In Section 4.3 we show our results and in Section 4.4 we end with a discussion of the results and our conclusions.

4.2 Data and methods

In this section we introduce the data we use, how we obtain it, and the corrections we make to it. Furthermore, we also discuss the methods and assumptions we use to integrate the stars in our sample and obtain their orbits.

4.2.1 Data

In this paper we used inner MW stars from the 17th data release (DR) of The Apache Point Observatory Galactic Evolution Experiments (APOGEE; Majewski 2016) and A2A DR2 surveys

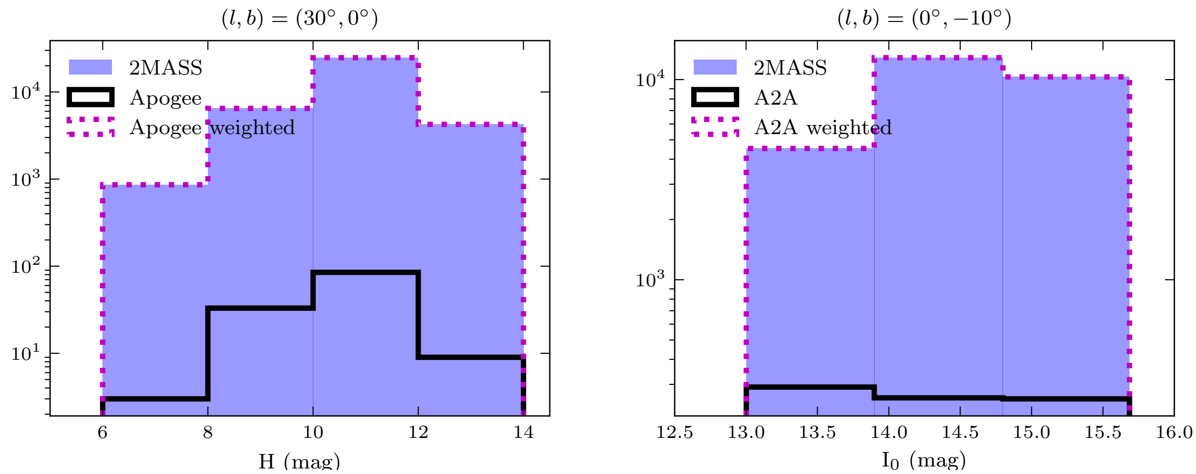

Figure 4.1: The weighted (magenta-dashed) and unweighted (black) APOGEE (left) and A2A (right) luminosity functions compared to the luminosity functions of their 2MASS parent samples (blue) in two example fields.

(Wylie et al. 2021). In the following two sections we describe the data and choices we made.

APOGEE

For the APOGEE DR17 stars, we obtained their metallicities ([Fe/H]), α-enhancements ([Mg/Fe]), effective temperatures (T_{eff}), surface gravities (log(g)), and line-of-sight velocities from the ASPCAP pipeline (García Pérez et al. 2016; Holtzman et al. 2018; Jönsson et al. 2020), their distances and ages from the AstroNN catalogue (Leung & Bovy 2019b), and their RA and Dec proper motions from the Gaia DR2 catalogue (Gaia Collaboration et al. 2018). As quality cuts, we also restricted the APOGEE samples to only stars with valid ASPCAP [Fe/H], [Mg/Fe], T_{eff}, and log(g) values and required the stars to have S/N > 60, no Star Bad flag set, $T_{eff} > 3200$ K, distance errors < 20%, and ages between 0 and 12 Gyrs. When we use the AstroNN ages we follow the recommendations of Bovy et al. (2019) and restrict the sample further requiring AstroNN log(g) errors <0.2 dex and AstroNN [Fe/H] > −0.5 dex. As we are interested in the inner MW, we applied a spatial cut of |b| < 15° and cylindrical distance from the Galactic centre of < 8 kpc. We correct the APOGEE stars for the survey selection function (SSF) though re-weighting the stars, as described below. Before our analysis, we required the stars to be part of the APOGEE main sample by setting the flag EXTRATARG to zero and also removed stars with SSF correction weights greater than 200 as large weights can cause noise. These cuts leave 63,689 stars in our APOGEE sample.

Stars in the APOGEE main sample were selected from a high quality subset of the Two Micron All Sky Survey (2MASS; (Skrutskie et al. 2006)). Depending on the field location and number of visits, the specific color and magnitude bins that a star was selected from varied. In our sample, the APOGEE stars were mainly selected from the following magnitude bins: $7 < H_0\,(\mathrm{mag}) < 11$, $7 < H_0\,(\mathrm{mag}) < 12.2$, or $7 < H_0\,(\mathrm{mag}) < 12.8$. In bulge and APOGEE-1 disk fields the selection colour limit was $(J - K_s)_0 \geq 0.5$ mag while in the APOGEE-2 disk fields the selection color limits

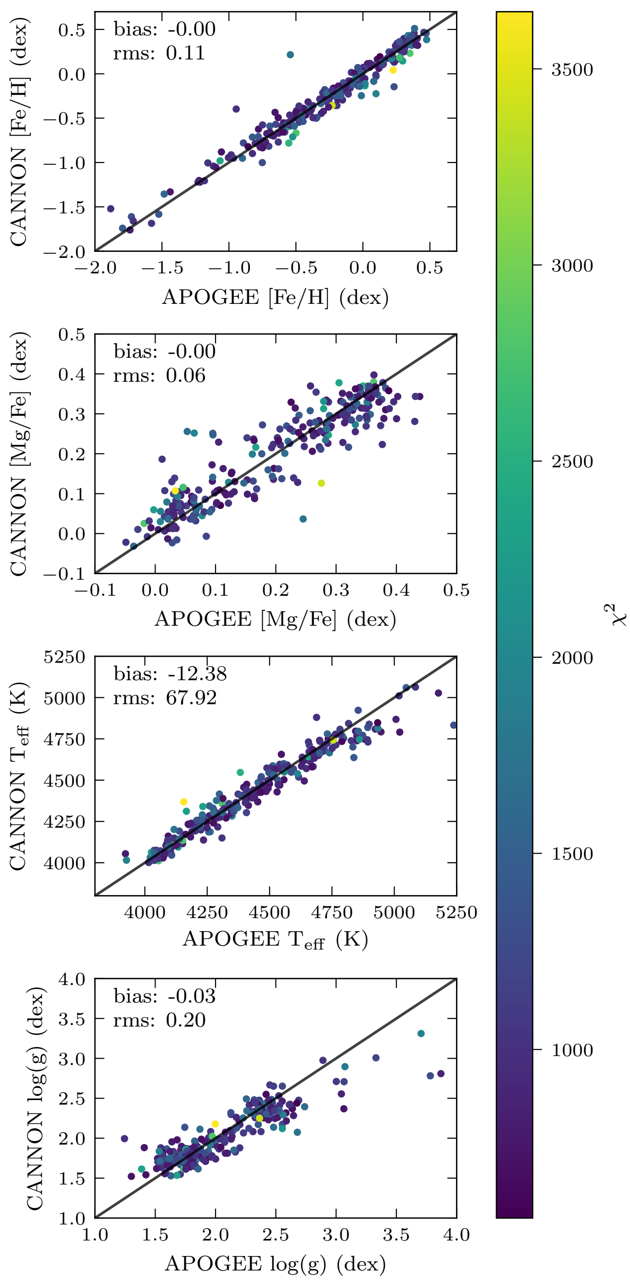

Figure 4.2: Pick-one-out test. Each point in each plot represents a different star in the training set. The X-value of each point is the respective star's APOGEE parameter value while the Y-value is the values given my a Cannon model trained on every other training set star. The color of the points represents the model χ^2 values. Each distribution's bias and rms are given in the upper left corners of each plot.

were $0.5 \leq (J - K_s)_0\,(\mathrm{mag}) \leq 0.8$ and $(J - K_s)_0 > 0.8$ mag. To correct for the APOGEE SSF we first obtained the color and magnitude limits of each set of stars observed together. The magnitude limits were the exact magnitude limits of the set (i.e. min and max H of a set). These values varied slightly from those reported by the APOGEE team as some stars were removed due to the quality cuts we applied, described previously. Then, we applied these limits to the 2MASS high quality parent samples. Following this, we binned the high quality 2MASS and APOGEE stars in bins of 2 mag and calculated the ratio of the number of high quality 2MASS stars to APOGEE stars within each magnitude bin. Finally, for each APOGEE star we assigned it a SSF correction weight equal to the ratio within the magnitude bin it belonged to. As the APOGEE main sample stars in each cohort were selected randomly, once the weights were applied to the APOGEE stars, the H-band luminosity function of the APOGEE stars matched the H-band luminosity function of the high quality 2MASS stars. See the left plot of Fig.4.1 which shows the unweighted APOGEE luminosity function, the weighted APOGEE luminosity function, and the high quality 2MASS luminosity function in a field at $(l, b) = (30°, 0°)$.

In this work we only correct the APOGEE survey to the high quality subset of the 2MASS survey from which they were selected. However, this subset is its self incomplete and we would ideally like to correct the APOGEE survey to a more complete survey such as VVV. However, our sky coverage is much larger than that of VVV which in the bulge only covers $-10° \leq l \leq 10°$ and $-10° \leq b \leq 5°$ and in the disk only covers $295° \leq l \leq 350°$ and $-2° \leq b \leq 2°$. Furthermore, the APOGEE stars are bright ($7 \gtrsim H_0\,(\mathrm{mag}) \gtrsim 12.8$) and therefore 2MASS should be roughly complete in this magnitude range, except perhaps at the very lowest latitudes. In future work we plan to correct the APOGEE stars to the full 2MASS and VVV catalogs however this is currently beyond the scope of this work.

A2A

The Abundance and Radial Velocity Galactic Origin Survey (ARGOS; Freeman et al. (2012); Ness et al. (2013a,b)) is a medium resolution spectroscopic survey that used the AAOmega fibre spectrometer on the Anglo-Australian Telescope to observe roughly 28,000 stars in 28 fields towards the Galactic bulge within the wavelength regime 840-885 nm. The survey was designed to mainly observe red clump stars which have highly accurate distances due to their narrow magnitude range. Following the methods outlined in Wylie et al. (2021) we re-calibrated the ARGOS catalog to the APOGEE DR17 parameter scales using the data driven method, *The Cannon* (Ness et al. 2015), making the two surveys combinable. The training set of A2A DR2 catalog consisted of 244 stars spread over the following parameter ranges: $-1.7 \leq [\mathrm{Fe/H}]\,(\mathrm{dex}) \leq 0.2$, $-0.06 < [\mathrm{Mg/Fe}]\,(\mathrm{dex}) < 0.66$, $4195 \leq T_{\mathrm{eff}}\,(\mathrm{K}) \leq 5432$, $1.4 \leq \log(g)\,(\mathrm{dex}) \leq 3.5$. Fig. 4.2 shows the results of the pick-one-out test which compares the APOGEE parameters of each training set star to the parameters generated by a Cannon model trained on all other training set stars. The close agreement indicates that *The Cannon* can successfully learn the APOGEE DR17 parameters for the A2A stars. We removed stars from the final A2A catalog that did not fall within the training set limits. The temperature cut due to the training set limits can be approximated as a color cut. Because of this, we apply a color cut of $0.45 \leq (J - K_s)_0\,(\mathrm{mag}) \leq 0.86$. to the A2A catalog. The final A2A catalog contains 21,842 stars.

We correct the A2A catalog for the ARGOS selection function as well as for our selection from the ARGOS catalog due to the training set cuts through weighting the stars. The ARGOS stars were selected from a high quality subsample of the 2MASS catalog that required the stars to have high photometric quality flags (see Freeman et al. 2012), magnitudes within $11.5 \leq K_s(\mathrm{mag}) \leq 14.0$ and colors of $(J - K_s)_0 \leq 0.38$ mag. I_0-band magnitudes for each 2MASS star that met these requirements were calculated using the equation:

$$I_0 = K_s + 2.095(J - K_s) + 0.421E(B - V). \tag{4.1}$$

Following this, the ARGOS team randomly selected roughly 300 stars from each field in each of the following I_0-bins: 13-14 mag, 14-15 mag, and 15-16 mag. The magnitude selection scheme allowed ARGOS to observe stars in the front, middle, and back of the Galactic bulge. To correct for this selection and the selection due to the training set cuts, we follow a similar procedure as what was done in Wylie et al. (2021). First, for each field we obtain the high quality 2MASS parent samples by applying the quality, color, and magnitude cuts described above to the full 2MASS sample in each field. Then, we apply the color cuts due to the temperature limits of the training set. For each remaining high quality 2MASS and A2A star in each field we then calculate their approximate I_0-band magnitude using the equation above. Following this, we bin the high quality 2MASS and A2A stars in the three I_0-bins and calculate the number ratio of high quality 2MASS stars to A2A stars in each bin. To correct for the ARGOS selection, we calculate which I_0-bin each A2A star belongs to and then weight the stars by this ratio. After the weights are applied to the A2A stars, the A2A luminosity functions in each field match the high quality 2MASS luminosity functions. In the right plot of Fig.4.1 we show the unweighted A2A luminosity function, the weighted A2A luminosity function, and the high quality 2MASS luminosity function in a field at $(l, b) = (0°, -10°)$.

As is the case with the APOGEE selection function, we only correct the A2A catalog to the high quality 2MASS parent samples. Ideally, we should apply an additional correction to correct to a more complete catalog like VVV. However, Portail et al. (2017a) showed that it is mainly the bright stars in the low latitude fields at $b = \pm 5°$ that are affected. We suspect that this correction will give slightly more weight to the metal rich stars in the survey as it will weight higher the low latitude fields which tend to contain more metal rich stars. This correction will be applied in future work but is currently beyond the scope of this thesis.

Following Wylie et al. (2021), we statistically select the red clump stars, separating them from the red giants, using the following procedure: First, we obtain each star's spectroscopic magnitude, M_k, by fitting their log(g), T_{eff}, [Fe/H] values to theoretical isochrones. Taking the intrinsic magnitude of the red clump to be $M_{rc} = -1.61 \pm 0.22$ mag (Alves 2000) and a total red clump magnitude error of $\sigma_{M_{K_s}} = 0.47$ (see section 2.4.4 of Wylie et al. 2021), we use the following equation to obtain a weight that gives the probability of them being part of the red clump:

$$\omega_{rc}(M_{K_s}) = \frac{1}{\sigma_{M_{K_s}}\sqrt{2\pi}} \exp\left(-\frac{1}{2}\frac{(M_{K_s} - M_{rc})^2}{\sigma^2_{M_{K_s}}}\right). \tag{4.2}$$

Essentially, by applying this weight to the A2A stars we extract the red clump by highly weighting likely red clump stars and de-weighting unlikely red clump stars.

To obtain the distances of each A2A star, we first assume each star is part of the red clump and assign each a absolute magnitude of −1.61 mag. Then, we de-redden their apparent magnitudes using the Schlegel et al. (1998) extinction maps re-calibrated by Schlafly & Finkbeiner (2011). Following this, we obtain a distance for each star by comparing the assigned red clump absolute magnitude to their de-reddened apparent magnitude. This is the distance a star would have if it were truly a red clump star. To account for not every star being a red clump star, we then weigh the stars by the weight in Equ. 4.2. This weighing scheme statistically removes stars that are not red clump.

4.2.2 Methods

We integrated each APOGEE and A2A star for 2 Gyr (saving every 1 Myr) in the rotating potential of one of the Portail et al. (2017a) dynamical bar-bulge models using the inbuilt drift-kick-drift leap frog integration algorithm written by Jonathan Clarke of the NMAGIC code (de Lorenzi et al. 2007a). The masses of the stellar and dark matter particles in these models were adapted using the made-to-measure method to fit bulge density and kinematic data from the VVV, UKIDSS, 2MASS, BRAVA, OGLE, and ARGOS surveys. During these fits, they assumed a bar angle and Sun's distance from the GC of $\phi_\odot = 28°$ and $R_0 = 8.2$ kpc respectively. For this work, we used the model with a mass to red clump star number of 1000 $M_\odot$, a central disc mass $M_c = 2 \times 10^9$ $M_\odot$, and a pattern speed of $\Omega_b = 37.5\,\mathrm{km\,s^{-1}\,kpc^{-1}}$ as this model fit well both the bulge proper motions (Clarke et al. 2019b) and inner Galaxy gas distribution (Li et al. 2022). Before the orbit integration, the APOGEE and A2A stars were transformed from the heliocentric frame to the bar frame, where X and Y are along the bar's major and minor axes, assuming a bar angle of $\phi_\odot = 28°$ and the Suns position and velocity of (R_{GC}, $Z_\odot$)=(8.178 kpc, 20.8 pc) and ($V_{\phi,\odot}$, $V_{r,\odot}$, $V_{z,\odot}$) = (248.54km s^{-1}, 11.1km s^{-1}, 7.25km s^{-1}), respectively (Schönrich et al. 2010; Bennett & Bovy 2019; Gravity Collaboration et al. 2019; Reid & Brunthaler 2020). In the bar frame, the Sun is at negative X and Y. We checked in Wylie et al. (2021) that the model and APOGEE data are consistent; see Fig. 1 in Wylie et al. (2021).

4.3 Results

4.3.1 The inner Milky Way's [Mg/Fe]-[Fe/H] distribution

The [Mg/Fe]-[Fe/H] distribution of the inner MW is known to be bi-modal with a [Mg/Fe]-poor maximum and a [Mg/Fe] rich maximum (Rojas-Arriagada et al. 2019a; Queiroz et al. 2020; Wylie et al. 2021). We confirm this in the left-most plot of Fig. 4.3 which shows the [Mg/Fe]-[Fe/H] distribution of our full inner MW sample (A2A + APOGEE). In the remaining three plots of Fig. 4.3 we color the distribution by mean eccentricity (Ecc), maximum height in Z (Z_{max}), and age finding that these parameters are dependent upon [Mg/Fe] and [Fe/H]. The [Mg/Fe]-rich stars have high mean Ecc and Z_{max} of roughly $\gtrsim$ 0.7 and $\gtrsim$ 1.25 kpc respectively. As the [Fe/H] increases and [Mg/Fe] decreases, the Ecc and Z_{max} of the [Mg/Fe]-rich stars gradually decrease. We have no age estimates for A2A stars and no accurate ages for APOGEE stars with

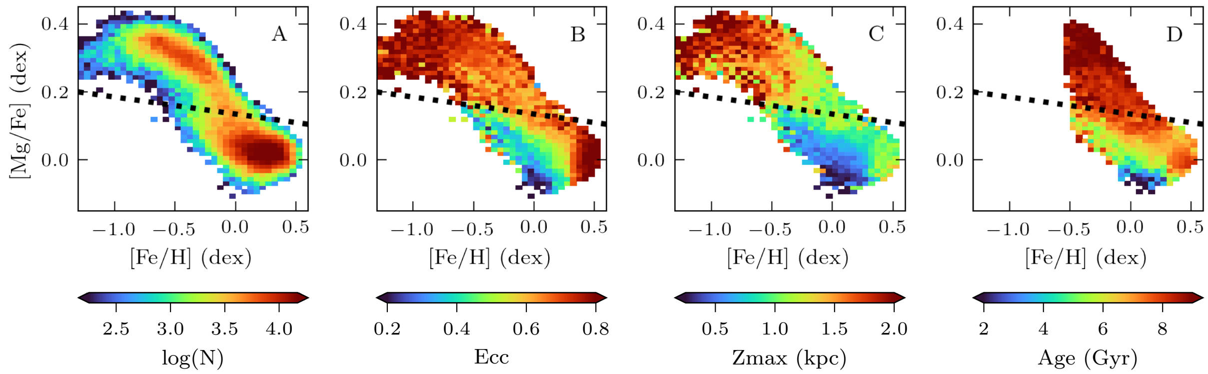

Figure 4.3: The [Mg/Fe]-[Fe/H] distribution of APOGEE and A2A stars in the inner MW with [Fe/H] > -1.3 dex. The [Mg/Fe]-[Fe/H] distribution colored by A: Logarithm of the number density, B: Eccentricity, C: Maximum height in Z, and D: Age. In all plots, the stars have been re-weighted to correct for their respective SSFs. The black dashed line indicates the cut we applied to separate the high and low [Mg/Fe] stars.

$\mathrm{[Fe/H]_{AstroNN}} \lesssim -0.5$ dex, however the remaining [Mg/Fe]-rich stars are old with mean ages of $\gtrsim 8$ Gyr. The mean Ecc, Z_{max}, and age of [Mg/Fe]-poor stars are highly dependant on [Fe/H]. The more [Fe/H]-poor the stars are the lower their mean Ecc, Z_{max}, and ages are. For example, stars with [Fe/H] $\lesssim 0.2$ have Ecc$\lesssim 0.4$, $Z_{max} \lesssim 1$ kpc, and mean ages $\lesssim 6$ Gyr with the stars at [Fe/H] $\approx 0 - 0.2$ dex and [Mg/Fe] $\lesssim 0$ dex having the youngest mean ages of around 2 Gyr. The stars with [Fe/H] $\gtrsim 0.2$ have Ecc $\gtrsim 0.8$, mean $Z_{max} \sim 1 - 1.25$ kpc, and mean ages ~ 8 Gyr. Normally, more metal poor stars tend to be older than more metal rich stars. However, the younger stars that are more metal poor than the older stars in the [Mg/Fe]-poor maxima could be the result of a more recent infall of pristine gas which would decrease the mean metallicity of the gas from which the new stars are born. This scenario is modelled and discussed in Lian et al. (2020a) for the Galactic disk.

4.3.2 Density and [Fe/H] structure of the high and low [Mg/Fe] inner Milky Way

As shown in Fig. 4.3, the orbital parameters change with [Fe/H] and [Mg/Fe]. We therefore divide our sample into high and low [Mg/Fe] (see black dashed line in Fig. 4.3) and examine the orbital density and [Fe/H] structure of each in the X-Z plane in Fig. 4.4. The b/p bulge is clearly visible in the density and metallicity maps of the total. Furthermore, the X-shape in the metallicity map of the total is highly "pinched" much more so than that of the [Mg/Fe]-poor or [Mg/Fe]-rich stars. For the [Mg/Fe]-poor stars, the [Fe/H]-rich stars are very concentrated in the plane for $|X| \gtrsim 4$ kpc but strongly vertically thicken for $|X| \lesssim 4$ kpc. This coherent structure in the [Mg/Fe]-poor stars is the MW's edge-on b/p bulge now clearly visible with the removal of the [Mg/Fe]-rich stars. The orbital density structure of the [Mg/Fe]-rich stars is much thicker than that of the [Mg/Fe]-poor stars. Furthermore, the density distribution of the [Mg/Fe]-rich stars becomes rounder and more [Fe/H]-poor towards the central kpc. The [Fe/H] structure of

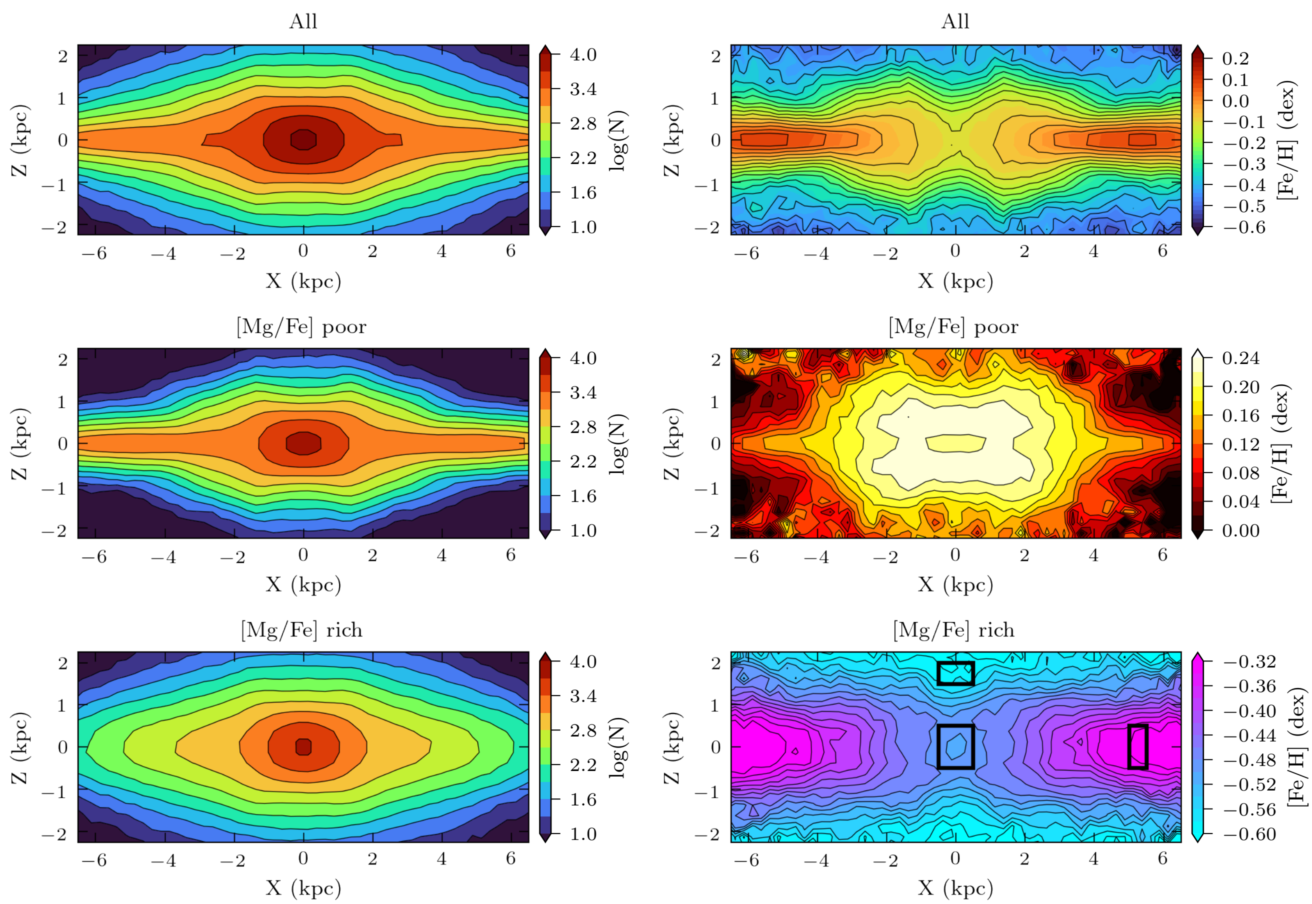

Figure 4.4: X-Z density (left) and metallicity (right) maps of stars with |Y| < 1 kpc and [Fe/H] > −1.3 dex. Top row: Maps of all stars. Middle: Maps of [Mg/Fe]-poor stars . Bottom: Maps of [Mg/Fe]-rich stars. The black boxes indicate the regions in which we calculate the MDFs and velocity distributions shown in Figs. 4.5 and 4.7. In all plots, the stars have been re-weighted to correct for their respective SSFs.

the [Mg/Fe]-rich stars is vertically thick and has a negative vertical [Fe/H] gradient for $|Z| > 0.5$ kpc. The horizontal in-plane [Fe/H] gradient is positive with no regions of inversion such that as the radius decreases the metallicity varies from ~ -0.3 dex for $|X| \gtrsim 4$kpc to ~ -0.5 dex in the central kpc. Lastly, the [Fe/H] contours towards the Galactic centre appear rounded in the [Mg/Fe]-rich stars.

4.3.3 Dependence of the [Mg/Fe]-rich inner Milky Way's MDF on position

The rounded density and [Fe/H] contours of the [Mg/Fe]-rich stars towards the inner kpc as well as the positive horizontal metallicity gradient suggest that a [Mg/Fe]-rich spheroid may be present in the inner MW in addition to the [Mg/Fe]-rich thick disk. The positive horizontal [Fe/H] gradient as well as the rounded [Fe/H] and density contours could be explained by the [Fe/H]-richer thick disk component dominating at large radii and the [Fe/H]-poorer spheroid dominating in the centre. To investigate this further, we examine the metallicity distribution functions (MDFs) of the [Mg/Fe]-rich stars (orbital time steps) in three different regions: central in-plane (CIP; $|Z| < 0.5$ kpc, $|X| < 0.5$ kpc, $|Y| < 1$ kpc), outer in-plane (OIP; $|Z| < 0.5$ kpc, $5 < |X| < 5.5$ kpc, $|Y| < 1$ kpc), and central out-of-plane (COP; $1.5 < |Z| < 2.$ kpc, $|X| < 0.5$ kpc, $|Y| < 1$ kpc). The regions we select from are encircled by black boxes in Fig. 4.4. The upper left plot of Fig. 4.5 shows the MDFs of CIP and OIP regions as well as the MDF of the solar neighborhood thick disk (black stars, $0.5 < |Z| < 3$ kpc, $6 < r < 9$ kpc, and $V_\phi > 150$ km/s) normalized to the scale of the OIP MDF (magenta histogram). The MDF of the thick disk solar neighborhood stars is similar to the OIP MDF with the exception that the OIP MDF has more metal rich stars which may arise due to contamination from the thin disk to the OIP MDF. The MDF built from CIP stars (blue histogram) is much is wider and reaches much lower [Fe/H] values than the OIP MDF. This wide distribution again suggests that there may be more than one [Mg/Fe]-rich population significantly contributing to the inner kpc.

We see from Fig. 4.5 that the metal rich stars are dominant near the bar ends and inner disk/ring. We explore the assumptions there are two [Mg/Fe]-rich populations present in the Galactic centre, an [Fe/H]-poor and an [Fe/H]-rich population, and that the [Fe/H]-rich population in the central kpc is the thick disk and its MDF is identical to the OIP MDF at the bar ends. To extract the MDF of the [Fe/H]-poor population in the central kpc, we normalised OIP MDF to the scale of the metal rich end of the CIP MDF and subtract them from each other. The MDF of the remaining distribution (RIP) is plotted in the upper right-hand plot of Fig. 4.5 (green histogram). In the same plot, we also plot the COP MDF as well the MDF of stars with Ecc> 0.7 and $Z_{max} > 2$, the region of the parameter space claimed by Queiroz et al. (2021) to be mainly occupied by a pressure supported component. The three distributions are strikingly similar with the RIP MDF having only slightly less [Fe/H]-rich stars than the other two. This excess of [Fe/H]-rich stars could be due to contributions by the disk or the result of gradients which we do not account for during the subtraction. Furthermore, we also plot the MDF from Fig. 2 of Gallart et al. (2019) of the red population of kinematically selected halo stars believed to be the in-situ halo (red points) and the MDF of slowly rotating/counter rotating ($V_\phi < 30$ km/s) out of plane [Mg/Fe]-rich solar neighborhood stars ($6 < r < 9$ kpc and $0.5 < |Z| < 3$ kpc, black pluses) which according to Belokurov et al. (2020) are likely to be mainly in-situ halo stars and some

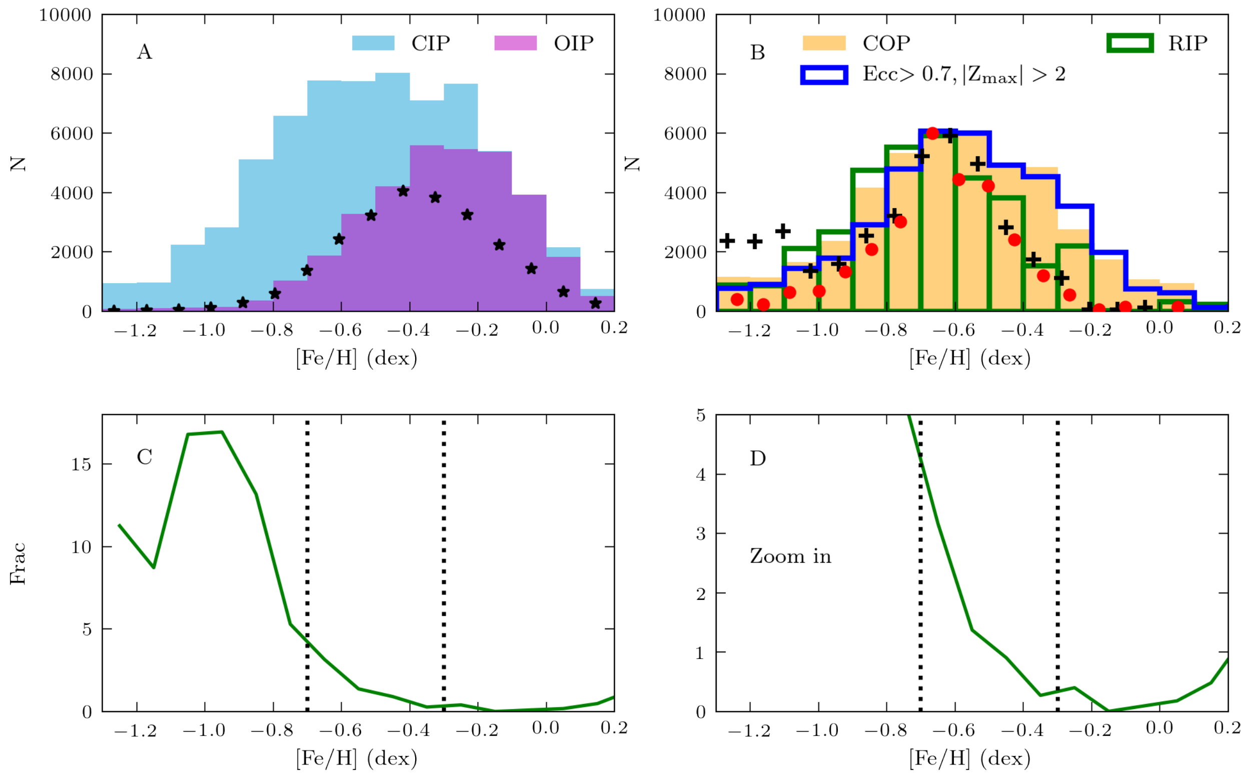

Figure 4.5: MDFs of [Mg/Fe]-rich stars. A: MDFs of CIP stars (|Z| < 0.5 kpc, |X| < 0.5 kpc, and |Y| < 1 kpc; cyan histogram), OIP stars (|Z| < 0.5 kpc, 5 < |X| < 5.5 kpc, and |Y| < 1 kpc; magenta histogram), and solar neighborhood out-of-plane thick disk stars (6 < r < 9 kpc, 0.5 < |Z| < 3 kpc, V_ϕ > 150 km/s; black stars). The OIP histogram has been normalised to the scale of the metal rich end of the CIP histogram while the thick disk histogram has been normalised to the scale of the OIP histogram. B: MDFs of COP stars (1.5 < |Z| < 2. kpc, |X| < 0.5 kpc, and |Y| < 1 kpc; orange histogram), stars with Ecc > 0.7 and Z_{max} > 2 (blue histogram), and RIP stars (green histogram). Note that in both A and B the stars are selected from the black boxes in right bottom plot of Fig. 4.4. The solar neighborhood out-of-plane in-situ halo stars (6 < r < 9 kpc, 0.5 < |Z| < 3 kpc, V_ϕ < 30 km/s; black crosses) and MDF of the red halo sequence in the solar neighborhood from Gallart et al. (2019) (red dots) are also plotted. The MDFs of the COP stars, high Z_{max}/high eccentricity stars, solar neighborhood out-of-plane in-situ halo stars, and solar neighborhood red halo sequence have all been normalized to the scale of the RIP MDF.C: Ratio of the RIP MDF to the OIP MDF (green histogram in B to the magenta histogram in A). D: A zoom-in of C. The dashed lines in C and D indicated the regions in [Fe/H] where the low and high [Fe/H] populations dominate.

ex-situ halo stars (more [Fe/H]-poor). Both of these MDFs have been normalized to the scale of the RIP MDF. Amazingly, while there are some differences at the low [Fe/H] end, the RIP MDF is roughly similar to the Gallart et al. (2019) red halo MDF and the MDF of the likely in-situ halo stars of the solar neighborhood seen in our data with all three peaking at [Fe/H] ~ -0.65 dex.

The similarity of the RIP MDF with not only the high Z MDF and the high Z_{max} high Ecc MDF but also the MDFs of the solar neighborhood in-situ halo stars indicates that the RIP population could be the inner in-situ halo also known as the Splash (Belokurov et al. 2020). Furthermore, the similarity of between the OIP MDF and the solar neighborhood thick disk MDF suggests that the OIP population could be the inner thick disk.

4.3.4 Density structure of the high [Mg/Fe] inner Milky Way as a function of [Fe/H]

The lack of distinct peaks in the CIP MDF in Fig. 4.5 suggests if there are two [Mg/Fe]-rich components present in the central kpc such as the in-situ halo and thick disk, then they overlap at least somewhat in [Fe/H], making a clear separation in [Fe/H] difficult. Therefore, to approximately separate them, we examine regions in [Fe/H] where each dominates and ignore the regions where both contribute significantly. To find these regions, we take the ratio of the RIP MDF to the OIP MDF (in Fig. 4.5 the green histogram in B to the magenta histogram in A). This ratio is shown in the bottom two plots Fig. 4.5 where the right-hand plot is a zoom in of the left-hand plot. We find that at [Fe/H] $\lesssim -0.7$ dex the RIP population dominates by at least 4 times while at [Fe/H] $\gtrsim -0.3$ dex the OIP population dominates by at least 1.5 times.

In Fig. 4.6 we examine the orbital density and Ecc-$|Z_{max}|$ distributions of [Mg/Fe]-rich stars in the metallicity ranges where the RIP population dominates ([Fe/H] < -0.7 dex), both populations contribute significantly ($-0.7 <$ [Fe/H](dex) < -0.3), and the inner thick disk population dominates (-0.3dex $<$ [Fe/H]). We find that as the metallicity decreases, fewer orbits support the bar and the density distributions become progressively more centrally concentrated. Specifically, the density distribution of stars with [Fe/H] > -0.3 is flatter, bar-like with a roundish centre and clearly supports the b/p bulge while the density distribution of stars with [Fe/H] < -0.7 dex is more spheroidal with little to no bar and is more vertically extended. The density distribution of stars with $-0.7 <$ [Fe/H](dex) < -0.3 is a hybrid of the other two in that it forms a very rounded bar and is more vertically extended than the more metal rich stars but less than the more metal poor stars. As the metallicity decreases, the Ecc-Z_{max} distribution also changes with there being progressively fewer low eccentricity and low Z_{max} stars. For stars with [Fe/H] > -0.7 dex most are high eccentricity but there is a significant fraction with low eccentricities. However, for stars with [Fe/H] < -0.7 dex almost all have high eccentricity with very few having low eccentricity.

4.3.5 Orbital kinematics of the inner Milky Way

In Fig. 4.7 we examine the kinematics in the V_{ϕ}-V_R plane of the [Mg/Fe]-rich stars in the three [Fe/H] ranges ([Fe/H] < -0.7 dex, $-0.7 <$ [Fe/H](dex) < -0.3, and [Fe/H] > -0.3 dex)

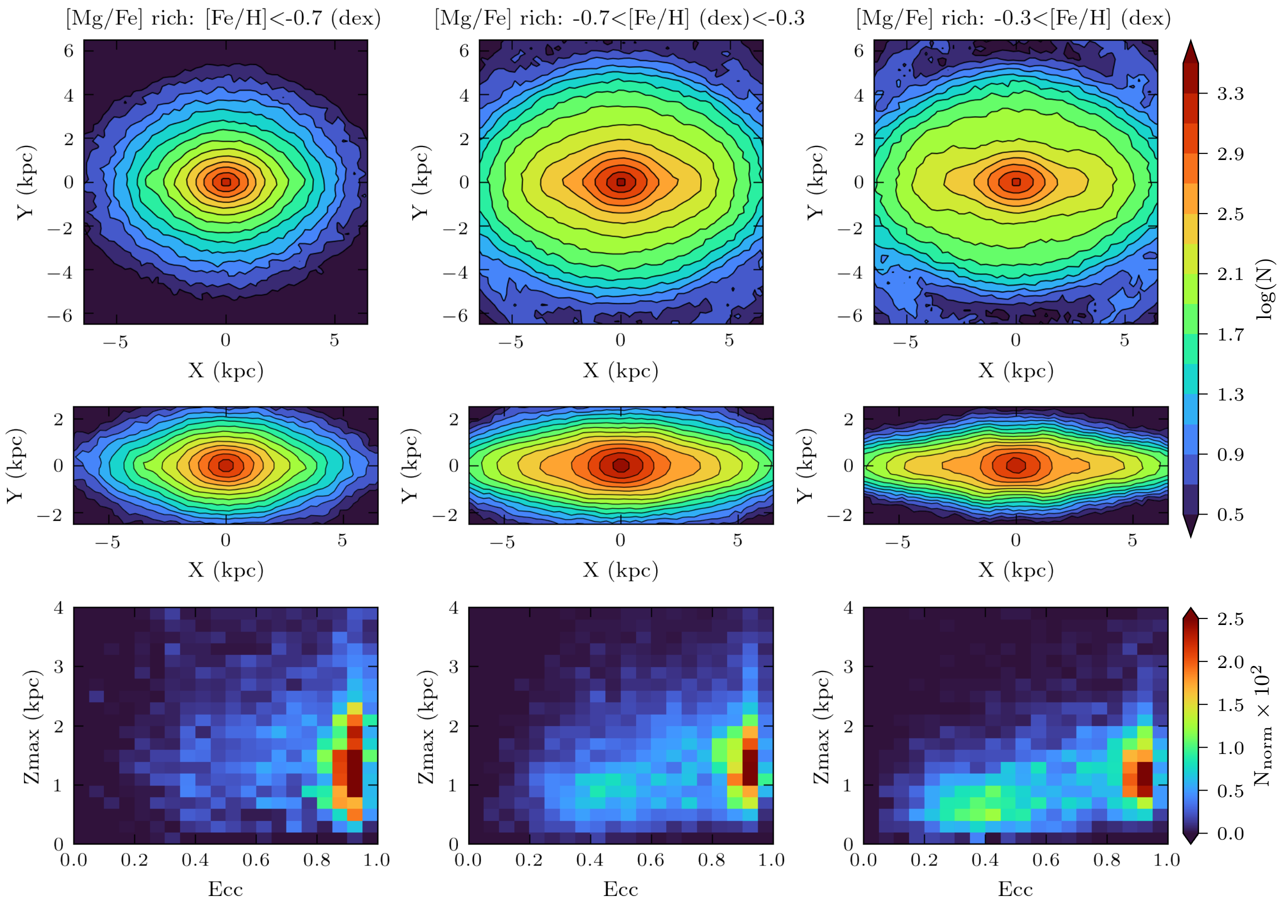

Figure 4.6: Spatial and orbital distributions of [Mg/Fe]-rich stars with [Fe/H] < −0.7 dex (left column), −0.7 < [Fe/H](dex) < −0.3 (middle column), −0.3dex < [Fe/H] dex (right column). First row: X-Y density maps with |Z| < 0.75 kpc. Second row: X-Z density maps with |Y| < 1 kpc. Third row: Ecc-Zmax maps. In all plots, the stars have been re-weighted to correct for their respective SSFs.

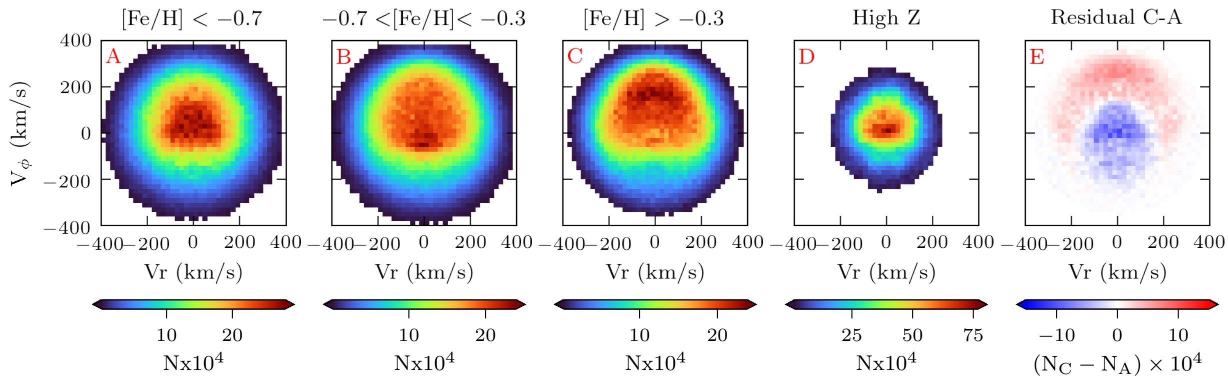

Figure 4.7: Polar kinematics of A-C: [Mg/Fe]-rich CIP MW stars (see inner black box in Fig. 4.4) separated into different [Fe/H] bins and D: [Mg/Fe]-rich COP stars (see upper black box in Fig. 4.4). E: Residual between plots C and A. In all plots, the stars have been re-weighted to correct for their respective SSFs and the distributions have been normalised.

finding that the amount of rotation progressively increases with increasing [Fe/H]. The rightmost plot of Fig. 4.7 shows the residual between the distributions with [Fe/H] > -0.3 dex and with [Fe/H] < -0.7 dex. From the residual it is readily apparent that the more metal poor stars are more radial, dynamically colder, rotate significantly slower, and have more counter rotating stars than the more metal rich stars. The most [Fe/H]-poor stars (A) have a similar velocity distribution to the high Z stars (D, second rightmost plot in Fig. 4.7) as they are also radial with little rotation. In fact, the distribution of the high Z stars appears to be a shrunken version of that of the [Fe/H]-poor stars. However, there are more prograde [Fe/H]-poor stars than prograde high Z stars.

Belokurov et al. (2020) examines the dependence of the abundances, kinematics, and ages of bright nearby Gaia DR2 stars on their positions in the [Fe/H]-V_ϕ plane, finding evidence of in-situ and ex-situ halo components in addition to the thin and thick disks. Specifically, they find that the in-situ halo component, the Splash, has little to no angular momentum, a significant amount of counter rotating stars, and metallicities between -0.7 dex and -0.2 dex. From Fig. 4.7, we see that many of the stars in a similar [Fe/H] range are radial but significant fraction show some rotation. The central MW metal poor [Mg/Fe]-rich population in our sample, the RIP population, could be related to this in-situ halo component. To investigate this, we replicate the key plots of Belokurov et al. (2020) using the orbits of our sample. For a better comparison, we redefine our sample to include more solar neighborhood stars by replacing the cut in Galactic latitude with a cut in |Z|, and integrating all APOGEE and A2A stars within 8 kpc from the Galactic centre and 3kpc from the Galactic plane. Additionally, as the plane will be dominated by thin disk stars, we only examine orbital time steps with $0.5 < |Z|(\mathrm{kpc}) < 3$.

To first check that the abundance scale of our sample are consistent with theirs, we restrict our sample to stars between 6 and 9 kpc from the Galactic centre and in Fig. 4.8 replicate the plots in Fig. 1 of Belokurov et al. (2020). In the top row we color the distribution by number density, row normalized number density, and column normalized number density:

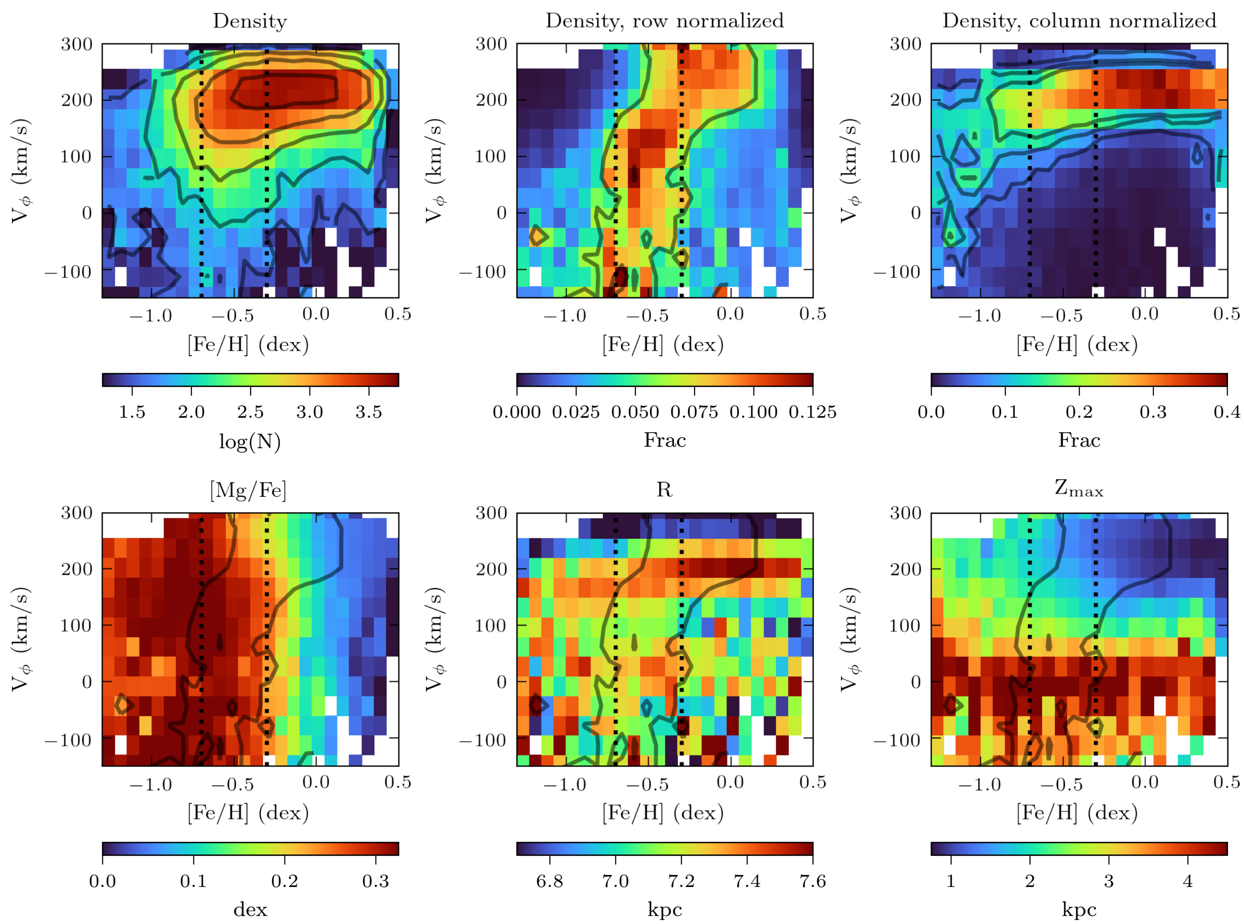

Figure 4.8: The [Fe/H]-V$_\phi$ distribution of stars (orbital time steps) with 6 < R < 9 kpc and between 0.5 < |Z| < 3 kpc from the plane. Top row: The left plot shows the logarithm of the stellar density. The middle plot shows the row normalized density. The right plot shows the column normalized density. Bottom row: The left plot shows the [Fe/H]-V$_\phi$ distribution colored by [Mg/Fe]. The middle plot shows the [Fe/H]-V$_\phi$ distribution colored by mean radius. The right plot shows the [Fe/H]-V$_\phi$ distribution colored by maximum height in Z. In all bottom row plots the row normalized density contours have been added to guide the eye. The black dashed lines in each plot mark -0.7 and -0.3 dex in [Fe/H]. In all plots, the stars have been re-weighted to correct for their respective SSFs.

1. The number density plot shows that stars with [Fe/H] > −0.3 dex exhibit mainly prograde rotation with velocities around ∼ 225 km/s. Less than 5% of stars with [Fe/H] > −0.3 dex have velocities less than 150 km/s while only 0.5% are counter rotating. For stars with [Fe/H] < −0.3 dex, most stars still exhibit prograde rotation with velocities also around ∼ 225 km/s, however there is a significant tail towards lower V_ϕ with 22% of stars rotating slower than 150 km/s and 3.5% counter rotating.

2. The row normalized density in the second plot in Fig. 4.8 gives the typical metallicity for a given V_ϕ bin. A ">" shape is clearly visible at large velocities. This shape corresponds to the thin and thick disks with the thin disk being the upper part of ">" and the thick disk being the lower part of ">" such that thin and thick disk stars decrease and increase respectively in V_ϕ with increasing [Fe/H]. Thin disk stars decrease in V_ϕ with increasing [Fe/H] because the higher V_ϕ stars come from larger radii and therefore have lower [Fe/H]. Most stars with $-150 \lesssim V_\phi(\mathrm{km/s}) \lesssim 100$ km/s have metallicities between -0.3 dex and -0.8 dex. This is roughly the region within which the Splash dominates according to Belokurov et al. (2020) (-0.7 dex to -0.2 dex).

3. The third plot in the top row of Fig. 4.8 shows the column normalized number density which gives the typical velocity of a given metallicity bin. Most stars with [Fe/H] > −0.3 dex have velocities between ∼ 200 km/s and ∼ 270 km/s. As the metallicity decreases below −0.3 dex a tail towards lower V_ϕ develops. Below -1 dex a significant fraction of stars are counter rotating.

In the second row of Fig. 4.8 we color the [Fe/H]-V_ϕ plane by mean [Mg/Fe], mean R, and mean Z_{max}:

1. The [Mg/Fe] plot shows that [Mg/Fe] anti-correlates with [Fe/H] as expected. For stars with $V_\phi \lesssim 200$ km/s, at [Fe/H] ≈ −0.2 dex there is a steep change in [Mg/Fe] from ∼ 0.1 dex to ∼ 0.3 dex.

2. The middle plot of the second row shows how R varies in the [Fe/H]-V_ϕ plane. Stars with [Fe/H] > −0.3 dex and velocities around ∼ 225 km/s have mean R ≳ 7.5 kpc. The mean R values in the region with [Fe/H] < −0.3 dex and $V_\phi \lesssim 150$ km/s strongly vary but generally have ≲ 7.4 kpc.

3. The third plot in second row shows how maximum height from the plane varies in the [Fe/H]-V_ϕ plane. The dependence is mainly on V_ϕ with the faster rotating stars being more strongly confined to the plane. At large V_ϕ, there is also a slight dependence with the more metal rich stars having lower Z_{max}.

When comparing to Fig. 1 of Belokurov et al. (2020), we find similar over densities in the row normalized density distribution corresponding to the thin disk, thick disk, and Splash. Furthermore, the over density which they identify as the Splash is slightly shifted to lower [Fe/H] in our results by about 0.1 dex. The Splash stars in our work have mean [Mg/Fe] ≈ 0.3 dex, R ≲ 7.4, and $Z_{\mathrm{max}} \gtrsim 3.5$ kpc. These values are roughly similar to the ones they find of mean

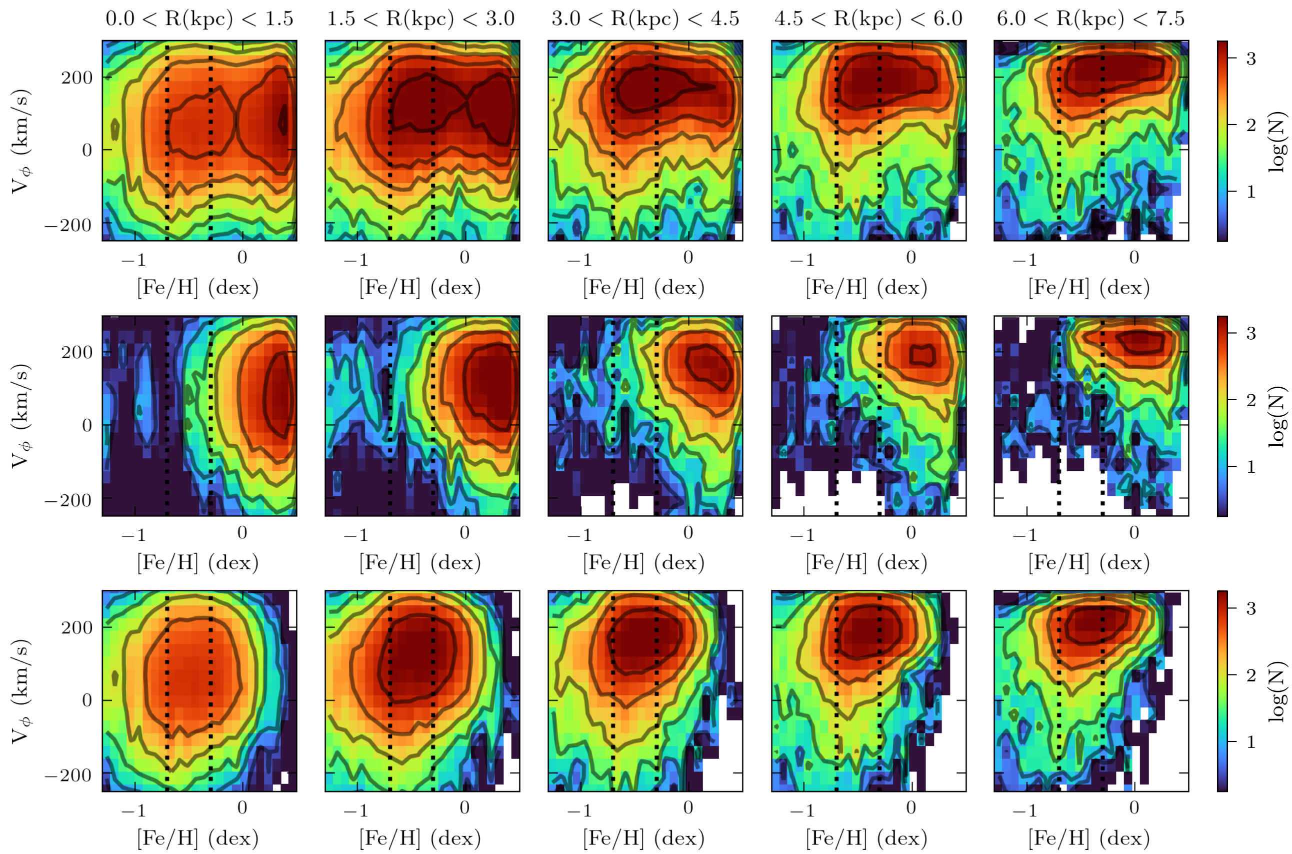

Figure 4.9: Rotational velocity as a function of [Fe/H] in different radial bins of stars with R < 8 and 0.5 < Z(kpc) < 3. Top row: All stars. Middle row: [Mg/Fe]-poor stars. Bottom row: [Mg/Fe]-rich stars (see Fig. 4.3[Mg/Fe] division). The black dashed lines mark [Fe/H] = −0.3 dex and [Fe/H] = −0.7 dex.

[α/Fe] ~ 0.23 dex, R $\lesssim$ 7.4, and 3 < Z_{max}(kpc) < 4.7. The small differences may be due to scale differences in [Fe/H] and [Mg/Fe] as well as selection function differences.

If there is a spheroidal population in the MW then it should be strongest near the Galactic centre and diminish in strength with increasing radius. In the top row of Fig 4.9 we plot V_ϕ versus [Fe/H] for different bins in radius. In the bin with stars with 6 < R(kpc) < 7.5 we see a similar distribution to the top left plot of Fig. 4.8 where most stars rotate prograde with a velocity of ~ 225 km/s and only some of the metal poor stars counter rotate. As radius decreases, the metal poor counter rotating tail increases in strength. Additionally, a less though still significant number of metal rich counter rotating stars appear with decreasing [Fe/H]. These stars form the bulge's peanut seen in Fig. 4.4. They counter rotate due to their orbits not conserving angular momentum in the bar potential. In the middle and bottom rows we divide the stars into low and high [Mg/Fe] respectively (black dashed line in Fig. 4.3). From the middle row we see that as the radius decreases the [Mg/Fe]-poor stars develop a tail towards lower V_ϕ that is stronger at high [Fe/H]. This is likely due to the more metal rich stars being initially kinematically cooler

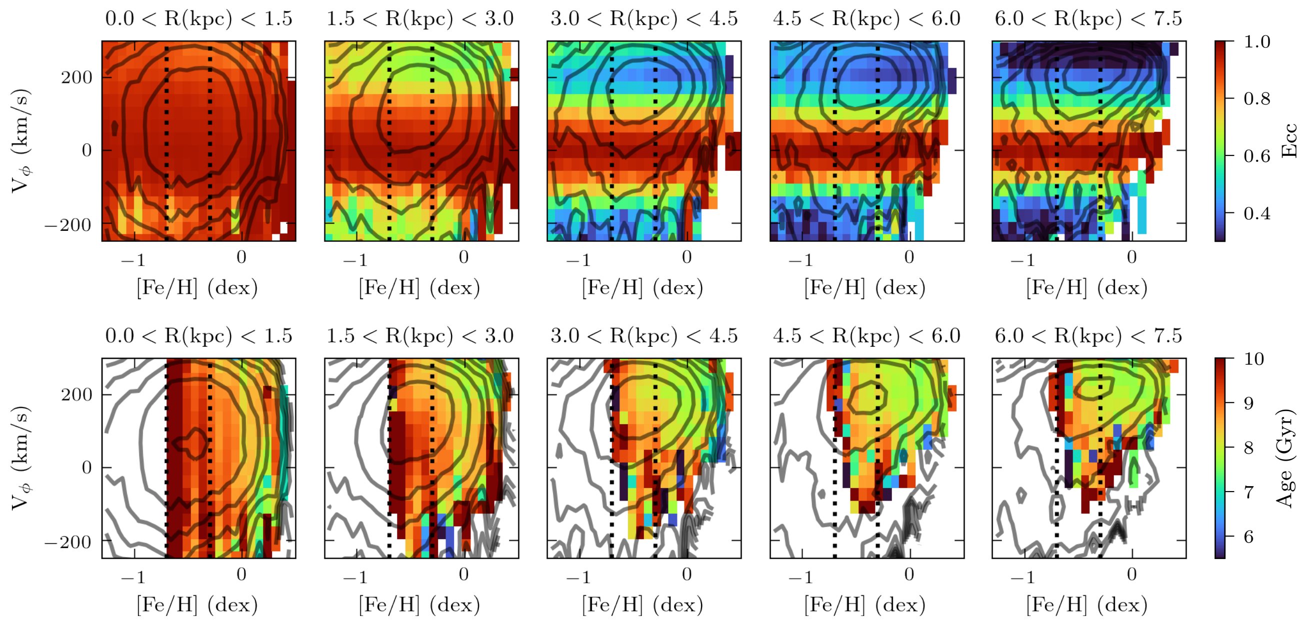

Figure 4.10: Rotational velocity as a function of [Fe/H] in different radial bins of [Mg/Fe]-rich stars with 0.5 < Z(kpc) < 3 colored by mean eccentricity (top row) and mean age (bottom row). The black dashed lines mark [Fe/H] = −0.3 dex and [Fe/H] = −0.7 dex.

than the more metal poor stars and therefore being preferentially mapped to the b/p bulge (Ness et al. 2013a; Debattista et al. 2017). From the bottom row we see that as the radius decreases the [Fe/H]-poor counter rotating tail of the distribution of [Mg/Fe]-rich stars increases in strength. However below 1.5-3 kpc, within the bar, there is a wide spread in V_ϕ such that there is little correlation between V_ϕ and [Fe/H]. This is again likely due to angular momentum not being conserved in the inner kpc due to the bar potential.

The top row of Fig. 4.10 shows the V_ϕ-[Fe/H] plane colored by the mean eccentricity of the [Mg/Fe]-rich stars in different radial bins. From this plot we see that near the solar neighborhood, the parameter region dominated by the Splash has a much higher mean eccentricity, Ecc $\approx$ 1, than the thin and thick disk regions,Ecc $\lesssim$ 0.6. As the radius decreases and the number of low rotation stars increases, the eccentricity of these stars remains high. The disk stars increase in eccentricity with decreasing radius. Below 1.5 kpc, eccentricity becomes a poor indicator as the minimum radii of all stars in this bin are small. In the bottom row of Fig. 4.10 the plots are similar, however now colored by mean age. For larger radii, the metal poor slowly rotating tail is older than the stars with velocities around $\sim$ 225 km/s. The noise in the tail is due to the high weights of the in-plane young stars which dominate in the low number density bins. As the radius decreases, all stars on average get older however the low angular momentum stars generally remain older than those with high angular momentum. For R < 1.5 kpc the stars with −0.7 < [Fe/H](dex) < −0.3 have ages greater than $\sim$ 8.5 Gyr regardless of V_ϕ. At higher [Fe/H], the stars have ages between $\sim$ 7 and $\sim$ 8.5 Gyr.

4.4 Discussion and conclusions

In this work, we obtained the orbits of a large sample of APOGEE and A2A stars by integrating them in a realistic bar-bulge potential with a slow pattern speed that was fit to multiple bulge and bar data-sets. Then, we applied a weight to each orbit, correcting it for the selection function of its parent survey. Using all weighted orbits, we then examined the abundance, age, kinematic, and orbital structures of the inner MW aiming to deconstruct it into its more basic components. One component, the in-situ halo, has been observed in the solar neighborhood (Haywood et al. 2018b; Gallart et al. 2019; Belokurov et al. 2020) and from simulations, is expected to have its highest densities in the bulge region (Grand et al. 2020). However, the other Galactic components also contribute significantly to this region making its detection challenging. Hence why evidence of a pressure supported component in the bulge has mainly been found at larger Z (Queiroz et al. 2020). However, through examining the parameter space of the [Mg/Fe]-rich stars the presence of the in-situ halo can also be detected in the inner MW.

In Fig. 4.4 we see that the [Mg/Fe]-rich stars near the Galactic centre are more metal poor than those at the bar ends. The presence of a positive horizontal gradient along the bar in the [Mg/Fe]-rich stars does not alone suggest the existence of a spheroid, however it does suggest that there may be more than one [Mg/Fe]-rich component contributing to this region as differing scale lengths could cause a metal poor component to dominate in the centre and a metal rich component to dominate at the bar-ends. A similar argument has been put forward to explain the positive horizontal gradient along the MW's bar seen when all stars (not just [Mg/Fe]-rich stars) are used (Fragkoudi et al. 2018; Wylie et al. 2021).

As stated previously, the positive horizontal gradient does not imply that a spheroid is present, however the rounded density and [Fe/H] contours of the [Mg/Fe]-rich stars towards the centre in Fig. 4.4 do. In fact, in Fig. 4.6, which further divides the [Mg/Fe]-rich density map into bins of [Fe/H], we see that the most metal poor [Mg/Fe]-rich stars are spheroidal-like and vertically extended, while the most metal rich [Mg/Fe]-rich stars have a bar-like density distribution, are more confined to the plane, and show a clear X-shape. Together these observations suggest the presence of a metal poor spheroidal population which dominates at small radii and a more metal rich thick disk population which dominates at larger radii forming the horizontal gradient in Fig. 4.4.

In Fig. 4.5 we examine the MDFs at various positions in the inner [Mg/Fe]-rich MW as multiple components may be visible as distinct peaks in the MDF while remaining hidden in the mean (Ness et al. 2013a). These regions, shown as black boxes in the lower right plot of Fig. 4.4, include: the central kpc in-plane region (CIP), the central kpc out-of-plane region (COP), and the outer kpc in-plane region (OIP). The MDF of the OIP region is metal rich with stars ranging between $-0.8 \leq$ [Fe/H] ≤ 0.2 and has a similar shape to that of the solar neighborhood kinematically selected thick disk stars. The MDF of the CIP region is wider than the OIP MDF with a metallicity range of $-1.2 \leq$ [Fe/H] ≤ 0.2. While the CIP MDF lacks distinct peaks, its wideness suggests that it could be composed of overlapping MDFs from different populations. To reveal the more metal-poor population's MDF, we explore the assumptions that the Galactic centre hosts two main [Mg/Fe]-rich populations, an [Fe/H]-rich and an [Fe/H]-poor population, and that the [Fe/H]-rich population is the inner thick disk and has an identical MDF as the OIP

MDF at the bar ends. We then normalise the OIP MDF to the scale of the CIP MDF and take the difference of the two MDFs. We find that the remaining distribution (RIP) is very similar not only to the MDF at large heights and small radii (COP) and the MDF of high eccentricity and high $|Z_{max}|$ stars but also the MDF of the solar neighborhood red halo sequence, believed to be the in-situ halo, as found by Gallart et al. (2019) and the MDF of the kinematically selected solar neighborhood in-situ halo stars (plus a small fraction of ex-situ halo) in our sample with all five MDFs peaking around ~ 0.65 dex; see upper right plot of Fig. 4.5. The fact that the RIP MDF agrees with the MDFs of the in-situ halo in the solar neighborhood suggests that it is also populated by the in-situ halo. Additionally, if a spheroidal component is present in the MW, it should dominate at large heights over the disk as a disk's density falls off more steeply with height, explaining the similarity of the RIP MDF to the COP MDF.

If the RIP MDF corresponds to a real distinct population, then this population dominates the [Mg/Fe]-rich stars below -0.7 dex while the inner thick disk dominates the [Mg/Fe]-rich stars above -0.3 dex as shown in Fig. 4.5. Figs. 4.6 and Fig. 4.7 show that stars in these metallicity ranges have distinct density and kinematic distributions. Stars with [Fe/H] > -0.3 dex have a bar-like in-plane concentrated distribution and show significant rotation with some dispersion. Stars with [Fe/H] < -0.7 dex have a spheroidal vertically extended distribution, radial kinematics, and show little rotation. The distribution of the stars with $-0.7 <$ [Fe/H](dex) < -0.3 appears to be a mixture of the other two in that there is a bar but it is short and very round and some stars exhibit significant rotation similar to the more metal rich stars however many still have low rotation. The distinct shape and kinematic differences in addition to the metallicity differences again imply the presence of distinct populations. Furthermore, a spheroidal supported component should show little rotation and be either radially anisotropic (GES) or isotropic in kinematics, all characteristics we see in the [Fe/H]-poor stars.

To investigate whether the metal poor population is the in-situ halo, we examine the stars in the V_ϕ-[Fe/H] plane. First of all, in Fig. 4.8 by reproducing the plots of Belokurov et al. (2020) where the V_ϕ-[Fe/H] plane is colored by different parameters for solar neighborhood stars, we see that we can identify similar structures: the thin disc, the thick disc, and the Splash (in-situ halo). We find similar [Mg/Fe], mean radius, mean $|Z_{max}|$, and [Fe/H] values for the Splash in our sample. This indicates that the Splash, at least in the solar neighborhood, is present in our sample. Then, to investigate whether the Splash is present at larger densities at lower radii as suggested by Grand et al. (2020), in Fig. 4.9 we plot the V_ϕ-[Fe/H] distribution of stars with $0.5 < |Z|(\mathrm{kpc}) < 3$ as a function of radius and separated into low and high [Mg/Fe]. The low [Mg/Fe] stars are clearly the thin disk at large radii and the peanut at small radii. For the high [Mg/Fe] stars, at large radii the stars with [Fe/H] $\gtrsim -0.1$ dex exhibit clear prograde rotation with the disk. These stars are likely the metal-rich thick disk or the metal-poor tail of the thin disk. For stars with [Fe/H] $\lesssim -0.1$ dex at large radii most still exhibit prograde rotation with the disk but a significant slowly rotating/counter rotating tail is present. This tail is also older and has higher eccentricity than the faster rotating stars as seen in Fig. 4.10. Grand et al. (2020) showed using simulations that the Splash should increase in density with decreasing radius as should the ex-situ halo. The fact that in the solar neighborhood we see slowly rotating/counter rotating stars with $-0.7 <$ [Fe/H](dex) < -0.2 and similar parameters to what Belokurov et al. (2020) obtain (see Fig. 4.8) and we see these stars grow in strength with decreasing radius indicates that the spherical population we saw previously is likely the Splash and ex-situ halo. Furthermore that these stars remain old and highly eccentric regardless of radius also suggests a coherent structure. However, we estimated that both the [Fe/H]-poor and [Fe/H]-rich [Mg/Fe]-rich stars should contribute significantly to the [Fe/H] range $-0.7 <$ [Fe/H](dex) < -0.3 and saw in Fig. 4.6 that orbits within this range trace a round short bar. Likely the faster rotating [Mg/Fe]-rich stars are the metal poor tail of the thick disk tracing the bar while the spheroidal part is the splash.

The fraction of higher metallicity [Mg/Fe]-poor slowly rotating/counter rotating stars increases with decreasing radius at a slower rate than the [Mg/Fe]-rich tail. This increase in higher metallicity low rotation stars is likely due to these stars being apart of the peanut as more metal rich stars have been shown to be more strongly trapped by the peanut (Ness et al. 2013a; Debattista et al. 2017).

In conclusion, we have found evidence for the presence of a metal poor [Mg/Fe]-rich spheroid in the inner MW that is likely the in-situ halo. The presence of a metal poor spheroid is supported by the metal poor [Mg/Fe]-rich stars' spheroidal shape and low angular momentum. Furthermore, once the inner thick disk MDF is subtracted away, the inner MDF is similar to that of the in-situ halo in the solar neighborhood and to the MDF of stars at large heights. That this spheroid is the Splash identified by Belokurov et al. (2020) is supported by many of these metal poor [Mg/Fe]-rich stars exhibiting slow rotation/counter rotation and that their metallicity range is similar to that identified by Belokurov et al. (2020). Furthermore, the density of the Splash should increase with decreasing radius and we find that the number of counter rotating metal poor and [Mg/Fe]-rich stars increases with decreasing radius while remaining old and highly eccentric. This finding further limits the available parameter space left for a classical bulge component making it more unlikely that our Galaxy contains one.

Chapter 5

Conclusions and future work

5.1 Conclusions

To understand the formation history of our own Galaxy, we first need to have a strong understanding of the Milky Way's current structure. This is both supported and complicated by us living and observing it from within as we can resolve billions of individual stars at the cost of stars often being obscured. This thesis is dedicated to revealing the current chemo-chronodynamical structure of the central kilo-parsecs of the Milky Way and then using this knowledge to understand its formation history through comparison with theoretical models. Such an analysis is only recently possible thanks to large spectroscopic, photometric, and astrometric surveys which have managed to peer through the dust and overcome crowding issues to observe hundreds of thousands of inner Milky Way stars.

In this work I used the APOGEE and A2A surveys whose unprecedented combined coverage of the inner Milky Way provided us with the distances, abundances, and ages of stars ranging from near the Sun to the far side of the bulge and allowed us to map the metallicity and α-enhancement of the bulge and bar in 3D in exquisite detail (Chapter 2). We then combined the APOGEE data with Gaia DR2 3D velocities and to-date the most realistic models of the inner Milky Way to obtain the orbits of tens of thousands of stars (Chapter 3). The orbital maps of this work confirm our previous findings but also reveal that the Galactic bar is encircled by a new Milky Way structure: the Milky Way's inner ring. Lastly, we expand on the previous work obtaining the orbits of A2A stars in addition to those of APOGEE, and perform an orbital analysis of the entire bulge, bar, and ring region finding evidence of the in-situ halo in the inner Milky Way. Through these results, we address many long standing questions about the inner Milky Way's formation.

5.1.1 The Galactic bulge and bar

It was originally thought due to its old age and negative vertical metallicity gradient (Zoccali et al. 2008; Pipino et al. 2008; Gonzalez et al. 2013), that the Milky Way's bulge was a dispersion dominated classical bulge formed from violent early mergers (Kormendy & Kennicutt

2004). However, with the huge influx of high quality data in the last decades, our view of the bulge has significantly changed. It is now widely established that the Milky Way hosts a type of pseudobulge known as a boxy-peanut bulge which forms secularly from disk instabilities (Bland-Hawthorn & Gerhard 2016). In particular, the independent work of McWilliam & Zoccali (2010) and Nataf et al. (2010) showed that the magnitude distribution of red clump stars from the 2MASS and OGLE-III surveys dips near the bulge's minor axis. This feature is not possible for a classical bulge, but instead can be easily explained by the presence of a boxy-peanut bulge. Furthermore, an X-shape in the morphology, a characteristic of boxy-peanut bulges, is clearly visible in mid in-fared images of the Galactic bulge (See Fig. 1.6).

While it is now widely accepted that the Galactic bulge has a secular origin, the exact initial conditions that lead to its current structure remain uncertain. In particular, while it appears that the Milky Way has a duel disk system (the thin and thick disks), it is unclear whether the bar and subsequently the bulge formed from an evolving thin disc, multiple discs, or a disc-continuum. While multiple bulge models with differing initial conditions have been put forward, it appears that matching the chemodynamics of bulge stars can be a discriminating factor. For example, single disk N-body models with inside-out population gradients that evolve to form a bar and boxy-peanut bulge have been able to reproduce both the vertical metallicity gradient (Martinez-Valpuesta & Gerhard 2011; Fragkoudi et al. 2017) and cylindrical rotation (Shen et al. 2010) observed in the bulge but fail to reproduce the stellar kinematics when separated by metallicity (Di Matteo et al. 2015). This dependence of the chemodynamical structure of the bulge upon the initial conditions motivated much of the work in Chapter 2.

Using the spectroscopic data from the APOGEE and A2A surveys, we examined how the metallicity and magnesium-enhancement of bulge stars varied with position and kinematics in the bulge and bar region. A main finding of the work of Chapter 2 is that the vertical metallicity distribution along the bar is more strongly X-shaped than the density distribution. This stronger pinching in the metallicity distribution was also seen in the model of Debattista et al. (2017) in which a single N-body disc with continuous star formation evolved to form a bar and boxy-peanut bulge. They attribute this stronger pinching to the process of kinematic fractionation which they define as the separation of the different populations due to differing initial radial kinematics. However, Di Matteo et al. (2019) showed using N-body models of boxy-peanut bulges formed from multiple discs with differing kinematics, that a stronger pinching in the metallicity X-shape also occurs when the different populations have different vertical kinematics. Thus, while the presence of a stronger X-shape in the metallicity is not a good discriminator for the number of initial discs, it does further confirm a disk origin for the bulge and bar.

Interestingly, the other two main findings in Chapter 2, the presence of a clear positive horizontal metallicity gradient along the bar and a negative vertical metallicity gradient in the bar, both suggest a multi-disk origin for the bulge and bar. Specifically, bulge models formed from single discs with strong negative radial metallicity gradients can reproduce the observed vertical gradients in the bulge however they continue to have a strong negative radial metallicity gradients at the end of their evolution (Di Matteo et al. 2015; Fragkoudi et al. 2017). Only the three-disk model of Fragkoudi et al. (2018) in which three discs with differing abundance distributions and scale heights and lengths are evolved to form a bar and boxy-peanut bulge, reproduced both the negative vertical metallicity gradient in the bulge and bar as well as the positive horizontal metallicity gradient along the bar. The positive horizontal metallicity gradient appears to be due to the differing fractional contributions of the populations at different radii. Specifically the more metal poor disc in this model had a shorter scale length than the more metal rich discs resulting in it dominating in the centre but not at large radii. On the other hand, the model of Di Matteo et al. (2019) which also formed a boxy-peanut bulge from three discs with the same scale lengths had flat to negative final horizontal metallicity gradients. Thus, the presence of a positive horizontal metallicity gradient along the bar rules out a single disk formation scenario instead suggesting multiple initial discs with differing scale lengths. However, it should be noted that the three-disk model of Fragkoudi et al. (2018) requires extreme scale lengths to reproduce the metallicity gradients seen in the Milky Way's bulge. In the multi-disc scenario, the observed negative vertical metallicity gradient in the bar also suggests that the initial discs must have differing scale heights. Di Matteo et al. (2019) showed using two sets of models that bulges formed from multiple discs with differing scale heights but the same scale lengths could reproduce the vertical gradient in the bar outside of the bulge while bulges formed from multiple discs with differing scale lengths but the same scale heights could not. The two-disc model of Fragkoudi et al. (2018) in which the initial discs also had different scale heights could also reproduce the vertical metallicity gradient in the bar while the single disc model of Fragkoudi et al. (2017) could only reproduce the vertical gradient in the bulge and not the bar.

Finally, we also find in Chapter 2 that bulge and bar stars increase in rotation and decrease in dispersion with increasing metallicity except for the most metal rich stars which show little kinematic dependence on metallicity. Di Matteo et al. (2015) showed that the more metal poor stars in boxy-peanut bulges formed from a single disc with a strong initial negative radial metallicity gradient should rotate faster and have higher dispersion as compared to the more metal rich stars. This comes about due to the metal poor stars originating from larger radii. Our finding then indicates that the bulge and bar of our Galaxy cannot originate form a single disc with a strong initial negative radial gradient but instead must originate from at least two discs with differing kinematics.

Together, from comparing the chemodynamical structure of the Galactic bulge and bar as seen with APOGEE and A2A data with that predicted from theoretical models we conclude that at least two discs with differing dispersions, scale heights, and scale lengths experienced kinematic fractionation and formed the bar and boxy-peanut bulge of the Galaxy.

5.1.2 The inner ring

The pronounced radial metallicity gradient along the Galactic bar that we find in Chapter 2 is not common but has been found in some other galaxies including M31 (Gajda et al. 2021). Through comparisons with N-body models in Chapter 2 we conclude that this gradient structure is the result of the bar and bulge forming from the dynamical instabilities of at least two disks with differing scale lengths. However, the initial scale lengths of these discs must be extreme to reproduce the observed Milky Way metallicity gradients (Fragkoudi et al. 2018). Understanding what mechanisms could cause this strong gradient structure was a strong motivator for the work of Chapter 3.

In Chapter 3 we computed the orbits of APOGEE stars using Gaia DR2 3D velocities and a state-of-the-art bar bulge potential (Portail et al. 2017b) with a slow pattern speed that was fit to multiple observational data sets. Then, exploiting the fact that orbits fill a 3D space, we used them to build detailed density, metallicity, and age maps of the inner Milky Way. Our main result of Chapter 3 is that we find a solar metallicity and middle aged inner ring encircling the Galactic bar. This ring dominates over the bar at distances greater than ~ 4 kpc from the Galactic centre. It has a radial width of roughly 2-3 kpc and an axis ratio of 0.7. Furthermore, we find that ring stars, especially the youngest, are highly concentrated in the plane. The ring plus the planner bar together compose a shallow long bar.

In disc galaxies, young gaseous inner rings are not rare phenomena with Buta et al. (2015) finding that 45% of S4G Sbc galaxies host inner rings. They are radially thin, tend to contain star forming regions (Buta 1995), and are observed to generally align with the bar of their host Galaxy. These inner rings are believed to be formed from gas being trapped around the 4:1 resonance of the bar. The presence of an inner ring in the Milky Way has been suggested before by Sevenster (1999) who proposed that the Milky Way's 3 kpc arm was in fact an inner ring. More recently, Li et al. (2022) from studying constrained hydrodynamical simulations of the inner Milky Way suggest that the 3 kpc arm along with the Norma arm and bar-spiral interfaces form an inner ring. The ring we find in our work is interesting in that it is a thick stellar ring composed of many middle aged stars (4-9 Gyr). Passive rings which are thick non-star forming rings are observed in external galaxies but so far have only been seen in earlier type galaxies ($\geq$ Sab, Comerón (2013)). One explanation may be that because we are observing in the infrared we can only see the older ring stars that have spread out with time.

The presence of a metal rich inner ring at the Galactic bar-ends enhances the radial metallicity gradient dismissing the need for extreme initial disc scale lengths. Furthermore, the age distribution of the ring can be used to estimate the bar's formation time. Specifically, if the ring forms from the bar's 4:1 resonance, then it must form after the bar. Fragkoudi et al. (2020) analyses two barred galaxy models that develop metal rich inner rings from the Auriga cosmological simulations finding that the star formation in the rings continues due to the transport of gas across corotation even after the bar's star formation begins to quench. They argue that a lower limit to the bar's age can be estimated as the time when the bar's star formation drops below that of the ring. Therefore, by comparing the age distributions of the bar and the ring in our sample we estimate a lower limit for the Galactic bar's formation of ~ 7 Gyr. This is consistent with bar formation time estimate of 8 Gyr by Bovy et al. (2019) but inconsistent with the estimate of 3-4 Gyrs of Tepper-Garcia et al. (2021).

In all, in the work of Chapter 3, we find that the inner Milky Way hosts a radially thick, vertically thin, on average solar metallicity and middle aged (4-9 Gyr with a peak at 7 Gyr) inner ring. This ring explains the extreme radial metallicity gradient along the bar's major axis in the context of the inner Milky Way having a two-disk origin. Furthermore, it can be used to estimate a lower limit for the bar's formation time of ~ 7 Gyr.

5.1.3 The in-situ halo

Metal rich and metal poor stars in the bulge and bar have been observed to display different kinematics and morphologies. For example, Ness et al. (2013a) found that the X-shape of the boxy-peanut bulge is stronger in the more metal rich cold populations and that it is entirely absent in the most metal poor hottest populations. This plus the dichotomy in the [α/Fe]-[Fe/H] distribution has led researches to propose that there are two main components contributing to the inner Milky Way: a metal rich component and a metal poor component. The nature of the metal rich component is well established, with most agreeing that it originates from the redistribution of angular momentum in the early thin disk leading to the bar and boxy-peanut bulge. On the other hand, the nature of the metal poor bulge is still unclear.

Recently, it was found by Haywood et al. (2018b) that when plotted on the color-magnitude diagram, kinematically selected halo stars near the Sun follow either a blue or a red sequence indicating distinct populations. They concluded that the blue sequence stars, which were found to be more metal poor but of similar age to the red sequence stars (Gallart et al. 2019), were likely the debris of the recently discovered “Gaia-Sausage”, a satellite galaxy that merged with the early Milky Way. Gallart et al. (2019) suggests that the red sequence stars are stars that were born in an early proto disc of the Milky Way and whose orbits were scattered by the GES merger. Belokurov et al. (2020) compared the azimuthal velocity of near by bright stars to their metallicities and found evidence of a thin disc, a thick disc, and a third component which smoothly transitioned from the thick disc. This third component, which they dub the Splash, is composed of many low rotation/counter rotating stars. Through comparisons with simulations, they suggest that the Splash component is also the merger heated proto disc also known as the in-situ halo. While the Splash has been seen in the solar neighborhood, it should also be seen in the inner Milky Way as it is composed of many radial orbits which pass through the centre. However, it is has yet to be seen in the inner Milky Way largely due to the fact that many massive components contribute to the inner Milky Way making detection of the Splash there difficult.

Using the orbits of A2A and APOGEE inner Milky Way stars, we dissect the bulge and bar region into its principle components in Chapter 4. From dividing the stars (orbital time steps) up by magnesium and iron abundance and examining their iron and density spatial distributions as well as kinematic properties, we find evidence of a metal poor magnesium rich spheroidal population in the bulge. In particular, we see that the most metal poor magnesium rich stars are spheroidal, centrally concentrated, vertically extended, show little to no bar, and have low angular momentum with many counter rotating stars. This is contrasted against the more metal rich magnesium rich stars which show a clear bar-like distribution with an X-shape and have significant rotation. The metallicity distribution of the magnesium rich stars at the central kpc of the Galaxy is wide suggesting the presence of more than one stellar population. When the thick disk metallicity distribution is subtracted away, the metallicity distribution that remains is very similar to that of the in-situ halo in the solar neighborhood and the stars at large heights from the plane. This indicates that the metal poor magnesium rich stars may belong to the in-situ halo. To investigate this, we plot the azimuthal velocity against the metallicity of the stars at different radii to attempt to identify the in-situ halo as was done by Belokurov et al. (2020) for the solar neighborhood. We find that in the solar neighborhood, the magnesium rich stars have a significant amount of slowly rotating/counter rotating metal poor stars high ages and eccentricities. This is a similar distribution with similar parameter values to the in-situ halo as suggested by Belokurov et al. (2020). We also find that as the radius decreases towards the Galactic centre the slowly rotating/counter metal poor stars increase in number but remains old and highly eccentric. Grand

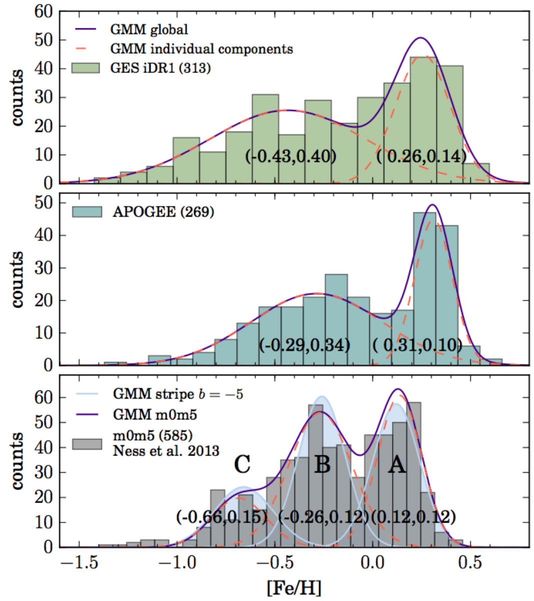

Figure 5.1: Metallicity distributions of stars in or near Baade's window from three different surveys, Gaia-Eso (top), APOGEE (middle), and ARGOS (bottom) Figure taken from Schultheis et al. (2017).

et al. (2020) from analysing Arugia simulations, finds that the in-situ halo should increase in density towards the Galactic centre. Thus it appears that the magnesium rich metal poor stars in the solar neighborhood do have an in-situ component and that this component grows in strength towards the Galactic centre as is expected. Furthermore, the fact the the eccentricities and ages of these stars remains constant with decreasing radius supports that this is a coherent structure.

In summary, in Chapter 4 we show evidence of a spheroidal metal rich magnesium poor population in the bulge. Additionally, we argue why this population is the in-situ halo component seen in the solar neighborhood. The presence of the in-situ halo in the inner Milky Way further reduces the available parameter space left for a classical bulge component making it even more unlike that the Milky Way hosts one.

5.1.4 Survey consistencies

As we have seen in this work, combining data from different surveys can extremely beneficial not only because one survey can fill in the gaps of another but also because different surveys can probe different populations, reach different depths, and provide different parameters. However, combining surveys can often be problematic as different survey may have different parameter and abundance scales. These differences come about due to differing science goals which lead to differing observing and data processing strategies. A prime example of this shown in Fig. 5.1 which was taken from Schultheis et al. (2017) and which depicts the metallicity distributions of stars in or near Baade's window (an area of the sky towards the bulge with little dust) from three different surveys: APOGEE, Gaia-Eso, and ARGOS. When comparing the three, the ARGOS metallicity distribution has three peaks instead of two and has fewer high metallicity stars. However, different surveys are often still combined. For example Portail et al. (2017b) created a chemodynamical model of the inner Milky Way through fitting a N-body model to APOGEE and ARGOS chemical data. Scale differences between the surveys may explain why the model fit is some-what un-physical at the highest metallicities, the region where the two surveys disagree most strongly. In the first half of Chapter 2, we rectify the scale differences between these surveys using the data driven method, The Cannon (Ness et al. 2015), to re-calibrate the parameters and abundances of the ARGOS survey to the scale of the APOGEE survey. After the re-calibration, the new catalog, which we call the A2A catalog, can be combined with the APOGEE catalog. The A2A catalog contains roughly 21,000 stars and has rms precisions of 0.1 dex, 0.07 dex, 74 K, and 0.18 dex for [Fe/H], [Mg/Fe], T_{eff}, and log(g) respectively.

5.2 Future work

5.2.1 The spiral ring connection: interpreting our recent discovery

In disc galaxies, gas is redistributed via angular momentum transfer resulting from nonaxisymmetries with pattern speeds like bars and spiral arms. Due to dynamical torques, gas can accumulate near dynamical resonances, like the bar's 4:1 resonances, triggering star formation. This process is the most widely believed theory for the formation of galactic rings, prominent ring-like structures visible in the luminosity distributions of external galaxies. An alternate theory, manifold theory, claims that rings are formed via the trapping of stars along tubes connecting the unstable Lagrangian points at the bar-ends (Athanassoula et al. 2011). Additionally, there is a type of ring called a ring-spiral or pseudoring which is a ring formed from spiral arms with low pitch angles.

In Wylie et al. (2022) we found that the Milky Way hosts an inner stellar ring which differs from inner rings seen in external Milky Way-like galaxies in that it is thick, older, and stellar as opposed to gaseous. An interesting future project could be investigating how the spiral arms of the Milky Way affect the stellar ring we find as spiral arms can perturb the potential near the ring. However, the N-body model we use to generate the potential in which we integrate our stars in lacks spiral arms making it currently impossible to see how the ring and spiral arms interact. Hence a future project could involve altering the Nmagic N-body model to include realistic spiral arms and then reintegrating the APOGEE and A2A data (and data from other surveys if available at the time). This project would make clear how the Milky Way's spiral arms are connected to the ring we find. Furthermore, examination on how the ring orbits connect to the spiral arms could shed light on how gas is transported across co-rotation.

5.2.2 Kinematic fractionation: understanding our bulge's formation

It has been shown in N-body simulations of bulges that stellar populations with differing initial kinematics can be separated by the bar (Debattista et al. 2017; Di Matteo et al. 2019). This process is called kinematic fractionation. A b/p bulge that undergoes kinematic fractionation will have an X-shaped metallicity structure that is more pinched than its density structure. This structure was confirmed for the Milky Way's bulge by Wylie et al. (2021) using A2A and APOGEE stars, indicating that our bulge underwent kinematic fractionation. A future project could involve a more through investigation of the process of kinematic fractionation by examining which orbits support the X-structure and what their metallicity, α-enhancement, age relationships are.

5.2.3 Made-to-Measure chemistry and age model of the bar: to pin down its formation over time

The Made-to-Measure (M2M) method is a particle based modelling method that can create N-body models of real galaxies (Syer & Tremaine 1996; de Lorenzi et al. 2007b). The M2M method has the advantage that it can (i) fit complicated systems like barred galaxies, (ii) simultaneously constrain the kinematic, spatial, and chemical distributions from multiple data sets with N-body orbital distributions, (iii) maximize observational information, (iv) account for the survey selection functions, and (v) set and keep constant during the fit global parameters. Originally the M2M particle weights represented mass elements allowing the models to be fit to density and kinematic observation data (Portail et al. 2015; Portail et al. 2017a). Portail et al. (2017c) extended this by assigning metallicity weights to the particles, creating the first chemodynamical M2M model.

A future project is to use the M2M method to create a completely self-consistent chemo-chrono-dynamical model through fitting the A2A, APOGEE DR17, and GES metallicity, α-enhancement, and age distributions. This would be the first chrono-dynamical M2M model as well as the first M2M model fit to α-enhancement. It would also be an improvement on the Portail et al. (2017c) model in that it would be fit to a much larger amount of in-plane data, the APOGEE stellar distances would be used, and the A2A, APOGEE DR17, and GES surveys would all be on the same parameter and abundance scales (Wylie et al. 2021). The initial N-body model used would be already fit using the M2M method to the red clump density from the VVV, UKIDSS, and 2MASS surveys and the stellar kinematics from the BRAVA and ARGOS surveys. The model will also be fit to the mean proper motions and dispersions from the VVV/VIRAC catalog (Clarke et al. 2019b; Clarke & Gerhard 2021) which would provide improved constraints on the Galaxy's dark matter profile.

The resulting model would provide the most realistic chemo-chrono-dynamical picture of the true Milky Way to date. Using it, the relationship between the orbits and their chemistry and age can be examined without being biased by survey magnitude or spatial selection functions. The structures composing the model's bulge and bar could be separated using orbital parameters and their individual age distributions and star formation histories could be examined. This model will place further constraints on the inner Milky Way's structure and formation history.

5.2.4 Data

For all projects mentioned above APOGEE and A2A can be used. However, data from other surveys could also be added such as data from the GES (Gilmore et al. 2012) and GIBS (Zoccali et al. 2014). We have seen in some preliminary work that GES can also be placed on the APOGEE abundance and parameter scales using the Cannon (Ness et al. 2015). Therefore, any project that uses it in conjuncture with APOGEE and A2A will have a consistent data set. Lastly, in the coming years a wealth of data is set to be released. For example on June 13 2022 the full Gaia DR3 catalogue will be released (Gaia Collaboration et al. 2018). This catalog will contain Gaia RVS spectra for 1 million objects. Gaia RVS covers the Calcium-triplet spectral range, the same spectral range of ARGOS. While it is unclear how deep into the bulge these stars will go, it is likely that parameters and abundances on the APOGEE and A2A scales could be obtained for these stars (Rampalli et al. 2021).

Appendix A

Effect of log(g) limits on the A2A red clump sample completeness

We can approximate the effect of the log(g) limits (2.8b) on the completeness of the A2A RC stars. In the top plot of Fig. A.1, the cyan histogram shows the number of ARGOS stars as a function of ARGOS log(g). The colour cut in Eq. 2.12 and reference set limits 2.7a, 2.8a, 2.8b have been applied. The gravity reference set limit 2.8b has not been applied. The blue histogram in the top plot of Fig. A.1 gives the number of A2A RC stars at each ARGOS log(g). It should be noticed that because the blue histogram is built from A2A stars, the log(g) limits (2.8b) have been applied and the blue histogram does not extend as far in log(g) as the cyan histogram. In the bottom plot of Fig. A.1, we take the ratio of the two histograms to get the fraction of A2A RC stars at each ARGOS log(g). At log(g) = 2.6 dex, 55.5% of the stars in the cyan histogram are A2A RC stars. The fraction decreases linearly outwards in both directions to 31% at 1.6 dex and 38.0% at 3.2 dex. We ignore the final bins because the log(g) limits fall within these bins causing the number of RC stars to be artificially lower. Assuming the linear trend on both sides continues past the limits, we fit a line to each side and extrapolated beyond the cuts to get the fraction of RC stars at each ARGOS log(g). We then multiplied the number of stars given by the cyan histogram in the outer bins by the fractions we got from extrapolating to get the approximate number of RC stars removed by the log(g) limits. Using this method, we find that approximately 200 RC stars are removed by the log(g) limits. Under the assumption that, to the first order, the other limits (2.7a, 2.8a, and 2.8b) affect the RC and non-RC stars equally, then 92% of the RC stars originally observed by ARGOS are accounted for in the A2A catalogue.

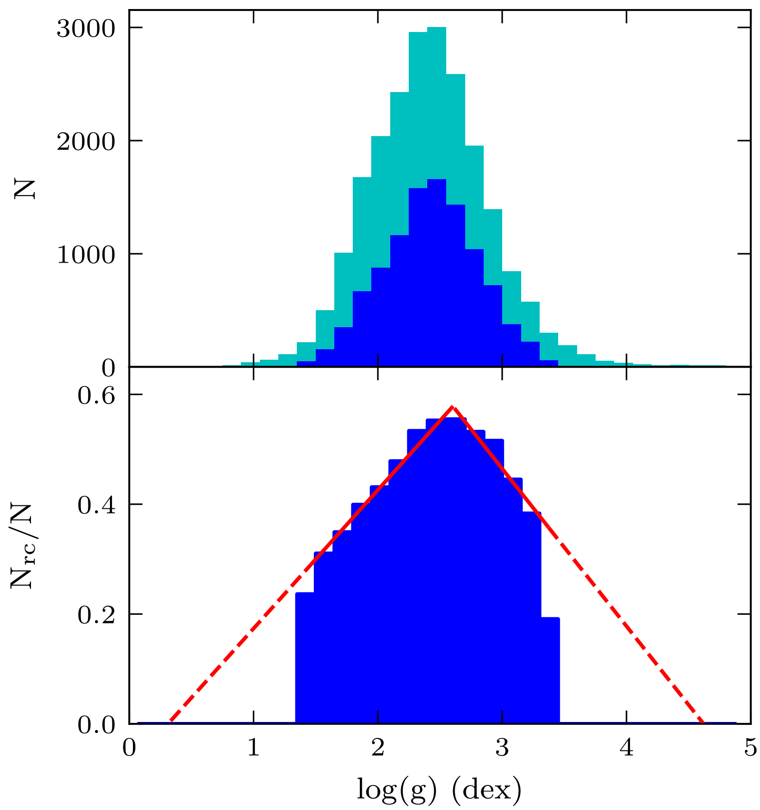

Figure A.1: Effect of the ARGOS log(g) limits on the completness of the RC in A2A. Top: Number of stars as a function of ARGOS log(g). The cyan histogram gives the number of stars after the T_{eff}, [Mg/Fe], [Fe/H], and colour limits (2.7a, 2.8a, 2.8b, and 2.12) have been applied. The blue histogram gives the number of A2A RC stars per ARGOS log(g) bin. Bottom: Fraction of A2A RC stars as a function of ARGOS gravity (ratio of blue to cyan histogram in the top plot). The red lines are linear fits to the distribution.

Appendix B

Abundance trends in APOGEE and the effect on A2A

It has been found in APOGEE that the ASPCAP T_{eff} is correlated with some of the ASPCAP abundances due to the physical stellar models (Jönsson et al. 2018; Jofré et al. 2019). We show the correlation between T_{eff} and [Mg/Fe] of stars in bins of [Fe/H] in Fig. B.1. For all plots, the stars are restricted to narrow ranges in distance, S/N, and height from the plane. The reference set we use to train *The Cannon* model to build the A2A catalogue does not span the entire T_{eff} range covered by the HQSSF APOGEE bulge MSp (see Fig. B.2).

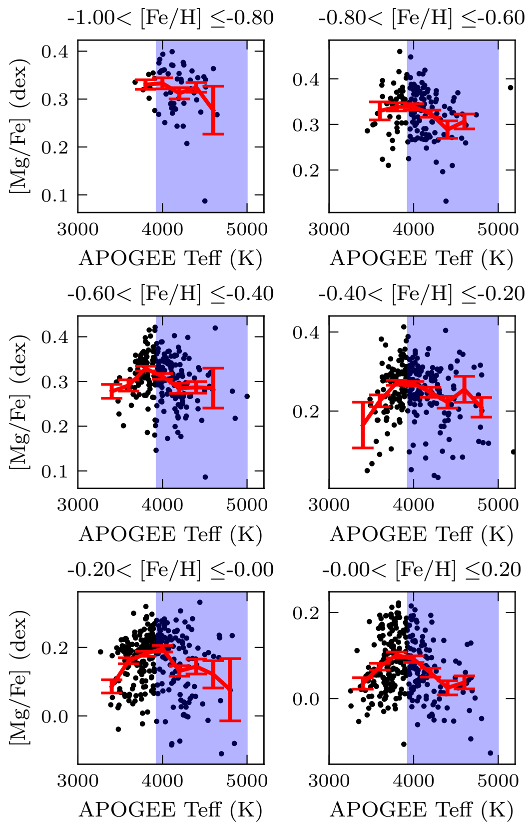

Figure B.1: ASPCAP T_{eff}-[Mg/Fe] distribution of APOGEE stars in different [Fe/H] bins with $6 < Ds\,(kpc) < 8$, $|Z| < 1$ kpc, and $100 < S/N < 200$. The red line gives the running mean of the distribution, while the blue shaded area gives the T_{eff} range spanned by the reference set on the APOGEE scale.

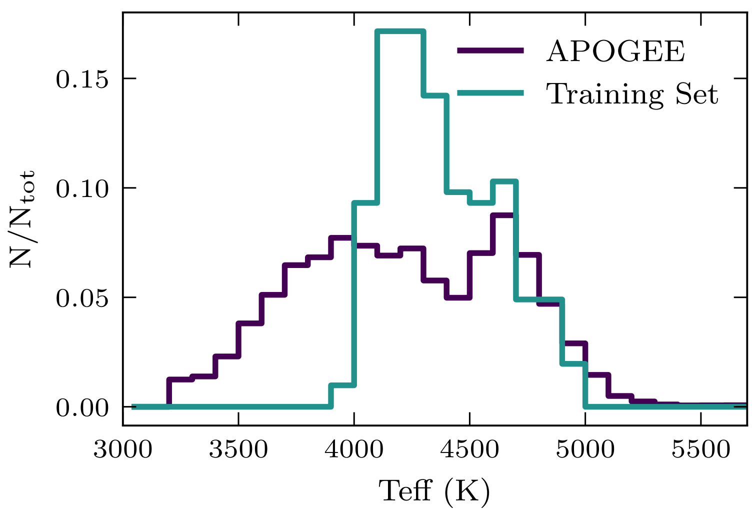

Figure B.2: T_{eff} distributions of the HQSSF APOGEE bulge MSp and of the reference set used to put the A2A survey on the APOGEE parameter scale.

Bibliography

Adibekyan, V. Z., Santos, N. C., Sousa, S. G., & Israelian, G. 2011, A&A, 535, L11

Ahumada, R., Prieto, C. A., Almeida, A., et al. 2019, The Sixteenth Data Release of the Sloan Digital Sky Surveys: First Release from the APOGEE-2 Southern Survey and Full Release of eBOSS Spectra

Alam, S., Albareti, F. D., Allende Prieto, C., et al. 2015, ApJS, 219, 12

Allende Prieto, C., Beers, T. C., Wilhelm, R., et al. 2006, ApJ, 636, 804

Alves, D. R. 2000, ApJ, 539, 732

Anderson, M. E. & Bregman, J. N. 2010, ApJ, 714, 320

Anderson, M. E. & Bregman, J. N. 2011, ApJ, 737, 22

Anderson, R. I. 2022, A&A, 658, A148

Asplund, M., Grevesse, N., Sauval, A. J., & Scott, P. 2009, ARA&A, 47, 481

Athanassoula, E. & Misiriotis, A. 2002, MNRAS, 330, 35

Athanassoula, E., Romero-Gómez, M., & Masdemont, J. J. 2011, Memorie della Societa Astronomica Italiana Supplementi, 18, 97

Auvergne, M., Bodin, P., Boisnard, L., et al. 2009, A&A, 506, 411

Babusiaux, C., Gómez, A., Hill, V., et al. 2010, A&A, 519, A77

Balick, B. & Brown, R. L. 1974, in H II Regions and the Galactic Centre, 261–265

Banerjee, A. & Jog, C. J. 2011, ApJ, 732, L8

Bartko, H., Martins, F., Fritz, T. K., et al. 2009, ApJ, 697, 1741

Basu, S., Chaplin, W. J., & Elsworth, Y. 2010, ApJ, 710, 1596

Bell, E. F., Zucker, D. B., Belokurov, V., et al. 2008, ApJ, 680, 295

Belokurov, V., Erkal, D., Evans, N. W., Koposov, S. E., & Deason, A. J. 2018, MNRAS, 478, 611

Belokurov, V., Sanders, J. L., Fattahi, A., et al. 2020, MNRAS, 494, 3880

Bennett, M. & Bovy, J. 2019, MNRAS, 482, 1417

Bensby, T., Feltzing, S., Gould, A., et al. 2018, in Rediscovering Our Galaxy, ed. C. Chiappini, I. Minchev, E. Starkenburg, & M. Valentini, Vol. 334, 86–89

Bensby, T., Feltzing, S., Gould, A., et al. 2017, A&A, 605, A89

Bensby, T., Feltzing, S., & Oey, M. S. 2014, A&A, 562, A71

Bensby, T., Yee, J. C., Feltzing, S., et al. 2013, A&A, 549, A147

Beraldo e Silva, L., Debattista, V. P., Nidever, D., Amarante, J. A. S., & Garver, B. 2021, MNRAS, 502, 260

Bessell, M. S., Castelli, F., & Plez, B. 1998, A&A, 333, 231

Binney, J. 2020, Monthly Notices of the Royal Astronomical Society, 495, 895

Birky, J., Hogg, D. W., Mann, A. W., & Burgasser, A. 2020, ApJ, 892, 31

Bland-Hawthorn, J. & Gerhard, O. 2016, ARA&A, 54, 529

Bonaca, A., Conroy, C., Cargile, P. A., et al. 2020, ApJ, 897, L18

Bond, N. A., Ivezić, Ž., Sesar, B., et al. 2010, ApJ, 716, 1

Bovy, J. 2016, ApJ, 817, 49

Bovy, J., Bahmanyar, A., Fritz, T. K., & Kallivayalil, N. 2016a, ApJ, 833, 31

Bovy, J., Leung, H. W., Hunt, J. A. S., et al. 2019, MNRAS, 490, 4740

Bovy, J., Nidever, D. L., Rix, H.-W., et al. 2014, ApJ, 790, 127

Bovy, J., Rix, H.-W., Liu, C., et al. 2012, ApJ, 753, 148

Bovy, J., Rix, H.-W., Schlafly, E. F., et al. 2016b, ApJ, 823, 30

Bressan, A., Marigo, P., Girardi, L., et al. 2012, MNRAS, 427, 127

Bureau, M., Aronica, G., Athanassoula, E., et al. 2006, MNRAS, 370, 753

Buta, R. 1991, ApJ, 370, 130

Buta, R. 1995, ApJS, 96, 39

Buta, R. & Combes, F. 1996, Fund. Cosmic Phys., 17, 95

Buta, R. J., Sheth, K., Athanassoula, E., et al. 2015, ApJS, 217, 32

Cabrera-Lavers, A., González-Fernández, C., Garzón, F., Hammersley, P. L., & López-Corredoira, M. 2008, A&A, 491, 781

Cabrera-Lavers, A., Hammersley, P. L., González-Fernández, C., et al. 2007, A&A, 465, 825

Carlin, J. L., Liu, C., Newberg, H. J., et al. 2016, ApJ, 822, 16

Carroll, B. W. & Ostlie, D. A. 2006, An introduction to modern astrophysics and cosmology (Cambridge University Press)

Casagrande, L., Silva Aguirre, V., Stello, D., et al. 2014, ApJ, 787, 110

Casey, A. R., Hawkins, K., Hogg, D. W., et al. 2017, ApJ, 840, 59

Castelvecchi, D. 2022, Nature, 605, 403

Chaplin, W. J., Basu, S., Huber, D., et al. 2014, ApJS, 210, 1

Chatzopoulos, S., Fritz, T. K., Gerhard, O., et al. 2015, MNRAS, 447, 948

Chen, Y., Bressan, A., Girardi, L., et al. 2015, MNRAS, 452, 1068

Chen, Y., Girardi, L., Bressan, A., et al. 2014, MNRAS, 444, 2525

Chiappini, C., Matteucci, F., & Gratton, R. 1997, ApJ, 477, 765

Chiba, R. & Schönrich, R. 2021, arXiv e-prints, arXiv:2102.08388

Clara, M. T. & Martins, C. J. A. P. 2020, A&A, 633, L11

Clarke, J. & Gerhard, O. 2021, arXiv e-prints, arXiv:2107.10875

Clarke, J. P. & Gerhard, O. 2022, MNRAS, 512, 2171

Clarke, J. P., Wegg, C., Gerhard, O., et al. 2019a, MNRAS, 489, 3519

Clarke, J. P., Wegg, C., Gerhard, O., et al. 2019b, MNRAS, 489, 3519

Clarkson, W., Sahu, K., Anderson, J., et al. 2008, ApJ, 684, 1110

Combes, F., Debbasch, F., Friedli, D., & Pfenniger, D. 1990, A&A, 233, 82

Comerón, S. 2013, A&A, 555, L4

Comerón, S., Knapen, J. H., Sheth, K., et al. 2011, ApJ, 729, 18

Comerón, S., Salo, H., Laurikainen, E., et al. 2014, A&A, 562, A121

Contopoulos, G. 1980, A&A, 81, 198

Cropper, M., Katz, D., Sartoretti, P., et al. 2018, A&A, 616, A5

Cyburt, R. H., Fields, B. D., Olive, K. A., & Yeh, T.-H. 2016, Reviews of Modern Physics, 88, 015004

Das, S., Mathur, S., & Gupta, A. 2020, ApJ, 897, 63

De Donder, E. & Vanbeveren, D. 2003, New A, 8, 817

de Lorenzi, F., Debattista, V. P., Gerhard, O., & Sambhus, N. 2007a, MNRAS, 376, 71

de Lorenzi, F., Debattista, V. P., Gerhard, O., & Sambhus, N. 2007b, MNRAS, 376, 71

Deason, A. J., Belokurov, V., & Evans, N. W. 2011, MNRAS, 416, 2903

Debattista, V. P., Ness, M., Gonzalez, O. A., et al. 2017, MNRAS, 469, 1587

Debattista, V. P. & Sellwood, J. A. 2000, ApJ, 543, 704

Dehnen, W., McLaughlin, D. E., & Sachania, J. 2006, MNRAS, 369, 1688

Di Matteo, P., Fragkoudi, F., Khoperskov, S., et al. 2019, A&A, 628, A11

Di Matteo, P., Gómez, A., Haywood, M., et al. 2015, A&A, 577, A1

Di Matteo, P., Haywood, M., Gómez, A., et al. 2014, A&A, 567, A122

Di Mauro, M. P. 2016, in Frontier Research in Astrophysics II (FRAPWS2016), 29

Editors, E. 2021, Heracleides Ponticus

Eggen, O. J., Lynden-Bell, D., & Sandage, A. R. 1962, ApJ, 136, 748

Eisenhauer, F., Schödel, R., Genzel, R., et al. 2003, ApJ, 597, L121

Evans, J. 2020, Aristarchus of Samos

Fang, T., Buote, D., Bullock, J., & Ma, R. 2015, ApJS, 217, 21

Ferrarese, L., Côté, P., Dalla Bontà, E., et al. 2006, ApJ, 644, L21

Feuillet, D. K., Bovy, J., Holtzman, J., et al. 2016, ApJ, 817, 40

Fields, B. D. 2011, Annual Review of Nuclear and Particle Science, 61, 47

Filippenko, A. V. 1997, ARA&A, 35, 309

Foreman-Mackey, D., Hogg, D. W., Lang, D., & Goodman, J. 2013, PASP, 125, 306

Fragkoudi, F., Di Matteo, P., Haywood, M., et al. 2017, A&A, 607, L4

Fragkoudi, F., Di Matteo, P., Haywood, M., et al. 2018, A&A, 616, A180

Fragkoudi, F., Grand, R. J. J., Pakmor, R., et al. 2020, MNRAS, 494, 5936

Freeman, K., Ness, M., Wylie-de Boer, E., et al. 2012, MNRAS, 428, 3660

Fritz, T. K., Patrick, L. R., Feldmeier-Krause, A., et al. 2021, A&A, 649, A83

Fuhrmann, K., Chini, R., Kaderhandt, L., & Chen, Z. 2017, MNRAS, 464, 2610

Gai, N., Basu, S., Chaplin, W. J., & Elsworth, Y. 2011, ApJ, 730, 63

Gaia Collaboration, Brown, A. G. A., Vallenari, A., et al. 2018, A&A, 616, A1

Gaia Collaboration, Brown, A. G. A., Vallenari, A., et al. 2021, A&A, 649, A1

Gajda, G., Gerhard, O., Blaña, M., et al. 2021, A&A, 647, A131

Galgano, B., Stassun, K., & Rojas-Ayala, B. 2020, AJ, 159, 193

Gallart, C., Bernard, E. J., Brook, C. B., et al. 2019, Nature Astronomy, 3, 932

García Pérez, A. E., Prieto, C. A., Holtzman, J. A., et al. 2016, AJ, 151, 144

Gatto, A., Fraternali, F., Read, J. I., et al. 2013, MNRAS, 433, 2749

Gebhardt, K., Richstone, D., Tremaine, S., et al. 2003, ApJ, 583, 92

Gennaro, M., Brown, T., Anderson, J., et al. 2015, in Astronomical Society of the Pacific Conference Series, Vol. 491, Fifty Years of Wide Field Studies in the Southern Hemisphere: Resolved Stellar Populations of the Galactic Bulge and Magellanic Clouds, ed. S. Points & A. Kunder, 182

Genovali, K., Lemasle, B., Bono, G., et al. 2014, A&A, 566, A37

Ghez, A. M., Salim, S., Weinberg, N. N., et al. 2008, ApJ, 689, 1044

Gibbons, S. L. J., Belokurov, V., & Evans, N. W. 2014, MNRAS, 445, 3788

Gillessen, S., Eisenhauer, F., Fritz, T. K., et al. 2009a, ApJ, 707, L114

Gillessen, S., Eisenhauer, F., Trippe, S., et al. 2009b, ApJ, 692, 1075

Gilliland, R. L., Brown, T. M., Christensen-Dalsgaard, J., et al. 2010, PASP, 122, 131

Gilmore, G., Randich, S., Asplund, M., et al. 2012, The Messenger, 147, 25

Gilmore, G. & Reid, N. 1983, MNRAS, 202, 1025

Gonzalez, O. A., Rejkuba, M., Zoccali, M., et al. 2013, A&A, 552, A110

Grand, R. J. J., Bustamante, S., Gómez, F. A., et al. 2018, MNRAS, 474, 3629

Grand, R. J. J., Kawata, D., Belokurov, V., et al. 2020, MNRAS, 497, 1603

Gravity Collaboration, Abuter, R., Amorim, A., et al. 2019, A&A, 625, L10

Gray, D. F. 2008, The Observation and Analysis of Stellar Photospheres (Cambridge University Press)

Grcevich, J. & Putman, M. E. 2009, ApJ, 696, 385

Griv, E., Gedalin, M., Pietrukowicz, P., Majaess, D., & Jiang, I.-G. 2020, MNRAS, 499, 1091

Griv, E., Gedalin, M., Pietrukowicz, P., Majaess, D., & Jiang, I.-G. 2021, MNRAS, 502, 4194

Groenewegen, M. A. T., Udalski, A., & Bono, G. 2008, A&A, 481, 441

Gupta, A., Mathur, S., Krongold, Y., Nicastro, F., & Galeazzi, M. 2012, ApJ, 756, L8

Gustafsson, B., Edvardsson, B., Eriksson, K., et al. 2008, A&A, 486, 951

Guth, A. H. 1981, Phys. Rev. D, 23, 347

Habing, H. J., Sevenster, M. N., Messineo, M., van de Ven, G., & Kuijken, K. 2006, A&A, 458, 151

Hammersley, P. L., Garzón, F., Mahoney, T. J., López-Corredoira, M., & Torres, M. A. P. 2000, MNRAS, 317, L45

Hasselquist, S., Zasowski, G., Feuillet, D. K., et al. 2020, ApJ, 901, 109

Hayden, M. R., Bovy, J., Holtzman, J. A., et al. 2015, ApJ, 808, 132

Haywood, M., Di Matteo, P., Lehnert, M., et al. 2018a, A&A, 618, A78

Haywood, M., Di Matteo, P., Lehnert, M. D., et al. 2018b, ApJ, 863, 113

Hekker, S., Elsworth, Y., Mosser, B., et al. 2013, A&A, 556, A59

Helmi, A. 2004, ApJ, 610, L97

Helmi, A., Babusiaux, C., Koppelman, H. H., et al. 2018, Nature, 563, 85

Henley, D. B., Shelton, R. L., Kwak, K., Joung, M. R., & Mac Low, M.-M. 2010, ApJ, 723, 935

Hernitschek, N., Cohen, J. G., Rix, H.-W., et al. 2018, ApJ, 859, 31

Herschel, W. 1785, Philosophical Transactions of the Royal Society of London Series I, 75, 213

Hill, V., Lecureur, A., Gómez, A., et al. 2011, A&A, 534, A80

Hilmi, T., Minchev, I., Buck, T., et al. 2020, MNRAS, 497, 933

Ho, A. Y. Q., Ness, M. K., Hogg, D. W., et al. 2017, ApJ, 836, 5

Hodges-Kluck, E. J., Bregman, J. N., & Li, J.-t. 2018, ApJ, 866, 126

Holtzman, J. A., Hasselquist, S., Shetrone, M., et al. 2018, AJ, 156, 125

Horta, D., Schiavon, R. P., Mackereth, J. T., et al. 2021, MNRAS, 500, 1385

Howard, C. D., Rich, R. M., Clarkson, W., et al. 2009, ApJ, 702, L153

Iocco, F., Mangano, G., Miele, G., Pisanti, O., & Serpico, P. D. 2009, Phys. Rep., 472, 1

Iorio, G. & Belokurov, V. 2019, MNRAS, 482, 3868

Iwanek, P., Soszyński, I., & Kozłowski, S. 2021, ApJ, 919, 99

Jofré, P., Heiter, U., & Soubiran, C. 2019, ARA&A, 57, 571

Johnson, C. I., Rich, R. M., Fulbright, J. P., Valenti, E., & McWilliam, A. 2011, ApJ, 732, 108

Johnson, H. L. & Morgan, W. W. 1953, ApJ, 117, 313

Jones, A. R. 2020, Ptolemaic System

Jones, A. R. 2021, Ptolemy

Jönsson, H., Allende Prieto, C., Holtzman, J. A., et al. 2018, AJ, 156, 126

Jönsson, H., Holtzman, J. A., Allende Prieto, C., et al. 2020, AJ, 160, 120

Jurić, M., Ivezić, Ž., Brooks, A., et al. 2008, ApJ, 673, 864

Kaaret, P., Koutroumpa, D., Kuntz, K. D., et al. 2020, Nature Astronomy, 4, 1072

Kafle, P. R., Sharma, S., Lewis, G. F., & Bland-Hawthorn, J. 2012, ApJ, 761, 98

Kahn, F. D. & Woltjer, L. 1959, ApJ, 130, 705

Koppelman, H., Helmi, A., & Veljanoski, J. 2018, ApJ, 860, L11

Kormendy, J. 1979, ApJ, 227, 714

Kormendy, J. & Bender, R. 2019, ApJ, 872, 106

Kormendy, J. & Kennicutt, Robert C., J. 2004, ARA&A, 42, 603

Kormendy, J. & Richstone, D. 1995, ARA&A, 33, 581

Kroupa, P., Tout, C. A., & Gilmore, G. 1993, MNRAS, 262, 545

Kruk, S. J., Erwin, P., Debattista, V. P., & Lintott, C. 2019, MNRAS, 490, 4721

Kuijken, K. & Rich, R. M. 2002, AJ, 124, 2054

Kunder, A., Koch, A., Rich, R. M., et al. 2012, AJ, 143, 57

Küpper, A. H. W., Balbinot, E., Bonaca, A., et al. 2015, ApJ, 803, 80

Kurucz, R. L. 1979, ApJS, 40, 1

Lagarde, N., Decressin, T., Charbonnel, C., et al. 2012, A&A, 543, A108

Law, D. R., Majewski, S. R., & Johnston, K. V. 2009, ApJ, 703, L67

Leavitt, H. S. & Pickering, E. C. 1912, Harvard College Observatory Circular, 173, 1

Leung, H. W. & Bovy, J. 2019a, MNRAS, 483, 3255

Leung, H. W. & Bovy, J. 2019b, MNRAS, 489, 2079

Li, Z., Shen, J., Gerhard, O., & Clarke, J. P. 2022, ApJ, 925, 71

Lian, J., Thomas, D., Maraston, C., et al. 2020a, MNRAS, 497, 2371

Lian, J., Zasowski, G., Hasselquist, S., et al. 2020b, MNRAS, 497, 3557

Lindqvist, M., Habing, H. J., & Winnberg, A. 1992, A&A, 259, 118

Loebman, S. R., Ivezić, Ž., Quinn, T. R., et al. 2014, ApJ, 794, 151

Lucas, P. W., Hoare, M. G., Longmore, A., et al. 2008, MNRAS, 391, 136

Lucey, M., Hawkins, K., Ness, M., et al. 2021, MNRAS, 501, 5981

Luck, R. E. & Lambert, D. L. 2011, AJ, 142, 136

Mackereth, J. T. & Bovy, J. 2020, MNRAS, 492, 3631

Mackereth, J. T., Bovy, J., Leung, H. W., et al. 2019a, MNRAS, 489, 176

Mackereth, J. T., Schiavon, R. P., Pfeffer, J., et al. 2019b, MNRAS, 482, 3426

Majaess, D. 2010, Acta Astron., 60, 55

Majewski, S. 2016, Astronomische Nachrichten, 337, 863

Maoz, D. & Graur, O. 2017, ApJ, 848, 25

Martig, M., Fouesneau, M., Rix, H.-W., et al. 2016, MNRAS, 456, 3655

Martinez-Valpuesta, I. & Gerhard, O. 2011, ApJ, 734, L20

Martinez-Valpuesta, I. & Gerhard, O. 2013, ApJ, 766, L3

Martinez-Valpuesta, I. & Shlosman, I. 2004, ApJ, 613, L29

Martynenko, N. 2022, MNRAS, 511, 843

Matteucci, F. & Greggio, L. 1986, A&A, 154, 279

Matteucci, F., Grisoni, V., Spitoni, E., et al. 2019, MNRAS, 487, 5363

Matteucci, F. & Recchi, S. 2001, ApJ, 558, 351

McWilliam, A. 1997, Annual Review of Astronomy and Astrophysics, 35, 503

McWilliam, A. & Zoccali, M. 2010, ApJ, 724, 1491

Mészáros, S., Allende Prieto, C., Edvardsson, B., et al. 2012, AJ, 144, 120

Minniti, D., Lucas, P. W., Emerson, J. P., et al. 2010, New A, 15, 433

Nataf, D. M., Udalski, A., Gould, A., Fouqué, P., & Stanek, K. Z. 2010, ApJ, 721, L28

Necib, L. & Lin, T. 2022, ApJ, 926, 189

Ness, M., Freeman, K., Athanassoula, E., et al. 2013a, MNRAS, 430, 836

Ness, M., Freeman, K., Athanassoula, E., et al. 2013b, MNRAS, 432, 2092

Ness, M., Hogg, D. W., Rix, H.-W., Ho, A. Y. Q., & Zasowski, G. 2015, ApJ, 808, 16

Ness, M. & Lang, D. 2016, AJ, 152, 14

Ness, M., Zasowski, G., Johnson, J. A., et al. 2016, ApJ, 819, 2

Nikzat, F., Ferreira Lopes, C. E., Catelan, M., et al. 2022, A&A, 660, A35

Nuza, S. E., Parisi, F., Scannapieco, C., et al. 2014, MNRAS, 441, 2593

Oakes, E. K., Hoyt, T. J., Freedman, W. L., et al. 2022, ApJ, 929, 116

Olling, R. P. & Merrifield, M. R. 2000, MNRAS, 311, 361

Oort, J. H. & Rougoor, G. W. 1960, MNRAS, 121, 171

Ortolani, S., Renzini, A., Gilmozzi, R., et al. 1995, Nature, 377, 701

Page, L., Nolta, M. R., Barnes, C., et al. 2003, ApJS, 148, 233

Paumard, T., Genzel, R., Martins, F., et al. 2006, ApJ, 643, 1011

Perivolaropoulos, L. & Skara, F. 2021, arXiv e-prints, arXiv:2105.05208

Perlmutter, S., Aldering, G., Goldhaber, G., et al. 1999, ApJ, 517, 565

Perryman, M. A. C., Lindegren, L., Kovalevsky, J., et al. 1997, A&A, 323, L49

Piddington, J. H. & Minnett, H. C. 1951, Australian Journal of Scientific Research A Physical Sciences, 4, 459

Pila-Díez, B., de Jong, J. T. A., Kuijken, K., van der Burg, R. F. J., & Hoekstra, H. 2015, A&A, 579, A38

Pinna, F., Falcón-Barroso, J., Martig, M., et al. 2019, A&A, 625, A95

Pinsonneault, M. H., Elsworth, Y. P., Tayar, J., et al. 2018, ApJS, 239, 32

Pipino, A., Matteucci, F., & D'Ercole, A. 2008, in Formation and Evolution of Galaxy Bulges, ed. M. Bureau, E. Athanassoula, & B. Barbuy, Vol. 245, 19–22

Planck Collaboration, Aghanim, N., Akrami, Y., et al. 2020, A&A, 641, A6

Plez, B. 2012, Turbospectrum: Code for spectral synthesis

Plez, B., Brett, J. M., & Nordlund, A. 1992, A&A, 256, 551

Portail, M., Gerhard, O., Wegg, C., & Ness, M. 2017a, MNRAS, 465, 1621

Portail, M., Wegg, C., Gerhard, O., & Martinez-Valpuesta, I. 2015, MNRAS, 448, 713

Portail, M., Wegg, C., Gerhard, O., & Ness, M. 2017b, MNRAS, 470, 1233

Portail, M., Wegg, C., Gerhard, O., & Ness, M. 2017c, MNRAS, 470, 1233

Posti, L. & Helmi, A. 2019, A&A, 621, A56

Prada Moroni, P. G., Valle, G., Dell'Omodarme, M., & Degl'Innocenti, S. 2016, Astronomische Nachrichten, 337, 819

Queiroz, A. B. A., Anders, F., Chiappini, C., et al. 2020, A&A, 638, A76

Queiroz, A. B. A., Chiappini, C., Perez-Villegas, A., et al. 2021, A&A, 656, A156

Raffelt, G. G. 2008, in Axions, ed. M. Kuster, G. Raffelt, & B. Beltrán, Vol. 741 (Springer), 51

Raha, N., Sellwood, J. A., James, R. A., & Kahn, F. D. 1991, Nature, 352, 411

Rampalli, R., Ness, M., & Wylie, S. 2021, ApJ, 921, 78

Rattenbury, N. J., Mao, S., Debattista, V. P., et al. 2007, MNRAS, 378, 1165

Recio-Blanco, A., de Laverny, P., Kordopatis, G., et al. 2014, A&A, 567, A5

Reid, M. J. & Brunthaler, A. 2004, ApJ, 616, 872

Reid, M. J. & Brunthaler, A. 2020, ApJ, 892, 39

Reid, M. J., Menten, K. M., Zheng, X. W., Brunthaler, A., & Xu, Y. 2009, ApJ, 705, 1548

Rich, R. M., Origlia, L., & Valenti, E. 2007, ApJ, 665, L119

Rich, R. M., Origlia, L., & Valenti, E. 2012, ApJ, 746, 59

Ricker, G. R., Winn, J. N., Vanderspek, R., et al. 2015, Journal of Astronomical Telescopes, Instruments, and Systems, 1, 014003

Riess, A. G., Filippenko, A. V., Challis, P., et al. 1998, AJ, 116, 1009

Rojas-Arriagada, A., Recio-Blanco, A., de Laverny, P., et al. 2017, A&A, 601, A140

Rojas-Arriagada, A., Recio-Blanco, A., Hill, V., et al. 2014, A&A, 569, A103

Rojas-Arriagada, A., Zasowski, G., Schultheis, M., et al. 2020, Monthly Notices of the Royal Astronomical Society, 499, 1037

Rojas-Arriagada, A., Zoccali, M., Schultheis, M., et al. 2019a, A&A, 626, A16

Rojas-Arriagada, A., Zoccali, M., Schultheis, M., et al. 2019b, A&A, 626, A16

Saha, K. & Gerhard, O. 2013, MNRAS, 430, 2039

Sahlholdt, C. L., Casagrande, L., & Feltzing, S. 2019, ApJ, 881, L10

Saito, R. K., Hempel, M., Minniti, D., et al. 2012, A&A, 537, A107

Salpeter, E. E. 1955, ApJ, 121, 161

Sanders, J. L., Smith, L., & Evans, N. W. 2019, MNRAS, 488, 4552

Schlafly, E. F. & Finkbeiner, D. P. 2011, ApJ, 737, 103

Schlaufman, K. C., Rockosi, C. M., Allende Prieto, C., et al. 2009, ApJ, 703, 2177

Schlegel, D. J., Finkbeiner, D. P., & Davis, M. 1998, ApJ, 500, 525

Schödel, R. 2021, in Astronomical Society of the Pacific Conference Series, Vol. 528, New Horizons in Galactic Center Astronomy and Beyond, ed. M. Tsuboi & T. Oka, 353

Schödel, R., Feldmeier, A., Kunneriath, D., et al. 2014, A&A, 566, A47

Schödel, R., Nogueras-Lara, F., Gallego-Cano, E., et al. 2020, A&A, 641, A102

Schönrich, R., Aumer, M., & Sale, S. E. 2015, ApJ, 812, L21

Schönrich, R., Binney, J., & Dehnen, W. 2010, MNRAS, 403, 1829

Schultheis, M., Rojas-Arriagada, A., García Pérez, A. E., et al. 2017, A&A, 600, A14

Schwarz, M. P. 1984, MNRAS, 209, 93

Scott, D. W. 1992, Multivariate Density Estimation (Wiley)

Searle, L. & Zinn, R. 1978, ApJ, 225, 357

Seidel, M. K., Falcón-Barroso, J., Martínez-Valpuesta, I., et al. 2016, MNRAS, 460, 3784

Sembach, K. R., Wakker, B. P., Savage, B. D., et al. 2003, ApJS, 146, 165

Sesar, B., Ivezić, Ž., Stuart, J. S., et al. 2013, AJ, 146, 21

Sevenster, M. N. 1999, MNRAS, 310, 629

Shank, D., Beers, T. C., Placco, V. M., et al. 2022, ApJ, 926, 26

Sharma, S., Bland-Hawthorn, J., Johnston, K. V., & Binney, J. 2011, ApJ, 730, 3

Shen, J., Rich, R. M., Kormendy, J., et al. 2010, ApJ, 720, L72

Skrutskie, M. F., Cutri, R. M., Stiening, R., et al. 2006, AJ, 131, 1163

Slizewski, A., Dufresne, X., Murdock, K., et al. 2022, ApJ, 924, 131

Smiljanic, R., Korn, A. J., Bergemann, M., et al. 2014, A&A, 570, A122

Smith, M. C., Evans, N. W., Belokurov, V., et al. 2009, MNRAS, 399, 1223

Sneden, C., Bean, J., Ivans, I., Lucatello, S., & Sobeck, J. 2012, ASCL, 02009

Sormani, M. C., Sanders, J. L., Fritz, T. K., et al. 2022, MNRAS, 512, 1857

Soszyński, I., Udalski, A., Szymański, M. K., et al. 2014, Acta Astron., 64, 177

Stanimirović, S., Dickey, J. M., Krčo, M., & Brooks, A. M. 2002, ApJ, 576, 773

Steigman, G. 2007, in American Institute of Physics Conference Series, Vol. 903, SUSY06: The 14th International Conference on Supersymmetry and the Unification of Fundamental Interactions, ed. J. L. Feng, 40

Stello, D., Chaplin, W. J., Bruntt, H., et al. 2009, ApJ, 700, 1589

Strömberg, G. 1925, ApJ, 61, 363

Surot, F., Valenti, E., Hidalgo, S. L., et al. 2019, A&A, 629, A1

Syer, D. & Tremaine, S. 1996, MNRAS, 282, 223

Tang, J., Bressan, A., Rosenfield, P., et al. 2014, MNRAS, 445, 4287

Tepper-Garcia, T., Bland-Hawthorn, J., Vasiliev, E., et al. 2021, arXiv e-prints, arXiv:2111.05466

Thomas, G. E. & Stamnes, K. 2002, Radiative transfer in the atmosphere and ocean (Cambridge University Press)

Uttenthaler, S., Schultheis, M., Nataf, D. M., et al. 2012, A&A, 546, A57

van der Marel, R. P., Fardal, M., Besla, G., et al. 2012, ApJ, 753, 8

Van Helden, A. 2022, Galileo

Wang, J., Hammer, F., & Yang, Y. 2022, MNRAS, 510, 2242

Watkins, L. L., Evans, N. W., & An, J. H. 2010, MNRAS, 406, 264

Wegg, C. & Gerhard, O. 2013, MNRAS, 435, 1874

Wegg, C., Gerhard, O., & Bieth, M. 2019a, MNRAS, 485, 3296

Wegg, C., Gerhard, O., & Portail, M. 2015, MNRAS, 450, 4050

Wegg, C., Rojas-Arriagada, A., Schultheis, M., & Gerhard, O. 2019b, A&A, 632, A121

Weiss, A. & Schlattl, H. 2008, Ap&SS, 316, 99

Westman, R. S. 2021, Johannes Kepler

Westman, R. S. 2022, Nicolaus Copernicus

Wheeler, A., Ness, M., Buder, S., et al. 2020, ApJ, 898, 58

Wielen, R. 1977, A&A, 60, 263

Wylie, S. M., Clarke, J. P., & Gerhard, O. E. 2022, A&A, 659, A80

Wylie, S. M., Gerhard, O. E., Ness, M. K., et al. 2021, A&A, 653, A143

Xue, X.-X., Rix, H.-W., Ma, Z., et al. 2015, ApJ, 809, 144

Xue, X. X., Rix, H. W., Zhao, G., et al. 2008, ApJ, 684, 1143

Yao, Y., Shull, J. M., Wang, Q. D., & Cash, W. 2012, ApJ, 746, 166

Yoachim, P. & Dalcanton, J. J. 2006, AJ, 131, 226

Zasowski, G., Cohen, R. E., Chojnowski, S. D., et al. 2017, AJ, 154, 198

Zasowski, G., Ness, M. K., García Pérez, A. E., et al. 2016, ApJ, 832, 132

Zoccali, M., Gonzalez, O. A., Vasquez, S., et al. 2014, A&A, 562, A66

Zoccali, M., Hill, V., Lecureur, A., et al. 2008, A&A, 486, 177

Zoccali, M., Vasquez, S., Gonzalez, O. A., et al. 2017, A&A, 599, A12

Danksagung

First of all, I would like to express my sincerest gratitude to my advisor Ortwin Gerhard for giving me this amazing opportunity and for his support and guidance through out these past years. His amazing attention to detail which caught numerous mistakes of mine over the years elevated my work to something I can truly be proud of. I enjoyed our many discussions over the years and am very grateful for all the knowledge he has shared with me.

I want to give special thanks to the love of my life, my husband Nils. His unwavering love, support, and amazing ability to always make me smile made the stressful times few and far between.

I want to thank my friend, college, and partial office mate Jonny. I can't believe our PhDs are coming to an end but I'm glad I got to share this journey with you. I'm going to miss all the amazing coffees breaks, game nights, and BBQs we have had over the years.

I next want to thank my parents for always encouraging and supporting me through the thick and thin. I want to thank my mom for instilling me with a strong fundamental knowledge in mathematics without which I would have never made it this far and I want to thank my dad for always reminding me that science is art and when things get too much to take a step back and try drawing. I also want to thank my little sister Annabronia for always being someone I can turn to no matter what and my grandmas for being amazing role models.

I of course must thank my morning coffee mates, Agne, Claudia, and Jonny (again), whose morning chats always brightened up my day and my office mates Isabella and Giorgous for always being able to make me laugh. I also want to thank my good friend Huda for being my little piece of America here in Germany. Lastly, I want to thank my fellow group members though out these past years for their help and friendship: Magda, Souradeep, Grzegorz, Sergey, Chiara, Matias, and Aakash.

I would like to thank my collaborator Dr. Melissa Ness for her helpful guidance and reassuring positivity through out all our meetings. I would also like to thank my other collaborators Joss Bland-Hawthorn and Kenneth Freeman.

Finally, even though they cannot understand this, I would like to thank my furry friends Batty, Trotsky, and Spotty for bringing me so much joy through out my life.